



The
University
Of
Sheffield.

Evolution of Residual Stress in Ti6Al4V components fabricated using Selective Laser Melting

By:

Haider Ali

A thesis submitted in partial fulfilment of the requirements for the degree of
Doctor of Philosophy

Academic Supervisors:

Dr. Kamran Mumtaz

Dr. Hassan Ghadbeigi

Industrial Supervisors at TWI

South Yorkshire:

Roger Fairclough

The University of Sheffield

Faculty of Engineering

School (or Department) of Mechanical Engineering

Submission Date: 17th of August, 2017.

Abstract

During the Selective Laser Melting (SLM) process large temperature gradients can form, generating a mismatch in elastic deformation that can lead to high levels of residual stress within the additively manufactured metallic structure. Rapid melt pool solidification causes SLM processed Ti6Al4V to form a martensitic microstructure with a ductility generally lower than a hot working equivalent. Post-process heat treatments can be applied to SLM components to remove in-built residual stress and improve ductility.

This investigation sought to investigate and understand the root cause of residual stress formation and lower ductility in Ti6Al4V components when processed by SLM, with the aim of ultimately being able to reduce the residual stress and enhance ductility by SLM parameter adjustment. The effect of individual SLM parameters on residual stress was studied by using hole drilling method. Microstructural analysis, tensile, and Vickers hardness testing was used to understand the effect of SLM parameters on mechanical properties of Ti6Al4V components. Experimental study was carried out using a commercial Renishaw AM250 SLM machine and a modified Renishaw SLM125 machine. FEA modelling in ABAQUS with user subroutines DFLUX and USDFLD was used to predict the correlation between SLM parameters, cooling rates and temperature gradients.

The experimental investigation included studying the effect of scanning strategy, layer thickness, rescanning, power and exposure variation keeping energy density

constant, and bed pre heating temperature on residual stress and mechanical properties of SLM Ti6Al4V parts.

Finally an I-Beam geometry was created to identify the geometrical dependence of residual stress in SLM Ti6Al4V components. Stress reduction strategies from the study of individual SLM parameters were strategically applied to high stress regions of the I-Beam geometry to devise techniques for stress reduction across the cross section of a complex geometry.

Acknowledgements

It was a difficult journey and I would never have imagined myself writing this without all the people who were there for me at every step. Every time I fell, the only reason I was able to get back on my feet was because of the supporting people around me. The success in this project belongs to my supervisors whose doors were always open for me, it belongs to that technicians who were the team I depended on, it belongs to the friends who were there to hear the problems I faced even though they did not belong to the field, it belongs above all to the family whose prayers made it possible. The list of names of the people involved at various points, all of whom have had an effect on the process and outcome of the work is endless. However, I feel it necessary to thank the following people specifically for their significant contributions and support:

I would like to thank my primary academic supervisor, Dr Kamran Mumtaz, for his support and guidance throughout this project. I would like to thank him for always being the beacon of light and hope at every stage. I would like to thank him for his encouragement when I achieved something small and his ingenious ideas when I got stuck. His knowledge of this field ensured a successful conclusion to this project, along with publication of part of this work in a high ranking journal.

I would also like to thank my secondary supervisor, Dr. Hassan Ghadbeigi, whose extensive knowledge of the field of mechanical testing and metallurgy showed me how to analyse results and what to look for. I would like to thank him for his enthusiasm and interest at every step to find new directions. In short I can say Dr.

Hassan's contributions were invaluable for the success of this project. I can attribute much of my learning regarding the fundamental aspects of testing and modelling to his guidance.

I thank TWI Ltd and EPSRC for their financial support in this project. I also wish to thank my industrial supervisor, Roger Fairclough, who was always there to hear my ideas and provide me an expert opinion. I would like to thank him for being patient with me and being an excellent mentor without whom the success of this project would not have been possible.

I would like to thank the whole team of TWI Technology Centre South Yorkshire for supporting me at every step of the project. I would like Dr. Emma Ashcroft (Section Manager) for allowing me to be a part of their team at TWI South Yorkshire. Dr. Carl Hauser's expert opinions and Utkarsha Ankalkhope's expertise and support deserve my gratitude as well.

I am specifically indebted to Tomasso Maccio the technician in the SLM lab, a friend, a colleague, a mentor, in short the one without whom I would never have been able to complete this work. Thank you Tom for your long hours and your invaluable support.

Thanks are also due to the modelling team at TWI Cambridge. I would like to thank Marcus Warwick (Manager - Numerical Modelling and Optimisation Section) at TWI Cambridge for allowing me to work with his team and learn about modelling and simulation in ABAQUS. I would like to thank Yang Yang and Sabrina Blackwell who provided me an extensive and expert support at every stage of modelling throughout the project.

I would like to express my gratitude to the testing team at TWI Cambridge. I am indebted to Stuart Green, Martin Frost, Jerry Godden, Ashley Spencer, and Ramin Taheri for their support.

I would like to express my gratitude to Dr. Raja Khan (Technology Specialist Materials and Joining) at TWI Cambridge for sharing his expertise of metallurgy and the field of SLM. I have learned from his expertise and I am really grateful to him.

I would like to thank Dr. Foroogh Hosseinzadeh (Lecturer in Energy and Materials Engineering Department at The Open University, Milton Keynes) and her team for offering free of cost Contour Method testing for I-Beam samples. Thank you very much for your support as this greatly helped us in studying a novel and challenging aspect of SLM technology.

I would like to thank my colleagues Omar Lopez, Pratik Vora, Neil Harrison, Rafael Martinez, Miguel Zavalla, Dr. James Hunt, and Marco Galindo without whose assistance I would not have been able to complete this work in its entirety.

I would also like to thank the Departments of Mechanical Engineering and Materials Science and Engineering at the University of Sheffield for administrative support.

I will like to thank my friends for their support and encouragement, specifically Dr. Bilal Ahmed who has been there for me at every step and who always had time to listen to my thoughts and help me straighten them out.

Perhaps the greatest thanks goes to my family, whose prayers, support, encouragement and love helped me to get through the difficult period of the last 4 years. It was the prayers of my parents Khkul Dada and Ya that kept me going. It was the trust my uncle Kaka had in me that kept me going. It was the encouragement

from my brothers and cousins and the love of my sisters that gave me the strength to undertake this task. Shah Nawaz Khan you were right that University of Sheffield should give you an honorary degree as well for you have listened to and helped me with each and every step of the project. I owe the success of this project to all of you, I love you all and thank you.

Contents

Abstract	ii
Acknowledgements.....	iv
List of Tables	xii
List of Figures	xiii
List of Abbreviations.....	xxiii
List of Symbols	xxvi
List of Publications	xxix
1 Introduction.....	1
1.1 Motivation.....	2
1.2 Challenges Associated with AM Manufactured Parts.....	3
1.3 Research Aims and Objective	7
1.4 Novelty	8
1.5 Brief Overview of Methodology.....	10
1.6 Outline	11
2 Literature Review.....	13
2.1 Additive Manufacturing Classification	13
2.2 Selective Laser Melting.....	17
2.3 Challenges Associated with SLM.....	19
2.4 Residual Stress.....	22
2.5 Residual Stresses in SLM	24
2.6 SLM Parameters and Their Effect on Parts.....	29

2.7	Residual Stress Reduction Strategies from Published Literature	40
2.8	Ti6Al4V and its Applications	46
2.9	Ti6Al4V Micro-structure and Mechanical Properties.....	48
2.10	Residual Stress Measurement Techniques.....	58
2.11	The use of modelling in the measurement of Residual Stress in SLM applications.....	63
2.12	Geometrical Dependence of Residual Stress in SLM Components.....	69
2.13	Knowledge Gap.....	71
3	Experimental Methodology.....	75
3.1	Titanium Alloy Powder	75
3.2	SLM Systems	75
3.3	Optimisation of parameters.....	77
3.4	Trials for Effect of SLM Process Parameters on Residual Stress and Mechanical Properties using Standard AM250 Machine.....	82
3.5	Residual Stress Measurement by Air-brasive Hole Drilling.....	95
3.6	Tensile Testing.....	99
3.7	Hardness and Micro Hardness Testing	100
3.8	Geometrical Dependence of Residual Stress.....	101
3.9	Contour Method Analysis.....	103
4	Modelling.....	104
4.1	Thermal Model.....	104
4.2	Heat Source	105
4.3	Material Properties.....	107
4.4	Initial Conditions.....	114

4.5	Heat Losses.....	114
4.6	Thermal Model Validation	116
4.7	Data Extraction from the Thermal Model	117
4.8	Modelling Trials.....	118
4.9	Validation of Thermal Modelling	120
4.10	Temperature Distribution and Solidification Behavior Predicted from FEA 125	
4.11	Validation of the effect of FEA Predicted Cooling Rate on Residual Stress 128	
5	Results (Effect of Individual SLM Parameters).....	131
5.1	SLM parameter optimisation for Ti6Al4V.....	131
5.2	Effect of Scanning Strategy	134
5.3	Effect of Layer Thickness.....	143
5.4	Effect of Re-Scanning Varying Exposure	149
5.5	Effect of Re-Scanning with Varying Power	156
5.6	Effect of Power and Exposure keeping Energy Density Constant	163
5.7	Effect of Bed Pre-Heat Temperature	170
6	Discussion (Effect of Individual SLM Parameters).....	184
6.1	SLM parameter optimisation for Ti6Al4V.....	184
6.2	Effect of Scanning Strategy	186
6.3	Effect of Layer Thickness.....	194
6.4	Effect of Re-Scanning Varying Exposure	202
6.5	Effect of Re-Scanning with Varying Power	213
6.6	Effect of Power and Exposure keeping Energy Density Constant	222

6.7	Effect of Bed Pre-Heat Temperature	230
7	Strategic Stress Reduction Strategy.....	245
7.1	Geometrical Dependence of Residual Stress.....	245
8	Conclusions and Future Work.....	270
8.1	Modelling.....	270
8.2	Effect of SLM Parameters	272
8.3	Strategic Stress Reduction	278
8.4	Suggestions for Future Work.....	278
Appendix-A.	Residual Stress Measurement Techniques	290
Appendix-B.	FORTRAN Subroutines.....	305
B.1	DFLUX	305
B.2	USDFLD	309

List of Tables

TABLE 2-1 MECHANICAL PROPERTIES OF AS BUILT AND HEAT TREATED SLM Ti6Al4V COMPONENTS.....	57
TABLE 3-1 COMPOSITION OF Ti6Al4V POWDER.....	75
TABLE 3-2 SLM BUILD PARAMETERS.....	79
TABLE 3-3 TEST ARRAY FOR POWER AND EXPOSURE.....	81
TABLE 3-4 SCANNING STRATEGY TEST CASES.....	84
TABLE 3-5 LAYER THICKNESS TEST CASES.....	87
TABLE 3-6 RE-SCAN WITH VARYING EXPOSURE TEST CASES.....	89
TABLE 3-7 RE-SCAN WITH VARYING POWER TEST CASES.....	89
TABLE 3-8 CONSTANT ENERGY DENSITY TEST CASES.....	90
TABLE 3-9. BED PRE-HEAT TEMPERATURE TEST CASES.....	95
TABLE 3-10 STRATEGIC STRESS REDUCTION TEST CASES.....	102
TABLE 4-1 SELECTED THERMOPHYSICAL PROPERTIES OF POWDER Ti6Al4V[63].....	108
TABLE 4-2 THERMAL CONDUCTIVITY OF POWDER Ti6Al4V[47].....	109
TABLE 4-3 THERMOPHYSICAL PROPERTIES OF SOLID Ti6Al4V[63].....	111
TABLE 4-4 THERMAL PROPERTIES Ti6Al4V[63].....	113
TABLE 4-5 PARAMETERS FOR SINGLE LINE MELTING.....	116
TABLE 4-6. OPTIMISED PARAMETERS FOR 75µm LAYER THICKNESS SLM BUILDS.....	128
TABLE 6-1 PART DENSITY FOR DIFFERENT POWER AND EXPOSURE TIME COMBINATION.....	184
TABLE 6-2. ENERGY DENSITY FOR DIFFERENT POWER AND EXPOSURE TIME COMBINATION.....	185

List of Figures

FIGURE 2-1 ADDITIVE MANUFACTURING TECHNOLOGIES CLASSIFICATION BY ASTM INTERNATIONAL[12].	13
FIGURE 2-2 SELECTIVE LASER MELTING PROCESS [18].	18
FIGURE 2-3 PROCESS WINDOW FOR (A) CONTINUOUS WAVE OPERATION AND (B) PULSED OPERATION[23].	20
FIGURE 2-4 EXAMPLE OF DISTORTION CAUSED WHEN PAIR OF COPLANAR PLATES IS WELDED TOGETHER AND JOINT IS ALLOWED TO COOL TO AMBIENT TEMPERATURE[27].	24
FIGURE 2-5 LEFT (A) INDUCED STRESSES AND DEFORMATION (STRAIN) DURING LASER BEAM HEATING.	26
FIGURE 2-6 RIGHT (A) OCCURRING STRESSES AND DEFORMATION (STRAIN) WHEN THE PART COOLS DOWN.	26
FIGURE 2-7 (A) RESIDUAL STRESSES AFTER ADDING TWO LAYERS OF MELTED POWDER ON A BASE PLATE.	28
FIGURE 2-8 (A) RESIDUAL STRESSES WITHIN AN SLM PART STILL CONNECTED TO THE BASE PLATE.	28
FIGURE 2-9 SLM PARAMETERS AFFECTING PART PROPERTIES.	29
FIGURE 2-10 (A) POINT DISTANCE (B) HATCH SPACING (C) CORE VOLUME AND CONTOUR SPACING	30
FIGURE 2-11 PROCESS WINDOW OF SLM MELT ZONES FOR Ti6Al4V [31].	31
FIGURE 2-12 THE WIDTH AND DEPTH OF THE MOLTEN POOL VERSUS IRRADIATION TIME. IRRADIATION TIME IS THE RATIO OF LASER SPOT DIAMETER TO SCANNING SPEED [34].	33
FIGURE 2-13 THE MAXIMUM TRUE TEMPERATURE OF MOLTEN POOL VERSUS IRRADIATION TIME AND LASER POWER [34].	34
FIGURE 2-14 SCANNING STRATEGIES [44].	36
FIGURE 2-15 MAX S11(X-DIRECTION) AND S22(Y-DIRECTION) STRESS COMPARISON FOR ALL SCANNING STRATEGIES CASES [44].	38
FIGURE 2-16. PRINCIPLE OF THE METHOD FOR IDENTIFYING THE RESIDUAL STRESSES IN THE TEST PARTS. (A) BEFORE, AND (B) AFTER REMOVAL FROM BASE PLATE. GEOMETRY OF THE TEST PARTS: (C) VARIABLE WIDTH W AND THICKNESS T TO OPTIMIZE THE BRIDGE STRUCTURE FOR REPEATABILITY. (D) FINAL DIMENSIONS OF THE OPTIMIZED BRIDGE GEOMETRY [MM][4].	41
FIGURE 2-17 PSEUDO-BINARY SECTION THROUGH A B ISOMORPHOUS PHASE DIAGRAM (SCHEMATICALLY) [69].	49

FIGURE 2-18 PROCESSING ROUTE FOR LAMELLAR MICROSTRUCTURES OF A+B TITANIUM ALLOYS (SCHEMATICALLY), ADAPTED FROM [69].	50
FIGURE 2-19. TYPICAL MICROSTRUCTURE ACHIEVED BY SLM TECHNOLOGY [70].	51
FIGURE 2-20 (A) GLOBULAR ‘REFERENCE’, (B) AS-BUILT SLM STRUCTURES AND EFFECT OF THERMOMECHANICAL TREATMENT ON THE MICROSTRUCTURE OF THE SLM SAMPLES (C-E), ADAPTED FROM [73].	53
FIGURE 2-21 (A) . INFLUENCE OF SLIP LENGTH (A COLONY SIZE) ON MECHANICAL PROPERTIES, (SCHEMATICALLY) (B) EFFECT OF COOLING RATE FROM THE B PHASE FIELD ON YIELD STRESS AND DUCTILITY OF FULLY LAMELLAR STRUCTURES [65, 81].	55
FIGURE 2-22 RESIDUAL STRESS MEASUREMENT METHODS	59
FIGURE 2-23 RESIDUAL STRESS SPECIMEN WITH STRAIN GAGE ROSETTE SHOWING HOLE DRILLED IN CENTRE	61
FIGURE 2-24 SCHEMATIC OF CONTOUR METHOD [53].	62
FIGURE 2-25 (1) SHOWING A GEOMETRY WITH A SHARP CORNER AND A SLIGHTLY LESS SHARP CORNER. (2) SAME GEOMETRY AS (1) BUT THE CURVATURE OF BOTH CORNERS IS INCREASED. ADAPTED FROM[110].	70
FIGURE 3-1 RENISHAW AM250 SLM MACHINE	76
FIGURE 3-2 DENSITY OPTIMISATION TRIAL	80
FIGURE 3-3 SCHEMATIC OF 90° ALTERNATING SCANNING STRATEGY	85
FIGURE 3-4 (A) SCHEMATIC OF CHESSBOARD SCANNING (B) SCHEMATIC OF CHESSBOARD SCANNING WITH ADJACENT CHESSBOARD SQUARES SCANNED IN 90° ROTATED DIRECTION	86
FIGURE 3-5 RENISHAW SLM 125 MACHINE CHAMBER WITH CUSTOM DESIGNED HEATED BED	92
FIGURE 3-6(A) RESIDUAL STRESS BLOCK BUILT AT 370°C (B) TENSILE SPECIMENS BUILT AT 370°C.	94
FIGURE 3-7. RESIDUAL STRESS SAMPLES REPRESENTATIVE BUILD FROM RENISHAW AM250 SLM MACHINE.	96
FIGURE 3-8 RESIDUAL STRESS SPECIMEN WITH STRAIN GAGE ROSETTE SHOWING HOLE DRILLED IN CENTRE TO MEASURE RESIDUAL STRESS ON THE TOP OF THE SPECIMEN IN XY PLAN.	97
FIGURE 3-9. RESIDUAL STRESSES ALONG HEIGHT DIRECTION IN THE THREE SAMPLES[113].	98
FIGURE 3-10. TENSILE SAMPLES REPRESENTATIVE BUILD FROM RENISHAW AM250 SLM MACHINE.	100

FIGURE 3-11. CROSS-SECTIONED 30X30X10MM RESIDUAL STRESS BLOCKS FOR (A) VICKERS MICRO-HARDNESS (HV0.2) AND (B) VICKERS HARDNESS (HV5).....	101
FIGURE 3-12 (A) DIMENSIONED I-BEAM GEOMETRY (B) I-BEAM REGIONS FOR STRATEGIC APPLICATION OF STRESS REDUCTION STRATEGIES.....	102
FIGURE 3-13(A) I-BEAM GEOMETRY WITH SUPPORTS (B) I-BEAM GEOMETRY WITHOUT SUPPORTS	103
FIGURE 4-1 (A) MODEL (B) MESH.....	105
FIGURE 4-2. LASER INTENSITY VARIATION IN Z-AXIS.....	107
FIGURE 4-3 (A) SURFACES FOR CONDUCTION TO SUBSTRATE. (B) SURFACES FOR CONDUCTION TO SURROUNDING POWDER.	115
FIGURE 4-4 (A) RED SPOT SHOWS THE CENTER OF THE SECOND LASER SPOT PICKED FOR CALCULATING COOLING RATE. (B) RED SPOTS SHOW SIX LOCATIONS PICKED FROM TOP OF THE SECOND SPOT TO A DEPTH OF 300 μ M IN INCREMENTS OF 50 μ M IN THE DEPTH DIRECTION.	118
FIGURE 4-5. EXPERIMENTAL AND MODEL PREDICTED MELT-POOL DIMENSIONS COMPARISON	121
FIGURE 4-6 (A) EXPERIMENTALLY MEASURED MELT-POOL DIMENSIONS (B) MELT-POOL DIMENSIONS PREDICTED BY ABAQUS FINITE ELEMENT THERMAL MODEL	122
FIGURE 4-7. (A) COMPARISON OF FEA MODEL PREDICTED TEMPERATURE IN XY-PLANE ALONG THE LASER SCANNING DIRECTION WITH EXPERIMENTALLY DETERMINED DISTRIBUTION OF THE BRIGHTNESS TEMPERATURE IN THE XY-PLANE ALONG THE LASER SCANNING DIRECTION; P=50 W, V=0.1 M/S VALUES ADAPTED FROM REF-[34]. (B) HIGHLIGHTS THE 325 μ M DISTANCE WITH POINTS CONSIDERED FOR FEA MODEL PREDICTED TEMPERATURE IN XY-PLANE ALONG THE LASER SCANNING DIRECTION.	124
FIGURE 4-8. (A) (TOP VIEW) TEMPERATURE AND MATERIAL SOLIDIFICATION EVOLUTION ALONG THE LASER SCAN PATH IN XY-PLANE ALONG THE LASER SCANNING DIRECTION. (B) DIMENSIONED ISOMETRIC VIEW SHOWING THE DEPTH USED FOR VOLUMETRIC HEAT ADDITION. (C) (FRONT VIEW) TEMPERATURE AND MATERIAL SOLIDIFICATION EVOLUTION ALONG THE DEPTH OF LASER SCAN PATH IN ZY-PLANE ALONG THE LASER SCANNING DIRECTION. (D) (SIDE VIEW) TEMPERATURE DISTRIBUTION ACROSS THE DEPTH (ZX PLANE OF THE MELT-POOL).....	126
FIGURE 4-9. (A) EFFECT OF POWER AND EXPOSURE COMBINATION KEEPING ENERGY DENSITY CONSTANT ON COOLING RATE AND RESIDUAL STRESS. (B) TEMPERATURE GRADIENT PREDICTION BETWEEN THE TOP SURFACE OF THE MELT-POOL AND 250 μ M DEPTH BELOW THE MELT-POOL FROM FEA SIMULATION FOR SLM Ti6Al4V SAMPLES, BUILT WITH DIFFERENT POWER AND EXPOSURE COMBINATIONS KEEPING ENERGY DENSITY CONSTANT AT OPTIMUM.	129

FIGURE 5-1 DENSITY OPTIMISATION TRIAL	132
FIGURE 5-2 (A) SAMPLE E3 WITH 99.99% DENSITY. (B) SAMPLE A1 WITH 90.49% DENSITY.....	133
FIGURE 5-3 <i>SAMPLE E3 WITH MARTENSITIC α' LATHS HIGHLIGHTED BY SOLID LINES, GROWING INSIDE COLUMNAR PRIOR B GRAINS HIGHLIGHTED BY THE DASHED LINE, WITH PORES HIGHLIGHTED BY ARROWS.</i>	134
FIGURE 5-4 EFFECT OF SCANNING STRATEGY ON % POROSITY	135
FIGURE 5-5. MARTENSITIC α' LATHS IN PRIOR B COLUMNAR GRAINS (A) TEST CASE S-1, 90° ALTERNATING SCANNING STRATEGY. (B) TEST CASE S-3, 3X3 CHESSBOARD SCANNING STRATEGY. (C) TEST CASE S-5, 5X5 CHESSBOARD SCANNING STRATEGY WITH SCAN VECTORS ROTATED AT 90° IN ADJACENT ISLANDS.	136
FIGURE 5-6 EFFECT OF SCANNING STRATEGY ON RESIDUAL STRESS	137
FIGURE 5-7 EFFECT OF SCANNING STRATEGY ON UTS, YIELD STRENGTH AND % ELONGATION.....	141
FIGURE 5-8 EFFECT OF SCANNING STRATEGY ON VICKERS HARDNESS	142
FIGURE 5-9 EFFECT OF LAYER THICKNESS ON % POROSITY	144
FIGURE 5-10. MARTENSITIC α' LATHS IN PRIOR B COLUMNAR GRAINS (A) TEST CASE LT-1, 25 μ M LAYER THICKNESS. (B) TEST CASE LT-2, 50 μ M LAYER THICKNESS. (C) TEST CASE LT-3, 75 μ M LAYER THICKNESS.	144
FIGURE 5-11 EFFECT OF LAYER THICKNESS ON RESIDUAL STRESS	145
FIGURE 5-12 EFFECT OF LAYER THICKNESS ON UTS AND YIELD STRENGTH AND % ELONGATION	147
FIGURE 5-13 EFFECT OF LAYER THICKNESS ON VICKERS HARDNESS	148
FIGURE 5-14 EFFECT OF RE-SCANNING WITH VARYING EXPOSURE ON % POROSITY	150
FIGURE 5-15 MARTENSITIC α' LATHS IN PRIOR B COLUMNAR GRAINS (A) TEST CASE S-1, 90° ALTERNATING SCANNING STRATEGY WITH NO RE-SCAN. (B) TEST CASE RSE-1, RE-SCAN WITH 50 μ s. (C) TEST CASE RSE-4, RE-SCAN WITH 150 μ s.	151
FIGURE 5-16 EFFECT OF RE-SCANNING ENERGY VARYING EXPOSURE ON RESIDUAL STRESS.....	152
FIGURE 5-17. EFFECT OF RE-SCANNING ENERGY VARYING EXPOSURE ON UTS AND YIELD STRENGTH AND % ELONGATION..	154
FIGURE 5-18 EFFECT OF RE-SCANNING ENERGY VARYING EXPOSURE ON VICKERS HARDNESS.....	155
FIGURE 5-19 EFFECT OF RE-SCANNING WITH VARYING POWER ON % POROSITY	157

FIGURE 5-20 MARTENSITIC A' LATHS IN PRIOR B COLUMNAR GRAINS (A) TEST CASE S-1, 90° ALTERNATING SCANNING STRATEGY WITH NO RE-SCAN. (B) TEST CASE RSP-1, RE-SCAN WITH 100W. (C) TEST CASE RSE-3, RE-SCAN WITH 200W.	158
FIGURE 5-21. EFFECT OF RE-SCANNING ENERGY VARYING POWER ON RESIDUAL STRESS	159
FIGURE 5-22. EFFECT OF RE-SCANNING ENERGY VARYING POWER ON UTS AND YIELD STRENGTH AND % ELONGATION	162
FIGURE 5-23 EFFECT OF RE-SCANNING ENERGY VARYING POWER ON VICKERS HARDNESS.....	163
FIGURE 5-24 EFFECT OF POWER AND EXPOSURE KEEPING ENERGY DENSITY CONSTANT ON % POROSITY.....	164
FIGURE 5-25. MARTENSITIC A' LATHS IN PRIOR B COLUMNAR GRAINS (A) TEST CASE S-1, 90° ALTERNATING SCANNING STRATEGY WITH OPTIMUM COMBINATION OF POWER (200W) & EXPOSURE (100μs). (B) TEST CASE CED-1, POWER (180W) & EXPOSURE (111μs). (C) TEST CASE CED-4, POWER (150W) & EXPOSURE (133μs).....	165
FIGURE 5-26. EFFECT OF VARYING POWER AND EXPOSURE TIME COMBINATION FOR A CONSTANT ENERGY DENSITY ON RESIDUAL STRESS	166
FIGURE 5-27. EFFECT OF VARYING POWER AND EXPOSURE TIME COMBINATION FOR A CONSTANT ENERGY DENSITY ON UTS, YIELD STRENGTH AND % ELONGATION	168
FIGURE 5-28 EFFECT OF VARYING POWER AND EXPOSURE TIME COMBINATION FOR A CONSTANT ENERGY DENSITY ON VICKERS HARDNESS	169
FIGURE 5-29 EFFECT OF BED PRE-HEAT TEMPERATURE ON % POROSITY	171
FIGURE 5-30 (A) TEST CASE T-1 (100°C) DISPLAYING PRIOR B COLUMNAR GRAINS. (B) TEST CASE T-6 DISPLAYING PRIOR B COLUMNAR GRAINS (770°C).....	172
FIGURE 5-31 MARTENSITIC MICROSTRUCTURE OF THE SAMPLES IN (A) TEST CASE T-1 (100°C) WITH (B) SHOWING DIFFERENT A' LATH SIZES (C) A' LATHS IN PRIOR B GRAINS IN CASE T2 (370°C). (D) TEST CASE T-2 SHOWS GROWTH IN A' LATHS SIZE (ELLIPSE) AND WHITE B PARTICLES STARTING TO FORM BETWEEN α' LATHS SHOWN BY THE ARROWS.....	173
FIGURE 5-32. (A) TEST CASE T-3 (470°C) SHOWS DECREASES IN α' MARTENSITIC LATHS DUE TO DECOMPOSITION INTO A, HIGHLIGHTED BY RED CIRCLES. (B) TEST CASE T-3, SHOWS WHITE B PARTICLES GROWING BETWEEN α/α' LATHS (INDICATED BY THE ARROWS). (C) TEST CASE T-4 (570°C) SHOWS α' MARTENSITE HAS DECOMPOSED INTO EQUILIBRIUM BASKETWEAVE A+B MICROSTRUCTURE, HIGHLIGHTED BY RED CIRCLES. (D) TEST CASE T-4 SHOWS B GROWING BETWEEN A LATHS AND B STARTING TO GROW INSIDE A LATHS (INDICATED BY ARROWS).....	174

FIGURE 5-33. (A) TEST CASE T-5 (670°C), SHOWING THE START OF GRAIN BOUNDARY A GLOBULORISATION, HIGHLIGHTED BY THE RED RECTANGLES. (B) TEST CASE T-5 SHOWING THE GROWTH IN WHITE B PARTICLES BETWEEN AND INSIDE A LATHS (INDICATED BY THE RED ARROWS). (C) TEST CASE T-6 (770°C) SHOWS AN INCREASE IN GLOBULAR A, HIGHLIGHTED BY THE RED RECTANGLES. (D) TEST CASE T-6 SHOWS AN INCREASE IN GRAIN BOUNDARY B AND B INSIDE A LATHS (INDICATED BY THE RED ARROWS).	176
FIGURE 5-34(A) OPTICAL MICROGRAPH OF 670°C SAMPLE AT 200X SHOWING GLOBULAR A HIGHLIGHTED BY RED RECTANGLES. (B) OPTICAL MICROGRAPH OF 770°C SAMPLE AT 200X SHOWING GLOBULAR A HIGHLIGHTED BY RED RECTANGLES. (C) SEM SECONDARY IMAGE OF 770°C SAMPLE SHOWING NANO B-PARTICLES INSIDE A-LATHS HIGHLIGHTED BY RED ELLIPSES.	177
FIGURE 5-35 EFFECT OF BED PRE-HEAT TEMPERATURE ON RESIDUAL STRESS	179
FIGURE 5-36 EFFECT OF BED PRE-HEAT TEMPERATURE ON UTS, YIELD STRENGTH AND % ELONGATION	181
FIGURE 5-37 EFFECT OF BED PRE-HEAT TEMPERATURE ON VICKERS MICRO HARDNESS.....	182
FIGURE 6-1 EFFECT OF SCAN VECTOR LENGTH ON TEMPERATURE	187
FIGURE 6-2 EFFECT OF SCAN VECTOR LENGTH ON COOLING RATE	188
FIGURE 6-3 EFFECT OF SCANNING STRATEGY ON RESIDUAL STRESS IN 25x25x10MM SAMPLES BUILT AT DIFFERENT BED PRE-HEAT TEMPERATURES USING RENISHAW SLM125 MACHINE.	192
FIGURE 6-4. RELATIONSHIP BETWEEN SCANNING STRATEGY % POROSITY, % ELONGATION AND YIELD STRENGTH.	194
FIGURE 6-5. EFFECT OF LAYER THICKNESS ON MELTPOOL DIMENSIONS (A) TEST CASE LT-1 (25µM LAYER THICKNESS). (B) TEST CASE LT-2 (50µM LAYER THICKNESS) AND (C) TEST CASE LT-3 (75µM LAYER THICKNESS).....	195
FIGURE 6-6 EFFECT OF LAYER THICKNESS ON COOLING RATES	196
FIGURE 6-7 INTER LAYER DEFECTS (A) LT-1 (B) LT-2 (C) LT-3	197
FIGURE 6-8 EFFECT OF LAYER THICKNESS ON TEMPERATURE GRADIENT	198
FIGURE 6-9 EFFECT OF LAYER THICKNESS ON COOLING RATE AND RESIDUAL STRESS	199
FIGURE 6-10 RELATIONSHIP BETWEEN LAYER THICKNESS, % POROSITY, % ELONGATION AND YIELD STRENGTH	200
FIGURE 6-11 EFFECT OF RE-SCANNING WITH VARYING EXPOSURE ON MELTPOOL DIMENSIONS (A) TEST CASE RSE-1 (50µS EXPOSURE), (B) TEST CASE RSE-2 (75µS EXPOSURE), (C) TEST CASE RSE-3 (100µS EXPOSURE) AND (D) TEST CASE RSE-4 (150µS EXPOSURE).....	203

FIGURE 6-12. EFFECT OF RE-SCANNING WITH VARYING EXPOSURE ON COOLING RATES.....	204
FIGURE 6-13. EFFECT OF RE-SCANNING WITH VARYING EXPOSURE ON MICRO POROSITY (A) TEST CASE S-1 (NO RE-SCANNING) (B) TEST CASE RSE-1 (50 μ S EXPOSURE), (C) TEST CASE RSE-2 (75 μ S EXPOSURE), (D) TEST CASE RSE-3 (100 μ S EXPOSURE) AND (E) TEST CASE RSE-4 (150 μ S EXPOSURE).....	206
FIGURE 6-14 EFFECT OF RE-SCANNING WITH VARYING EXPOSURE ON TEMPERATURE GRADIENT	208
FIGURE 6-15. EFFECT OF RE-SCANNING WITH VARYING EXPOSURE ON COOLING RATE AND RESIDUAL STRESS	209
FIGURE 6-16. EFFECT OF RE-SCANNING ENERGY VARYING EXPOSURE ON % POROSITY, % ELONGATION AND YIELD STRENGTH	211
FIGURE 6-17 EFFECT OF RE-SCANNING WITH VARYING POWER ON MELTPOOL DIMENSIONS (A) TEST CASE RSP-1 (100W POWER), (B) TEST CASE RSP-2 (150W POWER), AND (C) TEST CASE RSP-3 (200W POWER)	214
FIGURE 6-18 EFFECT OF RE-SCANNING WITH VARYING POWER ON COOLING RATES	215
FIGURE 6-19 EFFECT OF POWER ON MINIMUM ENERGY DENSITY REQUIRED FOR NEARLY FULL DENSE Ti6Al4V SLM PARTS.	216
FIGURE 6-20 EFFECT OF RE-SCANNING WITH VARYING POWER ON TEMPERATURE GRADIENT.....	218
FIGURE 6-21. EFFECT OF RE-SCANNING WITH VARYING POWER ON COOLING RATE AND RESIDUAL STRESS	219
FIGURE 6-22 EFFECT OF RE-SCANNING ENERGY VARYING EXPOSURE ON % POROSITY, % ELONGATION AND YIELD STRENGTH	220
FIGURE 6-23 EFFECT OF VARYING POWER AND EXPOSURE TIME COMBINATION FOR A CONSTANT ENERGY.....	223
FIGURE 6-24 EFFECT OF VARYING POWER AND EXPOSURE TIME COMBINATION FOR A CONSTANT ENERGY.....	224
FIGURE 6-25 EFFECT OF VARYING POWER AND EXPOSURE TIME COMBINATION FOR A CONSTANT ENERGY DENSITY ON TEMPERATURE GRADIENT	226
FIGURE 6-26 EFFECT OF VARYING POWER AND EXPOSURE TIME COMBINATION FOR A CONSTANT ENERGY DENSITY ON COOLING RATE AND RESIDUAL STRESS	227
FIGURE 6-27 EFFECT OF VARYING POWER AND EXPOSURE TIME COMBINATION FOR A CONSTANT ENERGY DENSITY ON %POROSITY, % ELONGATION AND YIELD STRENGTH	229

FIGURE 6-28 EFFECT OF BED PRE-HEAT TEMPERATURE ON MELTPOOL DIMENSIONS (A) TEST CASE T-1 (100°C). (B) TEST CASE T-2 (370°C), (C) TEST CASE T-3 (470°C), (D) TEST CASE T-4 (570°C), (E) TEST CASE T-5 (670°C) AND (F) TEST CASE T-6 (770°C).....	231
FIGURE 6-29 EFFECT OF BED PRE-HEAT TEMPERATURE ON COOLING RATES.....	232
FIGURE 6-30 EFFECT OF BED PRE-HEAT TEMPERATURE ON TEMPERATURE GRADIENT	235
FIGURE-6-31 YIELD STRESS AND YOUNG’S MODULUS OF WROUGHT ANNEALED Ti6Al4V AS A FUNCTION OF TEMPERATURE. DATA ADAPTED FROM [130].	236
FIGURE 6-32 EFFECT OF BED PRE-HEAT TEMPERATURE ON COOLING RATE AND RESIDUAL STRESS	237
FIGURE 6-33 EFFECT OF BED PRE-HEAT TEMPERATURE ON %POROSITY, % ELONGATION AND YIELD STRENGTH.....	239
FIGURE 7-1 (A) DIMENSIONED I-BEAM GEOMETRY (B) I-BEAM REGIONS FOR STRATEGIC APPLICATION OF STRESS REDUCTION STRATEGIES.....	245
FIGURE 7-2. RESIDUAL STRESS MAP STANDARD I-BEAM (TEST CASE IB-1) MANUFACTURED WITH OPTIMUM PARAMETERS FROM DENSITY OPTIMISATION TRIALS (HIGH STRESS REGIONS INDICATED BY DASHED BLACK RECTANGLES, REGION-2 AND REGION-4).....	246
FIGURE 7-3. COMPARISON OF RESIDUAL STRESS CONTOUR MAPS FOR VARIOUS TEST CASES (A) IB-1 (STANDARD I-BEAM WITH OPTIMISED PARAMETERS), (B) IB-2 (75µM LAYER THICKNESS FOR REGION-2 & REGION-4), (C)IB-3 (150W POWER AND 133µS EXPOSURE FOR REGION-2 & REGION-4), (D)IB-4 (570°C BED PRE-HEATING ON RENISHAW SLM-125 MACHINE), (E) IB-5 (75µM LAYER THICKNESS FOR REGION-1 & REGION-3) AND (F) IB-6 (150W POWER AND 133µS EXPOSURE FOR REGION-1 & REGION-3).	249
FIGURE 7-4. REGION-4 AREAS CORRESPONDING TO DIFFERENT STRESS LEVELS FOR VARIOUS TEST CASES (A) IB-1 (STANDARD I-BEAM WITH OPTIMISED PARAMETERS), (B) IB-2 (75µM LAYER THICKNESS FOR REGION-2 & REGION-4), (C)IB-3 (150W POWER AND 133µS EXPOSURE FOR REGION-2 & REGION-4), (D)IB-4 (570°C BED PRE-HEATING ON RENISHAW SLM-125 MACHINE), (E) IB-5 (75µM LAYER THICKNESS FOR REGION-1 & REGION-3) AND (F) IB-6 (150W POWER AND 133µS EXPOSURE FOR REGION-1 & REGION-3).....	251
FIGURE 7-5. REGION-4 RESIDUAL STRESS VARIATION IN VARIOUS TEST CASES (A) IB-1 (STANDARD I-BEAM WITH OPTIMISED PARAMETERS), (B) IB-2 (75µM LAYER THICKNESS FOR REGION-2 & REGION-4), (C)IB-3 (150W POWER AND 133µS EXPOSURE FOR REGION-2 & REGION-4), (D)IB-4 (570°C BED PRE-HEATING ON RENISHAW SLM-125 MACHINE), (E) IB-5 (75µM LAYER THICKNESS FOR REGION-1 & REGION-3) AND (F) IB-6 (150W POWER AND 133µS EXPOSURE FOR REGION-1 & REGION-3).....	253

FIGURE 7-6. REGION-2 AREAS CORRESPONDING TO DIFFERENT STRESS LEVELS FOR VARIOUS TEST CASES (A) IB-1 (STANDARD I-BEAM WITH OPTIMISED PARAMETERS), (B) IB-2 (75 μ M LAYER THICKNESS FOR REGION-2 & REGION-4), (C)IB-3 (150W POWER AND 133 μ S EXPOSURE FOR REGION-2 & REGION-4), (D)IB-4 (570 $^{\circ}$ C BED PRE-HEATING ON RENISHAW SLM-125 MACHINE), (E) IB-5 (75 μ M LAYER THICKNESS FOR REGION-1 & REGION-3) AND (F) IB-6 (150W POWER AND 133 μ S EXPOSURE FOR REGION-1 & REGION-3).....	256
FIGURE 7-7. REGION-2 RESIDUAL STRESS VARIATION IN VARIOUS TEST CASES (A) IB-1 (STANDARD I-BEAM WITH OPTIMISED PARAMETERS), (B) IB-2 (75 μ M LAYER THICKNESS FOR REGION-2 & REGION-4), (C)IB-3 (150W POWER AND 133 μ S EXPOSURE FOR REGION-2 & REGION-4), (D)IB-4 (570 $^{\circ}$ C BED PRE-HEATING ON RENISHAW SLM-125 MACHINE), (E) IB-5 (75 μ M LAYER THICKNESS FOR REGION-1 & REGION-3) AND (F) IB-6 (150W POWER AND 133 μ S EXPOSURE FOR REGION-1 & REGION-3).....	257
FIGURE 7-8. REGION-1 AREAS CORRESPONDING TO DIFFERENT STRESS LEVELS FOR VARIOUS TEST CASES (A) IB-1 (STANDARD I-BEAM WITH OPTIMISED PARAMETERS), (B) IB-2 (75 μ M LAYER THICKNESS FOR REGION-2 & REGION-4), (C)IB-3 (150W POWER AND 133 μ S EXPOSURE FOR REGION-2 & REGION-4), (D)IB-4 (570 $^{\circ}$ C BED PRE-HEATING ON RENISHAW SLM-125 MACHINE), (E) IB-5 (75 μ M LAYER THICKNESS FOR REGION-1 & REGION-3) AND (F) IB-6 (150W POWER AND 133 μ S EXPOSURE FOR REGION-1 & REGION-3).....	260
FIGURE 7-9. REGION-1 RESIDUAL STRESS VARIATION IN VARIOUS TEST CASES (A) IB-1 (STANDARD I-BEAM WITH OPTIMISED PARAMETERS), (B) IB-2 (75 μ M LAYER THICKNESS FOR REGION-2 & REGION-4), (C)IB-3 (150W POWER AND 133 μ S EXPOSURE FOR REGION-2 & REGION-4), (D)IB-4 (570 $^{\circ}$ C BED PRE-HEATING ON RENISHAW SLM-125 MACHINE), (E) IB-5 (75 μ M LAYER THICKNESS FOR REGION-1 & REGION-3) AND (F) IB-6 (150W POWER AND 133 μ S EXPOSURE FOR REGION-1 & REGION-3).....	262
FIGURE 7-10. REGION-3 AREAS CORRESPONDING TO DIFFERENT STRESS LEVELS FOR VARIOUS TEST CASES (A) IB-1 (STANDARD I-BEAM WITH OPTIMISED PARAMETERS), (B) IB-2 (75 μ M LAYER THICKNESS FOR REGION-2 & REGION-4), (C)IB-3 (150W POWER AND 133 μ S EXPOSURE FOR REGION-2 & REGION-4), (D)IB-4 (570 $^{\circ}$ C BED PRE-HEATING ON RENISHAW SLM-125 MACHINE), (E) IB-5 (75 μ M LAYER THICKNESS FOR REGION-1 & REGION-3) AND (F) IB-6 (150W POWER AND 133 μ S EXPOSURE FOR REGION-1 & REGION-3).....	264
FIGURE 7-11. REGION-3 RESIDUAL STRESS VARIATION IN VARIOUS TEST CASES (A) IB-1 (STANDARD I-BEAM WITH OPTIMISED PARAMETERS), (B) IB-2 (75 μ M LAYER THICKNESS FOR REGION-2 & REGION-4), (C)IB-3 (150W POWER AND 133 μ S EXPOSURE FOR REGION-2 & REGION-4), (D)IB-4 (570 $^{\circ}$ C BED PRE-HEATING ON RENISHAW SLM-125 MACHINE), (E) IB-5 (75 μ M LAYER THICKNESS FOR REGION-1 & REGION-3) AND (F) IB-6 (150W POWER AND 133 μ S EXPOSURE FOR REGION-1 & REGION-3).....	266
FIGURE 7-12 OVERALL RESIDUAL STRESS VARIATION IN VARIOUS TEST CASES (A) IB-1 (STANDARD I-BEAM WITH OPTIMISED PARAMETERS), (B) IB-2 (75 μ M LAYER THICKNESS FOR REGION-2 & REGION-4), (C)IB-3 (150W POWER AND 133 μ S	

EXPOSURE FOR REGION-2 & REGION-4), (D)IB-4 (570°C BED PRE-HEATING ON RENISHAW SLM-125 MACHINE), (E) IB-5 (75μM LAYER THICKNESS FOR REGION-1 & REGION-3) AND (F) IB-6 (150W POWER AND 133μS EXPOSURE FOR REGION-1 & REGION-3).....269

List of Abbreviations

M_s	Martensite Start Temperature
2D	Two Dimensional
3D	Three Dimensional
AC	Air Cooled
AM	Additive Manufacturing
ASTM	American Society for Testing and Materials
BCC	Body Centred Cubic
BCM	Bridge Curvature Method
CAD	Computer Aided Design
CED	Constant Energy Density
CFD	Computational Fluid Dynamics
CT	Computer Tomography
DED	Direct Energy Deposition
DMLS	Direct Metal Laser Sintering

EBM	Electron Beam Melting
EDM	Electric Discharge Machining
FEA	Finite Element Analysis
FEM	Finite Element Method
HCP	Hexagonal Close Packed
HIP	Hot Isostatic Pressing
HV	Vickers Hardness
IB	I-Beam
ISO	International Organization for Standardization
LC	Laser Cladding
LENS	Laser Engineered Net Shaping
LMD	Laser Metal Deposition
LOM	Light Optical Microscopy
LT	Layer Thickness
RSE	Re-Scanning with Varying Exposure
RSP	Re-Scanning with Varying Power

S	Scanning Strategy
SEM	Scanning Electron Microscopy
SLM	Selective Laser Melting
SLS	Selective Laser Sintering
T	Bed Pre-heat Temperature
TGM	Temperature Gradient Mechanism
TWI	The Welding Institute
UK	United Kingdom
USA	United States of America
UTS	Ultimate Tensile Strength
UV	Ultraviolet
WAAM	Wire + Arc Additive Manufacturing
WQ	Water Quenched
α	Hexagonal Close Packed phase in Ti6Al4V
α'	Hexagonal Close Packed martensitic phase in Ti6Al4V
β	Body Centred Cubic phase in Ti6Al4V

List of Symbols

ε	Strain	%
ε_{th}	Thermal Strain	%
ε_{el}	Elastic Strain	%
ε_{pl}	Plastic Strain	%
ε_1	Measured Strain from Gauge 1	%
ε_2	Measured Strain from Gauge 2	%
ε_3	Measured Strain from Gauge 3	%
σ_{yield}	Yield Stress	MPa
σ_{tens}	Tensile Residual Stress	MPa
σ_{comp}	Compressive Residual Stress	MPa
σ_{max}	Maximum Residual Stress	MPa
σ_{min}	Minimum Residual Stress	MPa
E	Youngs Modulus	MPa
v	Poisson's Ratio	

ED	Energy Density	$\frac{J}{mm^3}$
P	Laser Power	W
t	Exposure Time	μs
pd	Laser Point Distance	μm
h	Hatch Spacing	μm
lt	Layer Thickness	μm
v	Laser Scan Speed	$\frac{mm}{s}$
q_{cyl}	Cylindrical Laser Heat Flux	$\frac{J}{mm^2}$
$q_{mod\ cyl}$	Modified Cylindrical Laser Heat Flux	$\frac{J}{mm^2}$
r_{las}	Radius of Laser Spot	μm
η	Laser Absorptivity	-
I_r	Radial Laser Intensity	$\frac{J}{mm^2}$
I_z	Laser Intensity in Depth	-
flux(1)	Volumetric Laser Heat Flux	$\frac{J}{mm^3}$

K	Thermal Conductivity	mW/mm-K
κ	Thermal Conductivity Enhancement Factor	-
K'	Enhanced Thermal Conductivity	mW/mm-K

List of Publications

1. Ilie, A., H. Ali, and K. Mumtaz, In-Built Customised Mechanical Failure of 316L Components Fabricated Using Selective Laser Melting. *Technologies*, 2017. 5(1): p. 9.
2. Ali, H., et al., In-situ residual stress reduction, martensitic decomposition and mechanical properties enhancement through high temperature powder bed pre-heating of Selective Laser Melted Ti6Al4V. *Materials Science and Engineering: A*, 2017. 695: p. 211-220.

1 Introduction

Additive Manufacturing has been officially defined by the ASTM F42 committee as “the process of joining materials to make objects from 3D model data, usually layer upon layer, as opposed to subtractive manufacturing methods”[1].

Additive Manufacturing or AM is a general term for processes used to create complex 3D parts by adding material where needed as opposed to conventional machining where material is removed from where it is not needed. Parts are built in a layer by layer manner with each layer consisting of adjacent line tracks deposited/solidified next to each other. This approach provides a greater freedom for complex designs, but the physical and metallurgical phenomena associated with this type of manufacturing processes produce certain detrimental effects on the part properties, which will be made clear in this work. Selective Laser Melting (SLM) is a technique belonging to the Powder Bed Fusion family of AM processes, and is the main focus of this research.

A brief introduction is provided into some of the main issues that arise in SLM produced parts to help clarify the need for the work conducted in this research project. To conclude, the aims and objectives of the research with a brief overview of the methodology used to achieve these aims and objectives is presented in this introduction.

1.1 Motivation

Cleaner and resource-efficient production in manufacturing is the target of the whole industrial world. Additive manufacturing techniques present a viable solution towards achieving resource efficient production. AM techniques have the potential to approach zero wastage through in process recycling. Waste recycling would lead to reduced greenhouse emissions as fewer raw materials would need to be produced. AM techniques provide freedom of design without the need for part-specific tooling. AM is a key enabler for the design and topology optimization which could lead to cost and energy saving specifically in aerospace and automobile industries. AM techniques are environment friendly as they do not directly use any toxic chemicals like lubricant or coolant in any measurable amount.

Selective Laser Melting represent one of the areas of greatest potential due to the following reasons.

- A wider range of materials can be processed using lasers.
- SLM offers higher precision in comparison to other additive techniques because of the smaller laser spot size.
- Development in the field of lasers and optics can lead to cost reduction for SLM machines.

Hence, for the exploitation of sustainable AM techniques like SLM it is inevitable to enhance the performance and one of the main challenges is the buildup of high residual stress in the SLM parts. Therefore this work is focusing on identifying the

underlying reasons for residual stress in SLM parts and finding means to mitigate the residual stress.

1.2 Challenges Associated with AM Manufactured Parts

This section provides a brief introduction to the common structural integrity issues associated with AM parts and a brief introduction to the specific issues studied in this research work.

1.2.1 Structural Integrity Issues in AM Parts

AM provides many advantages over conventional manufacturing but several challenges need to be addressed and several aspects of AM process chain need improvement to realise the full potential of this technology.

Slow production time with some builds lasting over days is one major drawback. Even though time is saved in the pre-processing stage of the AM process chain, improvements in build rates are still needed to cut down the cost of AM parts. Another major issue that needs further work is expanding the material base that can be processed by AM. In order to expand the material base for AM processing, research is needed on design of new alloys as well as means of cutting down the costs of feedstock material production for AM applications.

The most important challenge that is a topic of widespread research and needs immediate attention is the in process quality control of the AM manufactured parts. Safety of AM parts and repeatability of the process can be improved only by addressing the in process challenges associated with AM. By addressing the process

induced structural integrity issues the full potential of AM techniques can be realised.

1.2.1.1 Process Induced Structural Integrity Issues

Process induced structural integrity issues associated with AM parts are associated with the characteristics of the process.

- Metastable microstructure results due to the high cooling rates associated with the process. The mechanical behavior of such microstructures is not yet completely documented and neither is the effect of conventional heat treatment strategies on such microstructure yet fully understood.
- Residual stress is yet another major challenge associated with the high cooling rates characteristic of AM processes. High residual stress limits the part size. It can induce cracking and lead to part deformations which can cause in process part failure. Materials available for AM processing are also limited due to the high residual stress generation associated with such processes.
- Porosity in AM parts is resulted by the choice of non-optimum processing parameters. Porosity in AM parts can be classified into irregular lack of fusion porosity (resulted due to insufficient energy supply) and spherical gas porosity (attributed to high energy input or entrapped gases in the feedstock material). Even though the inferior mechanical properties of AM parts is usually attributed to porosity but this mechanism still needs further

understanding as the influence of the microstructure or residual stresses on mechanical properties has been neglected so far.

- Even though great care is taken in keeping the trace elements (especially oxygen) content in feedstock material under control and AM processes are run under inert atmosphere but oxygen and nitrogen pickup during the process is still a major challenge to be addressed. The molten and resolidified material during the manufacturing of AM parts pick up a significant amount of oxygen and nitrogen. Even though the builds occur in an argon atmosphere, the hot melt pool easily picks up the trace oxygen and nitrogen present in the chamber. Oxygen and Nitrogen pick up is attributed to the high melt pool temperature and the time the material stays molten. Controlling the interstitial Oxygen and Nitrogen in AM parts is important as it can result in a decrease in the ductility.
- Surface finish of AM parts is a major challenge to be addressed for minimising the post processing requirements and as well as enhancing the part quality. Research is needed on improving the side surface finish and finding means of building overhanging structures to avoid the need of supports and improving surface finish for down facing surfaces.
- An important characteristic of the AM parts is the anisotropic mechanical properties associated with the layer wise building of parts. It is important to understand the effect of part orientation on this anisotropic mechanical behavior of final parts and determining means of minimising anisotropy.

Some of the challenges associated with AM processes can be associated to the processed material as well.

- The formation of Ti_3Al (α_2) phase is one such common challenge associated with Ti6Al4V processing via AM techniques. The existence of α_2 phase can lead to increase in yield stress but is responsible for increased crack nucleation, enhanced crack propagation and thus reduced ductility of AM parts.

In order to make AM technologies a viable manufacturing solution the inherent challenges associated with the processes need further research and ingenious solutions. The current work focuses on two of the main challenges high residual stress and low ductility of SLM parts focusing on Ti6Al4V material. A brief introduction of these two issues is presented in section-1.1.2.

1.2.2 Challenges Associated with SLM Manufactured Parts (Research Focus)

A significant challenge associated with components produced using the AM process is the development of high internal residual stresses, which are a result of the repeated heating and cooling of successive layers of powder during component build. Selective laser melting process produces rapid heating and cooling effects and high temperature gradients within the build. As a result, the general microstructural features produced by the SLM process are different to those obtained by conventional manufacturing and these complex thermal effects promote the development of residual stresses. If residual stresses are not recognised and accounted for in the design process, they can be a major factor in the subsequent

failure of a component in service, particularly one subjected to alternating loadings or corrosive environments [2-6]. Residual stresses can also cause deformation in SLM manufactured parts which is problematic when tight dimensional tolerances are required. Often, some form of post processing (Hot Isostatic Pressing or heat treatment) is required to relieve residual stresses which can substantially increase manufacturing time and costs [7]. It has been demonstrated that process parameters (i.e. scanning strategy, bed pre-heat, laser power, processing speed, layer thickness, and track overlap) determine the deformation magnitude, microstructure and the shape of residual stress profiles. By identifying the source of high residual stresses in advance and taking into account specific geometrical features, different process parameters can be applied for different regions of the part to reach high precision and performance [2, 4-6]. Another major issue with SLM is sub optimal ductility [8-10] due to the high cooling rates.

These two main problems associated with SLM produced parts warrant further investigation which justified the need for current research work.

1.3 Research Aims and Objective

The aim of this research was to understand Residual Stress development in SLM components using a combination of experimental and finite element analysis approaches.

The first stage in the experimental process involves optimising SLM parameters to achieve fully dense parts and using these parameters combined with residual stress

reduction strategies (Pre-Heating the bed, Scanning Strategy, Pre and Post scanning) from published literature to find the effectiveness of these strategies for minimising residual stress. The next stage will be understanding the combined effect of stress reduction strategies and determining the optimum combination for minimising residual stress. After establishing the optimum combination of SLM parameters and stress reduction strategies, test samples will be built on a bespoke heated bed to determine the effect of high bed temperature on residual stress and identify the range of pre-heat temperatures necessary for stress free SLM components. The final stage of the experimental approach will be drawing a relationship between residual stress reduction strategies and mechanical properties of SLM components.

A detailed FEA Thermo-Mechanical Model of the SLM process will be made to understand the physics of the problem. The FEA model will be verified by comparing results with experiments. A verified FEA model will be used to study the effect of process parameters and stress reduction strategies on residual stress.

Finally using the knowledge from the FEA model and experiments high stress areas in a geometry will be identified and residual stress will be reduced by intuitively applying stress reduction strategies to areas of high residual stress.

1.4 Novelty

An intuitive geometry dependent stress reduction strategy will be devised as a result of this research. A part with varying cross-section will be built and the residual stress profile will be generated using the contour method. Areas with higher residual

stresses will be identified and the optimum combination of stress reduction strategies will be intuitively applied to those areas.

This research is the first comprehensive study on establishing relationships between SLM parameters (scanning strategies, power, exposure, layer thickness, re-scanning strategies, build position on the platform and build platform temperature) and residual stress build up in the final parts. Secondly this research will provide insight into the combined effect of stress reduction strategies on residual stress and help in selecting the optimum combination of stress reduction strategies to obtain parts with minimum residual stress. Finally this research will illustrate the effects of stress reduction strategies on the mechanical properties of the final parts. This will be helpful in avoiding the combination of stress reduction strategies which reduces residual stress at the detriment of mechanical properties.

The novel aspects of this work can be listed as follows.

- This work is based on the Renishaw systems and thus is the first of its kind detailed work on the effect of modulated pulsed laser on the processing of Ti6Al4V SLM parts.
- Relationship between standard SLM parameters and residual stress is established.
- The effect of stress reduction strategies on mechanical properties is established.
- The effect of high bed pre-heat temperatures based on the material behavior (such as martensite decomposition and annealing temperature

range of Ti6Al4V) on residual stress and mechanical properties is established.

- Intuitive geometry dependent stress reduction strategies are devised for reducing stress across specific regions of a complex geometry.
- A verified novel enhanced volumetric heat source with isotropic enhanced thermal conductivity FEA model for SLM of Ti6Al4V is presented.

1.5 Brief Overview of Methodology

Test parts, comprising cubes for density optimisation, blocks for residual stress measurement, dog bone samples for tensile testing and I-Beam structures for understanding geometrical dependence of residual stress via the contour method were produced on a Renishaw-AM250 SLM machine. Heated Bed samples were produced on a Renishaw SLM-125. Microstructure was characterised by well-known techniques such as Light Optical Microscopy (LOM), and Scanning Electron Microscopy (SEM). Mechanical properties were determined by using Vickers hardness measurements and tensile testing. Residual stresses were measured via two distinctly different techniques. In the first method, residual stress was measured in the blocks using air-brasive hole drilling method. Secondly, the contour method was used to understand residual stress variation with geometrical features.

1.6 Outline

Chapter 2 features an extensive literature review of the following.

- Challenges associated with Selective Laser Melting.
- Residual stress and residual stress generation in SLM components.
- Effect of SLM parameters on residual stress.
- Ti6Al4V microstructure and mechanical properties.
- Effect of SLM parameters on Ti6Al4V microstructure and mechanical properties.
- Residual stress measurement techniques.
- SLM modelling.
- Geometrical dependence of residual stress in SLM components.

Chapter 3 presents details of the experimental methodology used for this work.

Chapter 4 presents details of

- FEA modelling methodology.
- Various modelling trials conducted for this work.
- Data extracted for different trials from the FEA model.
- Experimental validation of the FEA model.

Chapter 5 presents experimental results of the effect of individual SLM parameters variation on,

- Porosity.
- Microstructure.
- Residual stress.
- Mechanical properties.

of SLM Ti6Al4V components.

Chapter 6 presents a discussion on the experimental results of the effect of individual SLM parameters variation on,

- Porosity.
- Microstructure.
- Residual stress.
- Mechanical properties.

of SLM Ti6Al4V components using FEA modelling.

Chapter 7 highlights the results of contour method analysis for,

- Identifying high stress regions in a Ti6Al4V I-Beam geometry manufactured via SLM using parameters optimised for density.
- Effect of stress reduction strategies identified from Chapter 6 on residual in high stress regions of the I-Beam, when strategically applied to different locations across the build height.

Chapter 8 finally lists the overall conclusions drawn from this work and suggestions for future work.

2 Literature Review

2.1 Additive Manufacturing Classification

Additive Manufacturing processes create successive cross-sectional layers to fabricate a final part. Initially a solid model is designed in CAD or scanned as a digital CAD file, and then sliced into layers using build preparation software. The cross-sectional slicing is dependent upon the resolution of the process. Each layer of material is then selectively deposited. Some processes selectively apply energy to the cross-section to fuse the raw material[11]. According to ASTM F2792-12a [12] AM technologies are classified into seven categories as shown in Figure-2.1.

CATEGORIES	TECHNOLOGIES	PRINTED "INK"	POWER SOURCE	STRENGTHS / DOWNSIDES
Material Extrusion	Fused Deposition Modeling (FDM)	Thermoplastics, Ceramic slurries, Metal pastes	Thermal Energy	<ul style="list-style-type: none"> Inexpensive extrusion machine Multi-material printing Limited part resolution Poor surface finish
	Contour Crafting			
Powder Bed Fusion	Selective Laser Sintering (SLS)	Polyamides /Polymer	High-powered Laser Beam	<ul style="list-style-type: none"> High Accuracy and Details Fully dense parts High specific strength & stiffness Powder handling & recycling Support and anchor structure Fully dense parts High specific strength and stiffness
	Direct Metal Laser Sintering (DMLS)	Atomized metal powder (17-4 PH stainless steel, cobalt chromium, titanium Ti6Al-4V), ceramic powder		
	Selective Laser Melting (SLM)			
	Electron Beam Melting (EBM)		Electron Beam	
Vat Photopolymerization	Stereolithography (SLA)	Photopolymer, Ceramics (alumina, zirconia, PZT)	Ultraviolet Laser	<ul style="list-style-type: none"> High building speed Good part resolution Overcuring, scanned line shape High cost for supplies and materials
Material Jetting	Polyjet / Inkjet Printing	Photopolymer, Wax	Thermal Energy / Photocuring	<ul style="list-style-type: none"> Multi-material printing High surface finish Low-strength material
Binder Jetting	Indirect Inkjet Printing (Binder 3DP)	Polymer Powder (Plaster, Resin), Ceramic powder, Metal powder	Thermal Energy	<ul style="list-style-type: none"> Full-color objects printing Require infiltration during post-processing Wide material selection High porosities on finished parts
Sheet Lamination	Laminated Object Manufacturing (LOM)	Plastic Film, Metallic Sheet, Ceramic Tape	Laser Beam	<ul style="list-style-type: none"> High surface finish Low material, machine, process cost Decubing issues
Directed Energy Deposition	Laser Engineered Net Shaping (LENS) Electronic Beam Welding (EBW)	Molten metal powder	Laser Beam	<ul style="list-style-type: none"> Repair of damaged / worn parts Functionally graded material printing Require post-processing machine

Figure 2-1 Additive Manufacturing technologies classification by ASTM international[12].

2.1.1 Material Extrusion

The viscosity of a thermoplastic wire is lowered by feeding through a heated nozzle, to enable smooth deposition of continuous lines. The nozzle can move in X, Y and Z direction, while in some cases the Z direction movement is assigned to the baseplate onto which the material is deposited. It is a cost effective method common with the home users[13].

2.1.2 Powder Bed Fusion

Powder bed fusion techniques are characterised by the use of an energy beam such as laser or electron beam for selectively melting a layer of powder. Another layer of powder is deposited on top of the fused layer and subsequently scanned to fuse to the previous layer. Deckard and Beaman developed polymer powder bed fusion, in the mid-1980s, used for processing polyamides and polymer composites. Selective laser sintering is capable of creating ceramic and metal parts by melting polymer blends but high temperature post processing is required for fully sintering the structural powder. The most popular metal powder bed fusion processes are direct metal laser sintering (DMLS), selective laser melting (SLM) and electron beam melting (EBM). DMLS and SLM utilise a focussed laser beam, while EBM uses an electron beam as the energy source for fully melting metal powder. The possibility of achieving fully dense metal parts makes the powder bed fusion processes the AM category with widest applications in the building of functional and structural components building[13].

An important aspect of the SLM technology is the type of laser used in the machine. Concept laser M3 linear machine uses an Nd:YAG laser which can operate both in continuous wave and pulsed mode. EOS M250 uses a continuous wave CO2 laser, while Renishaw machines uses a modulated Nd:YG laser. The operation principle of the laser will determine the energy addition into the powder bed and thus it is important to consider this feature while comparing results across different platforms.

2.1.3 Vat Polymerization

Photopolymer is formed by curing a prepolymer resin, exposed to radiation. Photopolymerization uses these radiation curable resins, as the raw material. Irradiation by ultraviolet (UV) light causes the prepolymer to solidify upon polymerization. In the top down approach the parts are attached to a base plate which moves down into the liquid bath as each layer is irradiated from above, polymerized and solidified. The bottom up approach irradiates a thin resin layer from below and the base plate moves upward after the irradiation, polymerization and solidification of each layer[13].

2.1.4 Material Jetting

Photopolymers or wax is liquefied by passing through a heated nozzle and liquid droplets are deposited onto a baseplate. Further layers are deposited on top of the already solidified material. The process allows the deposition of multi materials on top of each other. The process is quite similar to 2D inkjet printing[13].

2.1.5 Binder jetting

In the early 1990s the binder printing method was primarily developed at MIT, where binder is jetted onto a powder layer to form cross sections of a part. After every layer of binder the machine deposits a new layer of binder and the process is repeated till the part geometry is complete. The binder is only acting to hold the part material together and through extensive post processing the binder is burnt out and the part material is sintered together[13].

2.1.6 Sheet Lamination

Sheet lamination involves cutting sheets into the right shapes first and then bonding the cross sections with each other via adhesive bonding, thermal bonding, clamping or ultrasonic welding[13].

2.1.7 Directed Energy Deposition or DED

The directed energy deposition method is used for metal parts forming similar to powder bed fusion processes, but DED involves a deposition head mounted on a robot arm for the delivery of the material. Powder is sprayed co-axially into the energy beam, or a wire is fed into the melt pool created by the beam. The combination of an electric arc as heat source and wire as feedstock is referred to as Wire + Arc Additive Manufacturing (WAAM). The Laser Engineered Net Shaping or LENS process, also called Laser Cladding (LC) or Laser Metal Deposition (LMD) is the most prominent technique in this category. Laser optics, powder nozzle(s) and inert gas tubing are integrated into a deposition head for DED. The process is capable of depositing onto a flat substrate for creating 3D parts, as well as the deposition head

can deposit material onto an already existing part for the purpose of creating addition geometry or repair. Relative movement of the deposition head and substrate is used for controlling the material deposition. The deposition head is usually attached to a robotic arm capable of multi axis movement. Since the material (powder or wire) is fed coaxially into the energy beam the process creates a larger meltpool compared with powder bed fusion and thus has a lower resolution than powder bed fusion processes[13].

2.2 Selective Laser Melting

Selective Laser Sintering (SLS) was developed by Carl Deckard at the University of Texas at Austin (USA) mainly to simplify the tedious process of prototyping. It was mainly aimed for processing polymers [14]. With advancement of the technology and a realisation of the capabilities of the SLS process it, began to be commonly used for producing functional products rather than just prototypes. As metals are most commonly used for building machine parts and the process had capabilities to produce metal parts with complex geometries so it interested most researchers and SLS began to be commonly used for producing small series production runs of fully functional metal parts [15-17]. The term Selective Laser Melting (SLM) is specifically used for AM process used to layer wise consolidate metallic material parts with high energy laser beam. SLM utilises a higher laser energy than SLS to fully melt metal layers and consolidate into final products. SLM produces nearly fully dense parts

with mechanical properties comparable to those of bulk materials, minimizing post processing requirements [2].

A typical configuration of an SLM system is shown in Figure-2.2. A metallic substrate plate is mounted and secured on the processing table that moves vertically in the build chamber. The table moves down equivalent to the layer thickness set in the CAD model. A container stores the metallic powder and delivers powder for each layer according to the dosage level set on the machine which is spread homogeneously across the substrate plate by a leveller. The laser beam scans the cross-section of the geometry of the CAD model into the powder with processing parameters set in the material file. Thus parts of the powder layer are selectively melted and consolidated defining the cross-section of the solid part. This process is repeated for each layer of the CAD model till the full part is completed.

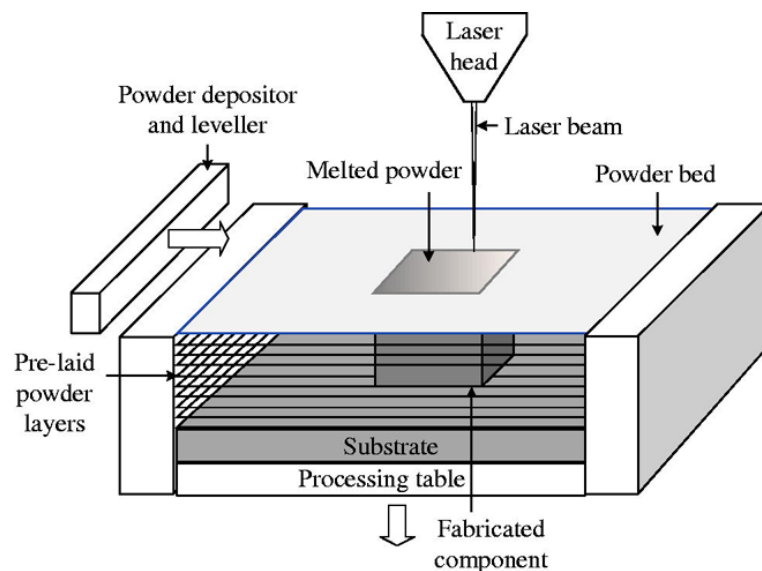


Figure 2-2 Selective Laser Melting Process [18].

2.3 Challenges Associated with SLM

The SLM process involves a number of characteristic challenges associated with the process, which require proper understanding and control to avoid problems with material processing.

2.3.1 Porosity

Porosity is a characteristic defect of the powder bed fusion process and is usually reported as % porosity in a volume or area. Achieving nearly fully dense SLM parts has been a focus of many earlier investigations [19-22]. It is evident from these investigations that porosity in SLM samples can be characterised into two broader categories, lack of fusion (irregularly shaped) and gas (spherical) porosity. Lack of fusion porosity is a consequence of insufficient energy input due to either insufficient melt overlap, or insufficient melting or fusion depth. Spherical porosity is attributed to either trapped gas in the feedstock or high energy input resulting in vaporisation. Porosity has a detrimental effect on mechanical properties as pores can act as crack initiation sites and therefore it is important to achieve a good density in SLM parts. Except porosity caused by trapped gas, porosity in the SLM samples can be controlled through scan parameter optimisation and determining the right amount of energy required for proper melting of the material.

2.3.2 Surface roughness

The phenomenon of molten metal solidifying as beads caused by insufficient wetting of the underlying material due to surface tension is called balling[23]. Figure-2.3

shows that insufficient energy supply can lead to balling phenomenon. positive effect on the balling phenomenon.

Liquid metals do not wet surface oxide films in the absence of a chemical reaction therefore it is very important to avoid oxidation. Sufficient remelting of the previous layer is necessary for removing surface contaminants, breaking down oxide films and providing a clean solid-liquid interface at the atomic level[23]. Balling can also be avoided by improving wetting by addition of various alloying elements. Applying very high pulse energies can also be useful in suppressing balling[23].

Balling creates a rough surface and hinders smooth deposition of further layers of powder, which leads to high porosity and higher surface roughness[23]. According to the process parameter window for continuous and pulsed laser systems shown in Figure-2.3, ref-[23] reported reduction in balling while high power and high speed combination was used.

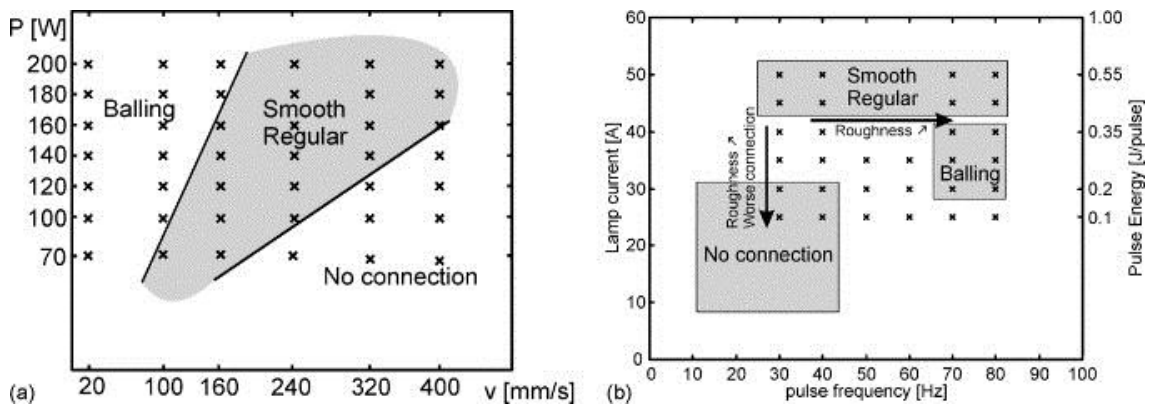


Figure 2-3 Process window for (a) Continuous Wave operation and (b) Pulsed operation[23].

In contrast, ref-[19] reported a reduction in balling when low power was used with slower scanning speeds. Thus proper parameter optimisation for the desired material can lead to a reduction in balling and result in an improved surface finish for SLM parts.

2.3.3 Process induced cracking

Micro or macro cracks forming in the SLM parts as a result of the process is termed as process induced cracking. Cracking in SLM parts is very much material dependant and some of the alloys susceptible to cracking are Inconel 738 [24] and Waspaloy [20].

2.3.4 Poor Mechanical Properties due to Non-Equilibrium Microstructure

Inherent high cooling rates associated with the SLM process lead to a non-equilibrium microstructure and the effect of this microstructure on the mechanical properties is not yet completely understood. The effect of SLM Ti6Al4V microstructure on mechanical properties is dealt with in more detail in Section-2.9.

2.3.5 Residual Stress

Residual stresses in SLM parts is a consequence of the high cooling rates associated with the process. Residual stress can lead to part deformation as well as induce cracking in SLM parts. Residual stress in SLM Ti6Al4V is the main focus of this research and therefore this problem is being detailed further in Section-2.4.

2.4 Residual Stress

“Residual stresses are stresses that remain inside a body that is stationary and at equilibrium with its surroundings” [25].

Stresses that remain in a material or a body without application of an external load (applied force, displacement or thermal gradient) are called residual stresses which originate due to heterogeneous plastic deformations, thermal contractions and phase transformations during manufacturing and processing of materials. Residual stresses can have a detrimental effect on the performance and life of a component. Alternatively, compressive surface residual stresses introduced deliberately can be beneficial. Positive values of stress indicate tensile stress while negative values of stress indicate compressive stress. Stress equilibrium is maintained in any free standing body; tensile residual stress in one region of the component will be balanced by a compressive stress elsewhere [26].

2.4.1 Nature of Residual Stress

Tensile surface residual stress is generally undesirable because it can result in fatigue failure, quench cracking and stress-corrosion cracking. While compressive surface residual stress can enhance both the fatigue strength and resistance to stress-corrosion cracking. In general, residual stresses operating in the plane of the applied load but in the opposite direction are beneficial. It is more difficult to predict residual stresses compared to the in-service stresses on which they superimpose. Residual stress can be characterised based on their self-equilibrating characteristic length scale [26, 27].

Macro Residual Stresses (Type-I): These stresses vary within a component over a range much larger than the grain size. Micro Residual Stresses (Type-II and Type-III): result from differences within the microstructure of a material. The sign and/or magnitude of these stresses can change over distances as small as the grain size of the material under analysis. They can be classified into two types, namely Type II or III. Type II residual stresses vary over the scale of on an individual grain, and can exist in single phase materials due to anisotropic behavior of each grain. While in multi-phase materials they exist as a result of variation in the properties of the different phases. Type III residual stresses exist within a grain, essentially as a result of the presence of dislocations and other crystalline defects [25-27].

2.4.2 Origin of Residual Stress

Mechanically generated residual stresses, occur due to non-uniform plastic deformation during the manufacturing process. The development can be natural due to the process or treatment or a particular stress profile in a component can be developed by deliberate introduction of residual stress. Rod or wire drawing, welding, machining (turning, milling) and grinding tend to produce undesirable surface tensile stresses, while shot peening, autofrettage of pressure vessels, toughening of glass or cold expansion of holes can be used to introduce beneficial compressive residual stresses. Macroscopic thermally generated residual stresses, occur as a result of non-uniform heating or cooling operations. While thermal residual stresses on microscopic level, develop due to a mismatch between the coefficient of thermal expansion of different phases or constituents in a material.

Chemically generated residual stresses, develop due to volume changes associated with chemical reactions, precipitation or phase transformations. Substantial residual stress gradients can develop in the surface layers of components during chemical surface treatments and coatings [25-27].

2.5 Residual Stresses in SLM

Selective Laser Melting (SLM) is specifically used for the AM process used to layer wise consolidate metallic material parts with a high energy laser beam. Figure-2.4 shows an example of distortion caused by residual stresses in a pair of coplanar plates welded together when the joint is allowed to cool to ambient temperature [27]. The SLM process in essence is producing a 3D geometry from the stacking of thousands of welds together.

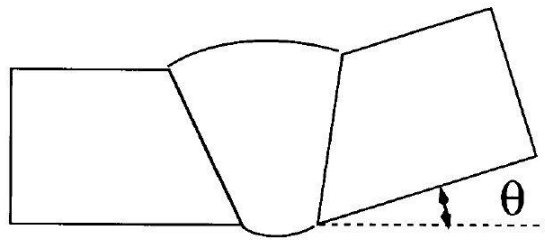


Figure 2-4 Example of distortion caused when pair of coplanar plates is welded together and joint is allowed to cool to ambient temperature[27].

The melt pool size in SLM process is much smaller compared with conventional welding processes, with melt pool dimensions in the order of $10^{-1}mm^3$. A significant problem associated with components produced using the AM process is the

development of high internal residual stresses, which are a result of the repeated heating and cooling of successive layers of powder during component build. The selective laser melting process produces rapid heating and cooling effects and high temperature gradients within the build. As a result, the general micro-structural features produced by the SLM process are different to those obtained by conventional manufacturing and these complex thermal effects promote the development of residual stresses. If residual stresses are not recognised and accounted for in the design process, they can be a major factor in the subsequent failure of a component in service, particularly one subjected to alternating loadings or corrosive environments [2-6]. The temperature gradient mechanism model and the cool-down phase model are being used to explain how thermal stresses build up in SLM[28].

2.5.1 Temperature Gradient Mechanism (TGM)

According to the temperature gradient mechanism[28], a compressive stress-strain condition builds up in the irradiated material due to partial inhibition of the thermal expansion (ϵ_{th}) of irradiated material by surrounding colder material as shown in Figure-2.5(a). Partially elastic (ϵ_{el}) and partially plastic (ϵ_{pl}) compressive strain will occur in the irradiated zone if the compressive stress is greater than the compressive yield stress (σ_{yield}) as shown in Figure-2.5(b). During cooling, plastic deformation (ϵ_{pl}) partially inhibits the shrinkage of the material in the irradiated zone resulting in the buildup of residual tensile stress (σ_{tens}) in the irradiated region as shown in Figure-2.6(a). Force and momentum balance in the part results in the buildup of

compressive residual stress (σ_{comp}) in the region surrounding the irradiated zone as shown in Figure-2.6(b).

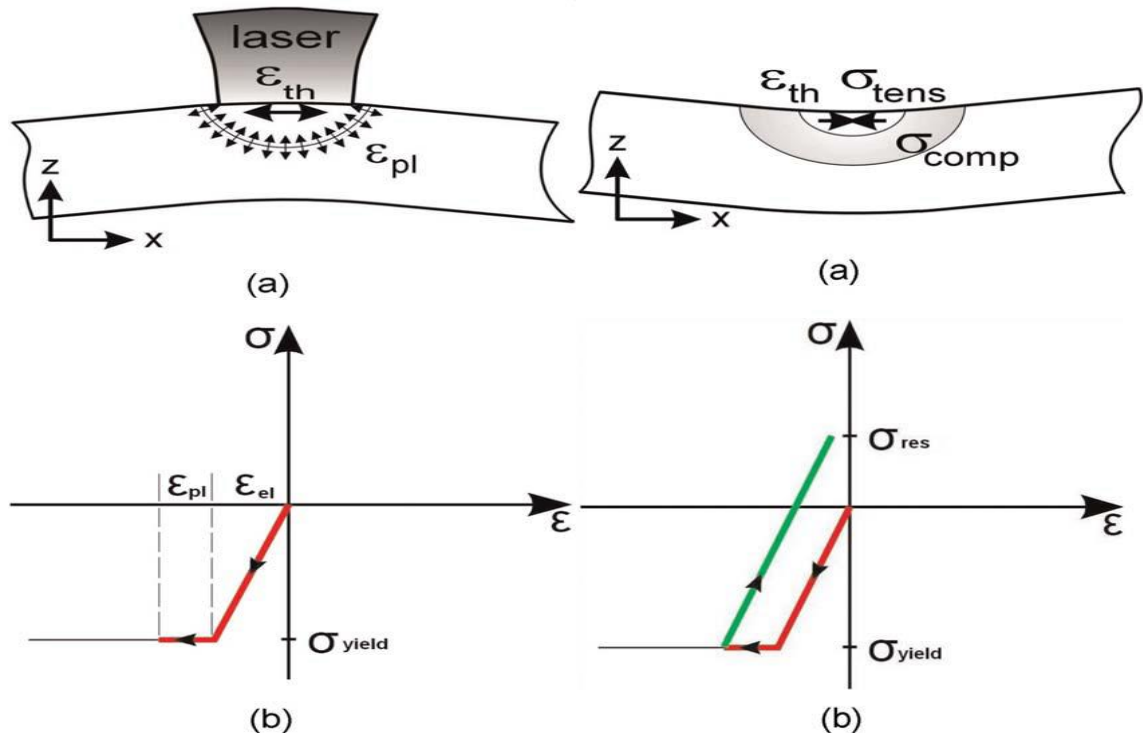


Figure 2-5 Left (a) Induced stresses and deformation (strain) during laser beam heating.
 (b) Simplified representation of the formation of thermal stress and strains in the irradiated zone. [28]

Figure 2-6 Right (a) Occurring stresses and deformation (strain) when the part cools down.
 (b) Simplified representation of the formation of residual stresses and strain in the irradiated zone. [28]

2.5.2 Cool-down Phase Model

According to the cool-down phase model the shrinkage of previously melted material during re-solidification is partially inhibited by underlying material which results in the buildup of tensile residual stresses (σ_{tens}) in the top layer. Using force

and momentum balance a simplified mechanical model is proposed to quantify the cool-down phase model.[28, 29]

Residual stresses in the latest added top layer are assumed to be equal to the yield strength of the material (σ_{yield}) as shown in Figure-2.7(a). High tensile stresses (σ_{tens}) shown by the (+) sign, buildup in the SLM part while compressive stresses (σ_{comp}) shown by (-) sign, build up in the upper part of the base plate and lower tensile stresses (σ_{tens}) build up in the lower part of the base plate due to the assumption that residual stresses in the top layer are equal to (σ_{yield}) as shown in Figure-2.7(b).

Figure-2.8(a) shows the SLM part connected to the base platform has high tensile stresses where the top surface has tensile stresses equal to yield stress(σ_{yield}). When the SLM part is removed from the base plate the high tensile stresses in the part partially relax. The constant part of the relaxation shown in Figure-2.8(b) is responsible for the uniform shrinkage of the part while the linear relaxation term shown in Figure-2.8(c) is responsible for the bending of the part. Figure-2.8(d) shows the stresses remaining in the part after relaxation and it can be seen that there are tensile residual stresses in the SLM part near the top and bottom surfaces which are balanced by compressive residual stress in the middle.

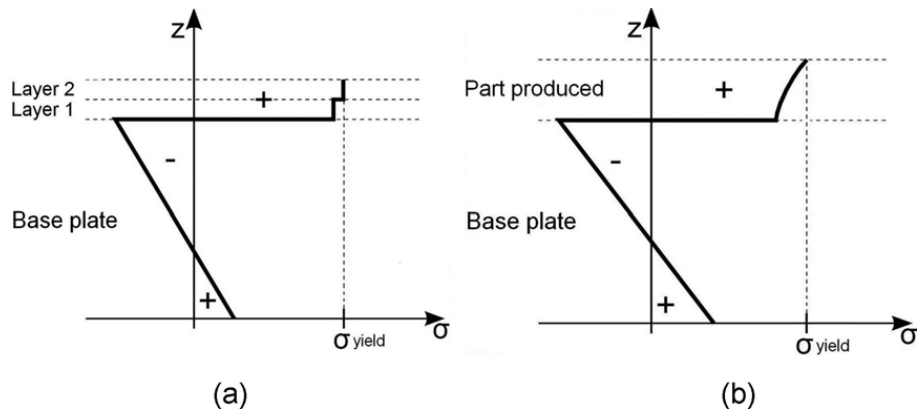


Figure 2-7 (a) Residual stresses after adding two layers of melted powder on a base plate.

(b) Residual stresses of a SLM part on a base plate after melting more or all layers

(simplified model).[28]

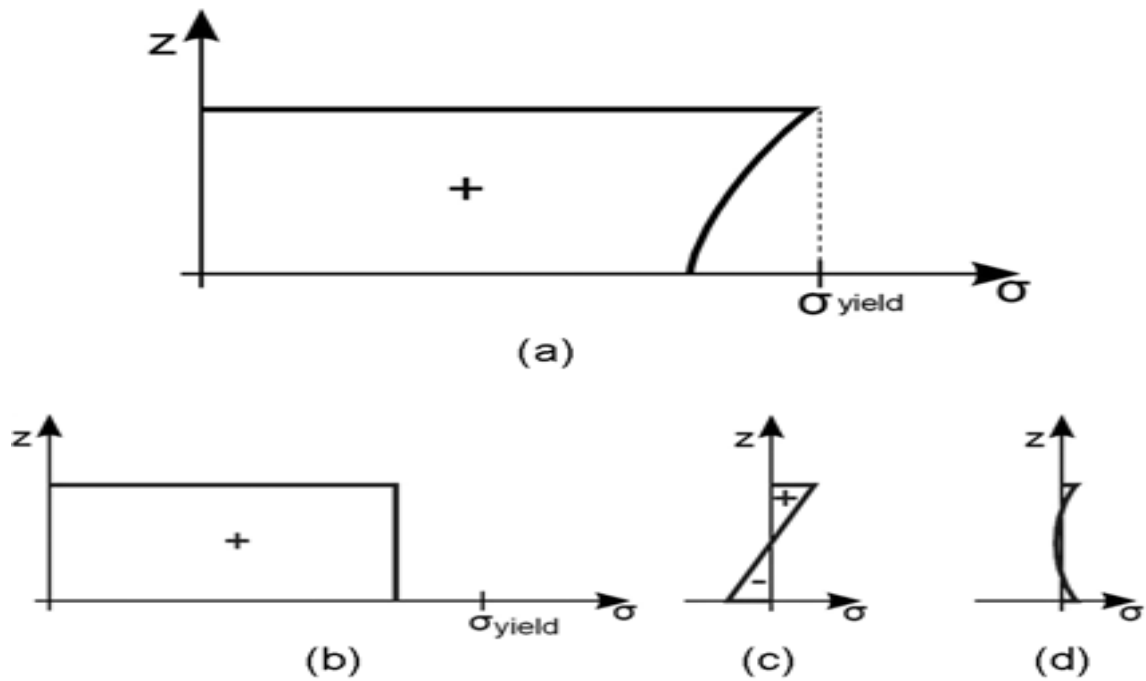


Figure 2-8 (a) Residual stresses within an SLM part still connected to the base plate.

(b) Constant relaxation term. (c) Linear relaxation term.

(d) Residual stresses in a SLM part removed from the base plate[28].

2.6 SLM Parameters and Their Effect on Parts

All additive manufacturing processes including SLM can be broken down into three stages and varying the parameters at each stage has an effect on the final part properties [13, 30].

The parameters affecting the final part properties at every stage are summarised in Figure-2.9 below.

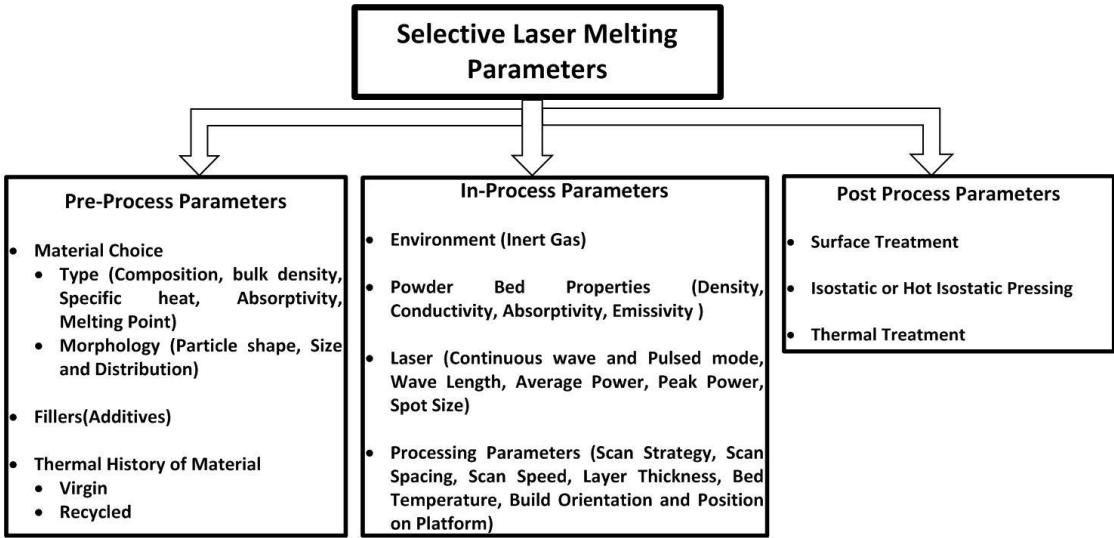


Figure 2-9 SLM parameters affecting part properties

This research mainly focussed on the second stage of the SLM process, while an attempt was made on in-situ integration of some of the parameters from the third stage.

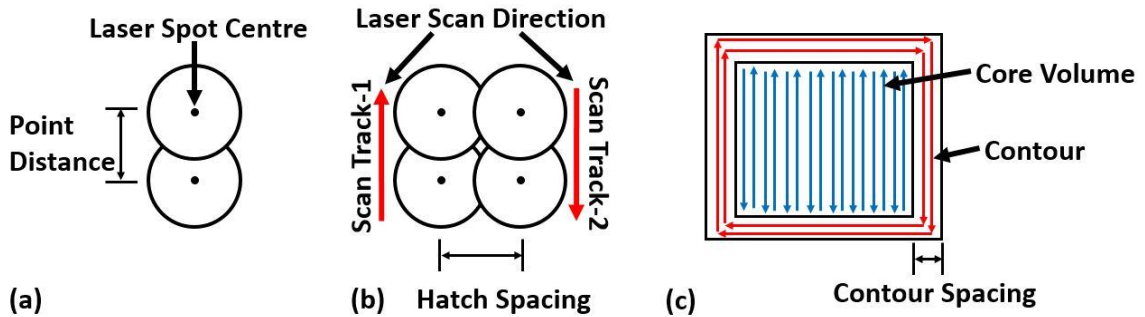


Figure 2-10 (a) Point Distance (b) Hatch Spacing (c) Core Volume and Contour Spacing

Figure-2.10 shows graphical representation of some of the important parameters referred to in this study. Figure-2.10(a) shows point distance, which is the distance between the centres of two consecutive laser spots. Figure-2.10(b) shows hatch spacing as the distance between the centres of two adjacent scanning tracks. Figure-2.10(c) shows the core volume with the blue arrows showing 90° alternating scanning strategy, while the contour (border) scanning is shown by the red arrows. Contour spacing is the width on the sides of the core volume to be scanned with the laser moving in a clockwise or anti clockwise manner. Contour is defined to improve the roughness of the side walls of a part by adjusting the scanning parameters separately than the core volume.

The most important in-process parameters are the laser power P [W], exposure time t [μ s], point distance pd [μ m], (some researchers combine pd distance and exposure time into a single parameter called scan speed v (mm/s)), hatch spacing h [μ m], layer thickness lt [μ m], and the scanning strategy. Density optimisation trials are based on these parameters as they directly determine how the layers are built up. Another important parameter is the bed preheat temperature. The substrate acts as a large heat sink and preheating can be used to lower the thermal gradients leading to lower residual stresses. P , t , pd , h , and lt are used to calculate the energy density E [J/mm^3], given by Equation-2.1.

$$ED = \frac{P.t}{pd.h.lt} \quad \text{Equation 2.1}$$

Point distance and exposure time are parameters specific to the Renishaw platforms and therefore the rest of this work uses Equation-2.1 for energy density calculations.

Equation-2.1 can also be written in terms of the scan speed (v) as shown in Equation-2.2.

$$ED = \frac{P}{v.h.lt} \quad \text{Equation 2.2}$$

Since the foremost objective is to get a fully dense material, this requires a sufficient amount of heat to fully melt a certain amount of material. Therefore exposure and laser power are always varied interdependently.

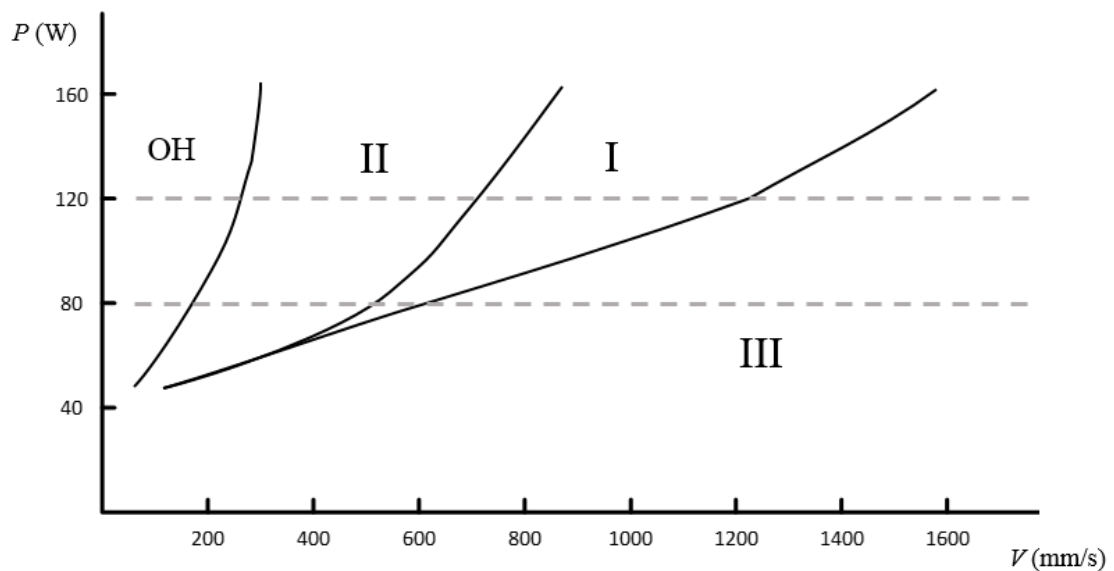


Figure 2-11 Process Window of SLM Melt Zones for Ti6Al4V [31]

Figure-2.11 shows a process window for SLM of Ti6Al4V, illustrating the effect of laser power and scan speed on porosity. Processing parameters are divided into four melting zones. Zone I results in almost fully dense specimens. Zone II parameters with high power and low speeds lead to over melting. Zone III parameters with low power and high speed, result in lack of fusion, while Zone OH parameters with high power and very low scan speeds cause serious thermal deformations in parts[31]. A combination of high power and lower scan speed results in keyhole generation due to excessive heat supply. The laser penetrates deep into the underlying material and rescanning the same layer or even deposition of further layers cannot get rid of keyhole defects [32]. Using the minimum value of energy density required for obtaining fully dense parts minimises the surface roughness, while remelting each layer can also result in improvements in density and surface finish [33].

As the SLM process can be approximated by the stacking of thousands of welds together so it is really important to understand the dynamics of a single weld or in the terminology of SLM a single melt pool. Melt pool size increases with increasing energy input [34] as shown in Figure-2.12. Laser Power has a more pronounced effect on the maximum temperature than exposure time [34] as shown in Figure-2.13.

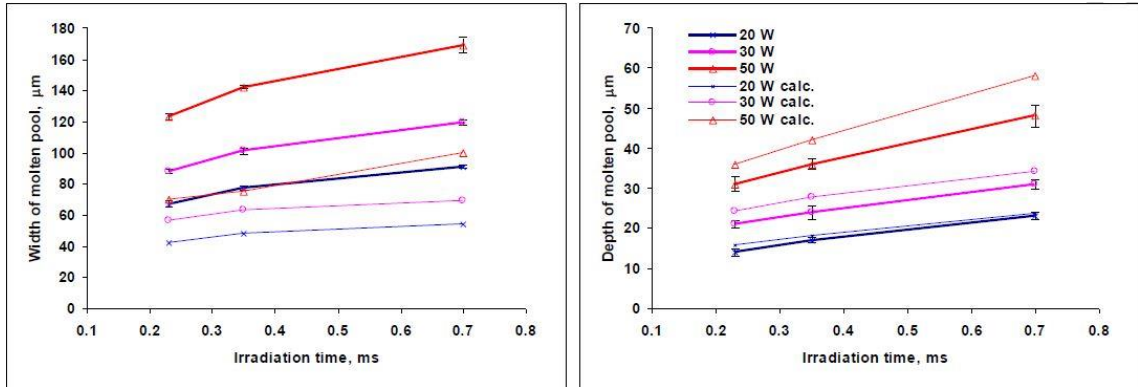


Figure 2-12 The width and depth of the molten pool versus irradiation time. Irradiation time is the ratio of laser spot diameter to scanning speed [34].

The maximum power depends on the laser hardware. Lowering the laser power reduces the maximum temperature of a melt pool [34-36] and also leads to a smaller melt pool, which results in higher cooling rates [35]. High laser power has been reported to result in lower deformation due to residual stress [37], while ref-[36] reports lower residual stresses for lower laser power.

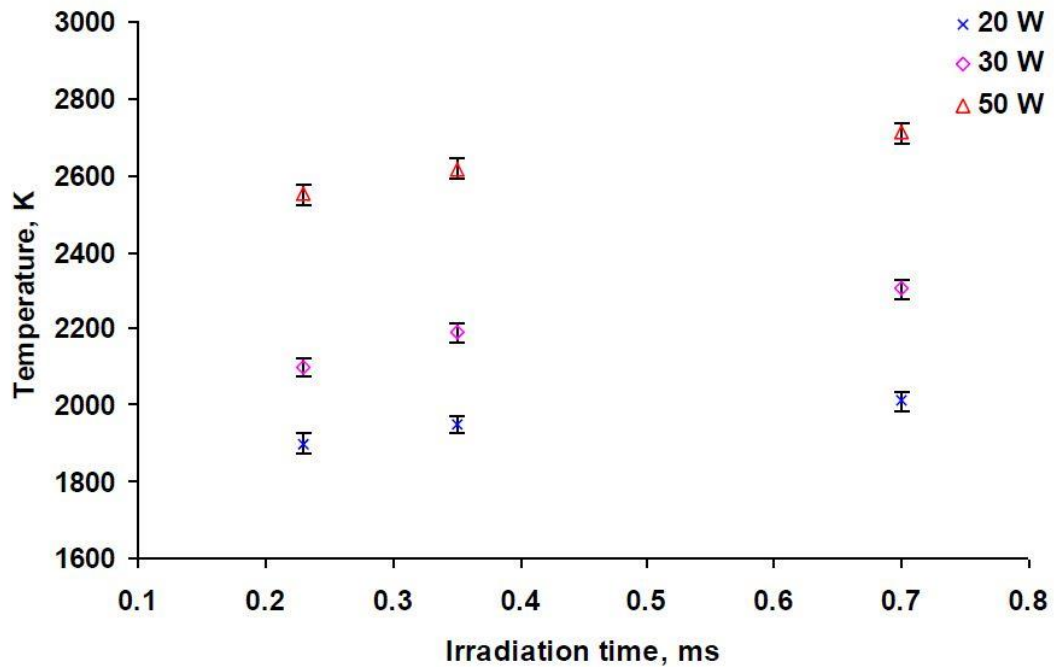


Figure 2-13 The maximum true temperature of molten pool versus irradiation time and laser power [34].

The lowest possible exposure time or scan speed is determined by the highest speed of the mirrors in the galvanoscanner. As for the effect of scan speed or exposure time it is the opposite of power. Reducing scan speed leads to lower temperature gradients [38], lower cooling rates[35], lower residual stresses [39], and reduced deformation. While higher scan speeds produce an increased cooling rate and lead to increased cracking [40]. Lower deformation for higher scan speed is reported by one author in ref-[41].

The limit on point distance is determined by the ability to produce a continuous melt track. Reducing the point distance too much will result in a bigger melt pool and a

balling effect while increasing the point distance too much will result in a broken melt track without proper melting.

Laser spot size (diameter of the laser spot on the powder bed), power and exposure time determine the width of the melt pool. Therefore the hatch spacing needs to be significantly less than the width of the melt pool to ensure enough overlapping between adjacent scan vectors. Tripling the hatch spacing has been reported to reduce the deflection of a steel sheet to half [41].

Powder particle size determines the lower limit of the layer thickness, while the need for full melt pool penetration into underlying layers determines the upper limit. Larger layer thicknesses can increase productivity at the detriment of geometrical resolution, as well as roughness of side surfaces. It has been reported in ref-[4, 42, 43], that increasing layer thickness results in reduced residual stresses due to a reduction in cooling rate. In reality all the parameters included in the calculation of energy density are seldom varied independently.

The scanning strategy determines how energy is supplied to each layer. Variation in the scan vector lengths, the sequence and direction of scan vectors and therefore the rotation of consecutive layers alters the way heat is supplied to the powder bed and affects the part properties. Figure-2.14 sums up a part of the different possibilities of scanning patterns. According to the FEA simulation prediction in ref-[44], 45° line scanning shown in Figure-2.14(c) resulted in the lowest residual stress and lowest deformation in IN-718. According to ref-[45], rotating the scan pattern every layer resulted in a decrease in distortion of the build and substrate.

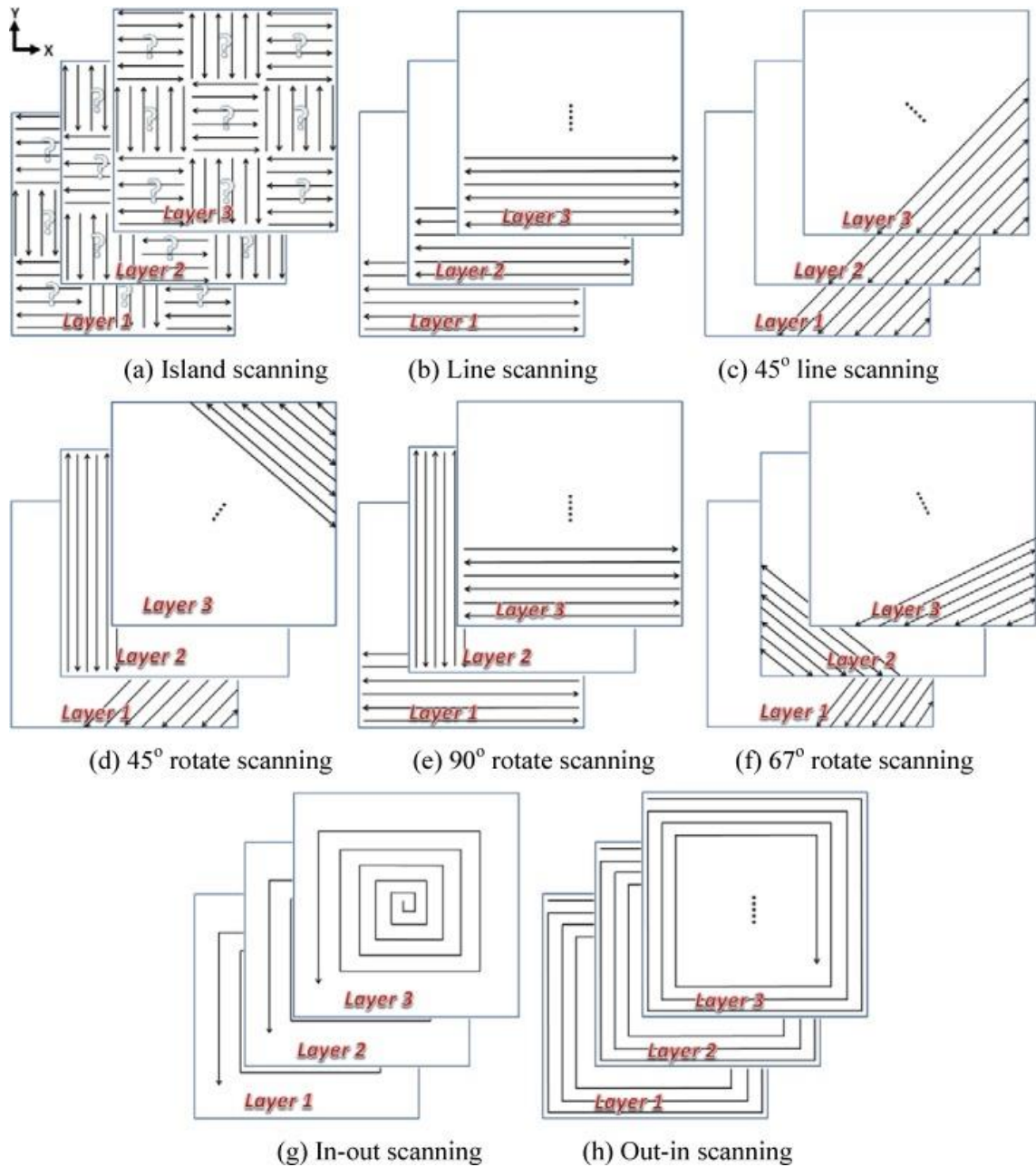


Figure 2-14 Scanning strategies [44].

Another important phenomenon related to the residual stress development is the difference in the directional stresses in SLM parts. According to ref-[44], line

scanning (shown in Figure-2.14(b)) resulted in the highest difference in directional stresses and rotation of the scan area resulted in reducing the difference between the directional stress components as shown in Figure-2.15. It can also be observed from the results of line scanning in Figure-2.15 that residual stress in the direction of the scan vector is much higher than in the transverse direction. Ref-[46] also reported higher residual stress in the direction of the scan vector. According to ref-[47], an increase in the scan vector length results in an increase in the longitudinal stress. Different researchers found that SLM parts or substrates deformed more along the scan direction, than the transverse direction [4, 43, 48]. It can be seen that the possibilities of scanning strategies are numerous and even though most studies claim a shorter scan vector length to be a means of reduction in residual stress, the phenomenon is not very clear.

An island scanning strategy is one of the most famous scanning strategy, being proposed for residual stress reduction by many researchers [4, 43, 49]. According to ref-[49] island size had no effect on residual stress and according to ref-[50], had no effect on residual stress. According to ref-[51], IN718 SLM samples manufactured with an island scanning strategy showed residual stresses in the following sequence 2x2mm lowest then 5x5mm, then 7x7mm and 3x3mm had the highest residual stress. The lowest residual stress in 2x2mm island size was attributed to probable relaxation due to cracking. It can be seen that different researchers have reported different effect of island size on residual stress and the relationship between scanning strategy and residual stress is still very unclear.

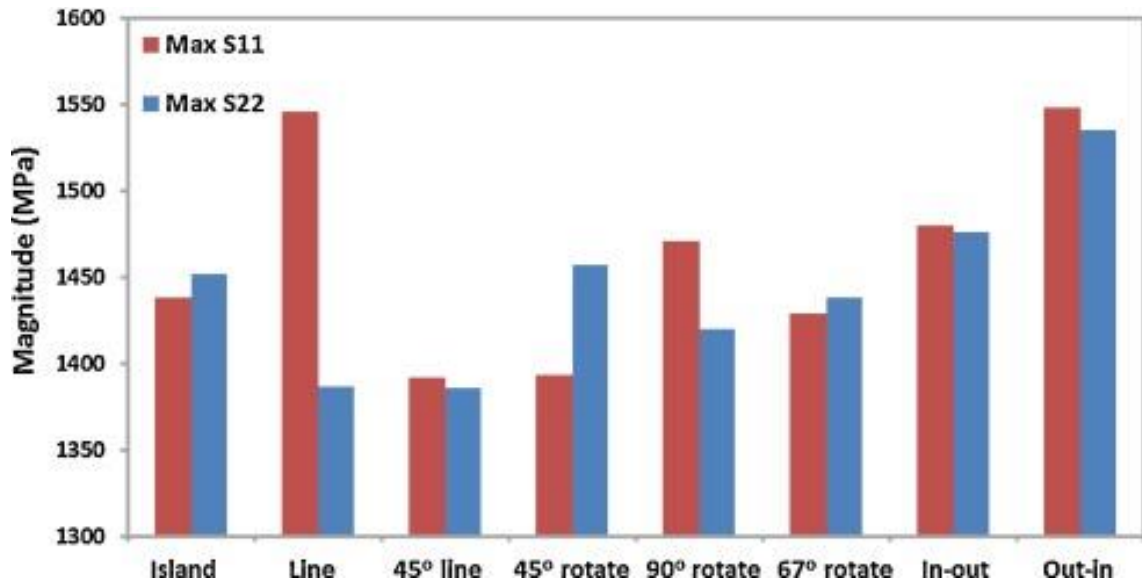


Figure 2-15 Max S11(X-direction) and S22(Y-Direction) stress comparison for all Scanning Strategies cases [44].

Finally the bed preheat temperature is an important parameter for reducing thermal gradients, and thus residual stresses. The build-up of thermal residual stresses [2, 4, 25, 27-29, 43, 49, 52-55] due to the high cooling rates and high temperature gradient between the melt-pool and surrounding material associated with the process is a major problem in SLM builds. Pre-heating the bed has been reported as the most efficient in-situ stress reduction strategy during the SLM build as illustrated in section-2.7, but as can be seen in section-2.7 different researchers report achieving different levels of stress reduction and various bed temperatures. This can be attributed to different factors such as the material, combination of other SLM parameters or even the geometry of the build component. Determining the optimum range of bed pre-heat temperature which will mitigate the residual stress and enhance the mechanical properties is still a venue for further research.

Electron Beam Melting processes Ti6Al4V at 650-750°C bed temperature achieved by pre-scanning the whole bed with the electron beam resulting in lowering the residual stress and improving the ductility as compared to SLM [56, 57]. The martensitic microstructure characteristic of SLM Ti6Al4V components is the reason for higher strength and low ductility of the parts [8, 58], and the temperature range for martensitic decomposition in Ti6Al4V is reported to be 600-650 °C [9, 59, 60], while Ti6Al4V components can be annealed between the temperature range of 700-790 °C [61].

Conventionally heat treatment can get rid of the residual stress in SLM parts [29, 54, 62], but SLM parts having a non-equilibrium martensitic microstructure results in conventional heat treatment strategies being unfit for achieving the desired results. Table-2.1 shows a range of heat treat temperatures and times used to get rid of residual stress. Heat treatment and Hipping are beneficial for post build stress relief but sometimes SLM parts start peeling off the substrate or cracking during the post processing and therefore there is a need for determining processing conditions that will yield better builds off the machine.

The build-up of residual stress in SLM parts depends on the combination of SLM parameters (laser scanning strategy, bed pre-heating, laser power, processing speed, layer thickness, track overlap) [2, 4-6], but the possible combinations can be numerous and thus determining the optimum combination can be a daunting and long task.

A simpler solution to the issues of non-equilibrium microstructure, sub optimal ductility and residual stress which are all related to the high cooling rates inherent in the SLM process can be achieved by raising the bed temperature above the martensitic decomposition temperature and possibly in the range of the annealing temperatures for Ti6Al4V. Raising the bed temperature will decrease the thermal gradient, cooling rates and let the microstructure of the parts homogenise at higher temperatures. The effect of bed pre-heat temperature on microstructure, residual stress and mechanical properties of Ti6Al4V SLM components is one of the main aims of this research. The goal is to determine the optimum bed pre-heat temperature which can mitigate residual stress, enhance mechanical properties and achieve parts with an equilibrium $\alpha+\beta$ microstructure.

2.7 Residual Stress Reduction Strategies from Published Literature

Considerable research has been conducted on understanding the effect of SLM process parameters on residual stress. Figure-2.16 shows the bridge geometry utilised in the Bridge Curvature Method to study the effect of SLM parameters on residual stress.

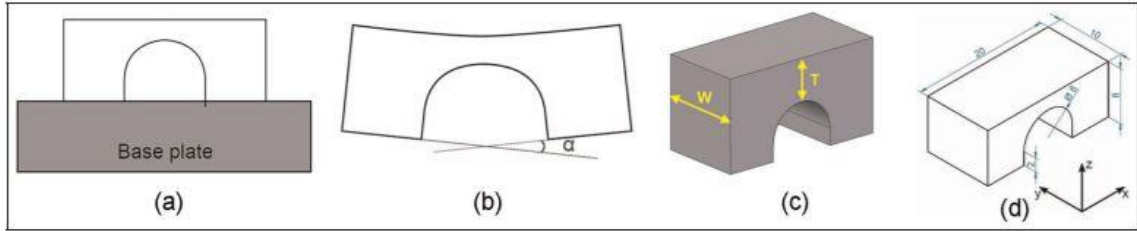


Figure 2-16. Principle of the method for identifying the residual stresses in the test parts. (a) Before, and (b) after removal from base plate. Geometry of the test parts: (c) variable width W and thickness T to optimize the bridge structure for repeatability. (d) Final dimensions of the optimized bridge geometry [mm][4].

Below is a list of process parameters and their effect on residual stress from published literature.

2.7.1 Heat Treatment

- Heat treatment is a post build process and published literature reports the effect of varying heat treatment on residual stress.
- The curling angle of a bridge shaped geometry was measured using the Bridge Curvature Method[4]. According to ref-[4], heat treatment at 550°C for two hours reduced the curling angle by 80%.
- The strain in a T-Shaped Cantilever was measured using Deflection Analysis[54]. According to ref-[54], heating in 25 degrees steps from $750\text{--}850^{\circ}\text{C}$ reduced strain by 84.4%.
- Stress in a beam geometry was measured using the Modified Layer Removal method[29]. According to ref-[29], stress relieving at 600°C and 700°C for one hour reduced residual stress by 70%.
- Stress in a cylinder was measured using the Hole Drilling method[55]. According to ref [55], stress relief at 650°C in a vacuum furnace for 8 hours

reduced the residual stress by 76-81%. Recrystallization Anneal at 950 °C in a vacuum furnace for 1 hour reduced the residual stress by 94-97%. Duplex Anneal at 950 °C for 1 hour and then 700 °C for 4 hours in a box furnace resulted in 91-95% reduction in residual stress. Beta Anneal at 1050 °C for 1 hour and then 700 °C for 4 hours in a box furnace reduced the residual stress by 90-91%.

2.7.2 In-situ Powder Bed Pre-Heating

- The curling angle of a bridge geometry was measured using the BCM[50]. According to ref-[50], pre-heating the bed to 180 °C resulted in a 10% reduction in the curling angle.
- Residual stress in a beam geometry measured using the Modified Layer Removal method reduced by 40% when the powder bed was pre-heated to 160°C [29].
- Residual stress in two 1x1mm layers was calculated using FEA and Surface Profilometry[63]. According to ref-[63], pre-heating the bed to 150 °C gave 18 % reduction in longitudinal stress & 65.9% in transverse stress. While a pre-heat temperature of 300 °C gave 51.8% reduction in longitudinal stress & 125% reduction in transverse stress[63].
- Deformation in a T-Shaped Cantilever and a Helical Spring were measured using optical microscopy and Image-J [64]. According to ref-[64], pre-heating the powder bed to 380 °C made the in-situ eutectic alloying of Al and Si12 powders and building of anchorless overhanging structures possible.

- The curling angle of a bridge shaped geometry was measured using the BCM and residual stress in block specimens was measured using X-Ray Diffraction and the Contour Method [52]. According to ref-[52], pre-heating the bed to 400 °C reduced residual stress by 50%.
- FEA Modelling, Neutron Diffraction and Coordinate Measurement were used to measure the deformation in a T-Shaped Cantilever[43]. According to ref-[43], pre-heating the bed to 100 °C resulted in 22.3% reduction in deformation of the ends, while a bed pre-heat temperature of 200 °C reduced the deformation of the ends by 87%.

2.7.3 Length of Scan Vectors

- FEA and Surface Profilometry was used to measure the residual stress in two 1x1mm layers [63]. According to ref-[63], using shorter scan vectors reduced the residual stress.
- The curling angle of a bridge shaped geometry was measured using BCM [50]. According to ref-[50], 2mm Scan Vectors gave 13% reduction in the curling angle compared to 20mm Scan Vectors.
- FEA Modelling, Neutron Diffraction and Coordinate Measurement were used to measure the deformation in a T-Shaped Cantilever[43]. According to ref-[43], shorter Scan Vectors reduce residual stress.

2.7.4 Island Size and Orientation of Scan Vectors

- Residual stress in a cube was estimated using the Theoretical Model, Crack Compliance and X-Ray Diffraction methods [49]. According to ref-[49], Island Size had no effect on residual stress. Randomised scanning order resulted in the lowest residual stress.
- The curling angle in a bridge geometry was measured using BCM [50]. According to ref-[50], Island Size had no effect on the curling angle. 45 degree rotation of the scan area from x-axis reduced the curling angle by 36% [50].
- FEA Modelling, Neutron Diffraction and Coordinate Measurement were used to measure the deformation in a T-Shaped Cantilever[43]. According to ref-[43], Island Scanning reduced Longitudinal Stress by almost 67%.

2.7.5 Post Scanning

- Residual stress in a cube was estimated using a Theoretical Model, Crack Compliance and X-Ray Diffraction methods [49]. According to ref-[49], post scanning each layer with 50% Energy reduced residual stress by 30%.
- Residual stress in a beam geometry measured using the Modified Layer Removal method reduced by 55% when each layer was re-scanned at 150% energy [29].

2.7.6 Pre-Scanning

- The curling angle of a bridge shaped geometry was measured using Bridge Curvature Method[4]. According to ref-[4], pre-scanning each layer with the build power and higher scan speed reduced curling angle by 8%.

2.7.7 Build Position on Platform

- Residual stress in a circular disc was measured using the Hole Drilling method [2]. According to ref-[2], placing the part on the centre of the baseplate resulted in minimum residual stress. This reduction in residual stress is a consequence of the laser beam being perpendicular to the surface [2].

2.7.8 Base Plate Material and Height

- FEA and Surface Profilometry was used to measure the residual stress in two 1x1mm layers [63]. According to ref-[63], using similar base plate material as the build reduced residual stress by 2%. Residual Stress increased with increasing base plate thickness while deformation decreased [63].
- Residual stress in a cube was estimated using the Theoretical Model, Crack Compliance and X-Ray Diffraction methods [49]. According to ref-[49], a thicker base plate resulted in lower residual stresses by reducing bending deformation.

2.7.9 Layer Thickness

- The curling angle in a bridge geometry was measured using BCM [50]. According to ref-[50], for the same Energy Density doubling the layer thickness reduced the curling angle by 6% [50].
- FEA and Surface Profilometry was used to measure the residual stress in two 1x1mm layers [63]. According to ref-[63], doubling the layer thickness reduced the residual stress by 5% [63].
- FEA Modelling, Neutron Diffraction and Coordinate Measurement were used to measure the deformation in a T-Shaped Cantilever[43]. According to ref-[43], increasing the layer thickness by 2.5 times decreased deformation of the ends by 82%.

2.8 Ti6Al4V and its Applications

Ti6Al4V refers to titanium with 6 percent by weight Aluminium and 4 percent by weight Vanadium. It is biocompatible, corrosion resistant, and has high strength with relatively low stiffness. Pure titanium occurs in two solid forms. At room temperature titanium occurs in the alpha phase of titanium which has hexagonal close packed (HCP) structure. Heating titanium to 882 °C which is the beta transus temperature for titanium rearranges the atoms to form the beta phase of titanium which has body centred cubic (BCC) structure. Both phases have different mechanical properties. The Beta phase has higher ductility and lower strength than the alpha phase. If alloying metals are added in small amounts, these phase

stabilizers can change the transformation temperature and the regions of stability. Aluminium is an alpha stabilizer, which raises the alpha to beta transformation temperature. Vanadium is a beta stabilizer, which lowers the transformation temperature.

Ti6Al4V is an alpha beta alloy and the final microstructure and behavior of Ti6Al4V depends on the microstructure which has a direct relation with the thermal processing of the material. Slow cooling of Ti6Al4V from above the β transus temperature (about 980°C) leads to the transformation of β phase mainly into globular α . Cooling rate determines the size of α laths. Higher cooling rate enhances the α nucleation rate but slows down the growth by diffusion. Higher cooling rate could lead to the existence of α inside prior β grains leading to a basketweave microstructure[61, 65]. If the cooling rate is higher than $410\frac{^{\circ}\text{C}}{\text{s}}$ the β phase will transform martensitically[66]. Martensite can exist as α' having a hexagonal structure and α'' having an orthorhombic structure[61, 65]. The type and amount of α' and/or α'' depends on the alloy chemistry and quenching temperature. Ti6Al4V quenched from above the beta transus could retain some β (although in some case no beta is observed), because the end of martensite transformation is below room temperature 25°C[61]. If Ti6Al4V is aged at around 500°C it can lead to the alloy partitioning effect and precipitates of α_2 (Ti_3Al) phase forms. α_2 phase can be concern where there is a possibility for stress corrosion cracking[61]. In Ti6Al4V the solvus temperature for Ti_3Al is 550°C and thus heat treatment at 600°C or above will not lead to the precipitation of Ti_3Al [61, 65].

It is commonly used for biomedical applications. Ti6Al4V is light weight and has excellent corrosion resistance besides being biocompatible and having good machinability. Aircraft turbine engine and structural components, aerospace fasteners, high performance automotive parts, marine applications, medical and the sports equipment industry prefer Ti6AL4V because it has high strength at low to moderate temperatures [61].

2.9 Ti6Al4V Micro-structure and Mechanical Properties

Ti6Al4V belongs to the group of $\alpha+\beta$ alloys with Figure-2.17 showing the phase diagram, showing that they lie between α and β alloys of titanium. Depending on the cooling rate from the β transus region the final microstructure will be $\alpha+\beta$ for slow cooling and martensitic for fast cooling, where the M_s line shows the martensitic start temperature. Therefore $\alpha+\beta$ alloys transform martensitically, if the cooling rate from the β field to room temperature is high[67]. Ti-6Al-4V has higher strength compared to α alloys, and a wider processing window as compared to both α and β alloys [68].

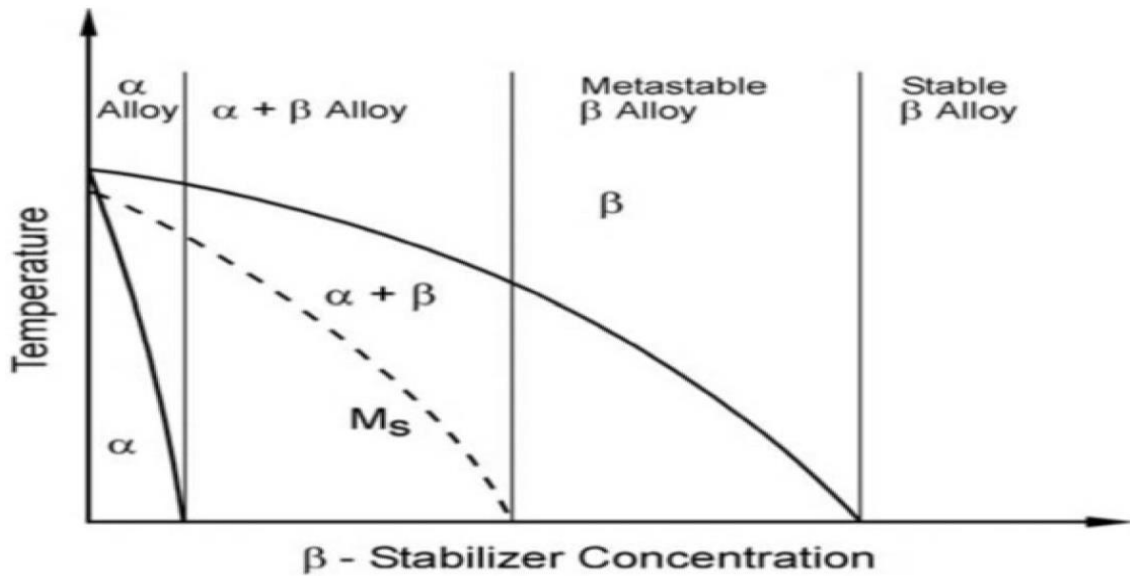


Figure 2-17 Pseudo-binary section through a β isomorphous phase diagram (schematically) [69].

In conventional manufacturing (Hot Working) the thermo-mechanical processing route, determines whether the final microstructures is going to be fully lamellar, bimodal or equiaxed. In this work only fully lamellar microstructure will be discussed further to draw inferences regarding SLM microstructure and how the difference in SLM microstructure can affect mechanical properties as compared to a fully lamellar hot worked microstructure.

2.9.1 Fully lamellar microstructure

Figure-2.18 shows the processing route for acquiring fully lamellar microstructure. It also shows what a fully lamellar microstructure looks like. The four stages shown in Figure-2.18 and especially the cooling rates from the first three steps determine the final microstructure and the size of α lamellae. In the homogenisation the

material is heated above the β transus temperature, shown by the dotted line in Figure-2.18 below. This transforms the whole microstructure into β phase and the cooling rate determines the α grains length scales.

The deformation stage performed above the β transus temperature, promotes recrystallization and growth of the β grains, while deforming the material below the transus temperature will deform the α grains, and will limit β recrystallization and therefore suppress any grain growth. Recrystallization is performed above the transus temperature and the cooling rate in this step determines the final lamellar microstructure size. The fourth and final step is only a stress relief annealing and has no effect on the microstructure.

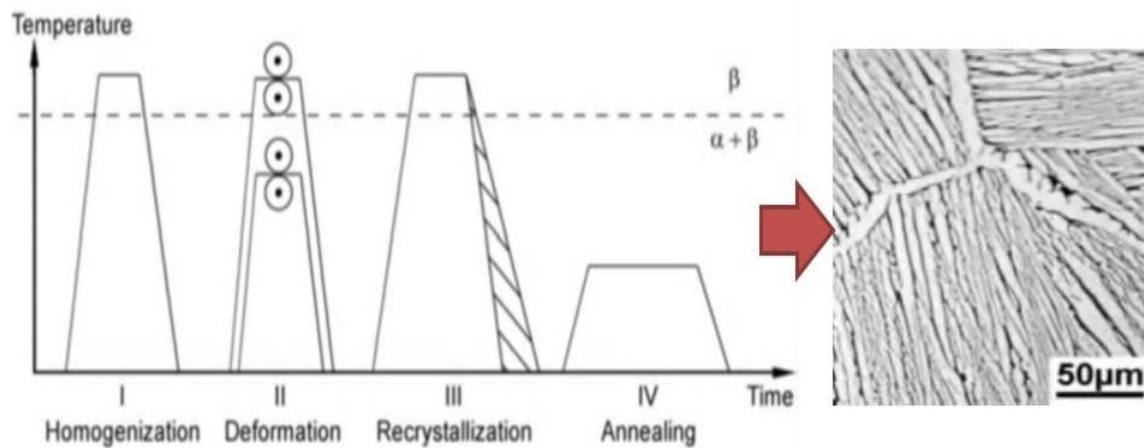


Figure 2-18 Processing route for lamellar microstructures of $\alpha + \beta$ titanium alloys (schematically), adapted from [69].

2.9.2 SLM Ti6Al4V Microstructure

SLM components have a characteristic acicular martensitic microstructure, due to the high cooling rates associated with the process. Figure-2.19 displays the typical SLM microstructure with acicular martensitic α' laths in prior columnar β grains[70]. Scanning strategy and the rotation of the scan vectors determine whether the columnar β grains are oriented along the build height, or slightly inclined to the vertical build direction[71]. The width of these columnar grain is closely related with the hatch spacing between the scan vectors[62]. α' martensite has a hexagonal shape, with high dislocation density, which leads to high yield strength and lower ductility[65]. α' martensite is a result of high cooling rates associated with the SLM process and bed building temperatures which effectively is the homogenisation temperature for the microstructure which is well below the martensitic transformation temperature (M_s) of Ti-6Al-4V, which is around 575°C [70].

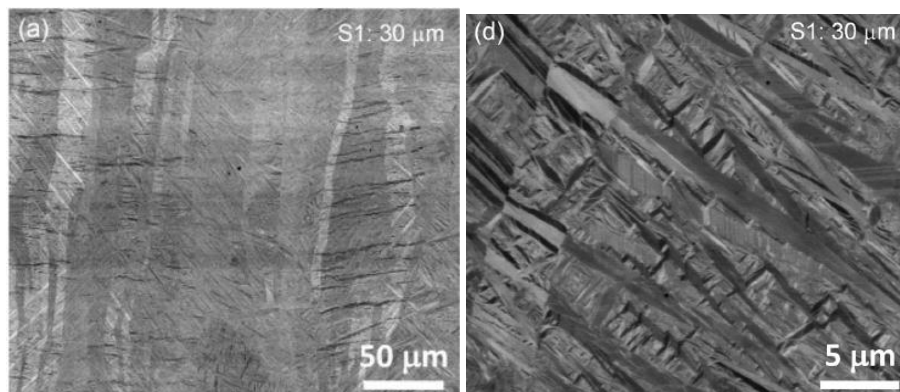


Figure 2-19. Typical microstructure achieved by SLM technology [70]

Post heat treatments have been reported to affect the SLM microstructure [58, 70, 72-75]. The issue with heat treatment is that the starting microstructure of SLM parts is different to conventional manufacturing and therefore the heat treatment temperatures and residence time need to be optimised accordingly to achieve the desired results[62]. Xu et-al [70] reported decomposing martensite into $\alpha+\beta$ microstructure by adjusting the laser focal offset.

Heat treatment can decompose martensite [72-74, 76, 77], but traditional heat treatments cannot resolve the issue of porosity, therefore; hot isostatic pressing (HIP) has been reported as an efficient technique, both for microstructural modification as well as resolving the issue of porosity[73].

Figure-2.20 shows a variation in SLM microstructure at different heat treatment temperatures and under HIPPING[73]. Figure-2.20a shows a reference equiaxed microstructure achieved by hot working. Figure-2.20b shows the typical martensitic microstructure of as built SLM samples. Annealing heat treatment at 700°C is shown in Figure-2.20c, which shows partial decomposition of martensite. Heat treating at 900°C shown in Figure-2.20d, resulted in the full decomposition of martensite into $\alpha+\beta$ microstructure, while Figure-2.20e shows a complete transformation to $\alpha+\beta$ along with α grain growth as a result of hot isostatic pressing at 900°C .

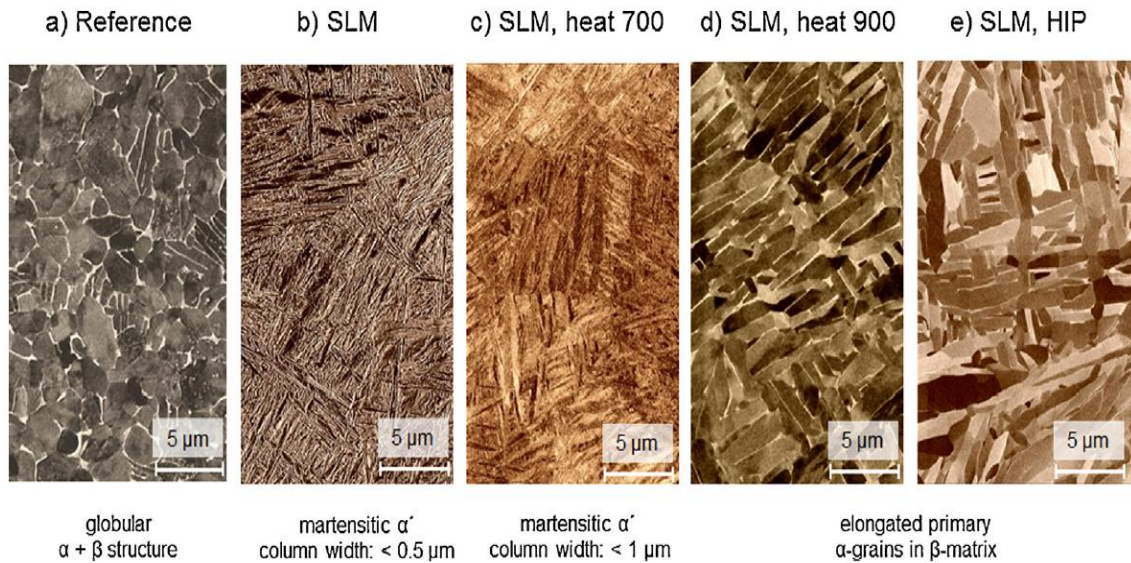


Figure 2-20 (a) Globular 'Reference', (b) as-built SLM structures and effect of thermomechanical treatment on the microstructure of the SLM samples (c-e), adapted from [73]

Different researchers have reported microstructural modification and mechanical properties enhancement as a result of heat treatment [8, 74, 77, 78].

2.9.3 Mechanical properties of $\alpha+\beta$ titanium alloys.

SLM parts tend to have higher yield strength and lower ductility. Sub optimal ductility is a main concern related to SLM build components [8-10, 79], resulting from thermally induced residual stresses, which can cause cracking of the produced parts [80], process-induced defects such as lack of fusion porosity due to insufficient energy input and gas porosity due to excess heat input within the structure, can act as stress concentrators which may lead to premature failure [72] and totally acicular

martensitic microstructure characteristic of the SLM process due to the high cooling rates [70]. According to Ahmed & Rack[66] cooling rates above $410\frac{^{\circ}\text{C}}{\text{s}}$ results in a fully martensitic microstructure. Decreasing the cooling rate leads to diffusion controlled Widmanstätten α formation[66]. SLM Ti6Al4V components have anisotropic properties, attributed to the variation of the orientation of the columnar grains relative to tensile test direction[79]. Conventional heat treatment can enhance the ductility of SLM parts [29, 54, 62], and HIPING has been found to result in the greatest improvement in ductility, making it comparable to hot worked and annealed samples, while the strength decreased slightly and was found to be higher than mechanically processed Ti6Al4V[79]. Figure-2.20 shows that heat treatment and HIPING can result in modified microstructure and therefore the improvement in ductility can be attributed to the microstructural modification.

Microstructural changes greatly affect the mechanical properties of $\alpha + \beta$ alloys. Lütjering [81] demonstrated how mechanical properties vary with lamellar, globular and equiaxed structures and concluded that α grain size has the highest impact on the mechanical behavior of $\alpha + \beta$ alloys. Decreasing α colony size improves yield strength, ductility and crack nucleation resistance[65, 81]

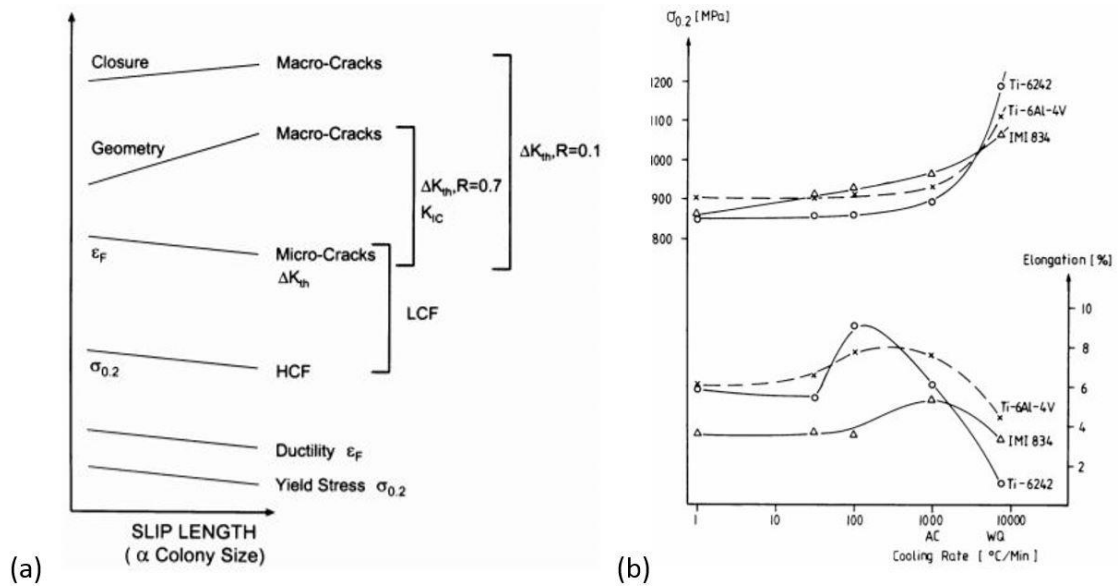


Figure 2-21 (a) . Influence of slip length (α colony size) on mechanical properties, (schematically) (b) Effect of cooling rate from the β phase field on yield stress and ductility of fully lamellar structures [65, 81].

Figure-2.21a shows how α colony size of Ti6Al4V affects the mechanical properties. According to Lütjering et-al, [65, 81] the effective slip length is dependent on the α colony size, and as explained in section-2.8.1 the cooling rate from the β phase field determines the size of α colonies. High cooling rate from the β phase results in martensitic microstructure and the slip length and colony size is equal to the width of an individual martensitic α' lath. Figure-2.21a shows an increase in $\sigma_{0.2}$ yield stress with decreasing slip length, while Figure-2.21b shows the dependence of yield stress on cooling rate, which shows a slight increase with increasing cooling rates initially, but above a certain cooling rate there is an exponential increase in yield stress with further increase in cooling rate.

As opposed to yield stress, which shows a clear direct relation with cooling rates, ductility according to Lütjering et al [65, 81] shows a complex behavior with variation in cooling rate. Figure-2.21b shows that ductility increases with increasing cooling rate and reaches a maximum, beyond this point ductility sharply decreases with increasing cooling rate. Sujoy Kumar[82] explains this behavior of ductility in terms of two competing effects. Initially higher cooling rate reduces slip length, which results in reduce pile-up length, which lowers stress concentrations, and results in delayed crack nucleation thus improving ductility. Figure-2.21a also shows that ductility increases with decreasing slip length. The second effect according to Sujoy Kumar [82] responsible for the decrease in ductility with further increase in cooling rate after the maximum point is a result of the refinement of lamellar structure. Refinement of α lamellae leads to an increasing the strength of the matrix, while coarser α -layers along the β -grain boundaries is weaker and this difference in strength of different microstructural features, results in the premature failure of samples due to preferential premature crack nucleation in the softer grain boundary α .

Manikandakumar et-al concluded that the α colony and lath size are responsible for the mechanical properties of SLM Ti6Al4V[83]. Since SLM microstructure is totally martensitic and martensite has a high dislocation density, therefore the α colony size is equal to a single martensitic lath, which results in dislocations pile ups, and restricts dislocations movement and therefore results in limited plastic deformation in SLM Ti6Al4V. These microstructural features lend SLM components much higher yield strength and ultimate tensile strength, but very low ductility.

Table-2.1 shows a brief comparison of the SLM mechanical properties in as built condition and the effect of different heat treatment and HIPPING cycles on the mechanical properties of SLM Ti6Al4V components from published literature. A full list of mechanical properties of SLM Ti6Al4V from different researchers can be found in the work by Li et-al[84].

Table 2-1 Mechanical Properties of as built and heat treated SLM Ti6Al4V components

Conditions	Specimen orientation	UTS (MPa)	Yield stress (MPa)	%Elongation
Study by Leuders et al [72].				
No heat treatment Machined surface	Vertical	1080 ± 30	1008 ± 30	2 ± 2
2hr @ 800°C Machined surface	Vertical	1040 ± 30	962 ± 30	5 ± 2
2hr @ 1050°C Machined surface	Vertical	945 ± 30	798 ± 30	12 ± 2
HIP:2hr @ 920°C and 100MPa Machined surface	Vertical	1005 ± 30	912 ± 30	8 ± 2
Study by Kasperovich & Hausmann [73].				
No heat treatment As-built surface	Vertical	1051	736	12
No heat treatment Machined surface	Vertical	1155	986	11
1hr @ 700°C Machined surface	Vertical	1115	1051	11

2hr @ 900°C Machined surface	Vertical	988	908	10
HIP: 2 hr @ 900°C and 100 MPa Machined surface	Vertical	973	885	19
Study by Vrancken et-al [62].				
SLM As built	Vertical	1110±9	1267±5	7.28±1.12
Reference	Vertical	960±10	1006±10	18.37±0.88
2hr @ 540°C then Water Quenched	Vertical	1118 ± 39	1223 ± 52	5.36 ± 2.02
2 hr @ 850°C then Furnace Cooled	Vertical	955 ± 6	1004 ± 6	12.84 ± 1.36
5 hr @ 850°C then Furnace Cooled	Vertical	909 ± 24	965 ± 20	– (premature failure)
0.5 hr @ 1015°C then Air cooled then 2 hr @ 843°C and Furnace Cooled	Vertical	801 ± 20	874 ± 23	13.45 ± 1.18
2hr @ 1020 °C then Furnace Cooled	Vertical	760 ± 19	840 ± 27	14.06 ± 2.53
3hr @ 705°C then Air Cooled	Vertical	1026 ± 35	1082 ± 34	9.04 ± 2.03
1hr @ 940°C then Air Cooled Then 2 hr @ 650°C followed by Air Cooling	Vertical	899 ± 27	948 ± 27	13.59 ± 0.32
0.5hr @ 1015°C then Air Cooled followed by 2hr @ 730°C then Air Cooled	Vertical	822 ± 25	902 ± 19	12.74 ± 0.56

2.10 Residual Stress Measurement Techniques

Residual stress cannot be measured directly and all the measurement techniques measure different material and geometrical properties of the test specimen to deduce residual stress information. Figure-2.22 shows a classification of the Residual Stress Measurement techniques. Residual stress measurement techniques

are usually classified as destructive or non-destructive. The layer removal method, the crack compliance method and contour method are some examples of destructive techniques while X-ray diffraction, neutron diffraction and bridge curvature method are some of the non-destructive techniques. Depending on the particular measurement method the results can either be qualitative or quantitative and the level of quantification also varies over a wide range. Which residual stress measurement technique to use is really a matter of choice depending on how the measurements are going to be used as well as the availability of resources. A detailed review and comparison of the residual stress measurement techniques is presented in Appendix-A.

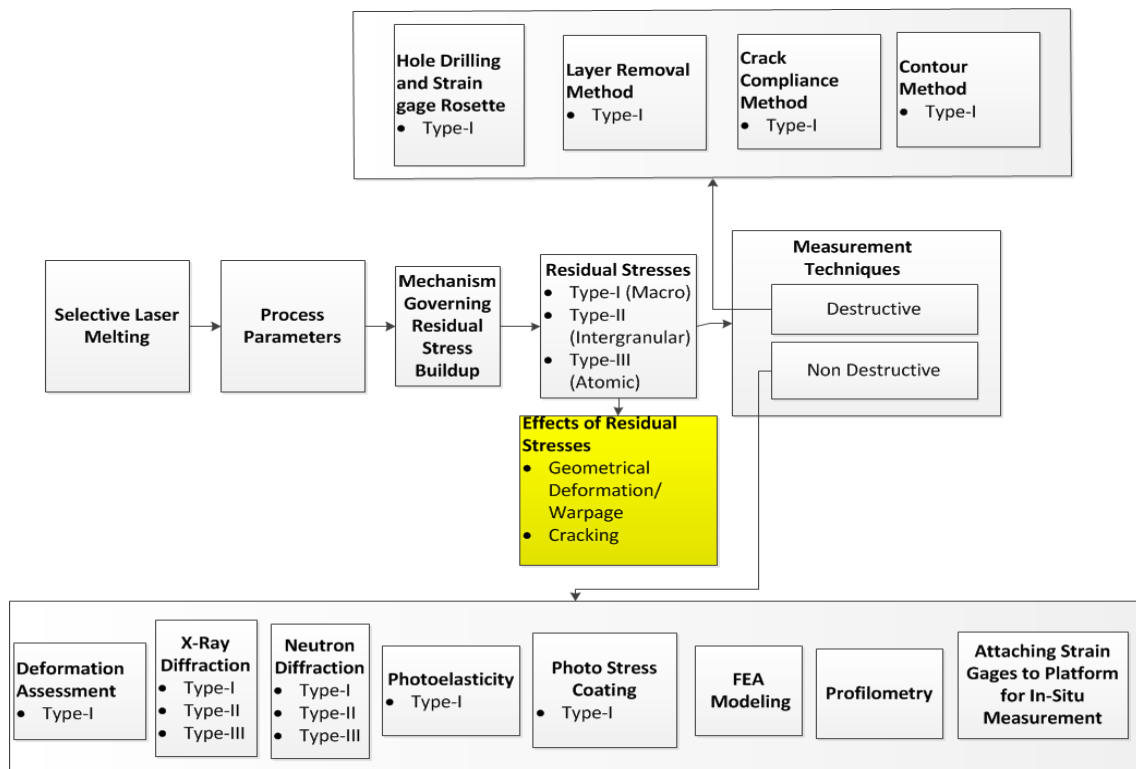


Figure 2-22 Residual stress measurement methods

Hole drilling is termed as a semi-destructive residual stress measurement technique and was chosen for initial residual stress measurements because of the in house availability and cost effectiveness as a large number of samples are to be tested for establishing the direction of research.

In the final part of the project the contour method will be used to determine a stress profile along the cross section of a geometry for identifying areas with higher residual stress for intuitive application of stress reduction strategies to those high stress specific areas.

2.10.1 Hole Drilling

A hole is drilled through the specimen and strain gages on the surface or full field optical techniques measure the change in strain. Strain relaxation in the surroundings of the hole gives a measure of the residual stress. Figure-2.23 shows a residual stress specimen attached with a strain gage rosette and a hole drilled in the centre. Residual stress can be measured up to 2mm depth and measurement precision typically ranges between 5–20%. Hole drilling is a semi-destructive method with portable equipment capable of measuring bi-axial stress σ_{xx} , σ_{yy} , and τ_{xy} . It is a quick, easy and cost effective method capable of measurements for both metals and non-metals as hole drilling is indifferent to grain structure.



Figure 2-23 Residual stress specimen with strain gage rosette showing hole drilled in centre

Hole drilling is only capable of near surface measurements of in-plane stress profiles. Stresses are non-uniform and max stress can range up to 70% of yield stress. Since it is a semi destructive technique, the hole needs to be filled after testing and since the hole is very small, the part can still be used. σ_{zz} cannot be measured and for residual stresses greater than 80% σ_{yield} the uncertainty in measurements increases. This method is not suitable for complex geometries as surface preparation is needed and measurements are sensitive to non-concentricity of the hole and strain gage [2, 5, 25, 27, 53, 85-88].

2.10.2 Contour Method

As shown in Figure-2.24 in the contour method a specimen is sectioned along its cross-section using a wire EDM. The surface height profiles of both the cut surfaces

are measured using a coordinate measuring machine or a laser profilometer to account for cutting asymmetry. The deformation of the cut surfaces are a result of the Residual Stresses (pull inwards for tensile stresses, bulge outward for compressive stresses). Residual Stresses normal to the cut are given by finite element calculations and are equal to the stresses required to return the deformed surface shape acquired from the average of the two cut surfaces to a flat plane. Strain Relaxation combined with Bueckner's superposition principle gives a measure of the Residual Stress.

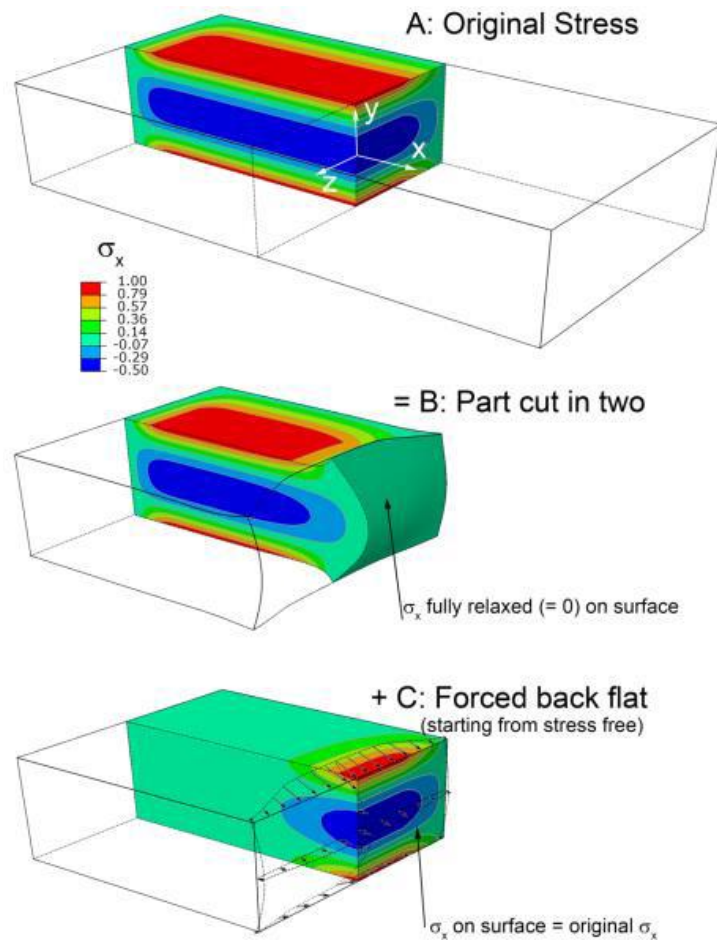


Figure 2-24 Schematic of Contour method [53].

The contour method gives a full 2D stress map along a specimen cross section and the measurements are accurate within 5–20%. Wire EDM and Coordinate Measurement Machine's axis ranges can limit the depth of measurement. Accuracy is independent of the depth of cut and is indifferent to grain structure. A good EDM cut can provide a surface for further processing such as etching.

It is a destructive technique which requires very accurate cutting and is not good for near-surface measurements. Data needs to be filtered and smoothed which compromises accuracy. Getting residual stress data from the contour measurement requires awareness of Finite Element Software. The costs of measurement are high and the availability of the testing equipment is limited which makes it very difficult for a large number of samples to be tested [5, 53, 89].

2.11 The use of modelling in the measurement of Residual Stress in SLM applications

There are various experimental residual stress measurement techniques available as detailed in Appendix-A. The qualitative measurements used by other researchers are comparatively quick, easy and cost effective and offer a good starting point for further experimentation. Quantitative measurements can be expensive and time consuming but give a more solid understanding of experimental results and assist in the future direction of the project. A further option is offered by simulation and modeling techniques.

Development of a powerful Finite Element Analysis simulation will save both time and effort in the process of identifying and rectifying residual stresses in the SLM process. Simulation could give greater freedom to quickly explore different possibilities, provide guidelines for targeting the direction of the research and potentially reduce the number of builds necessary to develop the project.

For accurate simulation of the SLM process, the dynamics of the process along with most process parameters should be considered. Several FEM thermal models developed by researchers can be found in literature [6, 90, 91], where a laser beam was modelled as a moving heat source, the effect of process parameters on stresses induced due to thermal gradients was studied. However, these models are based on assumptions for linearizing some of the inherent nonlinearities of the SLM process. On the one hand due to computational power limitation, it is not always feasible to model every single scanning vector within the energy application and it is better to follow the so called global model based on whole parts [43]. While on the other hand, a 3D thermo-mechanical finite element model including the effect of the powder-to-solid transition has been developed to investigate the transient temperature, transient stresses, residual stresses and distortion of the component made of multiple materials produced using a laser-assisted layer-by-layer fabrication approach [92].

The use of a high powered laser beam, for layer-by-layer fusion of metallic powder is a characteristic of the SLM process. The temperature profiles generated in the SLM process are most widely simulated using FEM [6, 90, 91, 93-101].

FEM simulating the melting and solidifying of powder was used by Shiomi et al [93] for developing an understanding of the laser forming mechanism. The calculated weight of the solidified powder was compared to the weight of experimentally solidified powder in order to validate the model. The simulation results agreed with the experimentally measured weights, and it was shown that the peak laser power affected the maximum temperature reached by the system more than the exposure time. The model was limited to simulating a single irradiation spot without considering the detailed powder thermophysical properties.

Computing the property change in properties from powder-liquid-solid, Matsumoto et al [6] proposed an FEM method for simulating the temperature distribution within a single SLM metallic layer, and predicting the development of stress based on the simulated temperature profile. The method developed is limited in not considering the effect of a substrate plate, which acts as a heat sink and will affect the temperature profile greatly. The model does not consider the thermal dependence of material properties, nor the laser absorptivity of the powder bed. There is no experimental validation of the simulation method, but it is one of the first works that takes into consideration the phase change from powder-liquid- solid.

Using the element birth and death technique for simulating the powder deposition, and introducing detailed thermal conductivity of the powder bed Roberts et al [90] developed an FEM simulation to predict the temperature profile for multiple layers of the SLM process. However, Zehner et al [102] proposed a more detailed model taking into consideration the mushy zone characteristics ignored By Roberts-et al. The model was experimentally validated providing a better insight on the SLM

process, but, for more accurately computing the solidification in SLM and predicting a more reliable thermal profile a more detailed model is needed.

Using basic thermal dependent properties Song et al [98] showed that SLM temperature distribution simulation can be really helpful for optimising processing parameters. Simulation results helped in fabricating a part with a desired degree of porosity, even though the predicted temperatures were extremely high. This work highlights the importance and need of a detailed FEM approach for accurately predicting the SLM temperature profile. A realistic temperature profile prediction can be helpful for optimising or predicting optimum processing parameters for a material under consideration.

The depth at which the intensity of the laser energy reduces to $\frac{1}{e}$ of the value at the powder bed surface is defined as the optical penetration depth of a laser beam[103]. Forroozmehr et al [101], simulated the melt pool size using an FEM approach based on the penetration of a laser beam into the powder bed. Using a volumetric heat source along with detailed thermal dependent properties of powder as well as solid, and ignoring the properties of the mushy zone, a 3D model of a single layer was developed, considering powder to liquid to solid phase transition. Optical penetration depth was calibrated through experiments to improve the reliability of the model and the simulated melt pool size agreed with the experimentally measured melt pool. The work did not look into the effect of adding more layers.

Using detailed temperature dependent thermo-mechanical properties of Ti6Al4V powder and solid material along with a volumetric heat source considering the

optical penetration of the laser into the powder bed, Parry et al [47] simulated the transition of powder to liquid to solid, for studying the effect of scanning strategy on residual stress. The model predicted very high temperatures and this high temperature was termed an isolated singularity and ignored in the stress calculation but the reason for this high temperature is actually associated with ignoring the heat transfer in the melt pool due to fluid flow.

Fluid flow in the melt pool greatly influences the heat transfer in the SLM process [104], and considering the powder without considering the effect of fluid flow in the melt pool can result in inaccuracies. Using a multi-physics simulation tool ALE3D, developed at Lawrence Livermore National Laboratory, Khairallah et al [105], created a three-dimensional mesoscopic micrometer scale model to illustrate that considering the stochastic nature of a powder bed is really important for accurate simulation of the SLM process. It was demonstrated that surface tension drives the physics of the melting phenomenon in SLM and affects the heat transfer in the melt pool as well as the final topology of the solidified melt pool. Using computational fluid dynamics, Yuan et al [106], created a three dimensional model of the SLM process for accurate prediction of melt pool size and temperature profile which was validated with experiments. CFD models take the physics of the SLM process into consideration and involve lesser simplifications of the process as opposed to FEM and therefore are capable of predicting the melt pool geometry and thermal distributions more accurately. CFD models are computationally expensive as opposed to FEM and expertise in fluid dynamics is required to be able to properly model the complex dynamics of the SLM melt pool.

Simulating the SLM process without considering the effect of heat transfer due to marangoni convection in the meltpool and taking the continuum approach for representing powder can result in very high temperatures as shown in the work by Fu et al [107]. If an effort is made to control the temperature that will lead to lower melting, this might not be representative of the experimental melt pool size. To overcome this issue and to achieve a reliable prediction of the melt pool size as well as the approximate temperature, various modelling approaches have been taken by different researchers.

Considering powder to solid transition and effectively simulating volume shrinkage, along with material removal using the concept of a sacrificial layer evaporation, to control the temperature from rising Loh et al [100] developed a single layer FEM model, to obtain the desired temperature profile and melt penetration. The assumptions in this work limits this modelling approach to simulating only a single layer and therefore it is not suitable for simulating multiple layers of real SLM process, even though the volume shrinkage was experimentally validated.

Another approach widely taken by researchers to be able to model the SLM process accurately using the simpler route of FEM, thus reducing the processing time is accounting for melt pool convection using the enhanced thermal conductivity approach. Safdar et al [99], showed that the anisotropic enhanced thermal conductivity approach gives a better estimation of the SLM process as opposed to isotropic enhanced thermal conductivity. Experimentally validating the melt pool size predicted by the anisotropic enhanced thermal conductivity approach, this work concluded that it is a viable approach for artificially simulating the heat flow

due to Marangoni convection in the SLM process. This approach can be useful for accurately modelling the melt pool and temperature profile, without needing the complex CFD models.

Recently Lopez et al [108], used the enhanced thermal conductivity approach, combined with detailed temperature dependent material properties considering the variation of properties in the mushy zone, along with a surface heat source to develop a two dimensional model to predict the thermal profile and cooling rates in SLM of AA-2024. The thermal profile was used for predicting the microstructure and dendritic spacing of AA-2024 and comparison with experimentally determined microstructure validated that the enhanced thermal conductivity approach can accurately predict the thermal mechanics of the SLM process.

FEM in general is a computationally efficient and a suitable technique for simulating the SLM process. Using the enhanced thermal conductivity approach can improve the accuracy of the simulation and therefore in this work the enhanced thermal conductivity FEM approach will be used for modelling the SLM process, to understand the effect of varying process parameters on the residual stress build up in SLM Ti6AL4V components.

2.12 Geometrical Dependence of Residual Stress in SLM Components

SLM part length and moment of inertia affects the magnitude of the residual stress build up [29]. According to Casavola et-al [2], circular specimens warp less as

opposed to, components where the geometrical dimensions have a greater relative variation. This work also concluded that for the same diameter, thicker specimens have lower stresses as opposed to thinner specimens.

Specimens of circular geometry (disks of 35 mm diameter) exhibit very small warping effect which would be instead very pronounced in specimens where one dimension predominates over the others.

Yadroitsava et-al [109], compared residual stresses in a parallelepiped built directly onto the substrate with a cantilever beam, where the overhanging parts were supported and found that the residual stresses in the cantilever structure were much higher than the parallelepiped. This work concluded that residual stress depends on the material properties, as well as sample and supports geometry.

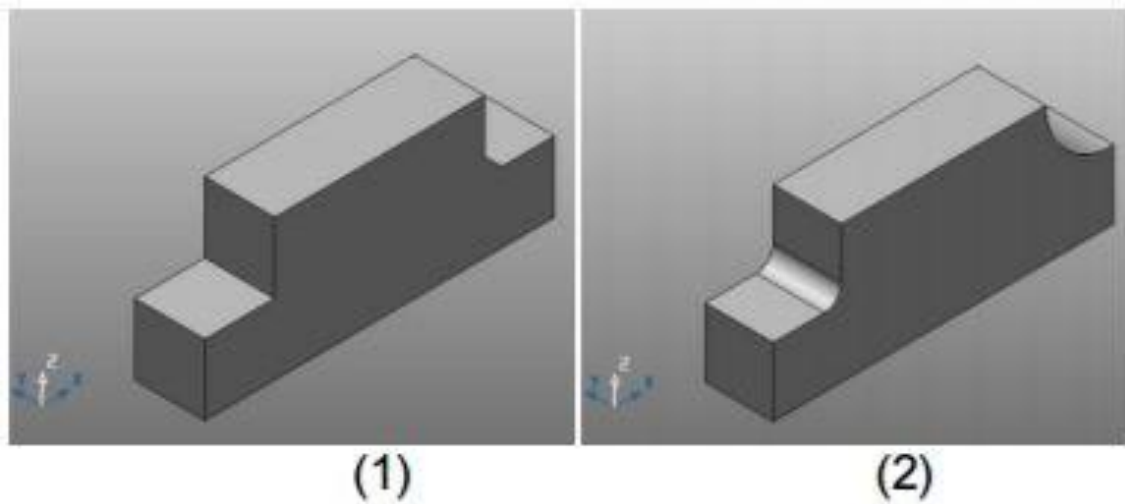


Figure 2-25 (1) Showing a geometry with a sharp corner and a slightly less sharp corner. (2) Same geometry as (1) but the curvature of both corners is increased. Adapted from[110].

Mugwagwa et-al [110], studied the effect of geometrical features on residual stress using the geometry shown in Figure-2.25 below. This work concluded on residual stress measurement on samples shown in Figure-2.25(1) that sharper edges of the specimens exhibited higher stresses. Increasing the curvature of the corners as shown in Figure-2.25(2) relaxed these stresses due to a reduction in sharpness.

2.13 Knowledge Gap

It can be seen from section-2.7 that different researchers have proposed different stress reduction strategies and the results vary from one work to another even with the application of similar stress reduction strategies. Some strategies have been claimed to be more useful than other but the combined effect of these various stress reduction strategies has not been investigated. The effect of various stress reduction strategies on the mechanical properties of SLM parts has not been investigated either.

Pre-heating the bed has been found to be the most effective in-situ stress reduction strategy but there is no guide as to what is the optimum pre-heat temperature. The optimum range of bed pre-heat temperature for a combination of minimum residual stress and acceptable mechanical properties yet need to be established. With Electron beam melting Ti6Al4V is being processed at 650-750°C [56, 57]. It might be useful to process Ti64 at 650-750°C bed pre-heat temperature and see what effect it has on the residual stress and mechanical properties.

An island scanning strategy with random scanning order reduces the build-up of Residual Stresses but commercial machines come with some pre-determined scanning orders and the scanning order is not completely random. Geometrical dependence of scanning strategies is yet a question to be resolved. Whether using the same scanning strategy for sections of varying heights and width is effective or varying the scanning strategy according to different sections of the same part can produce better results is yet a question to be answered.

Though not considerable both Pre and Post-scanning have a reducing effect on the build-up of residual stresses. The only question that needs to be resolved is whether the build time it adds is a cost effective trade off.

Placing the part on the centre of the build platform gives minimal residual stresses but a build containing multiple parts needs a better solution as all of the parts cannot be placed on the centre and it will not be efficient to build in batches of one part at a time. The effect of part positioning on the build platform needs further investigation as one study with a limited number of samples cannot be regarded as a conclusive argument to support the premise of stress build up variation due to positioning.

Base plate material has a minimal effect on the Residual Stress build-up but considering it in conjunction with other strategies will add to the combined effect and makes it feasible to use the same material base plate. Similarly base plate thickness effect needs to be probed further to establish a definite relationship with Residual Stress build-up.

Layer thickness has a reducing effect on the Residual Stress build up but its effect on consolidation of the material, part density and mechanical properties of the part needs to be verified as having lower density can have the effect of reducing residual stresses but can reduce mechanical properties.

Finally there is no study on applying the stress reduction strategies to areas of geometries with higher stresses as all studies have been concentrating on applying the stress reduction strategies globally. An intuitive geometric dependent application of stress reduction strategies and its effects on the final part is a totally novel area and that is the final goal of this research project.

The knowledge gap in published literature can be summarised as.

- Different researchers present contradicting results for the effect of stress reduction strategies on residual stress on SLM components.
- Combined effect of various stress reduction strategies has not been established.
- The effect of stress reduction strategies on mechanical properties has not been investigated.
- The effect of rescanning on mechanical properties has not been investigated.
- There is no study on the effect of varying parameters in combination to keep energy density constant on residual stress.
- The effect of layer thickness on mechanical properties has not been established.

- There is no guideline on the optimum bed pre-heating temperature for minimising residual stress.
- The effect of bed pre-heating on mechanical properties has not been established.
- The effect of bed pre-heat temperatures in the range of material microstructural transformation (such as martensite decomposition or annealing) on residual stress and mechanical properties has not been investigated.
- There is no study on applying stress reduction strategies to regions of interest in the part cross-section. All studies focused on global stress reduction strategies.

3 Experimental Methodology

3.1 Titanium Alloy Powder

The powder used in these trials was an argon gas atomised titanium alloy powder containing 6% aluminium and 4% vanadium, with a size range of +15-45 μ m. The powder was manufactured and supplied by a specialist German manufacturer TLS Technik Spezialpulver. The test certificate for the powder is shown in Appendix 1, indicating material composition and the percentage powder by volume within each size range between 0 and 55 μ m. The powder complies with international ISO standards for Ti6-4 powder. The composition of the powder is shown in Table-3.1.

Table 3-1 Composition of Ti6Al4V powder

Element	N	C	H	Fe	O	Al	V	Ti
% Composition	0.006	0.009	0.001	0.2	0.09	6.21	4.08	89.404

3.2 SLM Systems

Two different Renishaw machines were used for manufacturing all the samples in this research project.

3.2.1 Renishaw AM250 SLM machine

The Renishaw AM250 SLM machine used in the project is shown in Figure-3.1. It is sited at TWI Technology Centre in Yorkshire. The Renishaw AM250 machine uses a

200W fiber laser with 80-100 μ m spot size and has a build volume of 250mm x 250mm x 300mm. The machine is able to operate in an inert atmosphere and is able, therefore, to process reactive powders such as titanium and aluminium. It produces the inert atmosphere by firstly evacuating the build chamber using a vacuum pump and back filling with argon gas. The machine also has the facility to pre-heat the build chamber up to a temperature of 170 °C using heating elements under the build plate. There is also a comprehensive atmospheric filtration system which continually cleans the gases within the build chamber to remove any airborne powder particles or soot that may form during component builds and interfere with the operation of the laser beam delivery.



Figure 3-1 Renishaw AM250 SLM machine

This machine was used for manufacturing all the test parts used to study the effects of a standard industrial SLM machine's process parameters on residual stress and mechanical properties of Ti6Al4V SLM built components.

3.2.2 Renishaw AM125 SLM machine

The Renishaw AM125 SLM machine used in the project is sited at the University of Sheffield. The AM125 SLM machine is similar in principle to the larger AM250 machine, but has a smaller build volume of 125mm x 125mm x 120mm. It operates in the same way as the larger AM250 machine, with inert atmosphere capability, integrated filtration and initially, before modification, with a bed pre-heat temperature of up to approximately 170°C.

This machine, however, was modified to increase the bed pre-heat temperature and in doing so, the build volume was reduced to 65mm x 65mm x 100mm to enable insulation material to be added to prevent damage to the chamber and associated mechanics. The full details of the modifications are described in Section 3.4.5.

3.3 Optimisation of parameters

The in-process scan parameters are the most important ones and are most easily controllable as part of the programming for the build. These include:

- Scanning Strategy
- Exposure (E) (μs)
- Laser power (P) (W)

- Hatch spacing (h) (μm)
- Contour spacing (μm)
- Layer thickness (lt) (μm)
- Focus Offset

These parameters combine to form the energy density(ED) in (J/mm^3) for the process as shown by Equation-2.1 and also dictate the process window, within which an acceptable SLM build must operate. Within the process window a stable melt pool is attained and this is achievable within a small range of combinations of parameters. Operating at too high a power or too low a speed produces a keyhole effect, leading to substantial vaporisation of the melt pool and extensive porosity. Whereas a lower power, high speed combination is likely to result in a lack of fusion and a corresponding loss of density in the build.

It was necessary to develop and optimise build parameters that would be able to produce fully dense (>99.5%) SLM-built test sample blocks. These parameters would also be the baseline setting for all future trials and comparisons. These were carried out using the Ti 6-4 test powder and the Renishaw AM250 SLM machine to be used in all future work. In order to accomplish the parameter optimisation for density, a number of test samples were manufactured using a range of parameter combinations. They were checked for density, using optical microscopy for porosity analysis.

Great care was taken to ensure repeatability in both the parameter optimisation process and the subsequent sample builds. Consequently prior to each build, the

build chamber was scrupulously cleaned and the recoater blade and the machine filters were changed. Additionally, all build were positioned identically on the build plate to ensure that positional effects were minimised. All builds were designed and programmed using Autofab and Magics CAD software using standard SLM work instructions procedures.

3.3.1 Optimisation Trials for Density

Initially it was necessary to find the optimum combination of parameters for producing fully dense parts. As Ti64 is a commonly used powder for SLM applications, previous experience indicated that the ideal parameters fell within a fairly close range and it was possible to select and fix certain parameters quickly. Therefore it was decided that ideal parameters could be achieved by fixing other parameters and varying only power and exposure time.

Using the AM250 machine, 10X10X10mm blocks were manufactured at 100 °C bed pre-heat temperature for density optimisation trials. A process parameter optimisation trial was undertaken using the default Ti64 Renishaw SLM parameters shown in Table-3.2.

Table 3-2 SLM build parameters

Focus Offset	Hatch Spacing (mm)	Contour Spacing (mm)	Layer Thickness (µm)	Scanning Strategy
0	0.08	0.2	50	90° Alternate

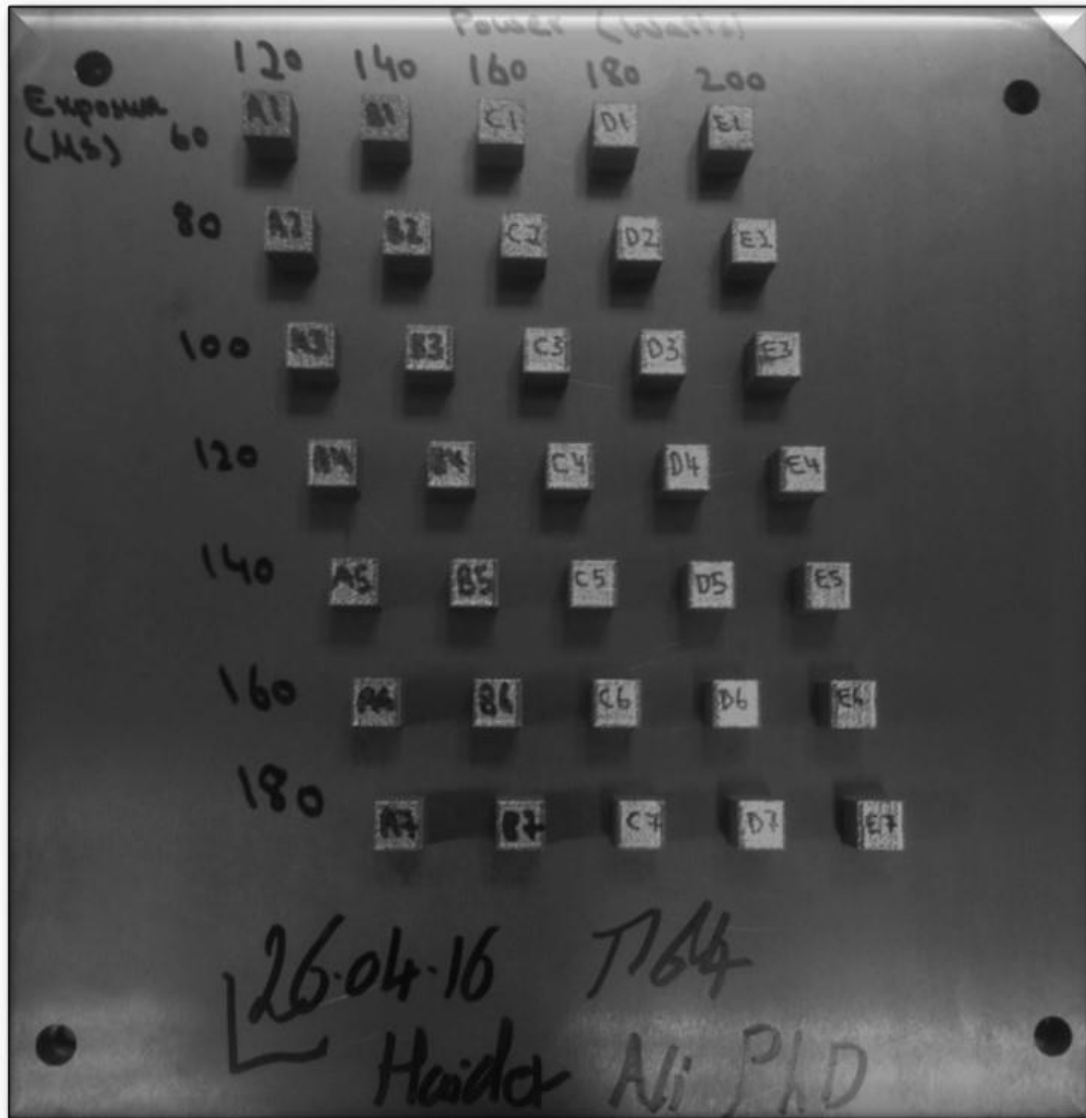


Figure 3-2 Density optimisation trial

Table-3.3 shows the laser power and exposure combination trials used for density optimisation trial shown in Figure-3.2.

Table 3-3 Test array for power and exposure

Power(<i>W</i>)	Exposure (μs)	60	80	100	120	140	160	180
120		A1	A2	A3	A4	A5	A6	A7
140		B1	B2	B3	B4	B5	B6	B7
160		C1	C2	C3	C4	C5	C6	C7
180		D1	D2	D3	D4	D5	D6	D7
200		E1	E2	E3	E4	E5	E6	E7

3.3.2 Optical Microscopy Porosity Analysis

The volume fraction of porosity in the specimen was estimated by area fraction analysis of representative micrographs/fields using a method based on ASTM E2109-01 (2007) and BS 7590:1992.[111, 112]. The property used to differentiate porosity from its surroundings was its apparent contrast under a microscope and subsequent thresholding of grey values to exclude all non-porosity constituents in the micrographs/live image.

The samples were cross sectioned perpendicular to build direction and hot mounted into resin using Struers LaboPress-1. The samples were then polished on LabPol Duo8 using grit sizes ranging from 120 to 1200 followed by 0.06 μm OPS general. The polished samples were etched with Kroll's and re-polished to get rid of the

smearing and be able to see the true porosity. The polished surface was analyzed for porosity by using an Olympus BX60 optical microscope and images were taken at 5X magnification. An open source software Image-J was used for porosity analysis by converting the images into binary and measuring the ratio of black (representing porosity) to white (representing fully dense material). The specimen were etched using Kroll's (92 ml distilled water, 6 ml Nitric Acid and 3 ml Hydrofluoric Acid) and optical microscope was used to investigate the microstructure of the test samples after etching.

3.4 Trials for Effect of SLM Process Parameters on Residual Stress and Mechanical Properties using Standard AM250 Machine

After finding the optimum combination of parameters for achieving nearly fully dense parts, the next stage was to evaluate the effect of SLM process parameters on residual stress and mechanical properties.

3.4.1 Effect of Scanning Strategy

Having fixed the build parameters, it was necessary to decide on the scan strategy to be used to control the sequence in which the beam is positioned and moved across the powder surface during a component build. This is important because it determines the time between adjacent spots being irradiated and melted by the laser beam, and hence will determine the temperature the first spot will have reached before being affected by the heat from the next spot. This will determine the highly

localised temperature gradients around this area and therefore influences the build-up of residual stress. It will also determine the microstructure of the built component in this small area and thus affect the final mechanical properties that will be exhibited. These effects are inevitably totally different to a conventionally manufactured component, eg. cast or forged, where temperature and temperature gradients are much more uniform and stable and more directly controlled.

3.4.1.1 Comparison of Alternating and Island Strategies

There are many scanning strategies that could be employed in the development of a component build procedure. However, there are two which have become predominant in general SLM manufacture – ‘90° alternating strategy’ and ‘island strategy’. There are conflicting views among researchers and also SLM machine manufacturers about which of these strategies produces the best results. The generally held view has been that the island scan strategy produced less overall residual stress, by as much as 70% in one research paper. However, this may have been machine or material specific at the time of the research and as equipment has developed these conclusions may have changed. Therefore it was felt important to confirm this using Ti64 and the Renishaw AM250 SLM machine.

For all test cases shown in Table-3.4, blocks of size 30mm x 30mm x 10mm high were built for residual stress measurement. This is a size suitable, after completion of the build, for the positioning and fixing of a strain gauge rosette. This is then suitable for subsequent precision drilling to enable the hole drilling method of residual stress measurement to be carried out.

For each test case shown in Table-3.4, on the same build platform, three tensile test specimens were also built to allow removal and testing. This is done to enable determination of the material properties relating to each build to check that tensile strength is not being sacrificed in the drive to reduce residual stress in the finished components.

Residual stress measurements, tensile testing and hardness measurement was carried out at TWI Cambridge.

Table 3-4 Scanning strategy test cases

Test Case	S-1	S-2	S-3	S-4	S-5
Scanning Strategy	90° Alternating	2x2mm chessboard	3x3mm chessboard	5x5mm chessboard	5x5mm chessboard with Opposite Scan Vectors.

3.4.1.1.1 90° alternating strategy

The 90° alternating strategy procedure involves turning the orientation of each over-building layer by 90° to try to evenly distribute any residual stress build up that is likely to occur (see Figure-3.3). The build strategy is, therefore, repeated every four layers until the required height is achieved, equivalent to approximately 200 layers in total for a 10mm high block. The first scan vector in each layer is shown by the blue arrow.

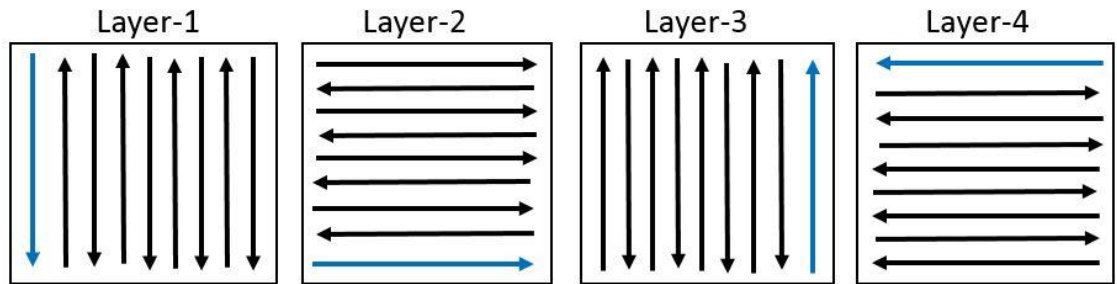


Figure 3-3 Schematic of 90° alternating scanning strategy

3.4.1.1.2 Chessboard strategy

The chessboard strategy procedure involves carrying out the block build in a series of smaller blocks spread around the build area. For example, if the 30mm x 30mm block is being built up in a series of 5mm x 5mm smaller blocks, each build layer would incorporate 36 of the smaller block sizes, each block meets and builds onto the adjacent blocks on all four sides during each layer build (see Figure-3.4(a)). This is continued until the full height of the required block is achieved.

To investigate the effect of altering the scan vector length on residual stress and mechanical properties, a number of blocks using different chessboard square sizes were built.

The following island sizes were produced for investigation:

- 2mm x 2mm chessboard
- 3mm x 3mm chessboard
- 5mm x 5mm chessboard

To investigate the effect of chessboard squares rotation relative to each other on residual stress and mechanical properties, 5mm x 5mm chessboard blocks were built scanning adjacent squares in 90° rotation as shown in Figure-3.4(b).

The built blocks were investigated for residual stress and mechanical properties to assess any variations caused by the various build strategies.

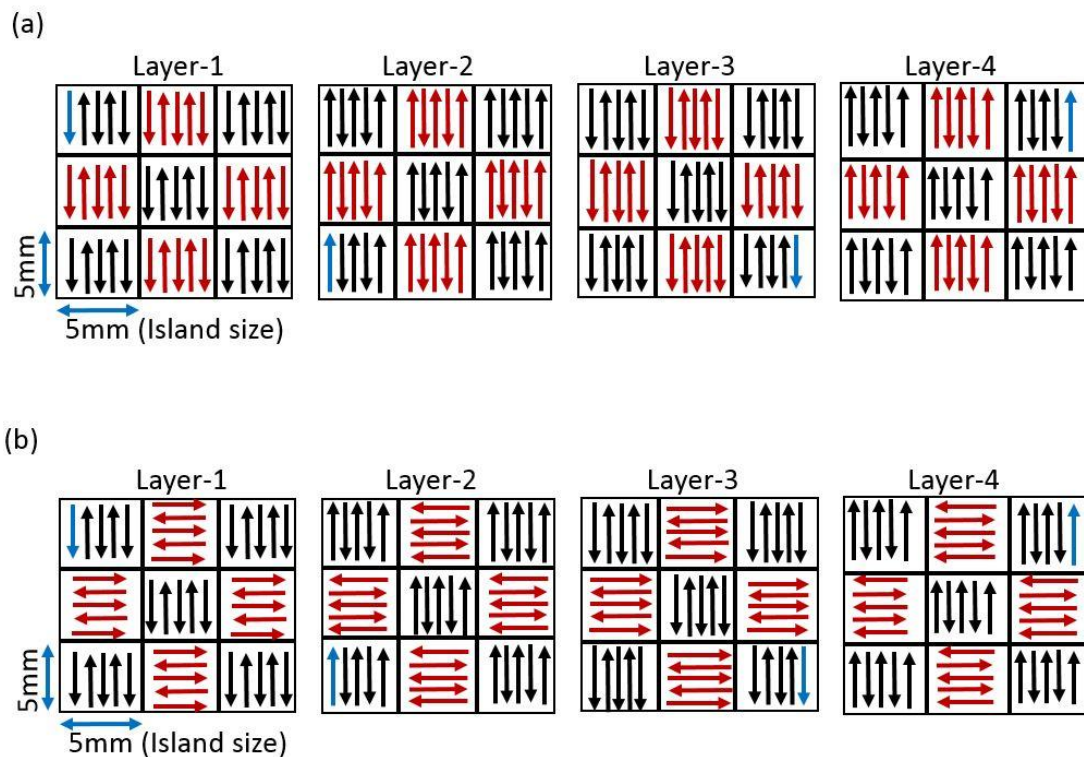


Figure 3-4 (a) Schematic of Chessboard Scanning (b) Schematic of Chessboard Scanning with Adjacent Chessboard Squares Scanned in 90° rotated direction

The first scan vector of each layer is shown by the blue arrows. Chessboard scanning started from the blue arrow, completing the scanning of all black squares in the first

row and then continuing on to the next row till all black squares have been scanned. Afterwards the laser started to scan the red squares, starting from row one and moving on to the next row till the completion of the whole layer. The same scanning order was repeated in all subsequent layers.

3.4.2 Effect of layer thickness

A further set of trials was carried out using layer thickness as the variable. Previous research on this topic concludes that increasing layer thickness reduces residual stress, but the results range from 5% when doubling the layer thickness to 80% for an increase of layer thickness by 2.5 times. In these trials, layer thickness was varied in 25 μm steps between 25 and 75 μm , with blocks and tensile samples being prepared for measurements to be taken for residual stress and mechanical properties. For each change in layer thickness, a new set of parameters was developed to provide full density and produce minimal defects. The builds were completed using 90° alternating strategy. Table-3.5 below shows the different layer thickness trials carried out in this work.

Table 3-5 Layer thickness test cases

Test Case	LT-1	LT-2	LT-3
Layer Thickness (μm)	25	50	75

3.4.3 Effect of re-scanning

This set of trials involved the building of standard 30mm x 30mm x 10mm test blocks and tensile specimens using the 90° build strategy and 50µm layer thickness. After each build layer, however, the surface was re-scanned but without adding the usual layer of powder to the scan. The effect of the second heating pass per layer could possibly reduce residual stress by acting as a heat treatment cycle but may also affect material properties by increasing grain size due to the longer time at temperature. A number of papers have been published citing reductions in residual stress build-up by using rescanning at various power levels. One suggests rescanning at 50% energy reduces residual stress by 30% and another states rescanning at 150% energy produces reductions of 55%.

To create a broader understanding of the effects, the re-scanning energy was varied between 50%, 75%, 100% and 150% of optimum build energy density, and residual stress and mechanical properties were measured. Rescan energy density was varied by varying either power or exposure.

3.4.3.1 Re-Scan with Energy Density Varied by Varying Exposure

Re-scanning energy density was varied by keeping all other parameters constant and varying the exposure time in proportion of the optimum exposure time calculated from initial density optimisation trials presented in section-3.3.1. Table-3.6 below shows the different re-scanning trials carried out in this work, where re-scan energy density was varied by varying exposure time.

Table 3-6 Re-scan with varying exposure test cases

Test Case	RSE-1	RSE-2	RSE-3	RSE-4
Re-Scan Energy Density (% of Optimum)	50	75	100	150
Re-Scan Exposure (μ s)	50	75	100	150

3.4.3.2 Re-Scan with Energy Density Varied by Varying Power

Re-scanning energy density was varied by keeping all other parameters constant and varying the power in proportion of the optimum power calculated from initial density optimisation trials presented in section-3.3.1. Table-3.7 below shows the different re-scanning trials carried out in this work, where re-scan energy density was varied by varying power.

Table 3-7 Re-scan with varying power test cases

Test Case	RSP-1	RSP-2	RSP-3
Re-Scan Energy Density (% of Optimum)	50	75	100
Re-Scan Power (W)	100	150	200

3.4.4 Effect of varying Power and Exposure Combinations at Constant Energy Density

In this set of trials, power and exposure time were varied, such that the energy density for each build remained the same as calculated from the optimum combination of parameters found in density optimisation trials (section-3.3.1).

Three 30x30x10mm blocks and three tensile specimens were manufactured using each combination of power and exposure time. Although not a universal term, the formula used for energy density for the Renishaw SLM system is shown by Equation-2.1.

Therefore, for example, if laser power was increased, then exposure time would be reduced by a similar ratio to ensure a constant energy density was applied to the material, other parameters remaining constant. Table-3.8 shows the different test cases for constant energy density trials carried out by varying power and exposure time in relative amounts.

Table 3-8 Constant energy density test cases

Test Case	S-1	CED-1	CED-2	CED-3	CED-4
Power(W) & Exposure(μ s)	200 & 100	180 & 111	170 & 118	160 & 125	150 & 133

3.4.5 Effect of varying Bed Pre-Heat Temperature

As discussed in Sections 2.5 and 2.6, the high heating and cooling rates (in the region of 10^6 °C /second) inherent in the SLM process lead to the build-up of thermal residual stresses and sub optimal ductility in components manufactured using this process.

Pre-heating the bed to higher temperatures could provide in-process heat treatment and lead to reduction in residual stress and improvement in mechanical properties. To achieve this, a retrofitting high temperature bed was designed for the Renishaw SLM-125 machine at the University of Sheffield.

3.4.5.1 Design Considerations

The objective was to design a retrofitting assembly for the SLM-125 machine capable of safely reaching approximately 800 °C bed temperature.

The following design requirements were set:

- Achieve maximum bed temperature of 800+ °C.
- Be able to retrofit the heated bed in the available 125mm x 125mm x 125mm build volume of the SLM-125 machine.
- Maximise the available build volume so that mechanical test specimens could be manufactured.
- Reduce the heat losses from the platform to the machine to maintain acceptable temperatures in the machine build chamber, electronics, optical-train and elevator mechanism.
- Maintain real time control of the bed temperature.
- Achieve a uniform bed temperature.

3.4.5.2 High Temperature Bed Design

The available bed area of the Renishaw AM 125 SLM machine is 125mm x 125mm, so it was important to choose the correct insulation material to achieve a maximum build area with minimum heat conduction to the rest of the machine. AISI 310 stainless steel was chosen for the assembly to reduce any deformation due to high temperature as well as getting good strength with minimum wall thickness. Controlled conductive heating element, capable of achieving 800+ degrees temperature in the constrained available area of 66mm X 66mm was used. The assembly was designed to follow the design of the original bed of the SLM-125 machine so it could be a direct replacement, shown in Figure-3.5.

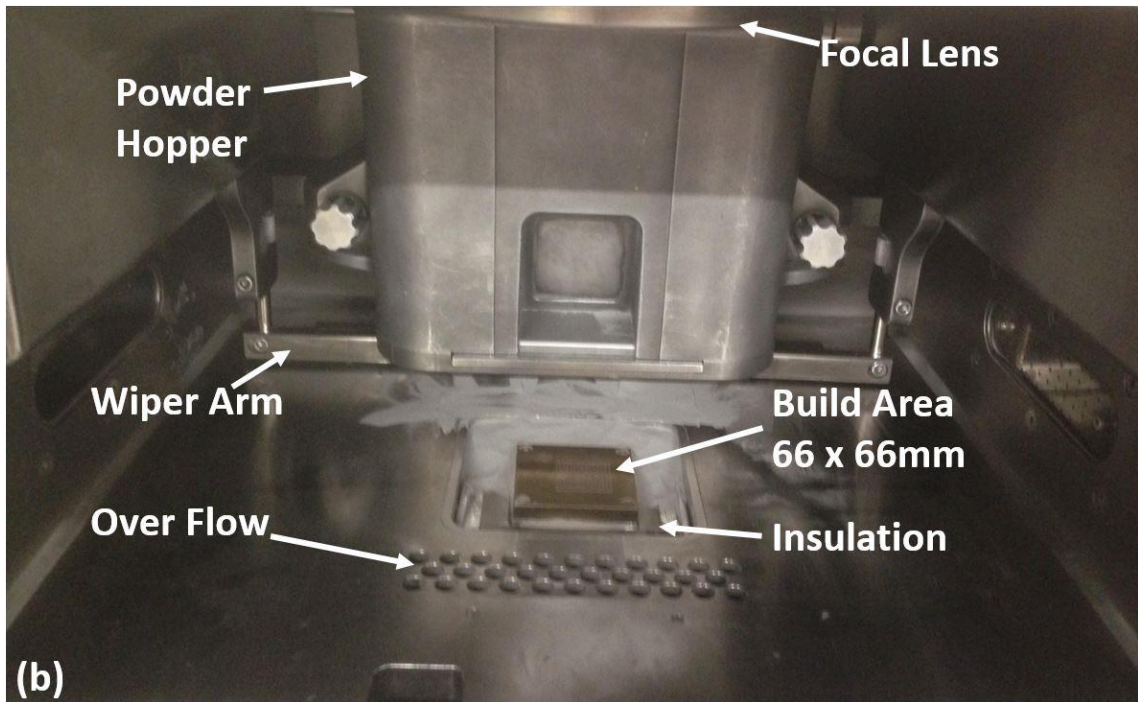


Figure 3-5 Renishaw SLM 125 Machine Chamber with Custom designed Heated Bed

3.4.5.3 High Temperature Bed Testing

The insulated assembly was initially tested before installation into the SLM machine to confirm:

- The highest temperature the assembly could achieve.
- The difference between the actual temperature of the heater and the substrate.
- The distribution of temperature on the substrate.
- The temperature on the outsides of the assembly.

The heated bed arrangement was assembled on the bench and the bed heater was fed via a step-down transformer and micro-controller. A set of thermocouples from the heater were fed back into the microcontroller to complete the control loop. Additional thermocouples connected to a PicoTech Thermocouple Data Logger model TC-08 were placed at different positions of the assembly. The recorder was used to record temperatures from three thermocouples placed on the surface and one thermocouple each on the side and base of the assembly.

Following these successful trials, the bed was installed into the Renishaw AM125 SLM machine at the University of Sheffield. Further successful trials were carried out with the heated bed inside the machine chamber before a number of heated builds were conducted.

3.4.5.4 High Temperature Trials

Using the SLM build parameters shown in Table-3.2 in combination with optimum combination of power and exposure from density optimisation trials, three 30x30x10mm blocks and three tensile test specimens were built for each bed pre-heat temperature. Figure-3.6(a) shows a representative residual stress block built at 370°C. Figure-3.6(b) shows representative tensile specimens built at 370°C.

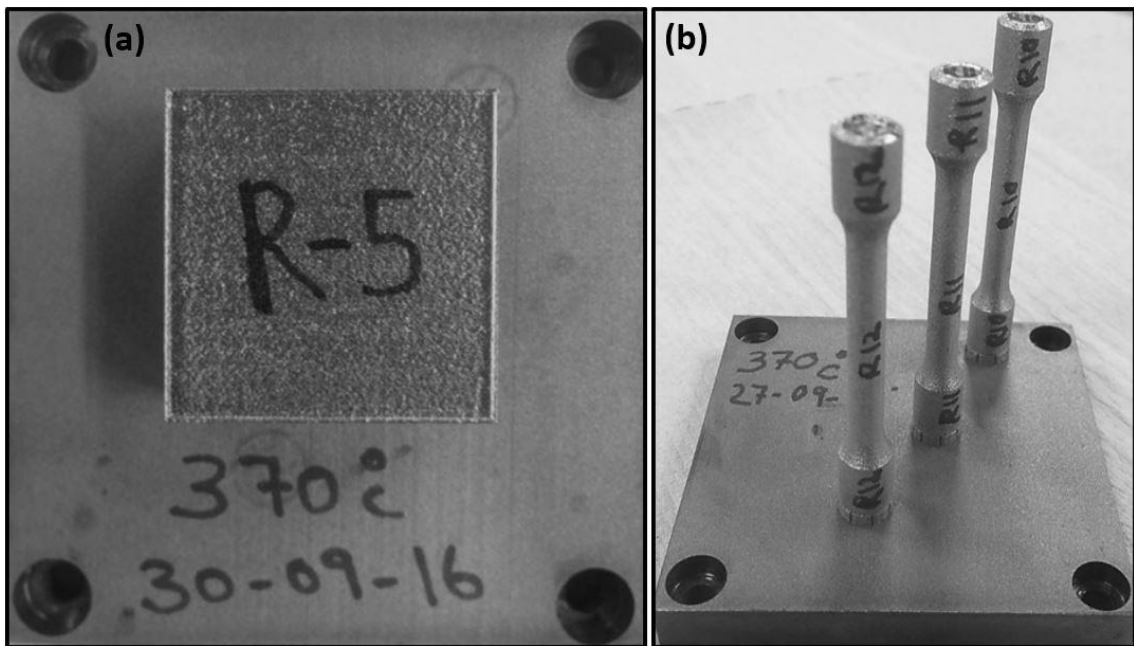


Figure 3-6(a) Residual stress block built at 370°C (b) Tensile specimens built at 370°C

Table-3.9 shows the different test cases of bed pre-heat temperatures used in this study.

Table 3-9. Bed pre-heat temperature test cases

Case Number	T1	T2	T3	T4	T5	T6
Bed Pre-Heat Temperature (°C)	100	370	470	570	670	770

Because of the smaller bed plate due to the insulation barrier around the platform, there was only room to build one block for residual stress measurement, therefore three builds were carried out for each test case to build blocks. The fourth build for each test case was undertaken to build the tensile specimens for mechanical testing at the TWI laboratories in Cambridge.

3.5 Residual Stress Measurement by Air-brasive Hole Drilling

Residual stress samples built on the Renishaw AM250 SLM machine were separated parameter wise into separate builds. To avoid variation in residual stress due to placement position on the build platform, each parameter set was used to build the residual stress blocks positioned in exactly the same position as shown in Figure-3.7. Samples were tested for residual stress to establish a baseline for comparison of residual stress reduction strategies given in section-2.7. ASTM E837-13a Standard Test Method for determining residual stresses by the Hole-Drilling Strain-Gage method was used for residual stress measurement. [85]

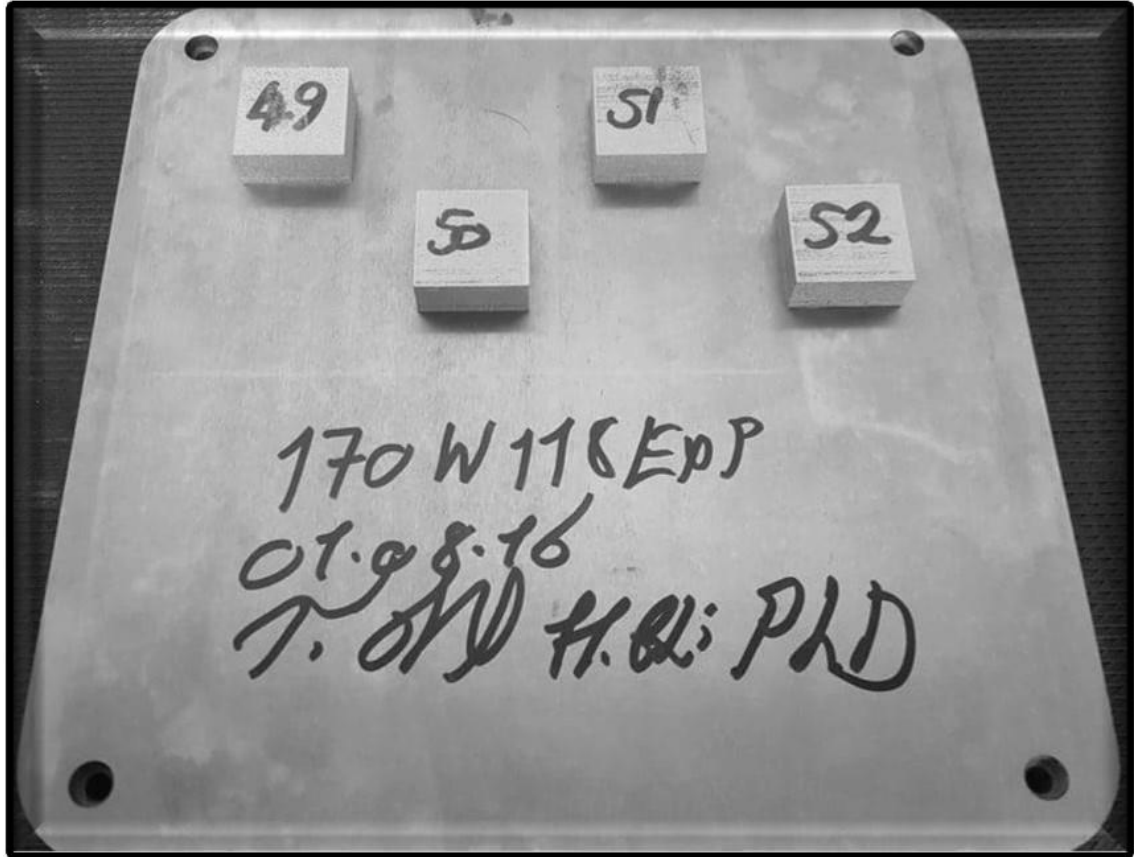


Figure 3-7. Residual stress samples representative build from Renishaw AM250 SLM machine.

Samples were manually removed from the substrate using a chisel and hammer. Removing the samples from the substrate could possibly result in relaxation and redistribution of the residual stress in the samples. The effect of residual stress relaxation and redistribution on removal from substrate can be assessed by measuring the residual stress in samples manufactured with same SLM parameters in both attached and detached states.

A hand-held polisher with successively finer grit abrasive from 8- 400 grade was used to prepare the surface for strain gauge installation. Care was taken that the specimens are not over heated which can modify the residual stress distribution in

the material under investigation. Strain gage was attached on the top surface of the sample measuring the residual stress in XY plan as shown in Figure-3.8.



Figure 3-8 Residual stress specimen with strain gage rosette showing hole drilled in centre to measure residual stress on the top of the specimen in XY plan.

Strain gage is commonly attached to the top surface for measurement of residual stress in the XY plan as reported in refs-[2, 86]. The reason for attaching the strain gage to the top surface is that the highest σ_x and σ_y values in SLM parts exist at the top surface as reported by Yang *et-al*[113]. Figure-3.9 shows that for three different samples Yang *et-al*[113] noticed the highest tensile σ_x and σ_y values near the top of the samples.

Since the highest tensile σ_x and σ_y measurement was the goal of this work, therefore the strain gage rosettes were connected to the top surface of the block samples as shown in Figure-3.8.

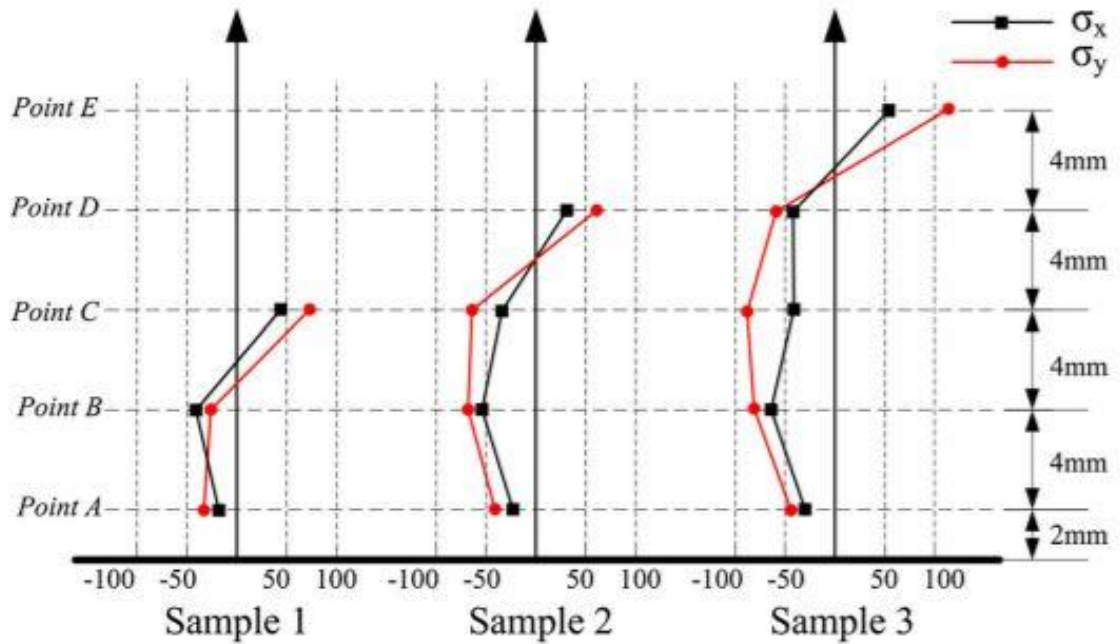


Figure 3-9. Residual stresses along height direction in the three samples[113].

An S.S.White abrasive machine, 6500 system with CEGB air-brasive drilling head fitted with a 0.46mm diameter sapphire nozzle blasting 50 micron aluminium oxide powder was used for drilling the hole in the centre of TML FRS-2-11 strain gauge rosettes. A CEGB optical alignment and hole measurement unit was used to measure the diameter and depth of the hole. For a standard 45° rectangular rosette format the principal stresses, principal directions and the relaxed strains relationship is shown in equation-1. [114]

$$\sigma_{max,min} = \left(-\frac{1}{K_1}\right) \left(\frac{E}{2}\right) \left[\frac{\varepsilon_1 + \varepsilon_3}{1 - \nu K_2 / K_1} + \frac{1}{1 - \nu K_2 / K_1} \left\{ (\varepsilon_1 - \varepsilon_3)^2 + [2\varepsilon_2 - (\varepsilon_1 + \varepsilon_3)]^2 \right\}^{\frac{1}{2}} \right] \quad (1)$$

Where

$\varepsilon_1, \varepsilon_2, \varepsilon_3$ are the strains measured in microstrain.

E is the Young's modulus in MPa .

$\frac{1}{K_2}$ and $\frac{\nu K_2}{K_1}$ are constants read from tables for particular strain gauge rosettes.

The Air-brasive method has the advantage over stepper motor hole drilling mechanisms that since there is no cutting tool involved, no external stresses are introduced during the hole drilling process. The short coming is that no incremental results can be achieved and sometimes the base of the hole is not perfectly flat due to differential abrasion of the softer and harder phases of material which makes taking results difficult.

3.6 Tensile Testing

Tensile testing samples built on the Renishaw AM250 SLM machine were separated parameter wise into separate builds. To avoid variation in mechanical properties due to placement position on the build platform, each parameter set was used to build the tensile specimens positioned in exactly the same position as shown in Figure-3.10.

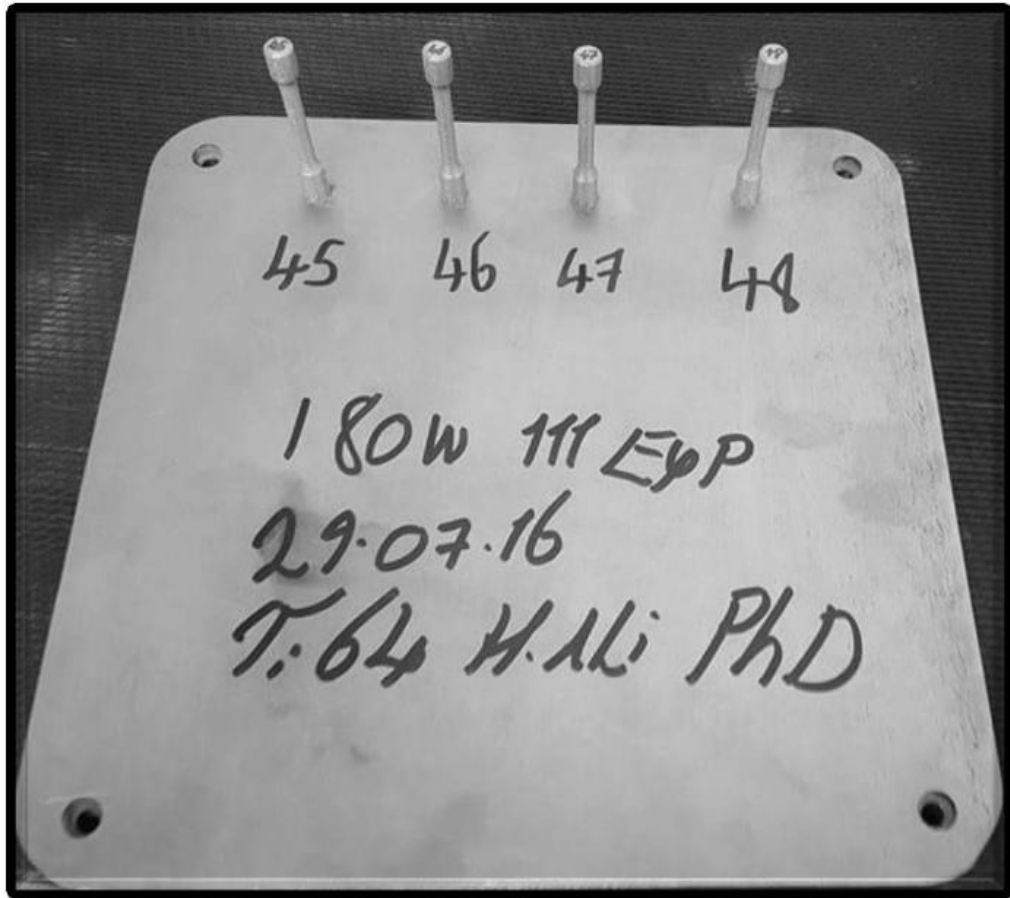


Figure 3-10. Tensile samples representative build from Renishaw AM250 SLM machine.

Tensile test specimens were manufactured according to the ASTM standard. [115]
The specimens were tested using an Instron5567B723 with extensometers using BS EN ISO6892-1 standards [116].

3.7 Hardness and Micro Hardness Testing

Vickers micro hardness and hardness tests were conducted according to B EN ISO 6507-1:2005[117]. Micro hardness was measured using a 200g load on a Zwick

Microhardness Tester. An average hardness value was calculated for each sample using 12 indentations taken along the build direction of the 30x30x10mm block cross section as shown in Figure-3.11(a). Vickers hardness was measured using a load of 5kg and an average hardness value was calculated for each sample using 5 indentations taken along the width of the sample as shown in Figure-3.11(b).

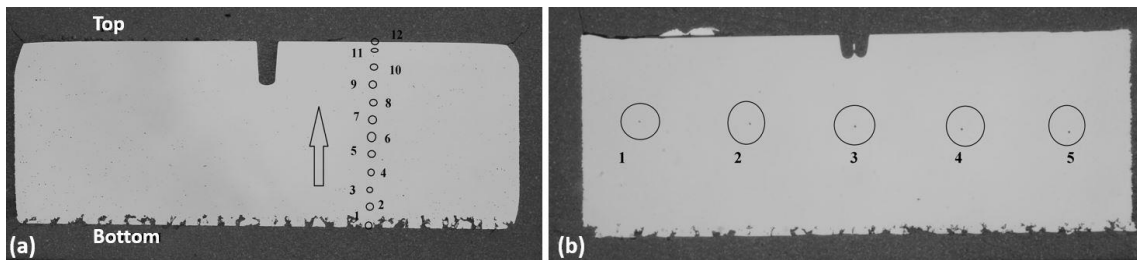


Figure 3-11. Cross-sectioned 30x30x10mm residual stress blocks for (a) Vickers Micro-Hardness (HV0.2) and (b) Vickers Hardness (HV5).

3.8 Geometrical Dependence of Residual Stress

This part of the trials was designed to understand the geometrical dependence of residual stress and validate the effects of residual stress reduction strategies identified in the earlier part of this work, through strategic application across different regions of the I-Beam section.

Initially an I-Beam section (see Figure-3.12(a)) was built on the SLM250 platform using optimum SLM parameters for Ti6-4, found in the first part of the work. The Contour method was used for measuring residual stress in the I-Beam, cross-sectioned through the XY plane. The 2D residual stress map identified the high stress regions in the I-Beam. Figure-3.12(b) shows the dimensions of the four regions for strategic application of residual stress reduction strategies.

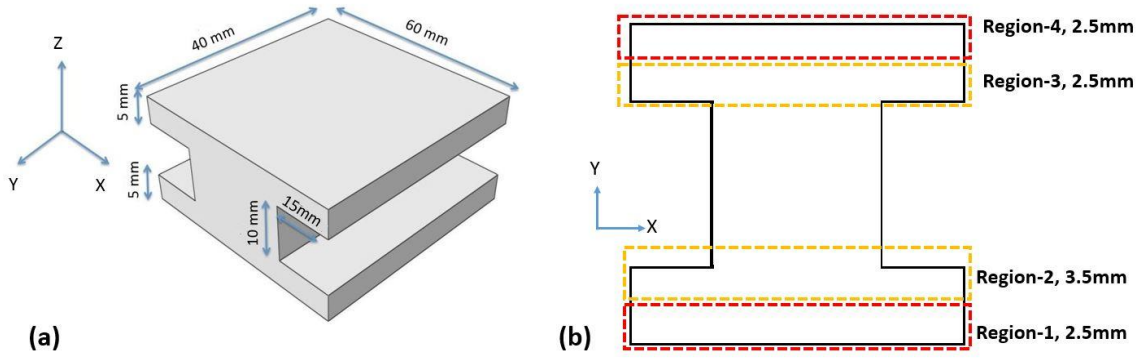


Figure 3-12 (a) Dimensioned I-Beam geometry (b) I-Beam regions for strategic application of stress reduction strategies.

After the high residual stress concentration regions were identified from the initial contour method 2D stress map, the stress reduction strategies identified in the first part of the project were applied to the various regions (see Figure-3.12(b)) of new I-Beam sections. Table-3.10 shows details of the different I-Beam test cases manufactured for this study.

Table 3-10 Strategic stress reduction test cases

Test Case	IB-1	IB-2	IB-3	IB-4	IB-5	IB-6
Strategy	Standard I-Beam with optimised parameters.	75 μ m Layer Thickness for Region-2& Region-4.	150W power and 133 μ s exposure for Region-2 & Region-4.	570 $^{\circ}$ C Bed pre-heating on Renishaw SLM-125 machine.	75 μ m Layer Thickness for Region-1 & Region-3.	150W power and 133 μ s exposure for Region-1 & Region-3.

Figure-3.13(a) shows a representative I-Beam geometry attached with substrate and with all the supports attached as well. Figure-3.13(b) shows an I-Beam geometry cut off from the substrate and supports removed.

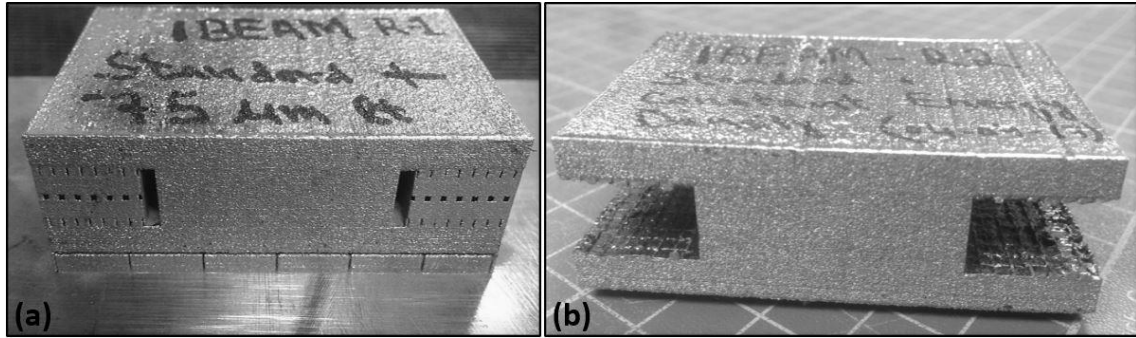


Figure 3-13(a) I-Beam geometry with supports (b) I-Beam geometry without supports

3.9 Contour Method Analysis

Contour measurement and analysis were conducted at The Open University, Milton Keynes.

The samples were sectioned with an Agie Charmilles EDM machine with a 0.15 mm wire diameter. In order to prevent the introduction of EDM cutting artefacts close to the sample surfaces, sacrificial layers were bonded on to the surfaces of the samples [118]. In order to prevent the specimens from moving on the EDM bed table, the specimens were held with finger clamps. Cutting was started after the specimens and fixtures had reached thermal equilibrium within the wire EDM deionised water tank. Contour measurement on the cut surfaces was taken using a Zeiss Eclipse CMM fitted with a Micro-Epsilon triangulating laser probe and a 2-mm diameter ruby-tipped Renishaw PH10M touch trigger probe. The touch probe was used to measure the perimeter of the samples. Triangulating laser sensor was used to measure the surface deformation of the cut surfaces on a (0.025×0.025) mm grid. The average measured deformation contour was applied to the cut face of a finite element linear elastic stress analysis (FE) model in ABAQUS.

4 Modelling

Finite element modelling can provide a very good understanding about the science of residual stress build up based on SLM parametric variation. It can provide a good direction for future experimental work by pointing out the trends in residual stress build up with parameter variations and reduce the number of experimental trials needed for charting out optimum combination of parameters for minimum residual stress.

Modelling was used as a tool to provide a better understanding of the physics of the residual stress build up in the SLM process and understanding the effects of parametric variations on the stress trends.

4.1 Thermal Model

A moving laser heat source and its interaction with the metal powders and the base platform was modelled to predict the thermal history of the SLM melting process. The scale of the meltpool in SLM and the complexity of the process dynamics makes it impossible to simulate the melting behavior of a whole part. This work simulated the melting behavior of a single line containing 14 laser spots.

A 1.04X0.33mm powder layer of 50 μ m thickness was deposited on to a substrate of 0.5mm thickness. Figure-4.1(a) shows the model with dimensions. Mesh element type DC3D8 (An 8-node linear heat transfer brick), was used. Figure-4.1(b) shows that a mesh size of 32.5x32.5x50 μ m was used for the powder layer. The substrate

mesh was biased to move from 50 μm at the top, increasing to 100 μm at the bottom to keep the number of mesh elements to a minimum, and reduce the model size and compilation time.

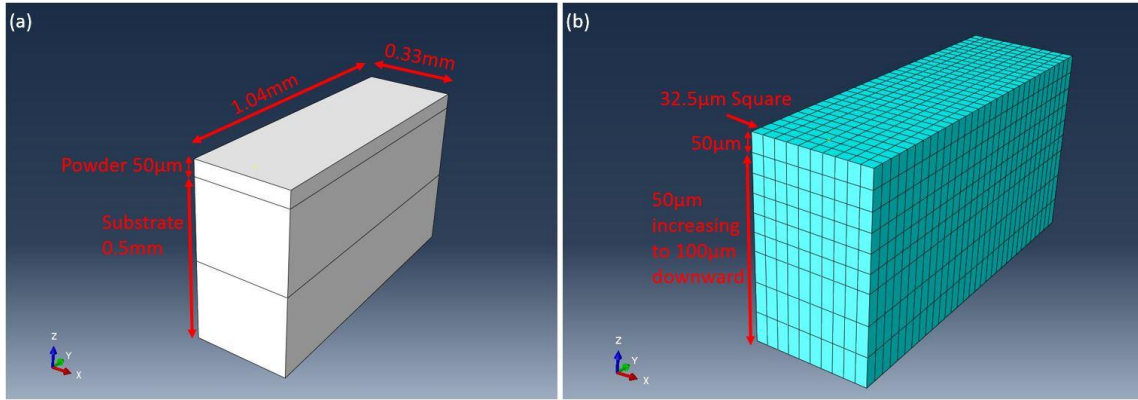


Figure 4-1 (a) Model (b) Mesh

The modelling approach taken in this work is based on the concept of a volumetric moving heat source, combined with enhanced thermal conductivity.

4.2 Heat Source

Using an ABAQUS DFLUX subroutine written in FORTRAN (Code in Appendix-B-1), a moving volumetric heat source was programmed to simulate the laser. A volumetric heat source was used to account for the laser penetration effect into the powder, which according to ref-[103], is 63 μm for titanium powder.

A Modified Cylindrical Laser Heat Flux model from ref-[63], was used in this research to represent the variation of laser intensity in the radial direction. It is an equivalent cylindrical heat flux representation of the computed numerical average of Gaussian distribution.

$$q_{cyl} = \frac{P}{\pi r_{las}^2} \quad \text{Equation-4.1}$$

Equation-4.1 shows the cylindrical heat flux density. Where P is the laser power in watts and r_{las} is the radius of the laser spot on the bed surface, which was taken as 50 μ m for the Renishaw AM250 SLM machine.

$$q_{mod\ cyl} = 0.864\eta q_{cyl} \quad \text{Equation-4.2}$$

Equation-4.2 shows the Modified Cylindrical Laser Heat Flux model, where η is the laser absorptivity value for Ti6Al4V. An absorptivity value of 0.6 was used for this work. According to ref-[119], $\eta=0.77$ for pure titanium. The value 0.6 was fitted after a few trials with different values around η for pure titanium. The factor 0.864 is derived from the numerical average computation of a Gaussian distribution.

$$I_r = 2.6q_{mod\ cyl} \quad \text{Equation-4.3}$$

$$I_r = \frac{2.6(0.864)\eta P}{\pi r_{las}^2} \quad \text{Equation-4.4}$$

Equation-4.3 shows the final definition of I_r , the intensity of laser in the radial direction used in this research. The factor of 2.6 was found to be a correction factor necessary for getting meltpool size and temperature right, which was calculated through FEA trials. Equation-4.4 shows the full form of the radial laser intensity, with all the parameters and it shows the manner it was coded in FORTRAN.

$$I_z = -15z^2 + 4z + 2 \quad \text{Equation-4.5}$$

Equation-4.5 shows the variation of laser intensity in the depth direction (z-axis), modelled as a parabolic relation (see Figure-4.2).

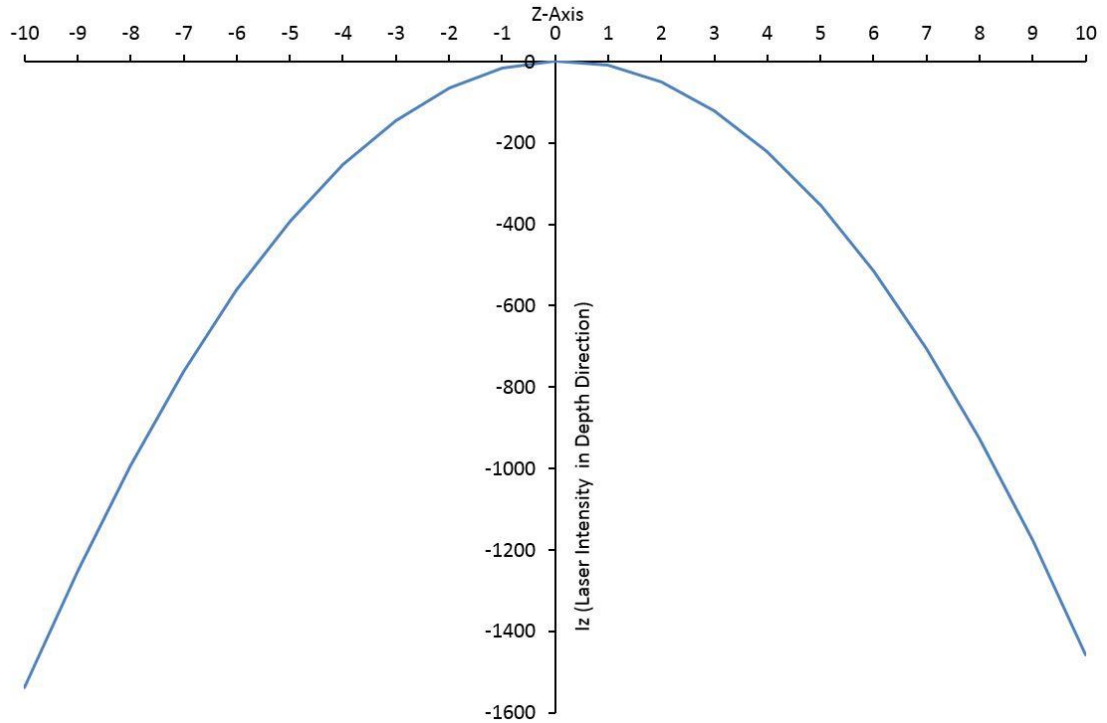


Figure 4-2. Laser intensity variation in Z-Axis

$$\text{flux}(1) = (I_r * I_z) \quad \text{Equation-4.6}$$

Equation-4.6 shows the definition of the heat flux used for simulating the moving heat source in this work.

4.3 Material Properties

During the SLM process the powder material undergoes a phase change from powder-to-liquid-to solid when irradiated by the high power laser. To accurately

represent these phase changes temperature dependent thermophysical properties need to be included in the model definition. ABAQUS USDFLD subroutine written in FORTRAN (Code in Appendix-B-2), was used to simulate this phase change of Ti6Al4V, based on the temperature of the laser irradiated region. Temperature dependent material properties of solid and liquid Ti6Al4V used in this research are presented in Table-4.1 to 4.4 below. The units of the data from ref-[47, 63] were converted from SI to SI (mm) for millimetre scale modelling in ABAQUS.

Table 4-1 Selected thermophysical properties of powder Ti6Al4V[63].

Temperature (°C)	Density (Tonne/mm ³)	Specific Heat (mJ/Tonne-°C)
25	2.43E-09	5.46E+08
100	2.45E-09	5.62E+08
200	2.55E-09	5.84E+08
300	2.63E-09	6.06E+08
400	2.84E-09	6.29E+08
500	2.83E-09	6.51E+08
600	2.95E-09	6.73E+08
700	3.03E-09	6.94E+08

800	3.02E-09	7.14E+08
900	3.01E-09	7.34E+08
995	3.21E-09	7.53E+08
1100	3.41E-09	6.60E+08
1200	3.49E-09	6.78E+08
1300	3.60E-09	6.96E+08
1400	3.80E-09	7.14E+08
1500	3.78E-09	7.32E+08
1600	3.78E-09	7.50E+08
1604	3.78E-09	7.55E+08

Table 4-2 Thermal conductivity of powder Ti6Al4V[47].

Temperature (°C)	Thermal Conductivity (mW/mm-K)
20	0.145
100	0.125

200	0.104
300	0.092
400	0.083
500	0.078
600	0.167
700	0.216
800	0.279
900	0.430
1000	0.813
1100	0.934
1200	1.09
1300	1.27

Table 4-3 Thermophysical properties of solid Ti6Al4V[63]

Temperature (°C)	Density (Tonne/mm ³)	Specific Heat (mJ/Tonne-°C)	Conductivity (mW/mm-°C)
25	4.42E-09	5.46E+08	7.0
100	4.41E-09	5.62E+08	7.5
200	4.40E-09	5.84E+08	8.8
300	4.38E-09	6.06E+08	10.2
400	4.37E-09	6.29E+08	11.4
500	4.35E-09	6.51E+08	12.6
600	4.34E-09	6.73E+08	14.2
700	4.32E-09	6.94E+08	15.5
800	4.31E-09	7.14E+08	17.8
900	4.29E-09	7.34E+08	20.2
995	4.28E-09	7.53E+08	22.7
1100	4.27E-09	6.60E+08	21.0
1200	4.25E-09	6.78E+08	22.9

1300	4.24E-09	6.96E+08	23.7
1400	4.23E-09	7.14E+08	24.6
1500	4.21E-09	7.32E+08	25.8
1600	4.20E-09	7.50E+08	27.0
1604	4.20E-09	7.55E+08	28.4
1610	4.19E-09	7.66E+08	29.2
1620	4.19E-09	7.69E+08	29.3
1630	4.19E-09	7.70E+08	29.4
1640	4.18E-09	7.74E+08	29.7
1650	4.17E-09	7.85E+08	30.4
1660	4.14E-09	8.31E+08	33.4
1670	4.14E-09	8.31E+08	34.6
1800	4.11E-09	8.31E+08	34.6
1900	3.75E-09	8.31E+08	34.6
2800	3.89E-09	8.31E+08	34.6

Table 4-4 Thermal properties Ti6Al4V[63]

Latent Heat (mj/Tonne)	Solidus Temp (°C)	Liquidus Temp (°C)
2.82E+08	1604	1660

In order to achieve a detailed model representative of the melting behavior of the SLM process, the temperatures and properties used in this research encompass the key phase transitions Ti6Al4V powder undergoes when irradiated with a laser beam. ABAQUS interpolates for each property value at intermediate temperatures.

In order to artificially simulate the Marangoni convection responsible for heat flow in the meltpool an enhanced thermal conductivity model presented by Safdar et al in ref-[99] has been used. The only difference being that in this work thermal conductivity has been considered as isotropic. Equation-4.7 defines this approach.

$$K' = \lambda K \quad \text{Equation-4.7}$$

Where K is the normal isotropic thermal conductivity at a given temperature and λ is the thermal conductivity enhancement factor, defined as:

$$\lambda = \begin{cases} 1 & \text{if } T < T_{melt} \\ \text{Multiplying factor} & \text{if } T > T_{melt} \end{cases}$$

The isotropic enhancement factor used in this research work is $\lambda=4.0$, based on trial and error to achieve the desired meltpool dimensions.

4.4 Initial Conditions

A temperature initial condition of 25°C was attributed to the powder. Substrate pre-heating was also applied as a temperature initial condition to the substrate. The value of the temperature applied to the substrate was varied according to the parameters being modelled.

4.5 Heat Losses

During the SLM process the majority of heat is lost through conduction to the substrate and surrounding powder. Convection and radiation from the top surface also account for heat loss during the process.

In this work radiation heat losses were not considered. The convective heat losses from the top surface due to flow of inert gas in the chamber were modelled by defining natural convection as a surface film interaction on the exposed top surface.

A Convective heat transfer coefficient of $0.02 \frac{mW}{mm^2-K}$ was used.

To simulate the conductive heat losses due to the substrate a surface film condition was defined on the five surfaces of the small substrate considered in this work. To properly approximate the conductive heat losses without having to model the whole substrate the temperature dependent conductivity of solid Ti6Al4V (see Table-4.3) was used as a convective heat transfer coefficient on the five surfaces of the small substrate. Figure-4.3(a) shows the surfaces where the conduction to substrate occurs, defined as a convection interaction.

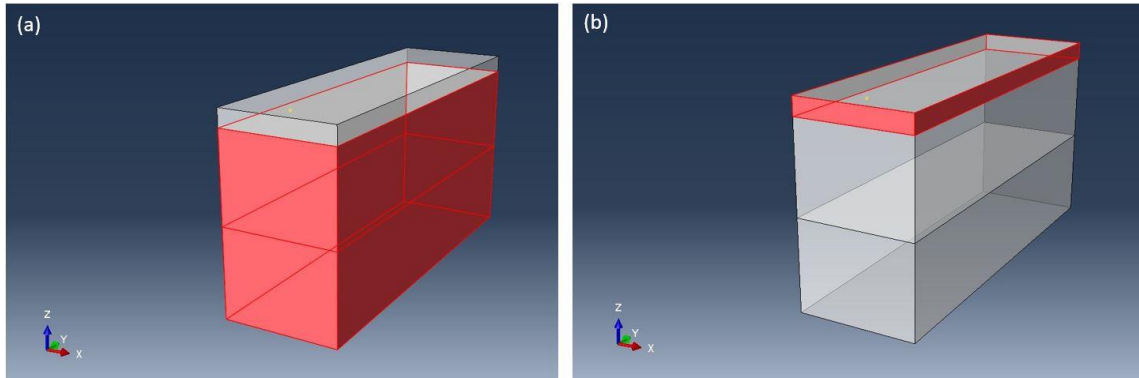


Figure 4-3 (a) Surfaces for conduction to substrate. (b) Surfaces for conduction to surrounding powder.

To simulate the conductive heat losses due to the surrounding powder, a surface film condition was defined on the four surfaces of the powder layer (see Figure-4.3(b)), considered in this work. To properly approximate the conductive heat losses without having to model the whole powder layer the temperature dependent conductivity of Ti6Al4V powder (see Table-4.2) was used as a convective heat transfer coefficient on the four surfaces of the small powder layer.

Defining the conductive heat losses to the substrate and surrounding powder as convective interaction helped in accurately modelling the heat losses of the SLM bed without having to model the whole bed. This helped in reducing the model size and thus computational time. This modelling reduction approach can be very helpful in making thermal modelling more efficient.

4.6 Thermal Model Validation

The thermal FEA model was validated by comparing the simulated meltpool dimensions with experimentally measured meltpool dimensions.

Experimental meltpool dimensions were measured using the Renishaw AM250 machine. A single 50 μm layer of Ti6Al4V powder was deposited onto a titanium substrate. Single lines were melted onto the substrate using parameters shown in Table-4.5 below.

Table 4-5 Parameters for single line melting

Power (W)	Exposure (μs)	Point Distance (μm)	Substrate Temperature ($^{\circ}\text{C}$)
200	100	65	100

The substrate was cross sectioned, mounted, polished and etched to reveal the meltpool. Using optical microscopy, an image of the substrate region with the melted line was taken and Image software was used to measure the meltpool dimensions.

The simulated meltpool dimensions were determined by taking a cross sectional view of the melted line and measuring the meltpool dimensions.

4.7 Data Extraction from the Thermal Model

Once the FEA thermal model was validated against experimental meltpool dimensions, the next step was to carry out modelling trials for the SLM parametric study.

Residual stress is dependent on the cooling rates of the SLM process and the temperature gradient between the meltpool and the surrounding material. Therefore the ABAQUS FEA simulation was used to extract data for calculating the effect of SLM parameter variation on cooling rates and temperature gradients in the SLM process.

Cooling rates were calculated by picking a point in the top center of the second simulated laser spot (see Figure-4.4(a)) and extracting the temperature-time data for the selected location until the time the laser finished melting the 14th spot, using an excel spreadsheet. In excel, the cooling rate was calculated by taking the slope of the cooling line after the highest temperature was reached and the selected location starts to cool down when the laser moves forward to the next spot.

In order to calculate the temperature gradient, six location (see Figure-4.4(b)) were chosen in the cross section of the second spot. The first spot was chosen at the top surface and consecutively in increments of 50 μm five more locations were chosen in the depth direction, with the final selected point located at 300 μm . Temperature-time data for the selected locations, till the time the laser finished melting the 14th spot, was exported into excel. In excel the temperature was plotted against time showing

the temperature difference in the meltpool moving down in the depth direction as well as the substrate region below the meltpool.

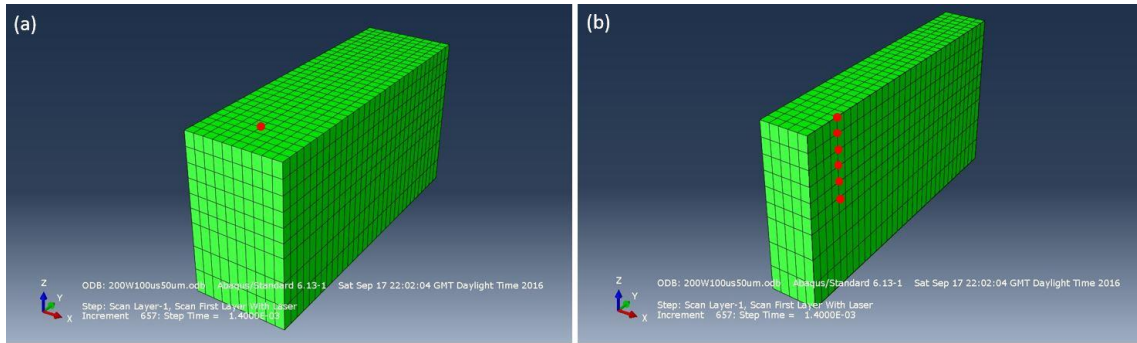


Figure 4-4 (a) Red spot shows the center of the second laser spot picked for calculating cooling rate. (b) Red spots show six locations picked from top of the second spot to a depth of $300\mu\text{m}$ in increments of $50\mu\text{m}$ in the depth direction.

4.8 Modelling Trials

The verified FEA thermal model was then used to study the effect of SLM parameters on cooling rates and temperature gradients. Changes were made to the ABAQUS model and the DFLUX subroutine to depict the SLM parameter variation.

4.8.1 Effect of Layer Thickness

The ABAQUS model was edited changing the layer thickness of the powder layer for the three cases of layer thickness presented in section-3.4.2. The variations in processing parameters such as power and exposure time for each case were modelled by making changes to the values of power and exposure in the DFLUX subroutine for each case.

4.8.2 Effect of Re-Scanning Varying Exposure

In order to simulate re-scanning effects the powder layer in the ABAQUS model was assigned the properties of solid Ti6Al4V and 14 spots were scanned for the different cases of re-scanning with varying exposure presented in section-3.4.3.1. The variation in exposure was modelled by making changes to the exposure values in the DFLUX subroutine for each case.

4.8.3 Effect of Re-Scanning Varying Power

In order to simulate the re-scanning effect the powder layer in the ABAQUS model was assigned the properties of solid Ti6Al4V and 14 spots were scanned for the different cases of re-scanning with varying power presented in section-3.4.3.2. The variation in power was modelled by making changes to the power values in the DFLUX subroutine for each case.

4.8.4 Effect of Power and Exposure keeping Energy Density Constant

In order to simulate the effect of varying power and exposure combinations keeping energy density constant, no changes were made to the ABAQUS model. The different cases of power and exposure for constant energy density presented in section-3.4.4, were modelled by changing the values of power and exposure in the DFLUX subroutine for each case.

4.8.5 Effect of Bed Pre-Heat Temperature

In order to simulate the effect of bed pre-heat temperature on cooling rates and temperature gradients the different bed pre-heat temperature cases presented in section-3.4.5.4, were modelled by changing the temperature initial condition of the substrate in the ABAQUS model for each case. No changes were made to the DFLUX subroutine.

4.9 Validation of Thermal Modelling

This section presents the model validation approaches taken for this work. Firstly the model was validated based on comparison of experimentally measured melt-pool dimensions against model predicted melt-pool dimensions. Secondly the model was validated based on the trend in temperature evolution history over a scanning length of 325 μ m. FEA predicted temperature distribution in the XY-plane along the laser scanning direction was compared with experimentally determined values for SLM of Ti64 by Yadroitsev *et-al.* [34]. The experimental measurement of temperature distribution in the melt-pool were carried out using a single-mode continuous-wave, 1075nm wavelength, Ytterbium fiber laser with 70 μ m spot size[34]. In the study by Yadroitsev *et-al.* [34], melt-pool temperature at the Ti6Al4V substrate without powder was measured at laser powers (P) of 20, 30 and 50 W, in combination with scanning speed (V) 0.1, 0.2 and 0.3 m/s from 10 single tracks of 10 mm length. Temperature distribution in the melt-pool was measured by a

specially designed coaxial optical system using 782x582 pixels resolution CCD camera[34].

4.9.1 Melt-Pool Dimensions

Experimental melt-pool dimensions from three 20mm long line samples cross-section were compared with model predicted melt-pool dimensions. Figure-4.5 shows a comparison of average experimental melt-pool width (186 μm) and depth (169 μm) against model predicted melt-pool width (159 μm) and depth (164 μm).

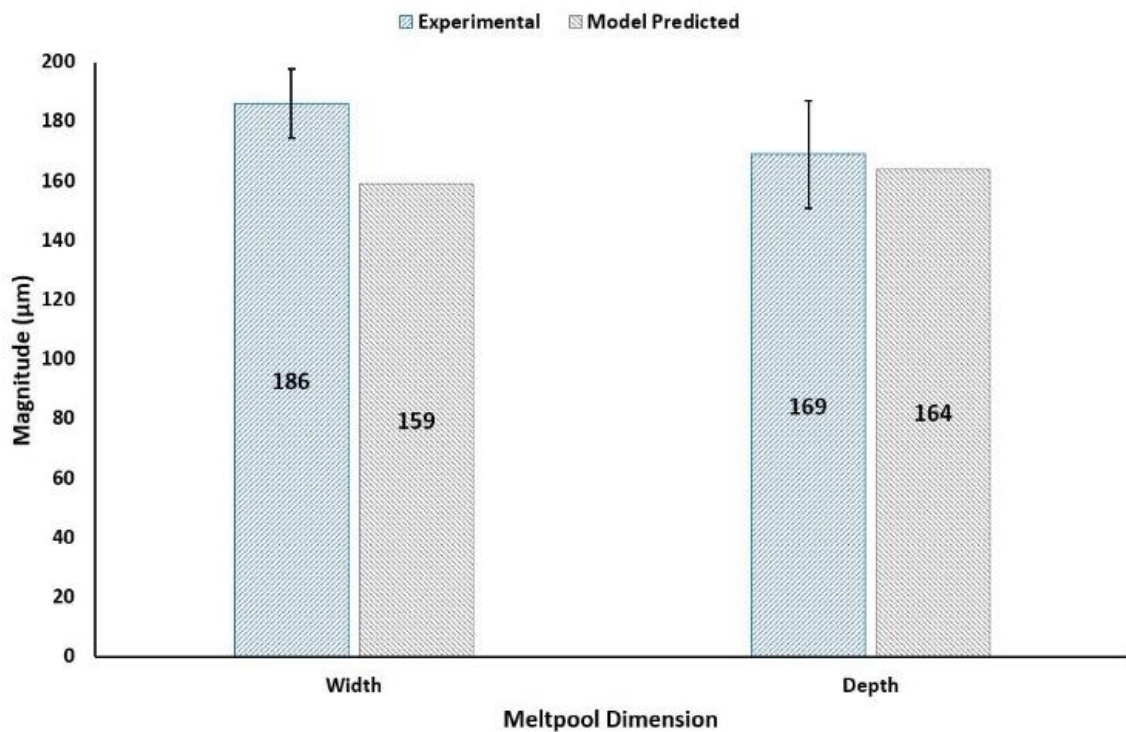


Figure 4-5. Experimental and Model predicted melt-pool dimensions comparison

Representative optical micrograph of the experimentally acquired melt-pool with average melt-pool dimensions is shown in Figure-4.6(a). Experimental melt-pool had an average width of $186\mu\text{m}$ and an average depth of $169\mu\text{m}$.

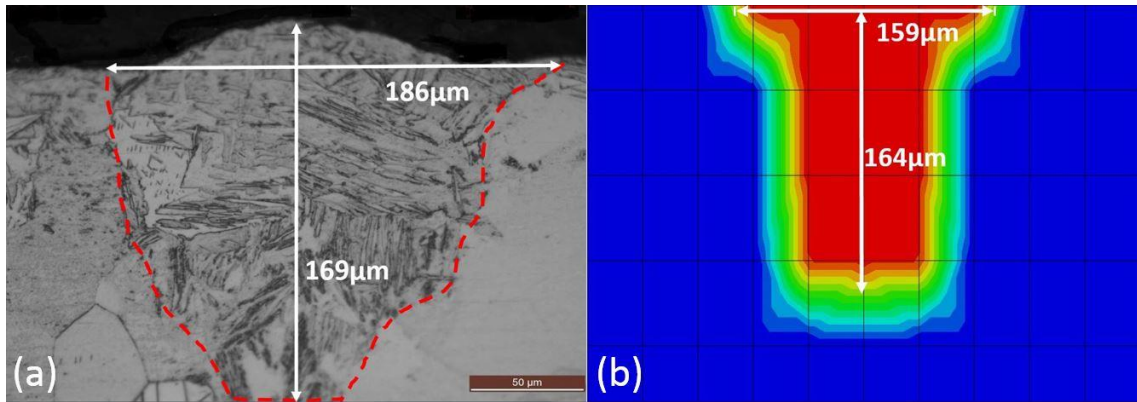


Figure 4-6 (a) Experimentally measured melt-pool dimensions (b) Melt-pool dimensions predicted by ABAQUS finite element thermal model

Figure-4.6(b) shows the melt-pool dimensions predicted from the ABAQUS finite element model, using optimised (>99% part density) SLM build parameters(details in ref-[120]). The FEA model predicted a melt-pool width of $159\mu\text{m}$. The predicted melt-pool width is 14.5% less than average experimentally measured melt-pool width of $186\mu\text{m}$. It can be seen from Figure-4.6(b) that the FEA model predicted a melt-pool depth of $164\mu\text{m}$. The predicted melt-pool depth is 3% less than average experimentally measured depth of $169\mu\text{m}$. Therefore based on the comparison of melt-pool dimensions shown in Figure-4.6, the FEA model prediction of the melting behavior of Ti6Al4V when irradiated by laser correlates well with experiments. This FEA model was used for studying the parametric dependence of residual stress in

SLM Ti6Al4V parts. It was used for estimating the effect that varying SLM process parameters had on cooling rates and temperature gradients within the process

4.9.2 Melt-pool Temperature Distribution

The second usage of the FEA model was to estimate the temperature distribution across the melt-pool. Figure-4.7(a) shows a comparison of FEA predicted temperature distribution in the XY-plane along the laser scanning direction (points of interest highlighted in sub Figure-4.7(b)), with experimentally determined distribution of the brightness temperature (radiation emission field is transformed into brightness temperature after camera calibration by a black body) for SLM of Ti64 [34], in the XY-plane along the laser scanning direction. Figure-4.7 shows a good correlation of the trend in FEA predicted temperature distribution with experimentally measured temperature distribution. In the experimentally determined temperature distribution [34], the material's solidification region is highlighted to commence at approximately 220 μ m behind the current position of the laser. Figure-4.7 shows that the FEA model predicted a similar solidification region.

The experimentally determined temperatures are for a solid Ti6Al4V substrate using a laser power of 50W and scanning velocity of 0.1 $\frac{m}{s}$ [34], while the FEA predicted temperature distribution is for 50 μ m Ti6Al4V powder layer on a solid substrate using a laser power of 200W and scanning velocity of .64 $\frac{m}{s}$. FEA predicted temperatures are higher than the experimentally measured values because the experimental temperatures are brightness temperature and according to Yadroitsev

et-al.[34-36], the true melt-pool temperature values should be higher. According to Yadroitsev *et-al.*[34-36], the true peak melt-pool temperature for 50W laser power and $0.1\frac{m}{s}$ scanning velocity was calculated to be 2710 K (corresponding brightness temperature being 2340 K).

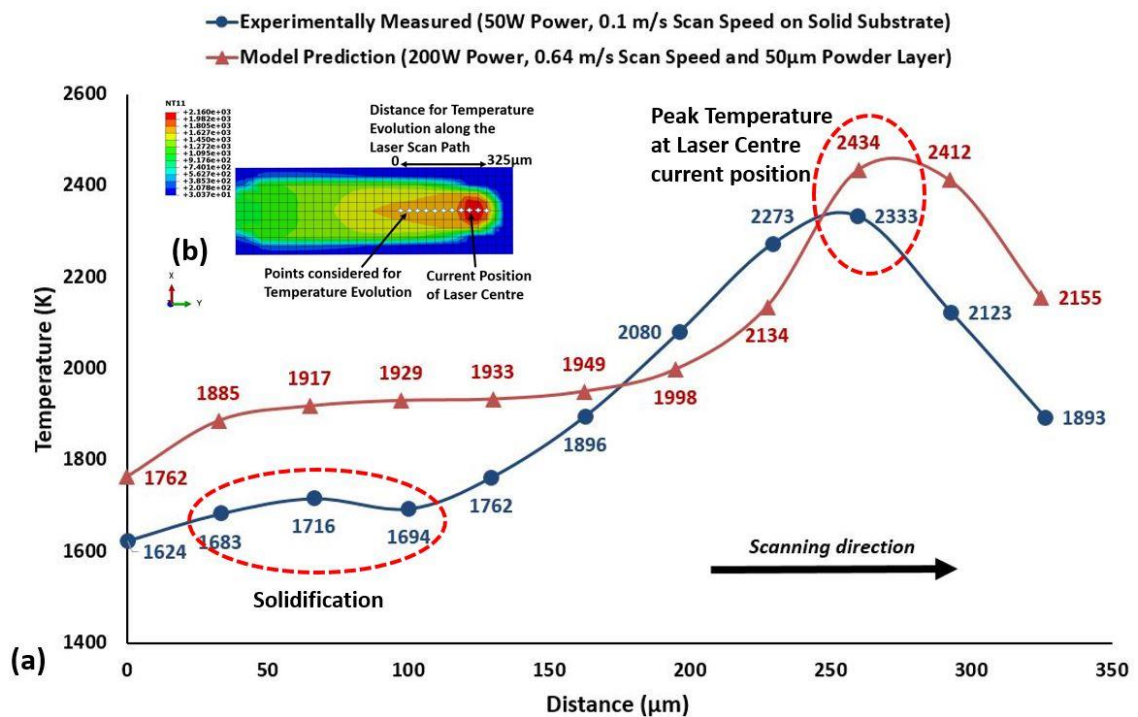


Figure 4-7. (a) Comparison of FEA model predicted temperature in XY-plane along the laser scanning direction with Experimentally determined Distribution of the brightness temperature in the XY-plane along the laser scanning direction; $P=50\text{ W}$, $V=0.1\text{ m/s}$ values adapted from ref-[34]. (b) Highlights the 325 μm distance with points considered for FEA model predicted temperature in XY-plane along the laser scanning direction.

According to ref-[34-36], laser power has a more pronounced effect on the melt-pool peak temperature compared with scan speed (exposure or irradiation time). Yadroitsev *et-al.*[34] experimentally determined the dependence of melt-pool peak

temperature on laser power and irradiation time concluding that the peak temperature of the melt-pool is more sensitive to laser power. Therefore the model predicted temperature should have been much higher than the true experimental temperatures as the model uses a much higher power. The reason for not achieving much higher temperatures could probably be attributed to the laser spot size, as the modelled laser spot size (100 μm) is bigger than the experimental laser spot size (70 μm) presented in the study by Yadroitsev *et-al* [34]. The results in Figure-4.7 show that the trend in model predicted temperature evolution over the laser scan path agrees well with the trend in experimental trends and therefore will result in accurate predictions of the cooling rate and temperature gradients. The predicted cooling rate and temperature gradients provides insight about the residual stress build up.

4.10 Temperature Distribution and Solidification Behavior Predicted from FEA

Figure-4.8(a) shows the temperature distribution in the XY-plane (Top View) along the laser scanning direction. It can be seen from Figure-4.8(a) that the melt-pool has an elongated tail surrounded by recently solidified material. The melt-pool is symmetrical around the line the laser centre traverses. Similar melt-pool shapes have been reported by Cheng *et al.* [121], from FEA model of IN718 and Polivnikova [122], reported similar shape of melt-pool for 18Ni(300) Maraging Steel using Mathematica software. The material starts solidifying around the edges first with the

material in the centre taking longer to solidify. This variation in temperature between the central molten material and the recently solidified material on the sides creates a temperature gradient and thus according to the temperature gradient mechanism [28, 123], will result in residual stress build-up in the SLM components. Figure-4.8(b) shows a dimensioned isometric view with laser scanning direction and the region used for volumetric heat addition.

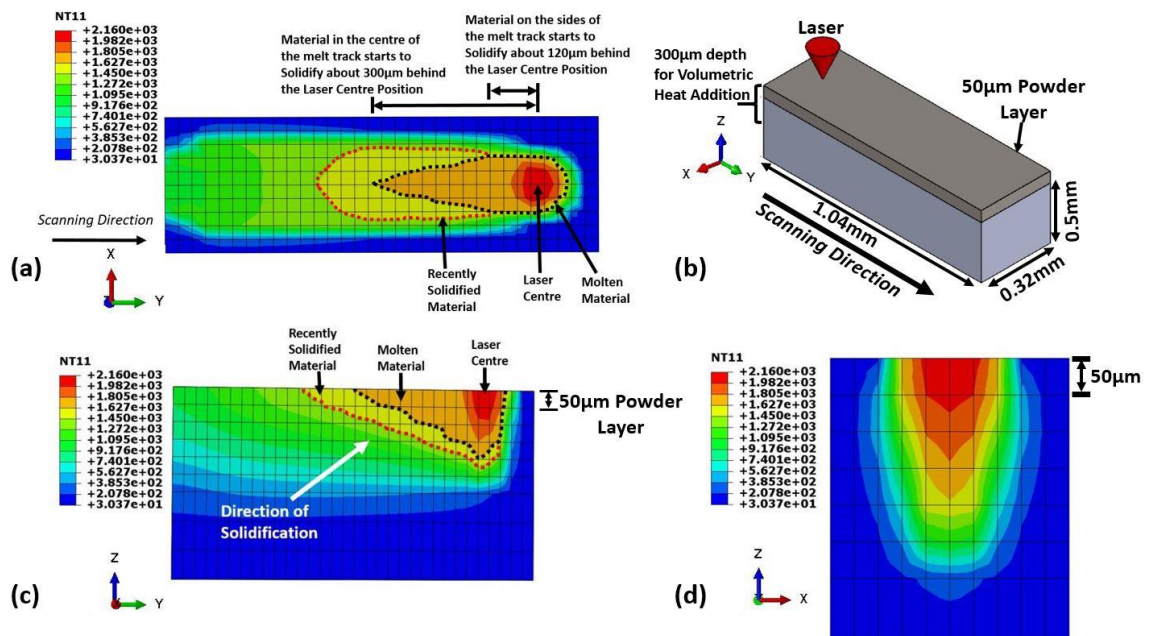


Figure 4-8. (a) (Top View) Temperature and Material Solidification Evolution along the Laser Scan Path in XY-plane along the laser scanning direction. (b) Dimensioned Isometric View showing the depth used for Volumetric Heat addition. (c) (Front View) Temperature and Material Solidification Evolution along the depth of Laser Scan Path in ZY-plane along the laser scanning direction. (d) (Side View) Temperature distribution across the depth (ZX plane of the melt-pool).

Figure-4.8(c) illustrates the temperature and material solidification evolution along the depth, ZY-plane (Front View) of laser scan path along the laser scanning direction. An important feature to note within Figure-4.8(c) is that the melt-pool starts solidifying from the bottom and moves upward. Thus the analysis of solidification front movement from Figure-4.8(a) and (c), is used to suggest the movement of solidification front indicated by the white arrow in Figure-4.8(c). Thus the underlying solidified material restricts the shrinkage of the molten material on top and according to the cool-down phase model[28, 29], is responsible for the generation of residual stress in SLM components.

Figure-4.8(d) shows the temperature distribution across the depth ZX plane (Side View) of the melt-pool. The highest temperature of 2160°C occurs at the top surface of the melt-pool. The temperature distribution spreads out along the X-axis in the substrate region due to higher conductivity of the solid substrate surrounding the melt-pool compared to the powder layer, whereas powder has lower conductivity. It can also be seen from Figure-4.8(d), that the temperature gradient along the depth (Z-axis) of the melt-pool increases in the substrate region. This high temperature gradient across the melt-pool depth will result in differential contraction upon cooling and according to temperature gradient mechanism[28, 123] and cool-down phase model[28, 29] is responsible for the development of residual stress in SLM components.

4.11 Validation of the effect of FEA Predicted Cooling Rate on Residual Stress

SLM Ti6Al4V samples built with process parameters shown in Table-4.6 based on the density optimisation trials for 75µm layer thickness resulted in 78MPa residual stress as shown in Figure-4.9(a).

Table 4-6. Optimised parameters for 75µm layer thickness SLM builds

Power (P) (W)	Exposure (t) (µs)	Point Distance (pd)(µm)	Hatch Spacing (h) (µm)	Substrate Temperature (°C)
200 W	120 µs	65 µm	80 µm	100°C

Keeping the energy density constant at $61.5 \frac{J}{mm^3}$ (optimum energy density for achieving nearly fully dense SLM Ti6Al4V parts with 75µm layer thickness), the required exposure time was calculated for 150W power using Equation-4.(a). FEA simulation predicted a lower cooling rate for 150W power and 160µs exposure time for 75µm layer thickness SLM Ti6Al4V parts. Blocks built with 150W power and 160µs exposure time resulted in 55MPa residual stress as shown in Figure-4.9(a). The decreasing trend in residual stress correlates with the FEA predicted trend in cooling rate and thus shows that the FEA simulation is a reliable tool for assessing the effect of SLM parameters on cooling rates and thus residual stress.

FEA simulation was also used to predict the temperature gradient for both sets of parameters used for creating the 75 μm layer thickness SLM Ti6Al4V samples. Figure-4.9(b) shows that the temperature gradient between the top of the melt-pool and 250 μm below the melt-pool top surface is higher for 200W power and 120 μs exposure combination compared with 150W power and 160 μs exposure. The decreasing trend in the FEA predicted temperature gradient according to temperature gradient mechanisms [28, 123], should result in a decreasing trend in residual stress. The decreasing trend in residual shown in Figure-4.9(a) agrees with the decreasing trend in temperature gradients (see Figure-4.9(b)) and therefore increases the confidence in results for the FEA simulation.

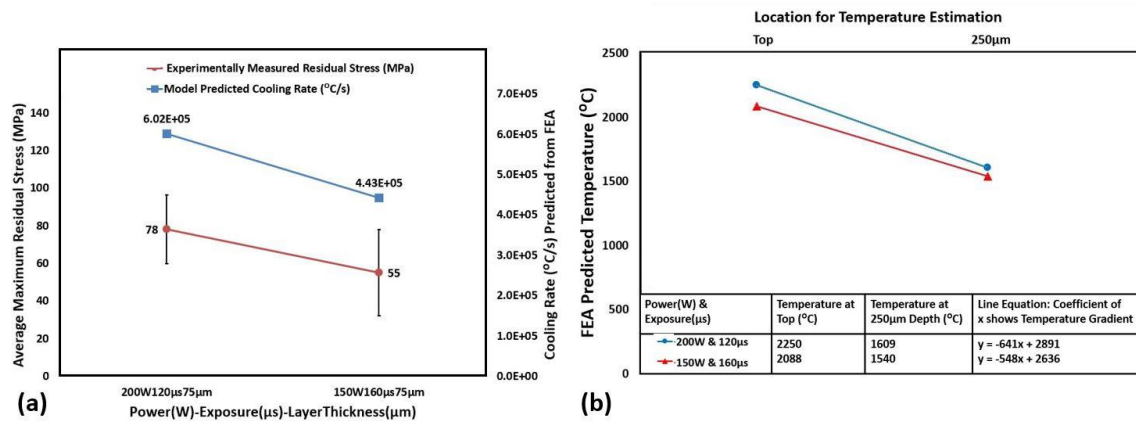


Figure 4-9. (a) Effect of Power and Exposure combination keeping Energy density constant on cooling rate and residual stress. (b) Temperature gradient prediction between the top surface of the melt-pool and 250 μm depth below the melt-pool from FEA simulation for SLM Ti6Al4V samples, built with different power and exposure combinations keeping energy density constant at optimum.

Another important observation from Figure-4.9(b) is that the highest temperature in the melt-pool decreases for a lower power of 150W and higher exposure of 160 μs

combination, compared with a high power of 200W and lower exposure of 120 μ s combination. This trend in peak temperature with laser power is in agreement with the findings of refs-[34-36], which reported that increase in laser power had a more pronounced effect on the melt-pool peak temperature compared with scan speed (exposure or irradiation time). This further provides as evidence for the validity of the FEA simulation as a tool for analysing the effect of SLM process parameters on residual stress.

5 Results (Effect of Individual SLM Parameters)

5.1 SLM parameter optimisation for Ti6Al4V

Figure-5.1 shows the optical micrographs of Ti6Al4V SLM samples produced for the density optimisation trial. Laser power and exposure time were varied to find the optimum combination for achieving nearly fully dense SLM Ti6Al4V parts. A combination of 200W laser power and 100 μ s exposure time produced samples with minimum internal defects and resulted in 99.99% dense parts. Figure-5.1 shows a clear variation in the morphology and level of porosity, in Ti6Al4V SLM samples built with different power and exposure combinations.

On the major diagonal within Figure-5.1, the top left corner corresponds to a low power and low exposure combination, which led to the formation of irregular shaped, lack of fusion pores. Following the major diagonal, to the bottom right corner, a region corresponding to high power and high exposure combination, the samples now contain spherical porosity, characteristic of over melting.

It can be seen that the power and exposure combinations lying on the opposite diagonal within Figure-5.1, from top right to bottom left of the array represents power and exposure combinations, which results in lower level of porosity in the samples. A careful analysis showed that sample E3, built with 200W laser power and 100 μ s exposure represents the optimum combination of power and exposure for building, nearly fully dense SLM, Ti6Al4V components.

5.1.1 Optical Microscopy

P(W)/E(μ s)	60	80	100	120	140	160	180
120 <u>500μm</u>							
140							
160							
180							
200							

Figure 5-1 Density optimisation trial

Figure-5.2(a) shows sample E3, representing the optimum combination of power and exposure to processing SLM, Ti6Al4V components. This combination resulted in minimising porosity defects and yielded a 99.99% dense part. Figure-5.2(b) shows sample A1, with irregular shaped, lack of fusion porosity, resulting in part density of 90.49%.

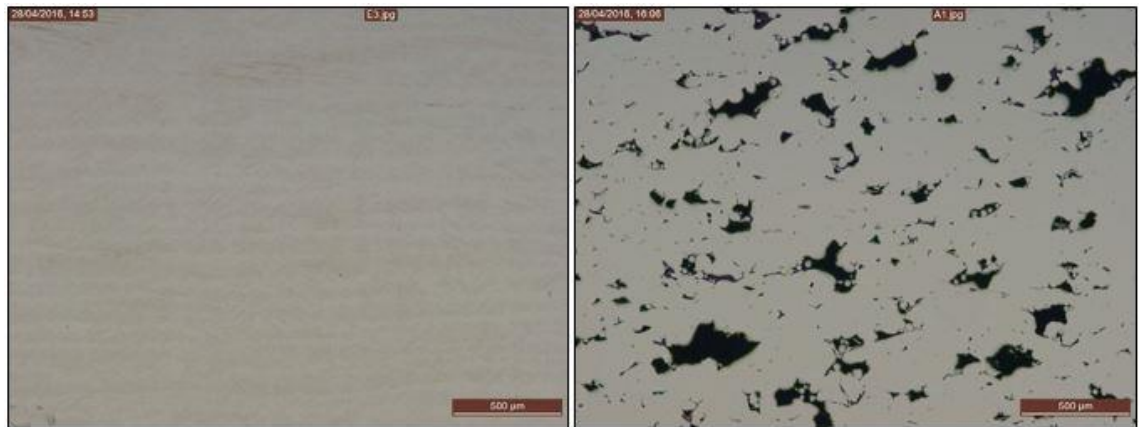


Figure 5-2 (a) Sample E3 with 99.99% density. (b) Sample A1 with 90.49% density

Etching sample E3 revealed a columnar microstructure (see Figure-5.3), characteristic of SLM Ti6Al4V, with some micro porosity. Figure-5.3 shows thin martensitic α' laths highlighted by the solid lines, growing inside columnar prior β grains highlighted by dashed lines. Prior β grains are seen to be extending over multiple layers.



Figure 5-3 *Sample E3 with martensitic α' laths highlighted by solid lines, growing inside columnar prior β grains highlighted by the dashed line, with pores highlighted by arrows.*

5.2 Effect of Scanning Strategy

Using the optimum combination of parameters for 50 μ m layer thickness, 30x30x10mm Ti6Al4V blocks were manufactured for residual stress measurement using the hole-drilling and strain gauge method.

5.2.1 Effect of Scanning Strategy on Porosity and Microstructure

Residual stress blocks were cross sectioned for further analysis, after residual stress measurement. Results of porosity analysis on samples created with different scanning strategies are presented in Figure-5.4. Test case S-1 built with 90° alternating strategy resulted in only 0.1% porosity as was found from the initial

parameter optimisation trials presented in section-5.1. Figure-5.4 shows a clear decreasing trend in the % porosity with increasing the scan vector length for samples built with the Island scanning strategy. Test case S-2 built with a scan vector length of 2mm resulted in 0.9% porosity, while increasing the scan vector length to 5mm for test case S-4 reduced the %porosity to 0.1. It can also be seen from Figure-5.4 that rotating the scan vectors by 90°, in adjacent squares for test case S-5, the %porosity for a 5mm scanning vector was reduced to 0.1.

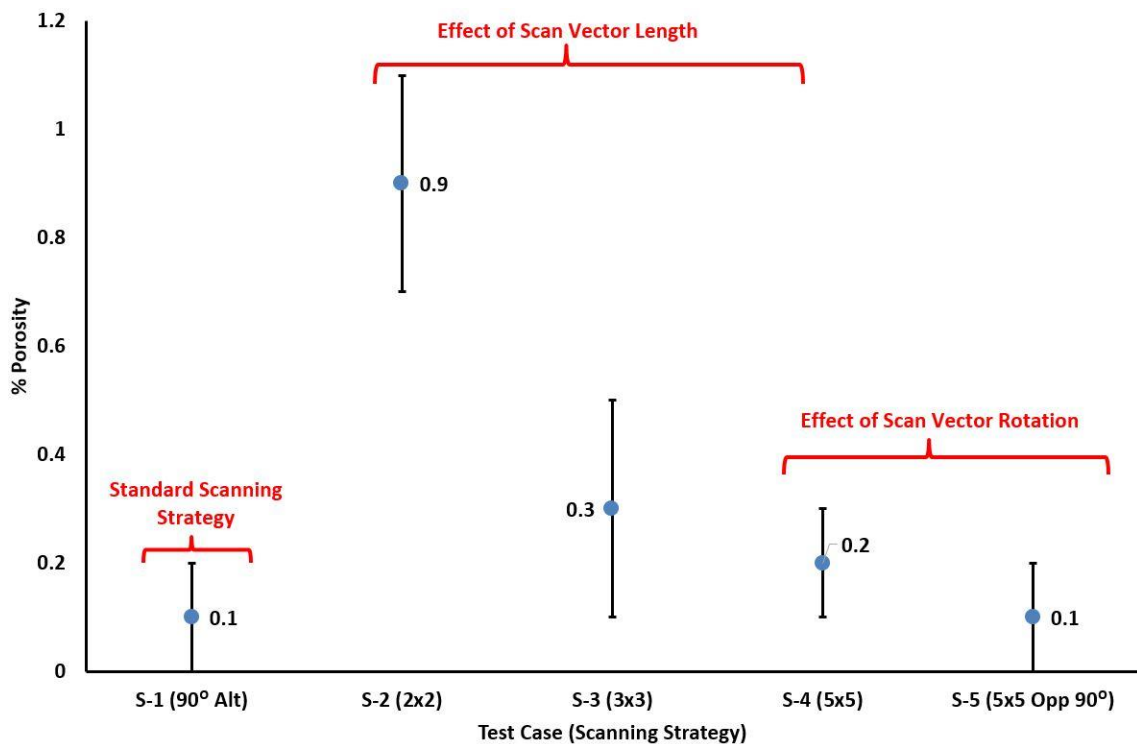


Figure 5-4 Effect of scanning strategy on % porosity

Samples prepared for porosity analysis were etched with Kroll's etching reagent to understand the effect of scanning strategy on the microstructure. Figure-5.5 shows

that irrespective of the scanning strategy the samples resulted in martensitic α' laths growing inside columnar prior β grains.



Figure 5-5. Martensitic α' laths in prior β columnar grains (a) Test case S-1, 90° alternating scanning strategy. (b) Test case S-3, 3x3 chessboard scanning strategy. (c) Test case S-5, 5x5 chessboard scanning strategy with scan vectors rotated at 90° in adjacent Islands.

5.2.2 Effect of Scanning Strategy on Residual Stress

Residual stress was measured on the 30x30x10mm test blocks manufactured using different scanning strategies by means of air-brasive hole drilling and strain gauge method. For test case S-1, samples built with 90° alternating strategy proved to be the best for achieving minimum residual stress and resulted in a value of 107MPa as shown in Figure-5.6. Island scanning strategy showed a trend of increasing Residual Stress with increasing Island size. Figure-5.6 shows that test case S-2, with a scan vector length of 2mm resulted in 173MPa residual stress. Dividing the scan area into 2x2mm chessboard squares resulted in an increase of 61.7% in residual stress, compared to test case S-1, samples built with standard 90° alternating scanning strategy. Increasing the scan vector length to 3mm, for test case S-3 resulted in a

further increase of 6.9% compared to S-2 and 72.9% compared to S-1. Increasing the chessboard squares size to 5x5 for test case S-4, resulted in a residual stress of 278MPa, which was 50.3% higher than S-3 and 159.8% higher compared to S-1. It can be seen from Figure-5.6 that for chessboard scanning strategy increasing the length of the scan vector resulted in an increase in residual stress.

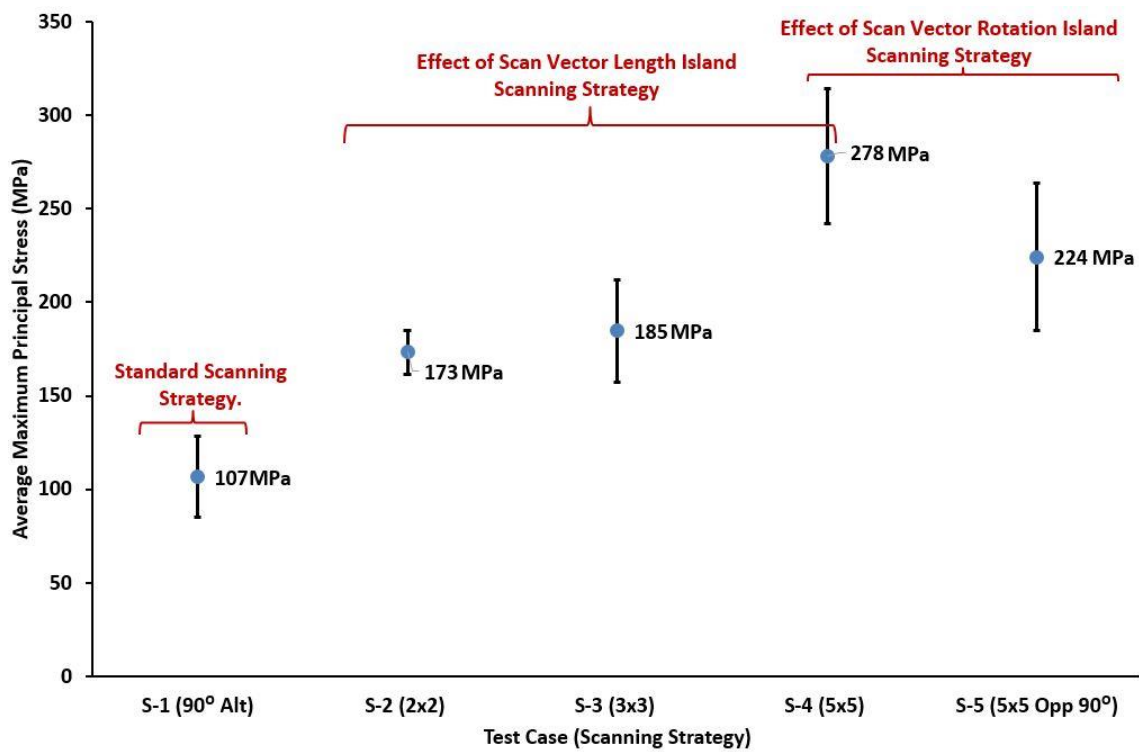


Figure 5-6 Effect of scanning strategy on residual stress

In order to understand the effect of scan vector rotation on residual stress using the chessboard scanning strategy, the orientation of the scan vectors in adjacent squares for the 5x5 chessboard case was rotated by 90°. Figure-5.6 shows that test case S-5, built with 5x5 chessboard scanning strategy with Scan Vectors perpendicular to

each other in adjacent squares and 90° rotation of the whole chessboard as well as Scan Vectors inside the squares in the next layer resulted in reducing the residual stress by 19.4% compared to S-4. The Residual Stresses in test case S-5 samples was 209% greater than test case S-1, samples built with the standard 90° Alternating Strategy as shown in Figure-5.6. Therefore the 90° Alternating strategy was chosen to be used for the rest of this work.

5.2.3 Effect of Scanning Strategy on Mechanical Properties

Mechanical properties were measured using dog bone specimens manufactured using different scanning strategies by means of tensile testing. In test case S-1, samples built with 90° Alternating strategy, achieved a UTS of 1174MPa as shown in Figure-5.7. The chessboard scanning strategy showed a trend of a slight increase in UTS values with increasing chessboard squares size. Figure-5.7 shows that for test case S-2, with a scan vector length of 2mm, the result was 1187MPa UTS. Dividing the scan area into 2x2mm squares resulted in an increase of 1.1% in UTS, compared to test case S-1, samples built with standard 90° Alternating scanning strategy. Increasing the scan vector length to 3mm, for test case S-3 resulted in a further increase of 2.2% compared to S-2 and 3.3% compared to S-1. Increasing the chessboard squares size to 5x5 for test case S-4, resulted in no further increase in UTS. It can be seen from Figure-5.7 that for the chessboard scanning strategy increasing the length of the scan vector resulted in a slight increase in UTS. Figure-5.7 shows that test case S-5, built with 5x5 chessboard scanning strategy with Scan

Vectors perpendicular to each other in adjacent squares and 90° rotation of the whole chessboard as well as Scan Vectors inside the squares in the next layer resulted in reducing the UTS by 2% compared to S-4. It is therefore clear from the results shown in Figure-5.7 that changing the scanning strategy had no significant effect on the UTS of the samples.

For test case S-1, samples built with a 90° alternating strategy, achieved a yield strength of 1079MPa as shown in Figure-5.7. The chessboard scanning strategy showed a trend of a slight increase in yield strength values with increasing chessboard squares size. Figure-5.7 shows that test case S-2, with a scan vector length of 2mm resulted in 1098MPa yield strength. Dividing the scan area into 2x2mm squares resulted in an increase of 1.8% in yield strength, compared to test case S-1, samples built with standard 90° alternating scanning strategy. Increasing the scan vector length to 3mm, for test case S-3 resulted in a further increase of 2.6% compared to S-2 and 4.4% compared to S-1. Increasing the chessboard squares size to 5x5 for test case S-4, resulted in no further increase in yield strength. It can be seen from Figure-5.7 that for the chessboard scanning strategy increasing the length of the scan vector resulted in a slight increase in yield strength. Figure-5.7 shows that test case S-5, resulted in reducing the yield strength by 3.2% compared to S-4. It is therefore clear from the results shown in Figure-5.7 that changing the scanning strategy had no significant effect on the yield strength of the samples.

Test case S-1, achieved a 6.9% elongation as shown in Figure-5.7. Chessboard scanning strategy did not show any clear trend in % elongation values with increasing chessboard squares size. Figure-5.7 shows that test case S-2, resulted in

6.7% elongation, 2.9% lower, compared to test case S-1. Increasing the scan vector length to 3mm, for test case S-3 resulted in a further decrease of 4.6% compared to S-2 and 7.4% compared to S-1. Increasing the chessboard squares size to 5x5 for test case S-4, resulted in an increase of 22.8% compared with S-3 and 13.8% compared with S-1. It can be seen from Figure-5.7 that for the chessboard scanning strategy no clear relationship can be established between scan vector length and %elongation. Figure-5.7 shows that test case S-5, resulted in increasing the elongation by 4.8% compared to S-4. It is therefore clear from the results shown in Figure-5.7 that changing the scanning strategy did not present any clear trend in the variation in %elongation of the samples.

The results of Figure-5.7 show no considerable variation in UTS and yield strength values for varying scanning strategy. % elongation does not show a discernible relationship with scanning strategy either. Even though samples S-4 and S-5 showed an improvement in %elongation but considering the residual stress values in those samples from section-5.2.2 (see Figure-5.6), 90° Alternating scanning strategy was used for the rest of this work.

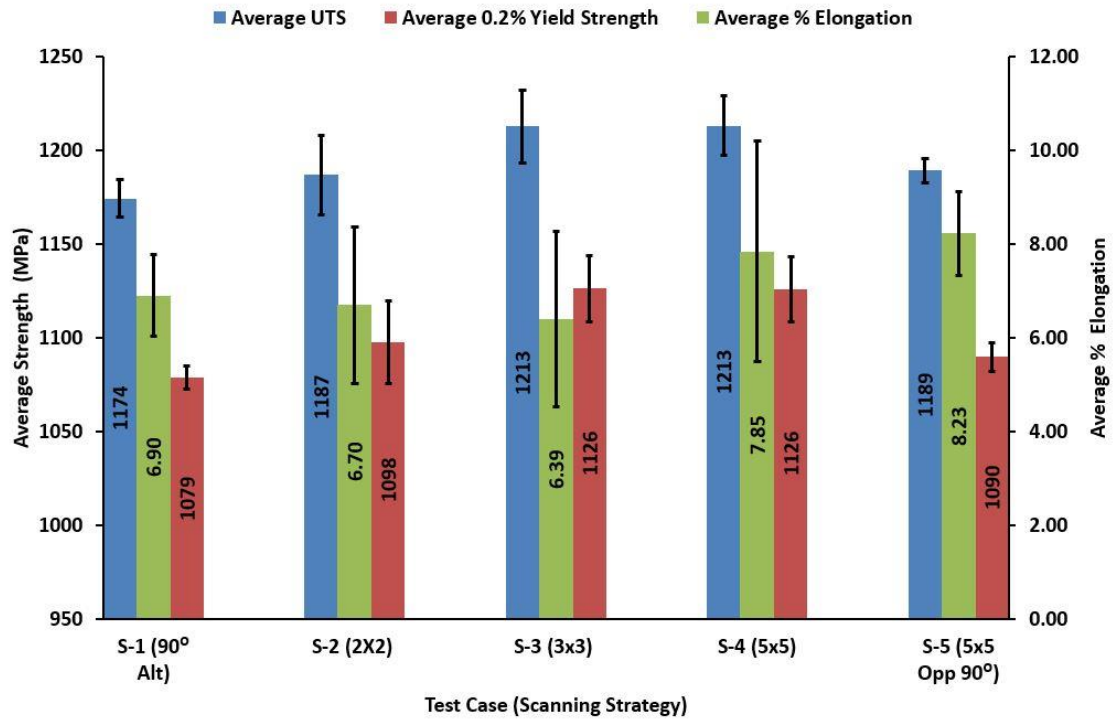


Figure 5-7 Effect of scanning strategy on UTS, Yield Strength and % Elongation

Cross sectioned residual stress blocks were used for hardness analysis, after residual stress measurement. Results of hardness test of samples created with different scanning strategies are presented in Figure-5.8.

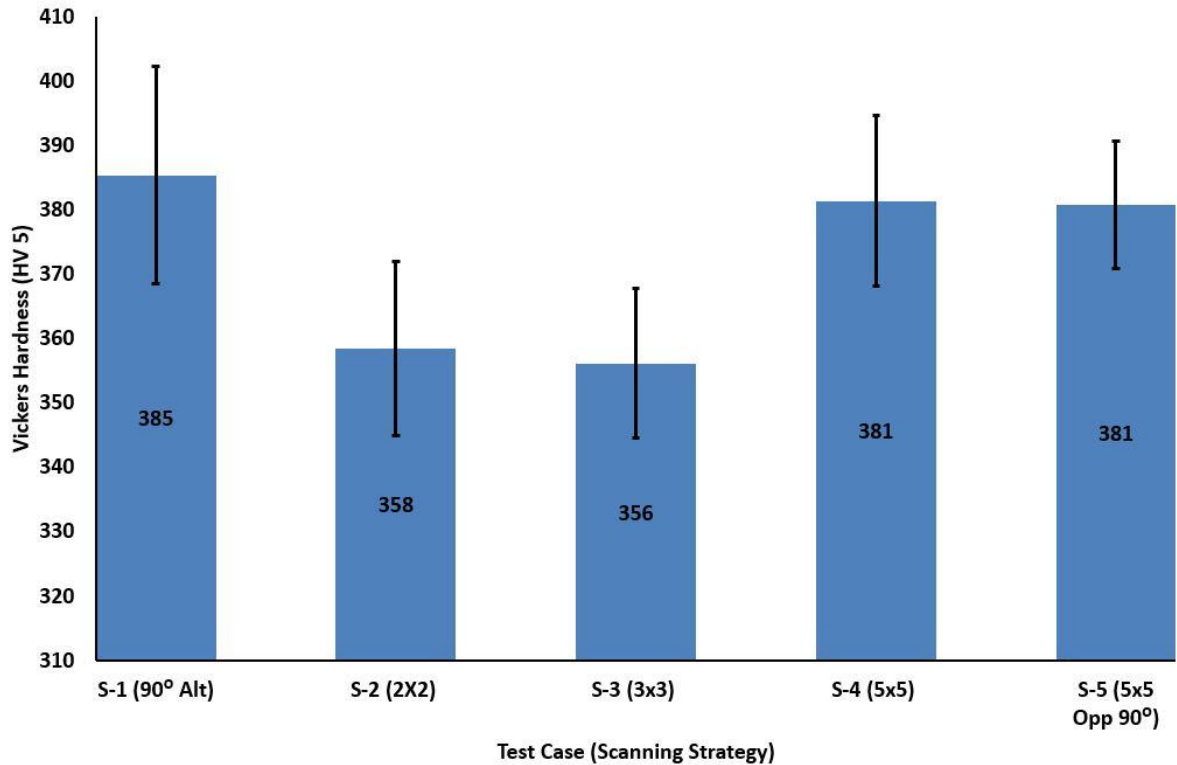


Figure 5-8 Effect of scanning strategy on Vickers Hardness

Test case S-1, resulted in 385 HV5 Vickers hardness as shown in Figure-5.8. Chessboard scanning strategies did not show any clear trend in hardness values with increasing chessboard squares size. Figure-5.8 shows that test case S-2, resulted in 7% lower hardness values, compared to test case S-1. Increasing the scan vector length to 3mm, for test case S-3 showed no effect on hardness. Increasing the chessboard squares size to 5x5 for test case S-4, resulted in an increase of 7% compared with S-3 and resulted in hardness values almost equal to S-1. It can be seen from Figure-5.8 that for chessboard scanning strategies no clear relationship can be established between scan vector length and hardness. Figure-5.8 shows that test case S-5, resulted in no variation in hardness. It is therefore clear from the

results shown in Figure-5.8 that changing the scanning strategy had no effect on the hardness of the samples. Therefore based on the hardness results the choice of using 90° alternating scanning strategy for the rest of this work was still a sensible choice.

5.3 Effect of Layer Thickness

The effect of layer thickness was studied by building 30x30x10mm Ti6Al4V blocks for residual stress measurement using the hole-drilling method and tensile samples for mechanical properties measurement using layer thicknesses of 25, 50 and 75µm. Samples for each layer thickness were built with optimised power and exposure time from the density optimisation trials carried out for each layer thickness.

5.3.1 Effect of Layer Thickness on Porosity and Microstructure

Residual stress blocks were cross sectioned for further analysis, following residual stress measurement. Results of porosity analysis on samples created with different layer thicknesses are presented in Figure-5.9.

Figure-5.9 shows that there is a clear increasing trend in the % porosity with increasing layer thickness. Test case LT-1 built with 25µm layer thickness had 0% porosity. LT-2 built with a layer thickness of 50µm resulted in 0.1% porosity, while increasing the layer thickness to 75µm for test case LT-3 increased the porosity value to 0.8%. Samples prepared for porosity analysis were etched with Kroll's etching reagent to understand the effect of layer thickness on the microstructure.

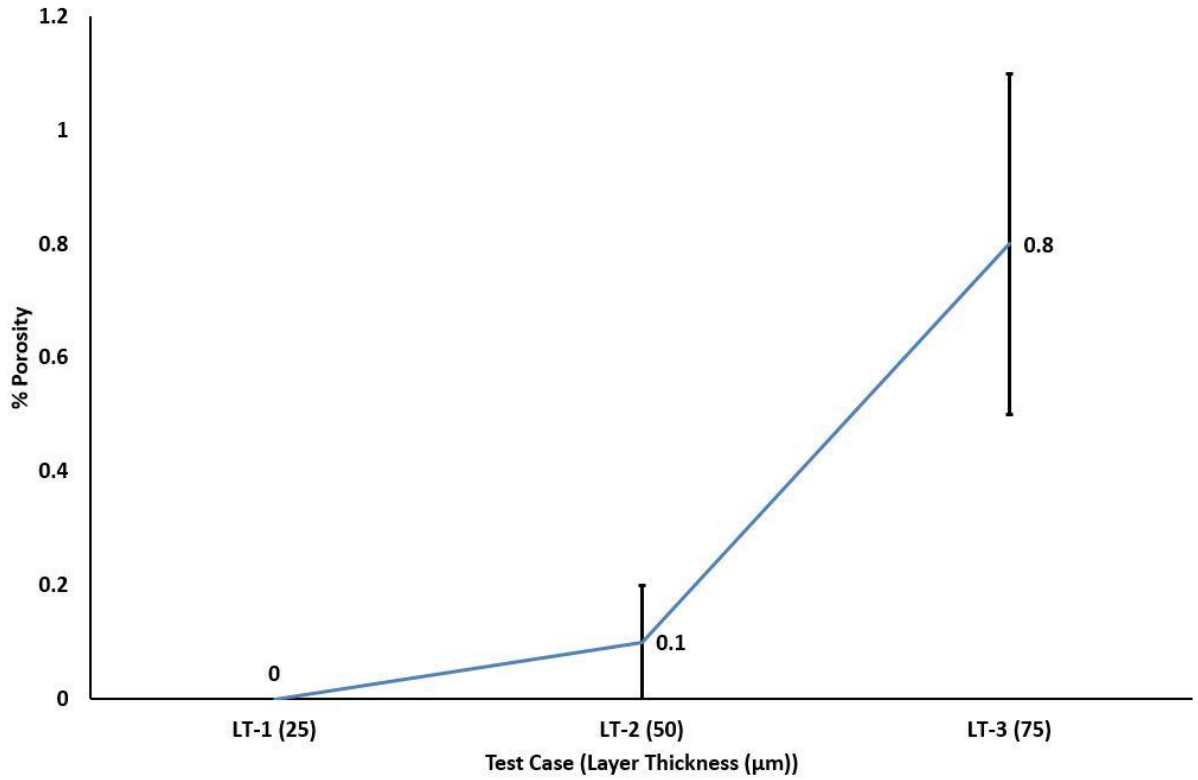


Figure 5-9 Effect of layer thickness on % porosity

Figure-5.10 shows that irrespective of the layer thickness the samples resulted in martensitic α' laths growing inside columnar prior β grains.

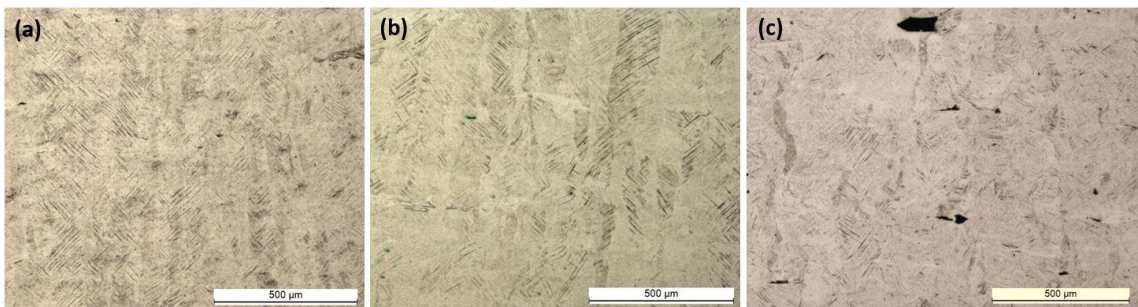


Figure 5-10. Martensitic α' laths in prior β columnar grains (a) Test case LT-1, 25 μ m layer thickness. (b) Test case LT-2, 50 μ m layer thickness. (c) Test case LT-3, 75 μ m layer thickness.

5.3.2 Effect of Layer Thickness on Residual Stress

Residual stress was measured on the 30x30x10mm test blocks manufactured using different layer thickness using the air-brasive hole drilling and strain gauge method. Figure-5.11 shows an inverse relation between residual stress and layer thickness. Test case LT-1, samples built with 25 μ m layer thickness resulted in 190MPa residual stress. Increasing the layer thickness to 50 μ m for test case LT-2, Figure-5.11 shows a decrease of 43.7% in residual stress, compared to test case LT-1. Increasing the layer thickness to 75 μ m, for test case LT-3 resulted in a further decrease of 27.1% compared to LT-2 and 58.9% compared to LT-1. It can be seen from Figure-5.11 that increasing the layer thickness resulted in a considerable decrease in residual stress.

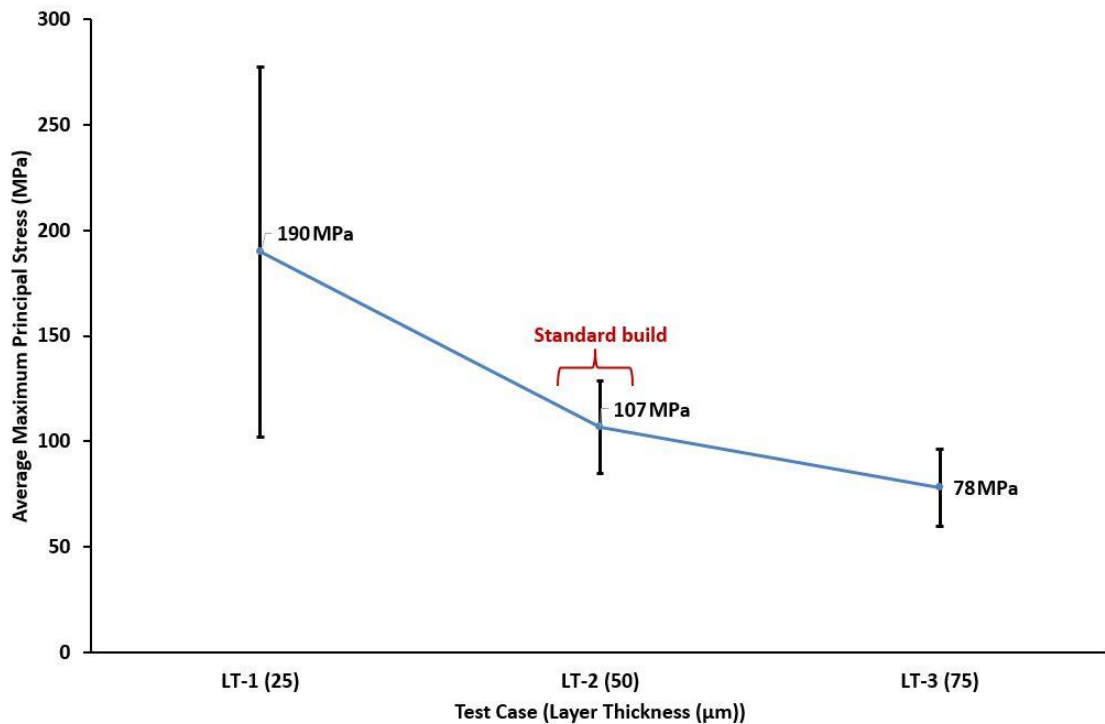


Figure 5-11 Effect of layer thickness on residual stress

5.3.3 Effect of Layer Thickness on Mechanical Properties

Mechanical properties were measured using dog bone specimens manufactured using different layer thickness by means of tensile testing. Figure-5.12 shows an inverse relationship between UTS and layer thickness. Test case LT-1, samples built with 25 μ m layer thickness, achieved a UTS of 1206MPa. Increasing the layer thickness to 50 μ m for test case LT-2, resulted in a decrease of 2.7% in UTS, compared to test case LT-1. Increasing the layer thickness to 75 μ m, for test case LT-3 resulted in a further decrease of 4.6% compared to LT-2 and 7.1% compared to LT-1. It is therefore clear from the results shown in Figure-5.12 that increasing the layer thickness resulted in a reduction in UTS but the effect was not significant.

Figure-5.12 shows an inverse relationship between yield strength and layer thickness. The test case LT-1, samples built with 25 μ m layer thickness, showed a yield strength of 1092MPa. Increasing the layer thickness to 50 μ m for test case LT-2, resulted in a decrease of 1.2% in yield strength, compared to test case LT-1. Increasing the layer thickness to 75 μ m, for test case LT-3 resulted in a further decrease of 3.9% compared to LT-2 and 5% compared to LT-1. It is therefore clear from the results shown in Figure-5.12 that increasing the layer thickness did not result in a significant reduction in yield strength.

Figure-5.12 shows an inverse relationship between %elongation and layer thickness. In test case LT-1, samples built with 25 μ m layer thickness, resulted in 11% elongation. Increasing the layer thickness to 50 μ m for test case LT-2, resulted in a decrease of 37.3% in elongation, compared to test case LT-1. Increasing the layer

thickness to 75 μm , for test case LT-3 resulted in a further decrease of 20.9% compared to LT-2 and 50.2% compared to LT-1. It is therefore clear from the results shown in Figure-5.12 that increasing the layer thickness had a significant reduction in the elongation of the samples.

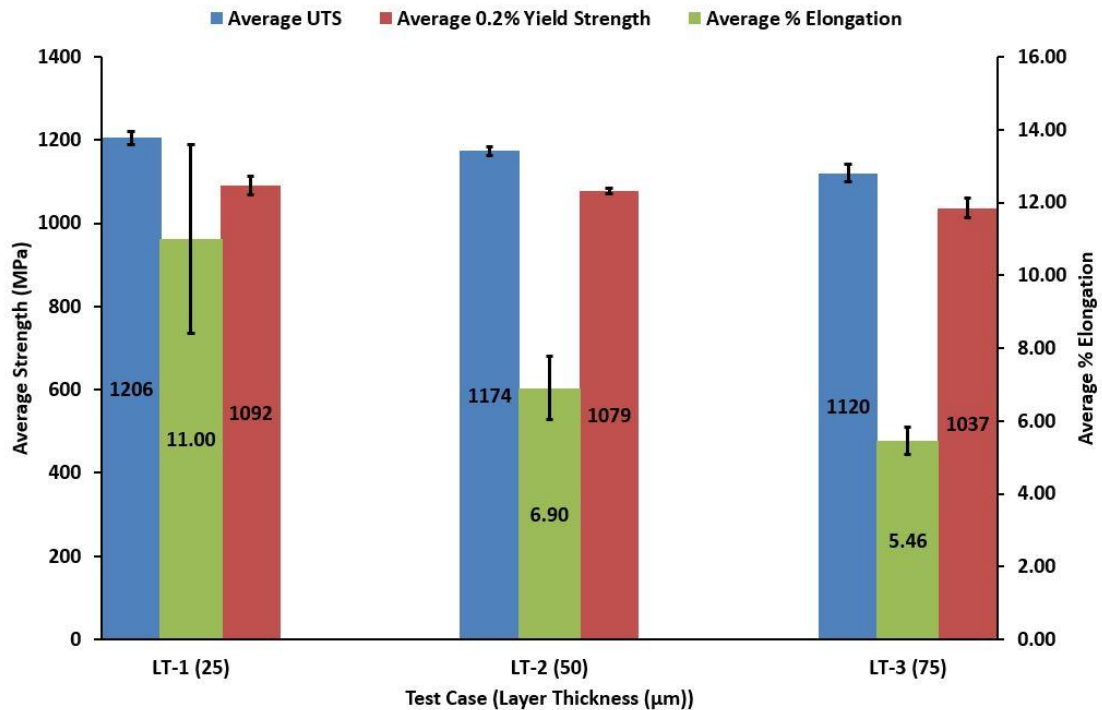


Figure 5-12 Effect of layer thickness on UTS and Yield Strength and % Elongation

The results of Figure-5.12 show no considerable variation in UTS and yield strength values for varying layer thickness. %elongation showed a clear decreasing trend with increasing layer thickness. Even though samples LT-1 showed an improved %elongation but considering the residual stress values in those samples from section-5.3.2(see Figure-5.11), 50 μm layer thickness was used for the rest of this work.

Cross sectioned residual stress blocks were used for hardness analysis, after residual stress measurement. Results of hardness tests of samples created with different layer thickness are presented in Figure-5.13. Figure-5.13 shows a direct relationship between Vickers hardness and layer thickness. Test case LT-1, samples built with 25 μ m layer thickness, resulted in 364 Vickers hardness.

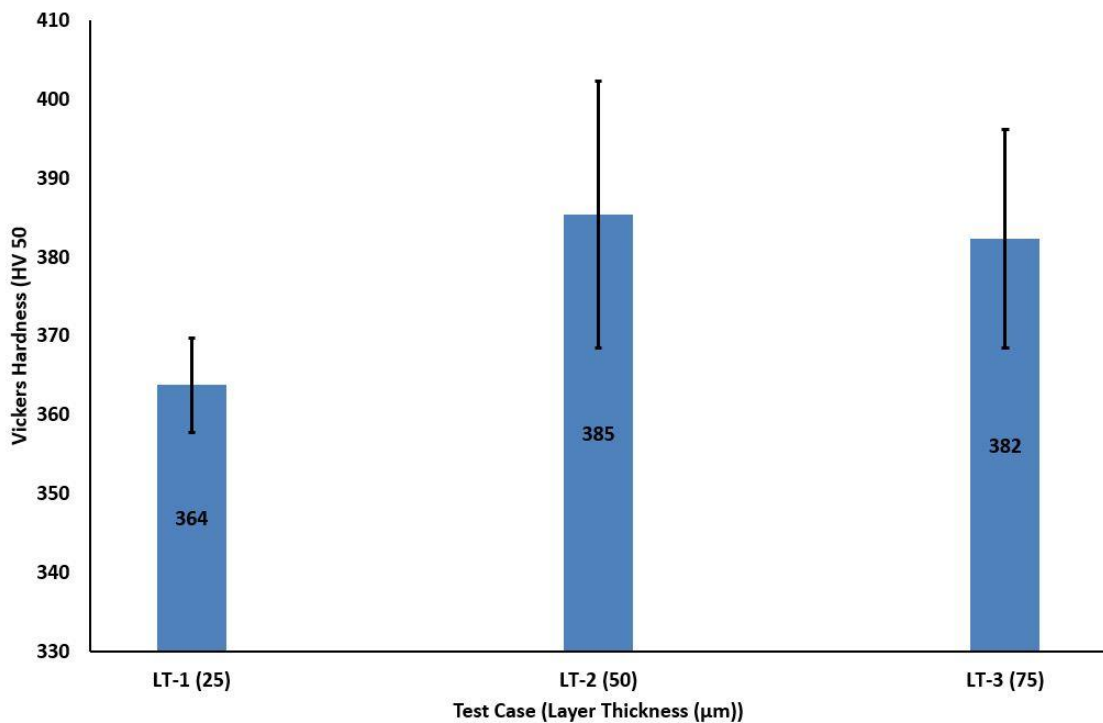


Figure 5-13 Effect of layer thickness on Vickers Hardness

Increasing the layer thickness to 50 μ m for test case LT-2, resulted in an increase of 5.8% in Vickers hardness, compared to test case LT-1. Increasing the layer thickness to 75 μ m, for test case LT-3 resulted in no further increase in hardness value. It is therefore clear from the results shown in Figure-5.13 that increasing the layer thickness did not have a profound effect on the hardness of the samples. Therefore

based on the hardness results the choice of using 50 μ m layer thickness for the rest of this work was still a sensible choice.

5.4 Effect of Re-Scanning Varying Exposure

Using the optimum combination of parameters for 50 μ m layer thickness, 30x30x10mm Ti6Al4V blocks were manufactured for residual stress measurement with hole-drilling. Each layer was re-scanned with a proportion of the optimum Energy Density ($76.92\frac{J}{mm^3}$) calculated from the density optimisation trials for 50 μ m layer thickness (see section-5.1). The Energy Density used for re-scanning each layer was varied by keeping power constant at 200W and varying the exposure time in proportion to the optimum exposure time of 100 μ s.

5.4.1 Effect of Re-Scanning with Varying Exposure on Porosity and Microstructure

Residual stress blocks were cross sectioned for further analysis, after residual stress measurement. The results of porosity analysis on samples created with different re-scanning strategies with varying exposure time are presented in Figure-5.14.

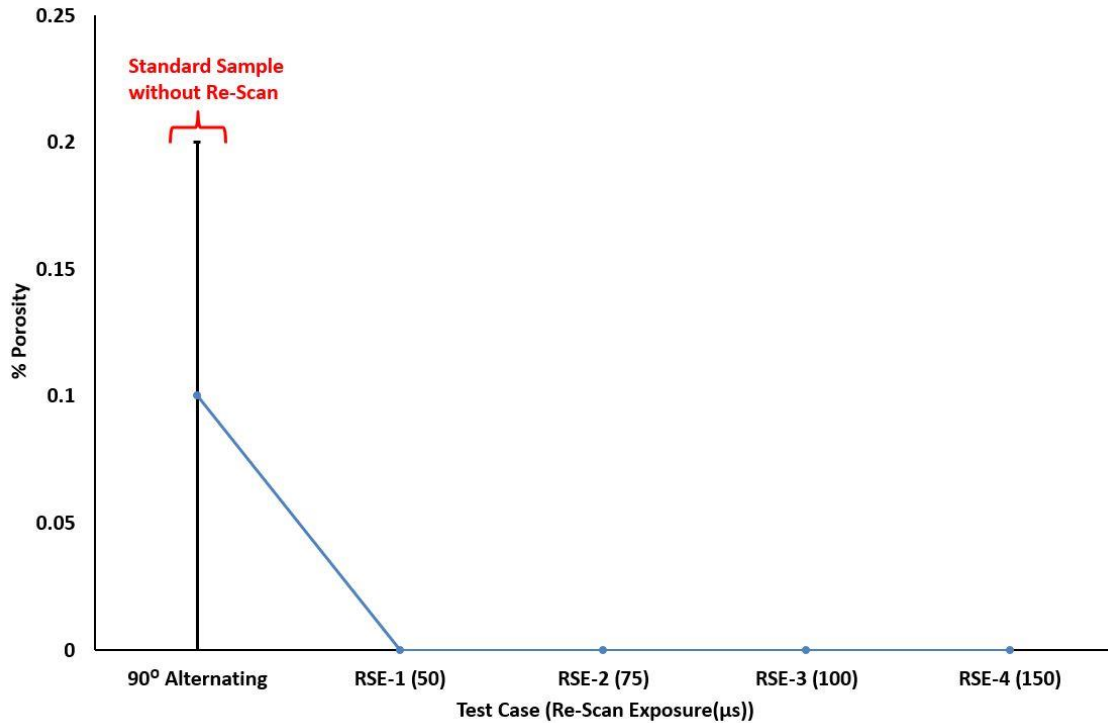


Figure 5-14 Effect of re-scanning with varying exposure on % porosity

Figure-5.14 shows that all re-scanning test cases resulted in fully dense blocks without any porosity. Samples prepared for porosity analysis were etched with Kroll's etching reagent to understand the effect of re-scanning with varying exposure on the microstructure. Figure-5.15 shows that irrespective of the re-scanning Energy Density the samples resulted in martensitic α' laths growing inside columnar prior β grains, as with the standard 90° alternating test case S-1 samples (see Figure-5.15(a)).

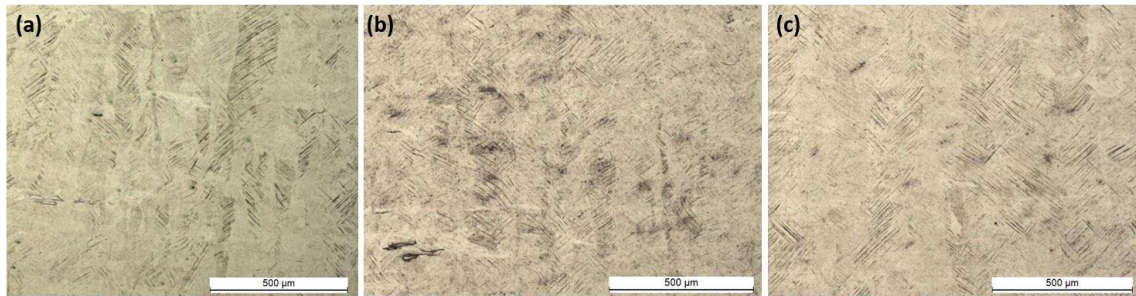


Figure 5-15 Martensitic α' laths in prior β columnar grains (a) Test case S-1, 90° alternating scanning strategy with no re-scan. (b) Test case RSE-1, Re-scan with $50\mu\text{s}$. (c) Test case RSE-4, Re-scan with $150\mu\text{s}$.

5.4.2 Effect of Re-Scanning with Varying Exposure on Residual Stress

Residual stress was measured on the 30x30x10mm test blocks manufactured using different re-scanning strategies with varying exposure time in proportion to the exposure time for standard 90° Alternating samples, by means of the air-brasive hole drilling and strain gauge method. For test case RSE-1, samples built with rescanning every layer using $50\mu\text{s}$ exposure time resulted in 125MPa residual stress, a 16.8% increase compared to standard samples, test case S-1 without any rescanning as shown in Figure-5.16. Test case RSE-2, with a re-scan exposure time of $75\mu\text{s}$ resulted in 165MPa residual stress, an increase of 32% in residual stress, compared to test case RSE-1, and 54.2% compared with standard test case S-1. Increasing the exposure time for rescanning to $100\mu\text{s}$, test case RSE-3 resulted in a decrease of 17.6% compared to RSE-2 but the residual stress was 27.1% higher greater than S-1. Increasing the exposure time to $150\mu\text{s}$, test case S-4, resulted in a

residual stress of 71MPa, which was 47.8% lower than RSE-3 and also 33.6% lower compared to S-1.

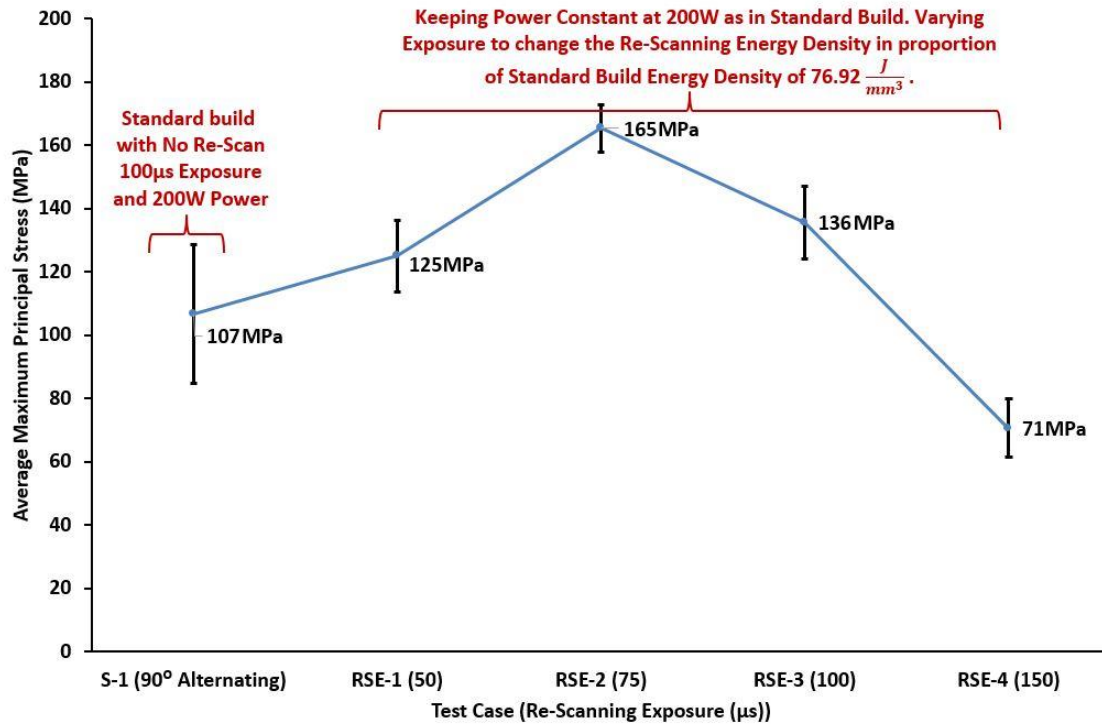


Figure 5-16 Effect of re-scanning energy varying exposure on residual stress

It can be seen from Figure-5.16 that rescanning with varying exposure time showed promising results for achieving a reduction in residual stress if every layer is rescanned with 150% Energy Density of the build parameters.

5.4.3 Effect of Re-Scanning with Varying Exposure on Mechanical Properties

Mechanical properties were measured using dog bone specimens manufactured using different rescanning strategies with varying exposure by means of tensile testing. UTS values shown in Figure-5.17 do not show any considerable variation for test cases RSE-1 to RSE-3 compared with the standard test case S-1 without any rescan. Test case RSE-4, rescanning with 150 μ s exposure showed a decrease of 13% compared with S-1. It is therefore clear from the results shown in Figure-5.17 that changing the rescanning exposure had no significant effect on the UTS of the samples.

Figure-5.17 does not show any clear trend in yield strength for test cases RSE-1 to RSE-3 compared with the standard test case S-1 without any rescan. Test case RSE-4, rescanning with 150 μ s exposure showed 0.03MPa yield strength, which is quite an unexpected drop suggesting pre-mature failure of the tensile samples. It is therefore clear from the results shown in Figure-5.17 that changing the rescanning exposure had no remarkable effect on the yield strength of the samples.

Rescanning with varying exposure did not show any clear trend in %elongation values with increasing exposure time. Test case RSE-1, resulted in 6.51% elongation, which was 5.7% lower than the elongation of standard samples, test case S-1 built without rescanning as shown in Figure-5.17. Test case RSE-2, showed 51% improvement in elongation, compared to test case RSE-1 and the elongation was 42.5% higher compared with S-1. Increasing the rescan exposure to 100 μ s, test case RSE-3 resulted in a sharp drop of 67.3% compared to RSE-2 and 53.5% compared to

S-1. Increasing the exposure to 150 μ s, test case RSE-4, resulted in 0% elongation, which is quite an unexpected drop suggesting pre-mature failure of the tensile samples. It can be seen from Figure-5.17 that for rescanning with varying exposure no clear relation can be established between rescan exposure time and %elongation.

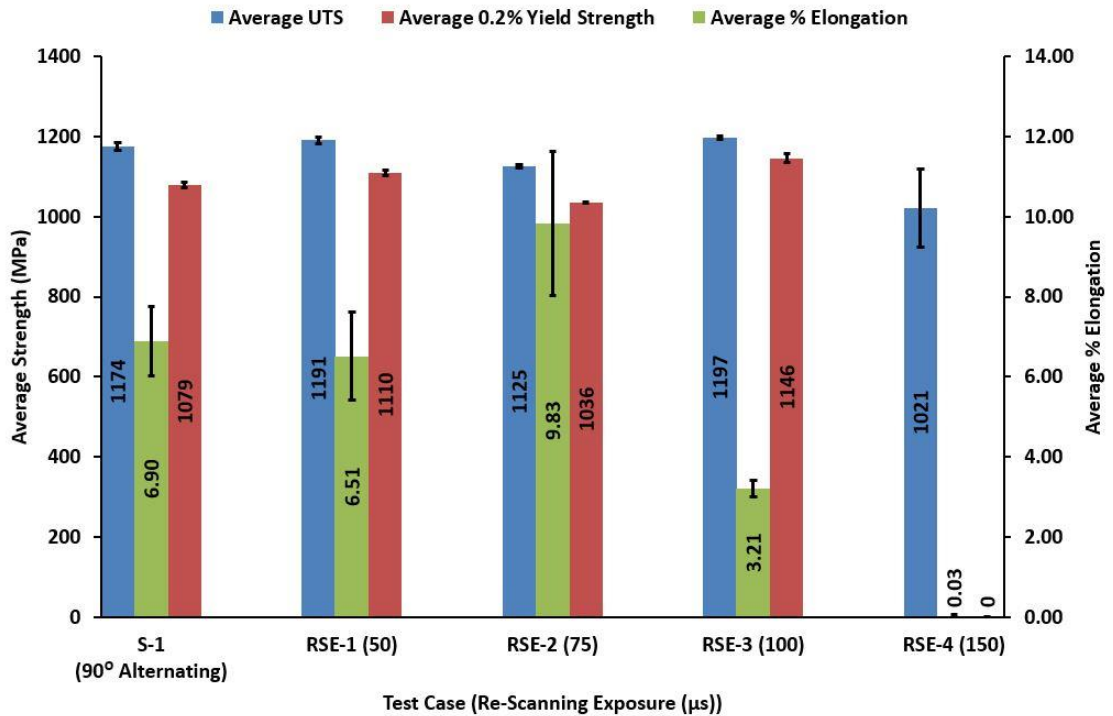


Figure 5-17. Effect of re-scanning energy varying exposure on UTS and Yield Strength and % Elongation

The results of Figure-5.17 show no considerable variation in UTS and yield strength values for varying rescanning exposure. %elongation does not present a discernible relation with either. Even though samples RSE-2 showed an improvement in % elongation, considering the residual stress values in those samples from section-

5.4.2 (see Figure-5.16), rescanning does not fall into the optimum combination of SLM parameters for reducing residual stress and enhancing mechanical properties.

Cross sectioned residual stress blocks were used for hardness analysis, after residual stress measurement. The results of hardness tests for samples created with rescanning varying exposure are presented in Figure-5.18. Figure-5.18 shows no variation in Vickers hardness between the standard test case S-1 without rescanning and rescanned samples. Therefore based on the hardness results the choice of dropping rescanning in the combination of optimum parameters is still a sensible choice.

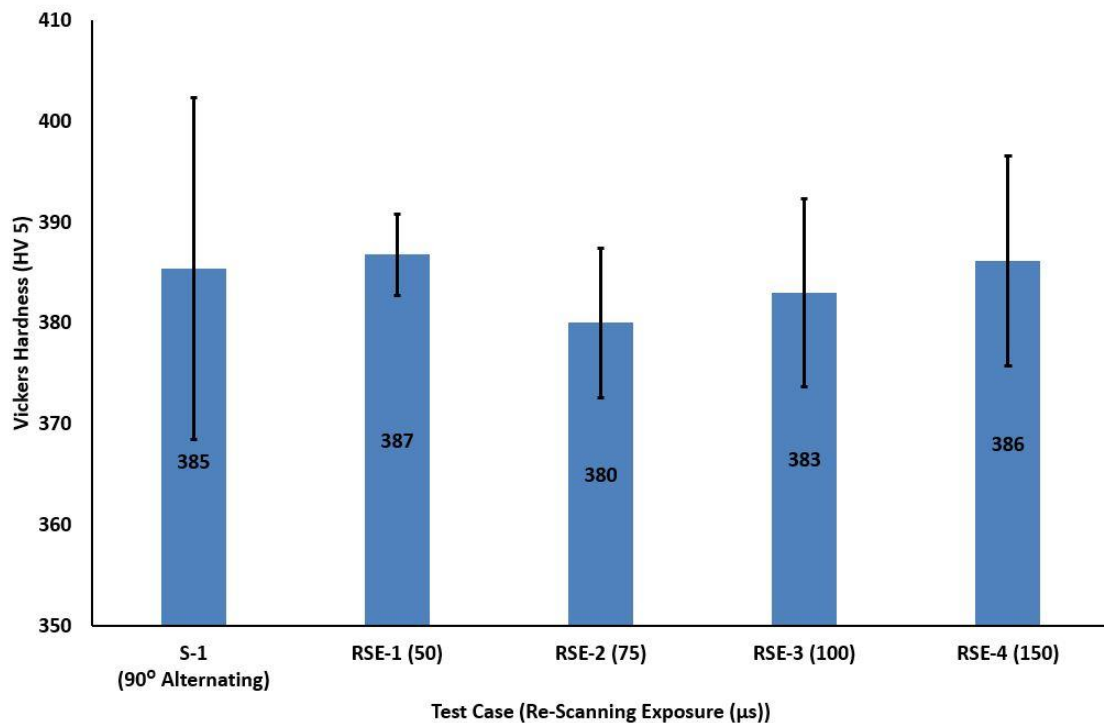


Figure 5-18 Effect of re-scanning energy varying exposure on Vickers Hardness

5.5 Effect of Re-Scanning with Varying Power

Using the optimum combination of parameters for 50 μ m layer thickness, 30x30x10mm Ti6Al4V blocks were manufactured for residual stress measurement using the hole-drilling method. Each layer was re-scanned with a proportion of the optimum Energy Density ($76.92\frac{J}{mm^3}$) calculated from the density optimisation trials for 50 μ m layer thickness (see section-5.1). Energy Density for re-scanning each layer was varied by keeping exposure time constant at 100 μ s and varying the power in proportion to the optimum power of 200W.

5.5.1 Effect of Re-Scanning with Varying Power on Porosity and Microstructure

Residual stress blocks were cross sectioned for further analysis, after residual stress measurement. Results of porosity analysis on samples created with different re-scanning strategies with varying power are presented in Figure-5.19. Figure-5.19 shows that for test case RSP-1, samples built with a rescanning power of 100W resulted in a 2.3% increase in porosity compared with the standard test case S-1, built without any rescanning. Increasing the rescanning power to 150W, test case RSP-2 resulted in reducing the porosity to 1.8%, while rescanning with 200W power, test case RSP-3 resulted in fully dense blocks without any porosity.

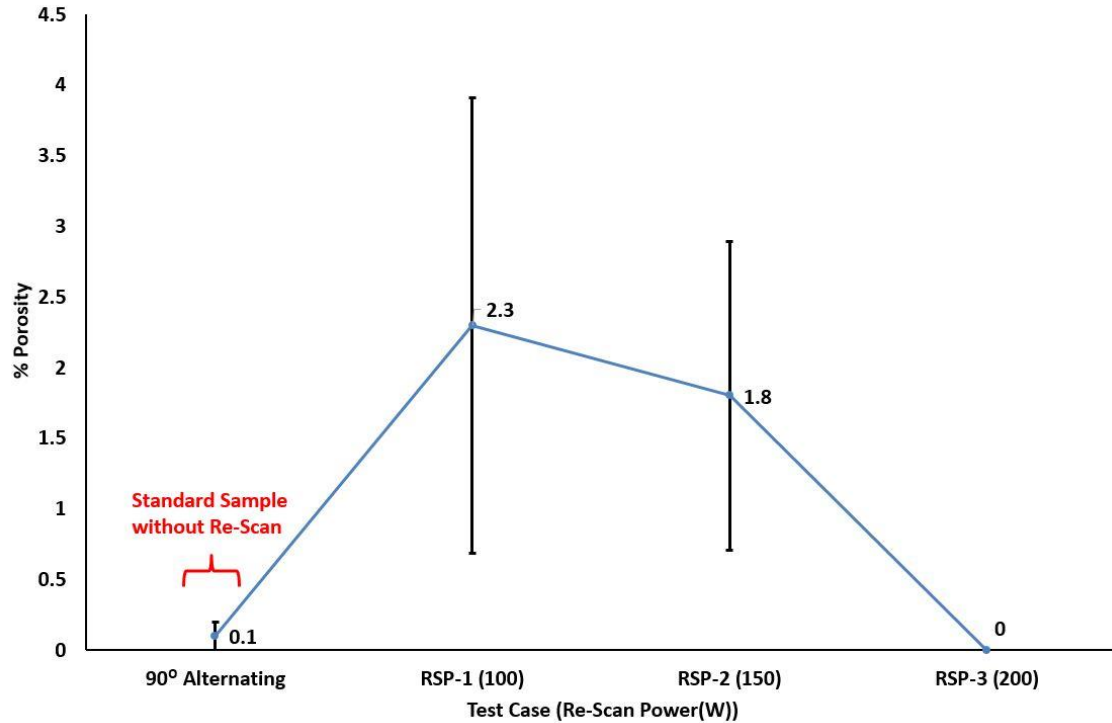


Figure 5-19 Effect of re-scanning with varying power on % porosity

Samples prepared for porosity analysis were etched with Kroll's etching reagent to understand the effect of re-scanning with varying power on the microstructure. Figure-5.20 shows that irrespective of the re-scanning Energy Density the samples resulted in martensitic α' laths growing inside columnar prior β grains, same as the standard 90° alternating test case S-1 samples (see Figure-5.20(a)).

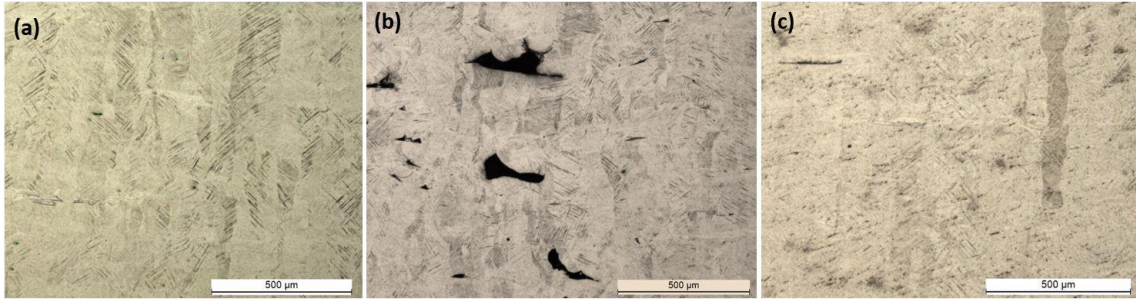


Figure 5-20 Martensitic α' laths in prior β columnar grains (a) Test case S-1, 90° alternating scanning strategy with no re-scan. (b) Test case RSP-1, Re-scan with 100W. (c) Test case RSE-3, Re-scan with 200W.

5.5.2 Effect of Re-Scanning with Varying Exposure on Residual Stress

Residual stress was measured on the 30x30x10mm test blocks manufactured using different re-scanning strategies with varying power in proportion to the 200W power for standard 90° Alternating samples, by means of the air-brasive hole drilling and strain gauge method. For test case RSP-1, samples built with rescanning every layer using 100W power resulted in 180MPa residual stress, a 68.2% increase compared to standard samples, test case S-1 without any rescanning as shown in Figure-5.21.

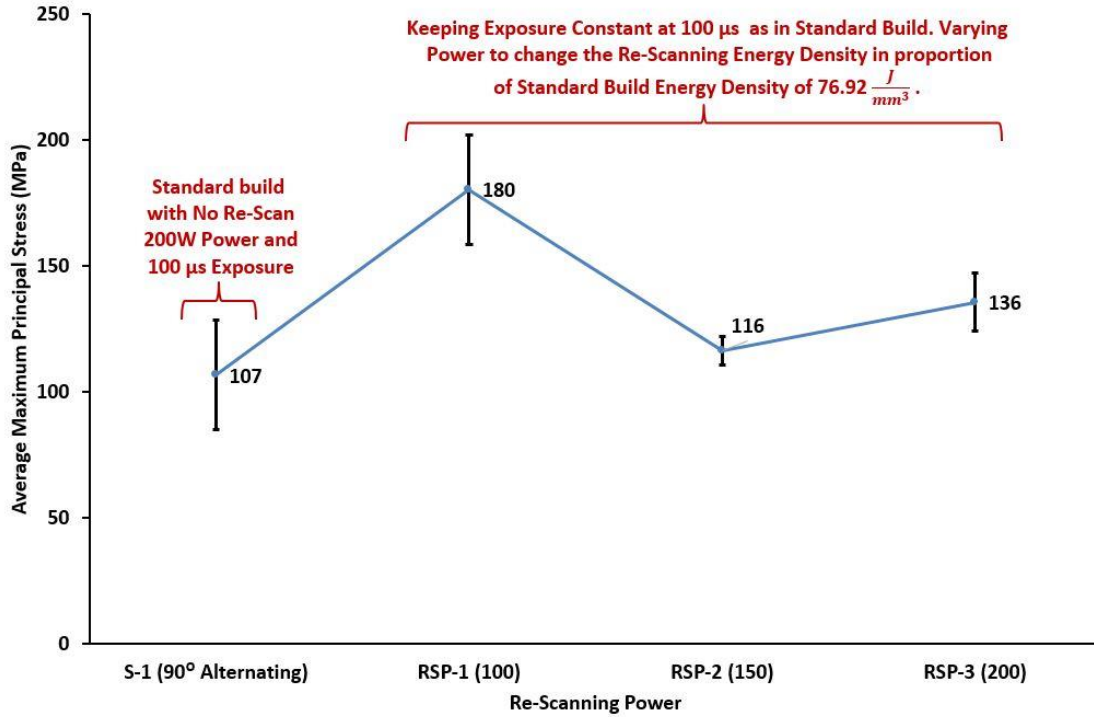


Figure 5-21. Effect of re-scanning energy varying power on residual stress

Test case RSP-2, with a re-scan power of 150W resulted in 116MPa residual stress, a decrease of 35.6%, compared to test case RSP-1, while it was 8.4% higher than residual stress in the standard test case S-1. Increasing the power for rescanning to 200W, test case RSP-3 resulted in an increase of 17.2% compared to RSP-2 but the residual stress was 27.1% higher compared to S-1. It can be seen from Figure-5.21 that rescanning with varying power did not show any promising results for achieving a reduction in residual stress. Therefore rescanning was not considered for the rest of this work.

5.5.3 Effect of Re-Scanning with Varying Power on Mechanical Properties

Mechanical properties were measured using dog bone specimens manufactured using different rescanning strategies with varying power by means of tensile testing. UTS values shown in Figure-5.22 do not show any clear trend with varying rescanning power. For test case RSP-1, rescanning with 100W power showed a decrease of 3.2% compared with S-1, standard samples without any rescanning. Increasing the rescanning power to 150W, test case RSP-2, resulted in a further decrease of 12.8% compared to RSP-1, while the UTS was lower by 15.9% compared with S-1. The UTS value for test case RSP-3, rescanning with 200W power, rose by 20.8% compared with RSP-2 and was higher by 2% than S-1. It is therefore clear from the results shown in Figure-5.22 that changing the rescanning power did not show any clear correlation with changes in the UTS of the samples.

Figure-5.22 does not show any clear trend in yield strength for test cases RSP-1 to RSP-3 compared with the standard test case S-1 without any rescan. For test case RSP-1, rescanning with 100W power, resulted in a 2.9% decrease in yield strength compared to S-1. Increasing the rescanning power to 150W, test case RSP-2 resulted in a further decrease of 11.4% compared with RSP-1 while the yield strength was lower by 13.9% compared with S-1. For test case RSP-3, rescanning with 200W power showed an improvement of 23.4% compared to RSP-2, while the yield strength was higher by 6.2% compared with S-1. It is therefore clear from the results shown in Figure-5.22 that changing the rescanning power did not show any clear relation with changes in the yield strength of the samples.

Rescanning with varying power did not show any clear trend in %elongation values with increasing power. Test case RSP-1, resulted in 9.64% elongation, which was 39.7% higher than the elongation of standard samples, test case S-1 built without rescanning as shown in Figure-5.22. Test case RSP-2, showed 24.2% decrease in elongation, compared to test case RSP-1 but the elongation was 5.9% higher compared with S-1. Increasing the rescan power to 200W, test case RSP-3 resulted in a sharp drop of 56.1% compared to RSP-2 and 53.5% compared to S-1. It can be seen from Figure-5.22 that for rescanning with varying exposure no clear relation can be established between rescan power and %elongation.

The results of Figure-5.22 show no discernible relation between UTS, yield strength and %elongation with varying rescanning power. Even though samples RSP-1 showed an improvement in %elongation but considering the increase in residual stress section-5.5.2(see Figure-5.21), and increase in porosity section-5.5.1 (see Figure-5.19), rescanning with 100W power is not a viable option. Similarly RSP-2 showed a little enhancement in %elongation at the detriment of yield strength, residual stress and porosity, therefore rescanning with 150W is also not a viable option. The results from rescanning with varying power do not fall into the optimum combination of SLM parameters for reducing residual stress and enhancing mechanical properties. Therefore rescanning is not used for the rest of this work.

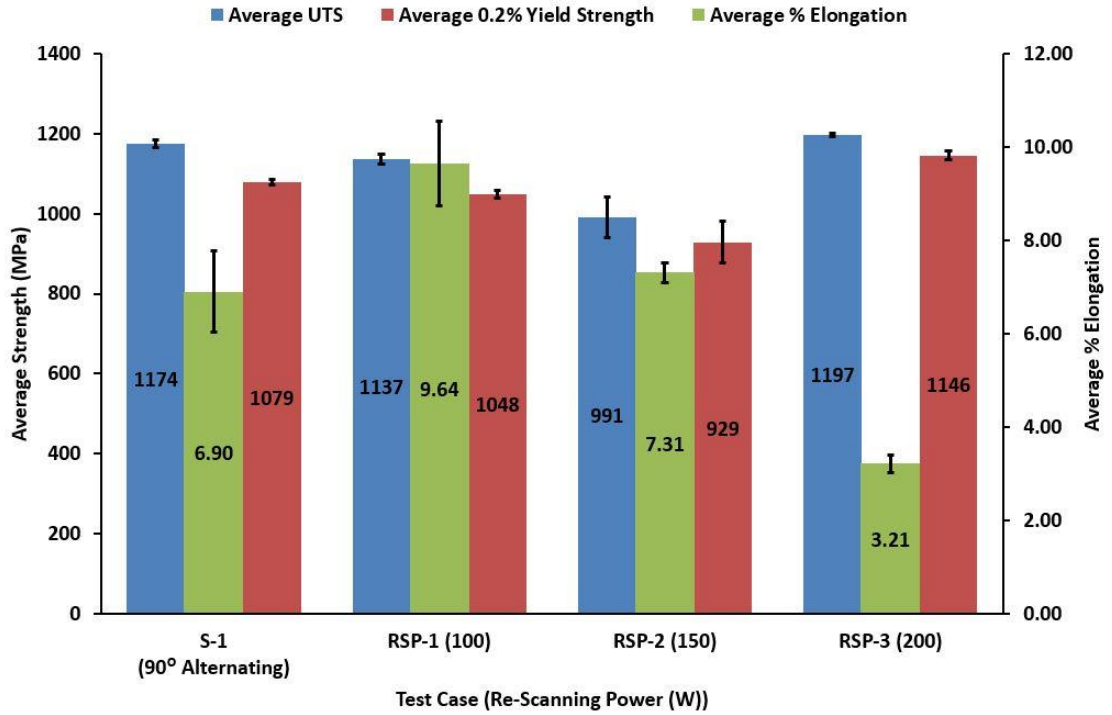


Figure 5-22. Effect of re-scanning energy varying power on UTS and Yield Strength and % Elongation

Cross sectioned residual stress blocks were used for hardness analysis, after residual stress measurement. Results of hardness test for samples created with rescanning varying power are presented in Figure-5.23. Figure-5.23 shows no variation in Vickers hardness between the standard test case S-1 without rescanning and rescanned samples. Therefore based on the hardness results the choice of dropping rescanning in the combination of optimum parameters is still a sensible choice.

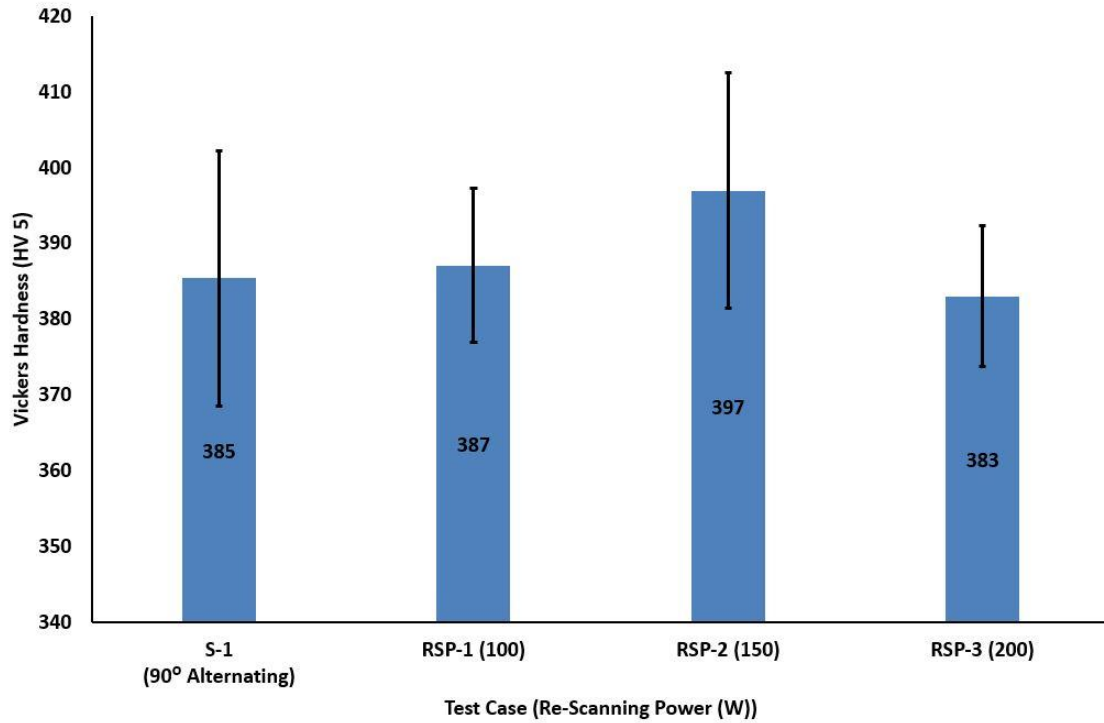


Figure 5-23 Effect of re-scanning energy varying power on Vickers Hardness

5.6 Effect of Power and Exposure keeping Energy Density Constant

Energy Density for the optimum combination of parameters found from the density optimisation trials for 50µm layer thickness (see section-5.1), was calculated using Equation-, resulting in an optimum Energy Density of $76.92 \frac{J}{mm^3}$. Keeping the Energy Density constant, 30x30x10mm Ti6Al4V blocks were manufactured for residual stress measurement, using different combination of power and exposure time.

5.6.1 Effect of Power and Exposure keeping Energy Density Constant on Porosity and Microstructure

Residual stress blocks were cross sectioned for further analysis, after residual stress measurement. Results of porosity analysis on samples created with different combinations of power and exposure for constant Energy Density are presented in Figure-5.24.

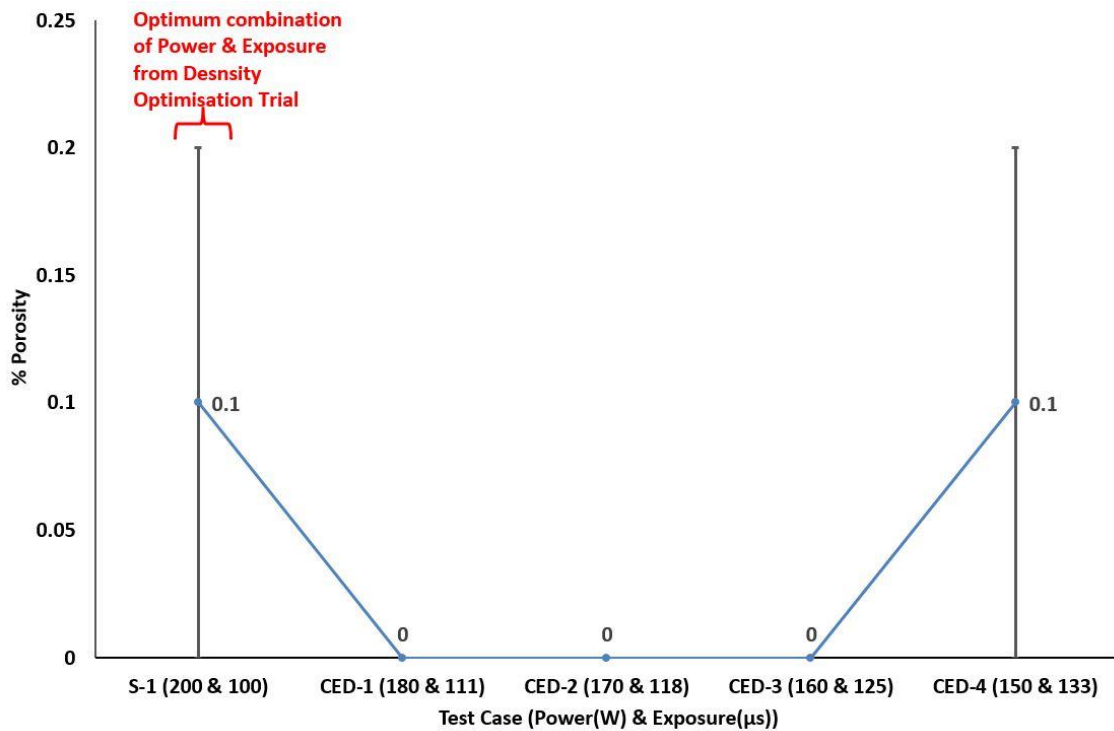


Figure 5-24 Effect of power and exposure keeping energy density constant on % porosity

Figure-5.24 shows that keeping the Energy Density constant, nearly fully dense SLM Ti6Al4V parts can be achieved with any combination of power and exposure. Samples prepared for porosity analysis were etched with Kroll's etching reagent to

understand the effect of varying power and exposure combinations for constant Energy Density, on the microstructure. Figure-5.25 shows that irrespective of the power and exposure combination with constant Energy Density the samples resulted in martensitic α' laths growing inside columnar prior β grains, same as the standard 90° Alternating test case S-1 samples (see Figure-5.25(a)), created with optimised power and exposure values (see section-5.1).

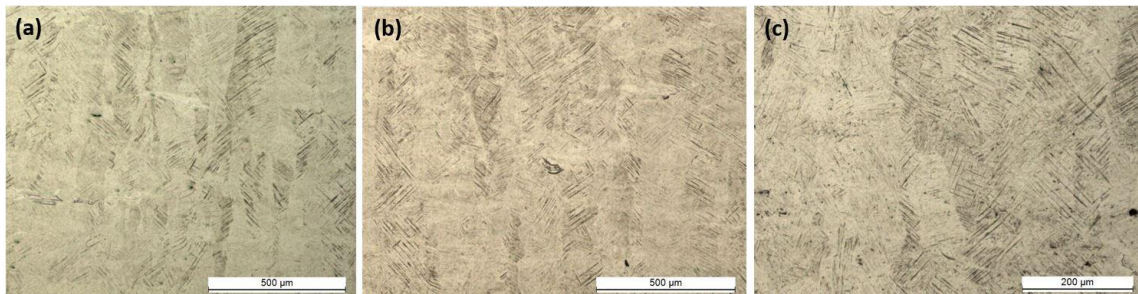


Figure 5-25. Martensitic α' laths in prior β columnar grains (a) Test case S-1, 90° alternating scanning strategy with optimum combination of power (200W) & exposure (100 μs). (b) Test case CED-1, power (180W) & exposure (111 μs). (c) Test case CED-4, power (150W) & exposure (133 μs)

5.6.2 Effect of Power and Exposure keeping Energy Density Constant on Residual Stress

Residual stress was measured on the 30x30x10mm test blocks manufactured using different combinations of power and exposure keeping Energy Density constant using the air-brasive hole drilling and strain gauge method. For constant Energy Density, Figure-5.26 shows a decreasing trend in residual stress with decreasing

power and increasing exposure. For test case S-1, samples built with optimum combination of power (200W) and exposure (100 μ s) resulted in 107MPa residual stress as shown in Figure-5.26. Test case CED-1, built with 180W power and 111 μ s exposure resulted in 3.7% reduction in residual stress compared with S-1.

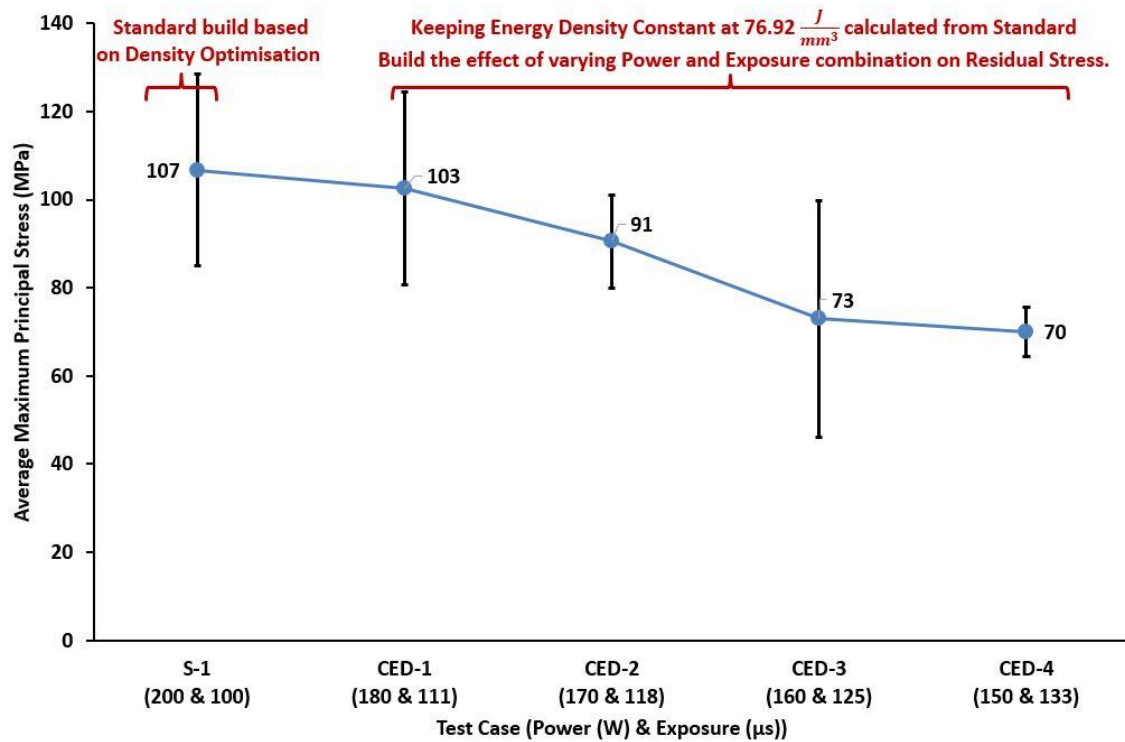


Figure 5-26. Effect of varying power and exposure time combination for a constant energy density on residual stress

Decreasing the power to 170W and increasing the exposure to 118 μ s, test case CED-2, resulted in 15% reduction in residual stress compared with S-1. Test cases CED-3 resulted in 19.8% decrease in residual stress compared with CED-2 and the residual stress was lower by 31.8% compared with S-1. Test case CED-4 resulted in 4.1%

decrease in residual stress compared with CED-3 and the residual stress was lower by 34.6% compared with S-1. The results in Figure-5.26 show that scanning and melting Ti6Al4V powder with slower scan speed and lower power, maintaining the optimum Energy Density, results in a reduction in residual stress within the parts.

5.6.3 Effect of Power and Exposure keeping Energy Density Constant on Mechanical properties

Mechanical properties were measured using dog bone specimens manufactured using different combinations of power and exposure keeping Energy Density constant by means of tensile testing. For constant Energy Density, UTS values do not show any considerable variation (see Figure-5.27) with decreasing power and increasing exposure time. Test case CED-4, built with 150W power and 133 μ s exposure showed a slight improvement of 2.9% in UTS, compared with S-1. Figure-5.27 shows that for constant Energy Density, the yield strength did not change considerably with decreasing power and increasing exposure time. Test case CED-4, built with 150W power and 133 μ s exposure showed a slight improvement of 3.9% in yield strength, compared with S-1.

For constant Energy Density, Figure-5.27 shows an increasing trend in % elongation with decreasing power and increasing exposure time. Test case CED-1, built with 180W and 111 μ s, resulted in 31.3% improvement in elongation compared with S-1. Decreasing the power to 170W and increasing exposure to 118 μ s resulted in 13.8% decline in elongation compared with CED-1 but the elongation was 13.2% higher

compared with test case S-1. Further decreasing the power to 160W and increasing exposure to 125 μ s, test case CED-3 resulted in an increase of 3.7% improvement in elongation compared with CED-2 and 17.4% compared with S-1. Test case CED-4, built with 150W and 133 μ s, resulted in a further improvement of 5.1% in elongation compared with CED-3 and 23.33% compared with S-1.

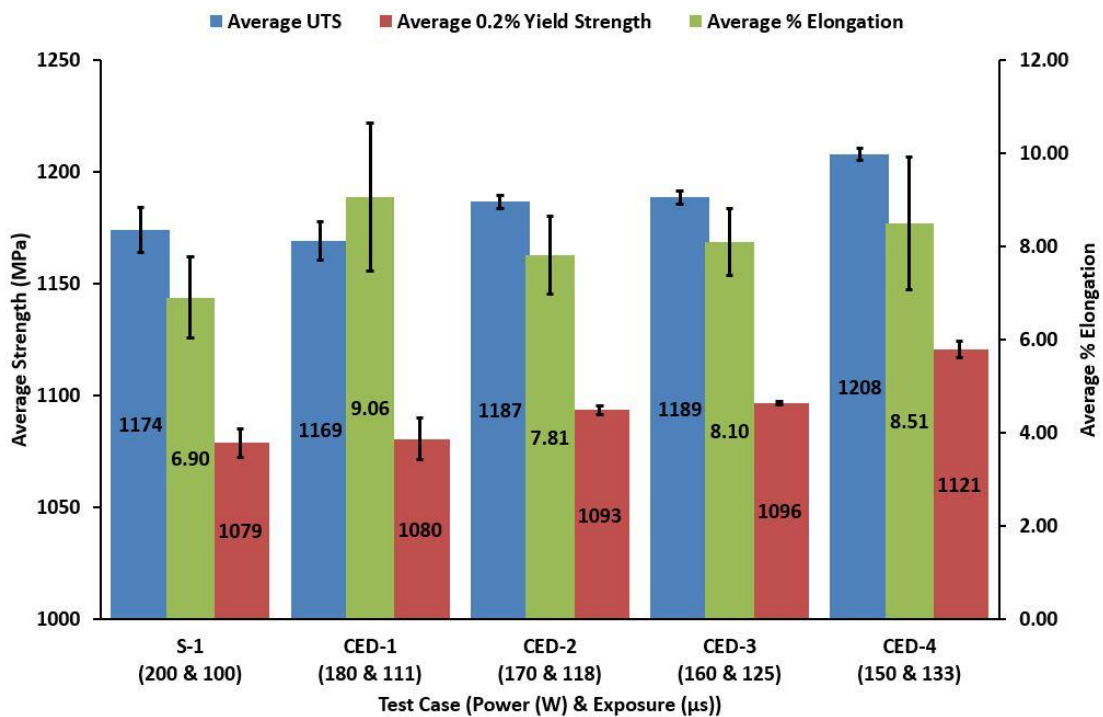


Figure 5-27. Effect of varying power and exposure time combination for a constant energy density on UTS, Yield Strength and % Elongation

The results of Figure-5.27 show no considerable variation in UTS and yield strength values for varying combinations of power and exposure, maintaining constant Energy Density. Scanning slowly with lower power, using the optimum Energy

Density resulted in considerable improvement in %elongation of the samples. Even though samples CED-1 resulted in the highest %elongation considering the residual stress values in those samples from section-5.6.2(see Figure-5.26), this combination of power and exposure was not considered any further. Test case CED-4 resulted in the second highest elongation and from section-5.6.2(see Figure-5.26), an improvement in residual stress was also recorded for 150W power and 133 μ s exposure. Therefore the power and exposure combination from test case CED-4 was used further in the investigation of strategic residual stress reduction in a complex geometry.

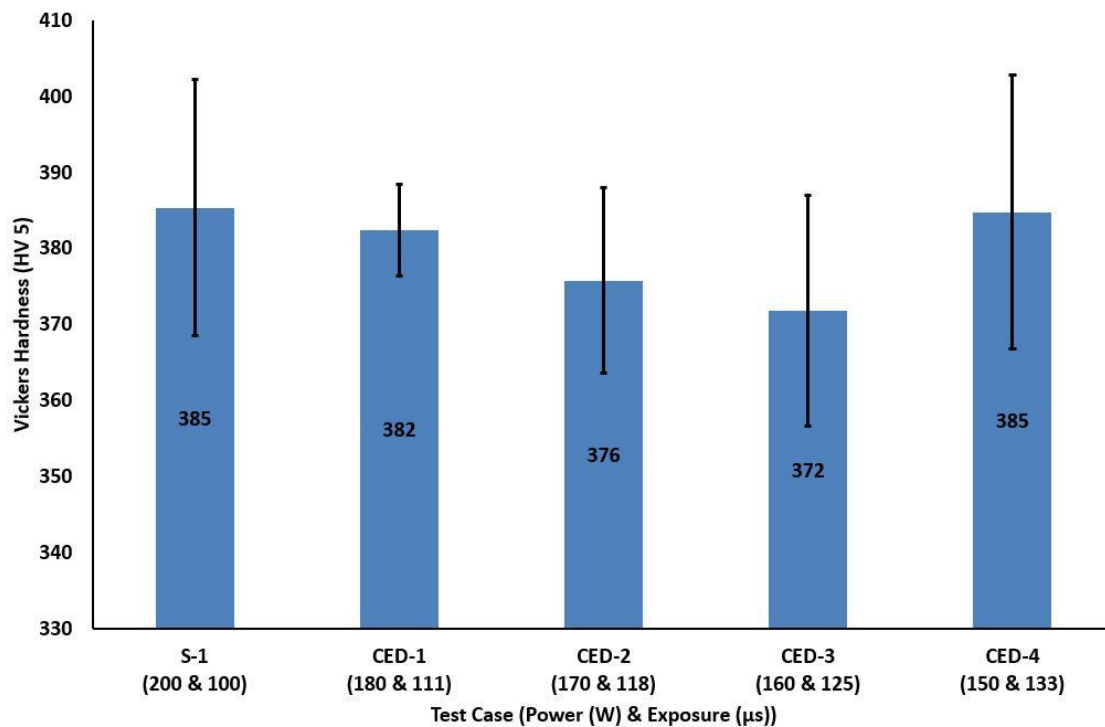


Figure 5-28 Effect of varying power and exposure time combination for a constant energy density on Vickers Hardness

Cross sectioned residual stress blocks were used for hardness analysis, after residual stress measurement. Results of hardness tests for samples created with different combinations of power and exposure for constant Energy Density are presented in Figure-5.28. Figure-5.28 shows no variation in Vickers hardness between the standard test case S-1, built with optimum of power and exposure from density optimisation trials (see section-5.1) and samples built with decreased power and increased exposure combinations. Therefore based on the hardness results the choice of using test case CED-4, power and exposure combination in the strategic residual stress reduction in a complex geometry, is still a sensible choice.

5.7 Effect of Bed Pre-Heat Temperature

Using the optimum combination of parameters found from the density optimisation trials for 50 μ m layer thickness (see section-5.1), 30x30x10mm Ti6Al4V blocks were manufactured for residual stress measurement, using different bed Pre-Heat temperatures.

5.7.1 Effect of Be Pre-Heat Temperature on Porosity and Microstructure

Residual stress blocks were cross sectioned for further analysis, after residual stress measurement. Results of porosity analysis on samples created with different Bed Pre-Heat Temperatures are presented in Figure-5.29. Figure-5.29 shows that there was no considerable variation in porosity with changing Bed Pre-heat Temperature and all temperature test cases resulted in nearly fully dense blocks.

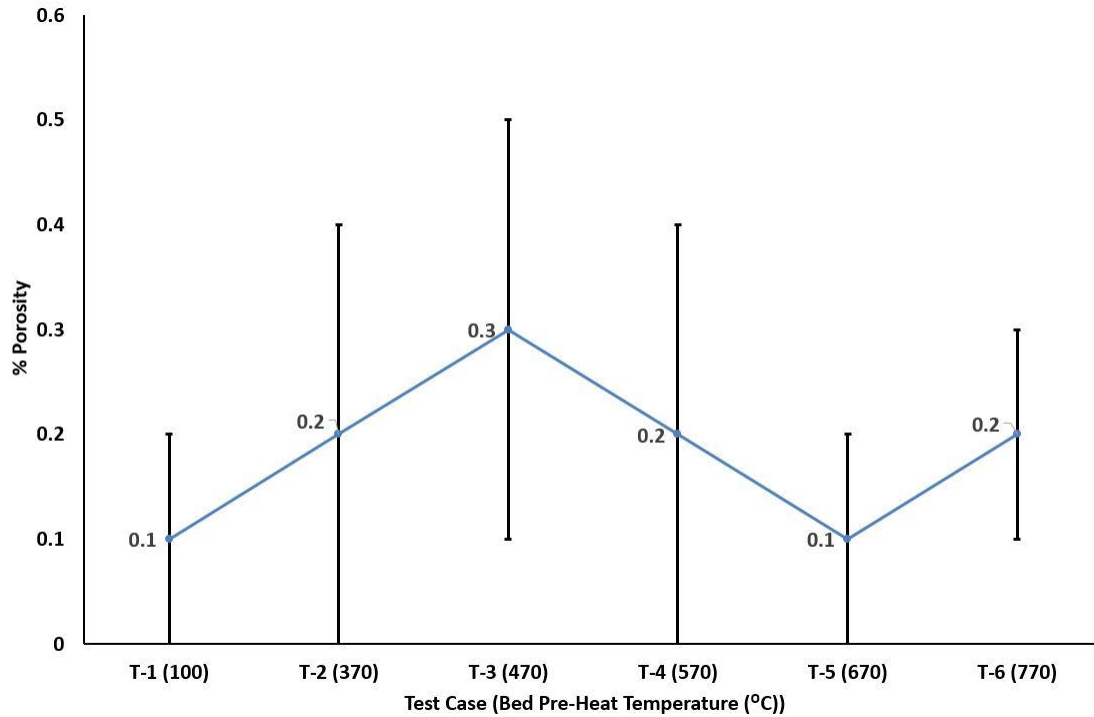


Figure 5-29 Effect of bed pre-heat temperature on % porosity

Samples prepared for porosity analysis were etched with Kroll's etching reagent to understand the effect of varying Bed Pre-Heat Temperature, on the microstructure. The 5X optical micrograph of Test case T-1, built at 100°C bed pre-heat temperature is shown in Figure-5.30(a). Test case T-1 has completely martensitic microstructure with martensitic α' laths within prior columnar β grains. The 5X optical micrograph of test case-T6 built at 770°C is shown in Figure-5.30(b). Test case T-6 shows that even at the highest bed pre-heat temperature used in this study, prior β grains are still present in the samples. It can be seen from Figure-5.30 that prior columnar β grains extending over multiple layers is a characteristic of SLM Ti6Al4V and

irrespective of the bed temperature, prior columnar β grains are present in all samples.

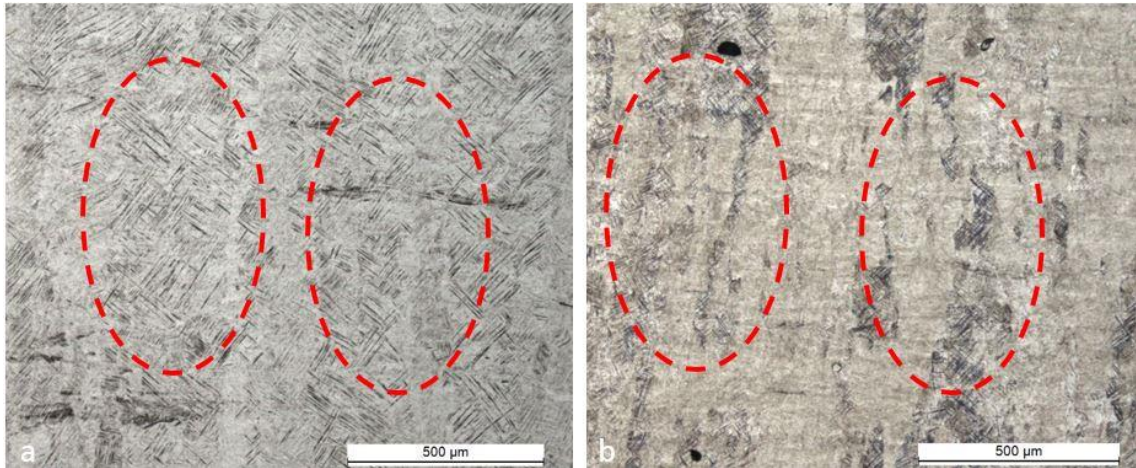


Figure 5-30 (a) Test Case T-1 (100°C) displaying prior β columnar grains. (b) Test Case T-6 displaying prior β columnar grains (770°C).

Figure-5.31 shows the microstructure of test case T-1 built at 100°C bed pre-heat temperature and test case T-2 built at 370°C. The optical micrographs in Figure-5.31(a) and (c) shows a martensitic microstructure for both test cases T-1 and T-2. Higher magnification SEM micrographs Figure-5.31(b) and (d), show that increasing the bed temperature to 370°C, test case T-2, resulted in an increase in α' lath size, as shown by the dashed ellipse. Arrows in Figure 31(d) indicate that white β particles have started forming between the α' laths in samples built for test case T-2. Some α' may also have transformed into equilibrium α .

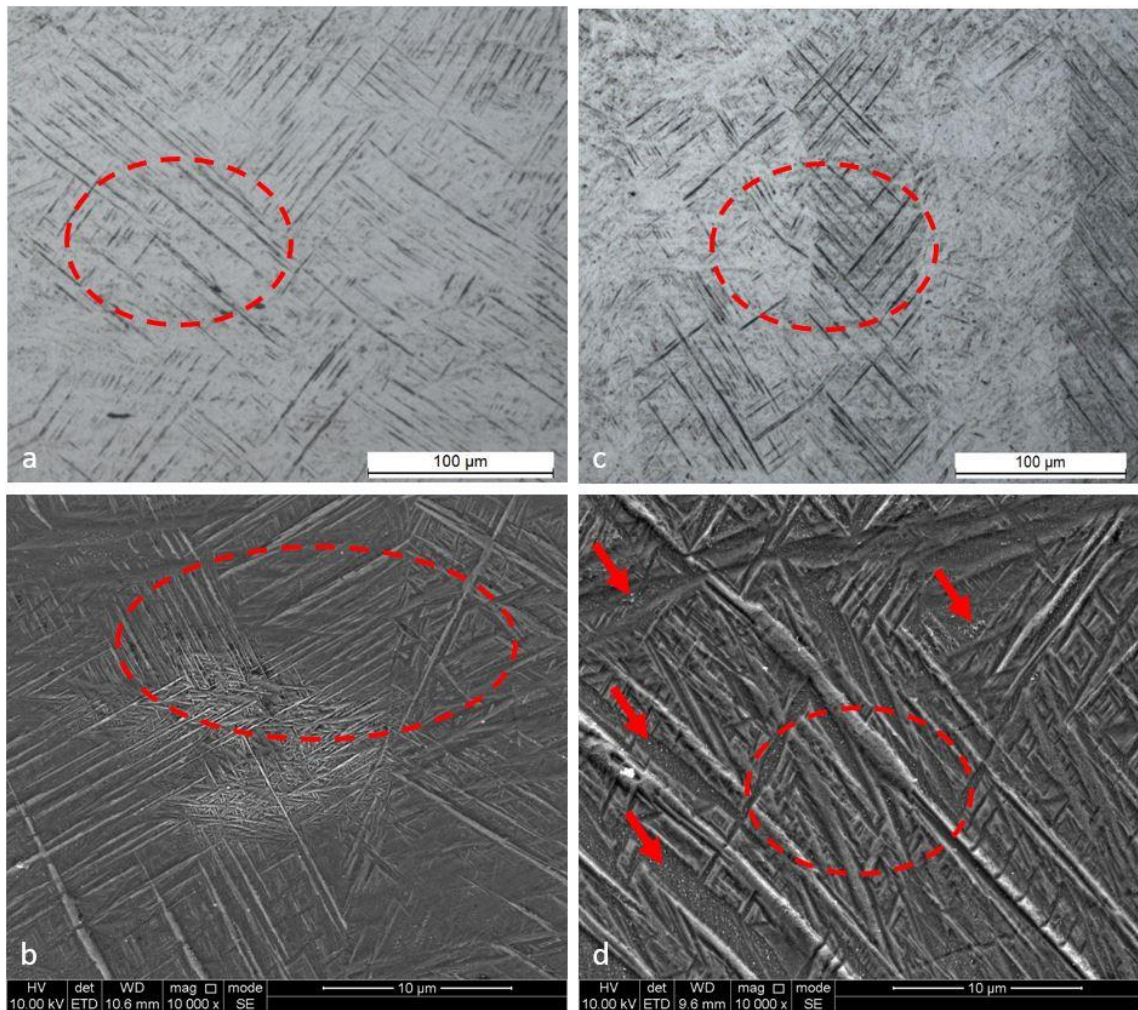


Figure 5-31 Martensitic microstructure of the samples in (a) Test Case T-1 (100°C) with (b) showing different α' lath sizes (c) α' laths in prior β grains in Case T2 (370°C). (d) Test Case T-2 shows growth in α' laths size (ellipse) and white β particles starting to form between α' laths shown by the arrows.

Figure-5.32(a) shows that increasing the bed temperature to 470°C, test case T-3 resulted in a martensitic microstructure with a considerable α' decomposition into equilibrium α , highlighted by the red circles. The SEM micrographs of Figure-5.32(b), show that raising the bed temperature to 470°C led to an increase in the lath

size compared with test case T-2. Test case T-3 also shows an increase in the amount of β between the α'/α laths compared to T-2.

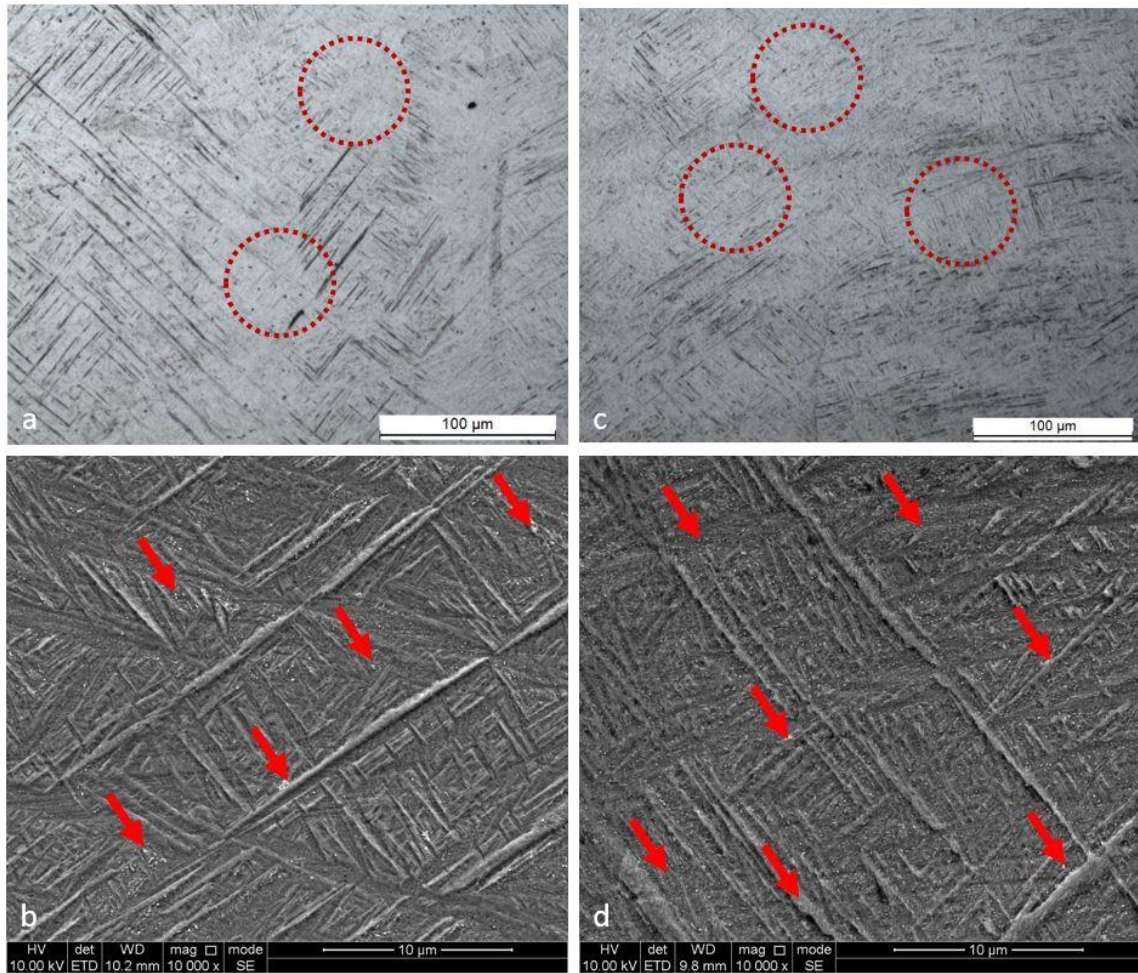


Figure 5-32. (a) Test Case T-3 (470°C) shows decreases in α' martensitic laths due to decomposition into α , highlighted by red circles. (b) Test Case T-3, shows white β particles growing between α/α' laths (indicated by the arrows). (c) Test Case T-4 (570°C) shows α' martensite has decomposed into equilibrium basketweave $\alpha+\beta$ microstructure, highlighted by red circles. (d) Test Case T-4 shows β growing between α laths and β starting to grow inside α laths (indicated by arrows).

Test case T-4 samples were built a bed temperature of 570°C just below the Ti6Al4V martensitic decomposition range of 600-650°C. Figure-5.32(c) show that there is no martensite phase present within test case T-4 samples. The α colonies within the basketweave microstructure of the test case T-4 sample are highlighted by red circles in Figure-5.32(c). The grain boundary β between α colonies is indicated by arrows in Figure-5.32(d). Samples built at 570°C, show an increase in lath size and the amount of β between α laths (see Figure-5.32(d)), compared to samples produced at lower bed temperatures. Another important feature in test case T-4, samples is the formation of nano β inside α laths.

Increasing the bed temperature to 670°C, Test Case T-5, Figure-5.33(a) resulted in an increase in α lath size. Red rectangles in Figure-5.33(a) highlight the start of grain boundary α globulorisation in samples built at 670°C, bed pre-heat temperature. The amount of white β particles between α laths and nano β particles growing inside α laths show an increase in samples for test case T-5(see Figure-5.33(b)).

Figure-5.33(c) shows a further increase in α lath size as well as globular grain boundary α , for test case T-6, samples built at 770°C bed pre-heat temperature. The amount of white β particles between α laths and nano β particles growing inside α laths shows a further increase in samples for test case T-6, highlighted by the red arrows in Figure-5.33(d).

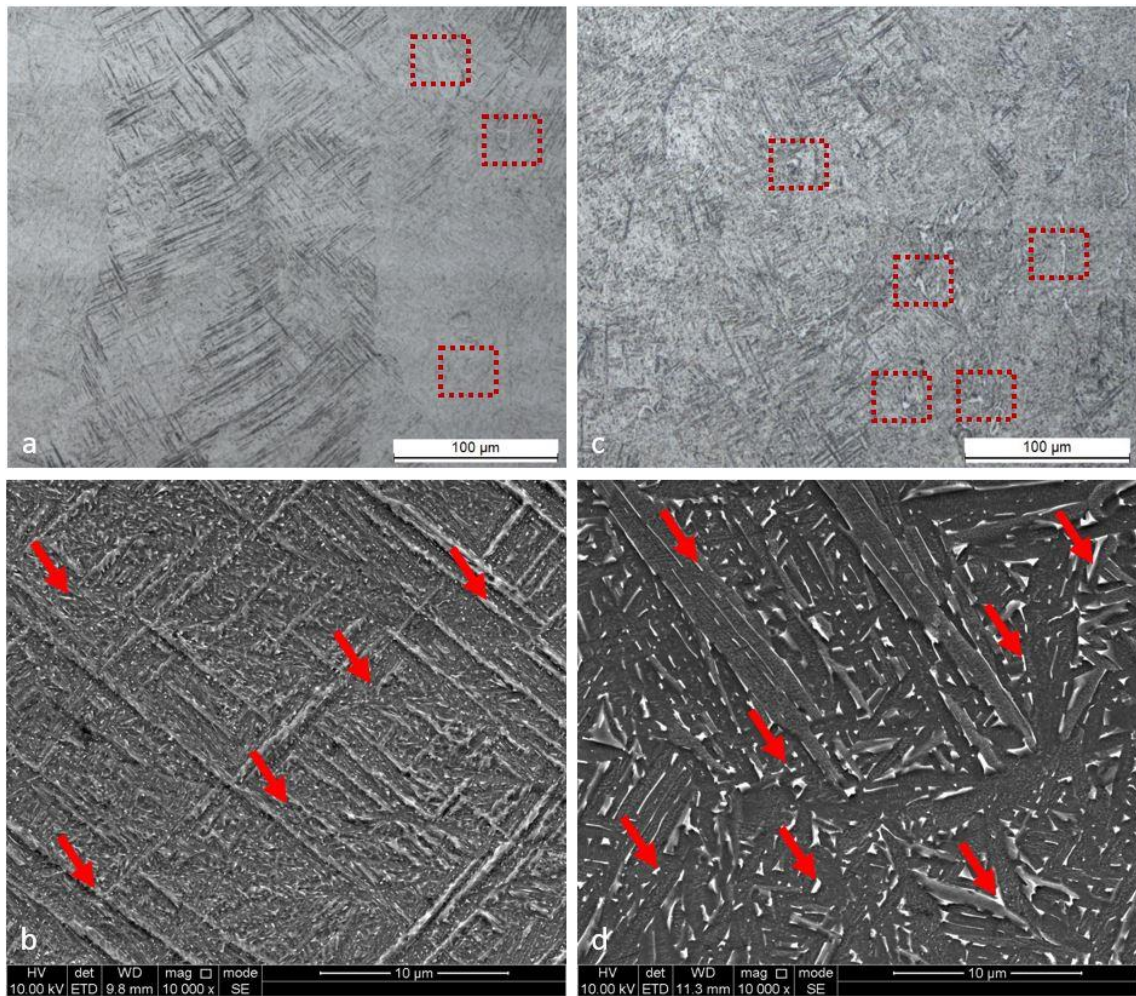


Figure 5-33. (a) Test Case T-5 (670°C), showing the start of grain boundary α globulorisation, highlighted by the red rectangles. (b) Test Case T-5 showing the growth in white β particles between and inside α laths (indicated by the red arrows). (c) Test Case T-6 (770°C) shows an increase in globular α , highlighted by the red rectangles. (d) Test Case T-6 shows an increase in grain boundary β and β inside α laths (indicated by the red arrows).

The results in Figure-5.33, show that bed pre-heat temperatures of 670°C and 770°C led to a considerable increase in α lath and colony size. Higher bed temperatures have also led to an increase in the amount of β phase growing between α lath

colonies. The growth of nano β particles inside α laths as well as grain boundary globular α has also increased with raising the bed temperature (670°C and 770°C).

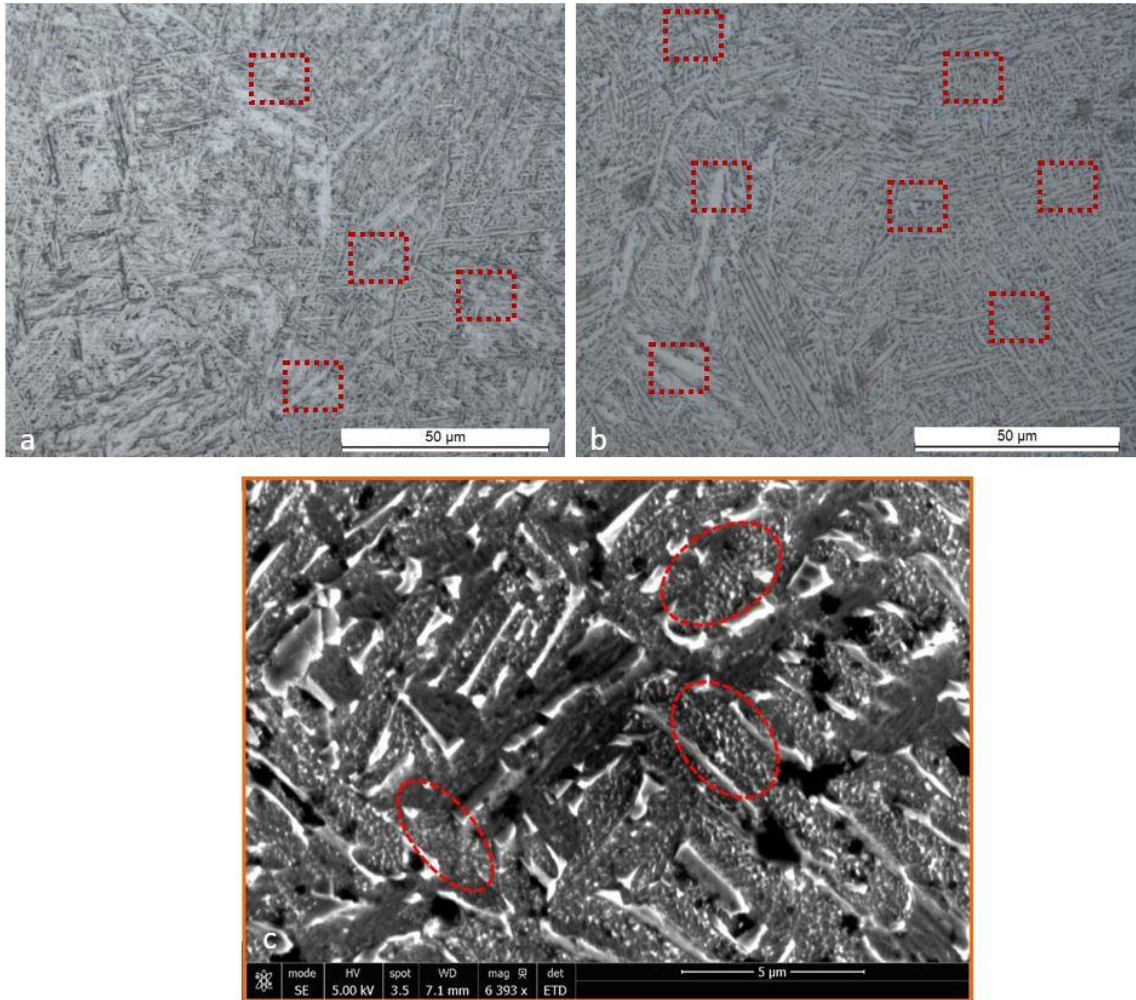


Figure 5-34(a) Optical micrograph of 670°C sample at 200X showing globular α highlighted by red rectangles. (b) Optical micrograph of 770°C sample at 200X showing globular α highlighted by red rectangles. (c) SEM secondary image of 770°C sample showing nano β -particles inside α -laths highlighted by red ellipses.

The start of grain boundary α globulorisation is highlighted by red rectangles in Figure-5.34(a), samples built with a bed pre-heat temperature of 670°C. Figure-

5.34(b) shows that raising the bed pre-heat temperature to 770°C, enhanced this effect of grain boundary α globulorisation, where red rectangles highlight globular α grains. Figure-5.34 (a) and (b) also show that a wide size range of α laths exists in samples built at 670°C and 770°C bed temperatures. Nano β particles growing inside α laths are highlighted by the red ellipses in Figure-5.34(c), for samples built at 770°C. White nano β particles first appeared in samples built at 570°C and increased further with increasing bed pre-heat temperatures.

5.7.2 Effect of Bed Pre-Heat Temperature on Residual Stress

Residual stress was measured on the 30x30x10mm test blocks manufactured at different bed pre-heat temperatures using optimum combination of parameters from density optimisation trials, by means of the air-brasive hole drilling and strain gauge method. Figure-5.35 shows a clear inverse relation between bed pre-heat temperature and residual stress. Test case T-1, standard samples built at 100°C bed pre-heat temperature resulted in 214MPa residual stress. Increasing the bed temperature to 370°C, test case T-2, resulted in 71.5% reduction in residual stress compared to test case T-1. Increasing the bed temperature to 470°C, test case T-3, resulted in a further decrease of 59% compared with test case T-2 and the residual stress was 88.3% lower compared with standard samples built at 100°C. Increasing the bed temperature to 570°C, just below Ti6Al4V martensitic decomposition range of 600-650°C for test case T-4 resulted in samples with practically no residual stress.

Further increase in bed temperature to 670°C for test case T-5 and 770°C for test case T-6 also resulted in practically no residual stress in the samples as well.

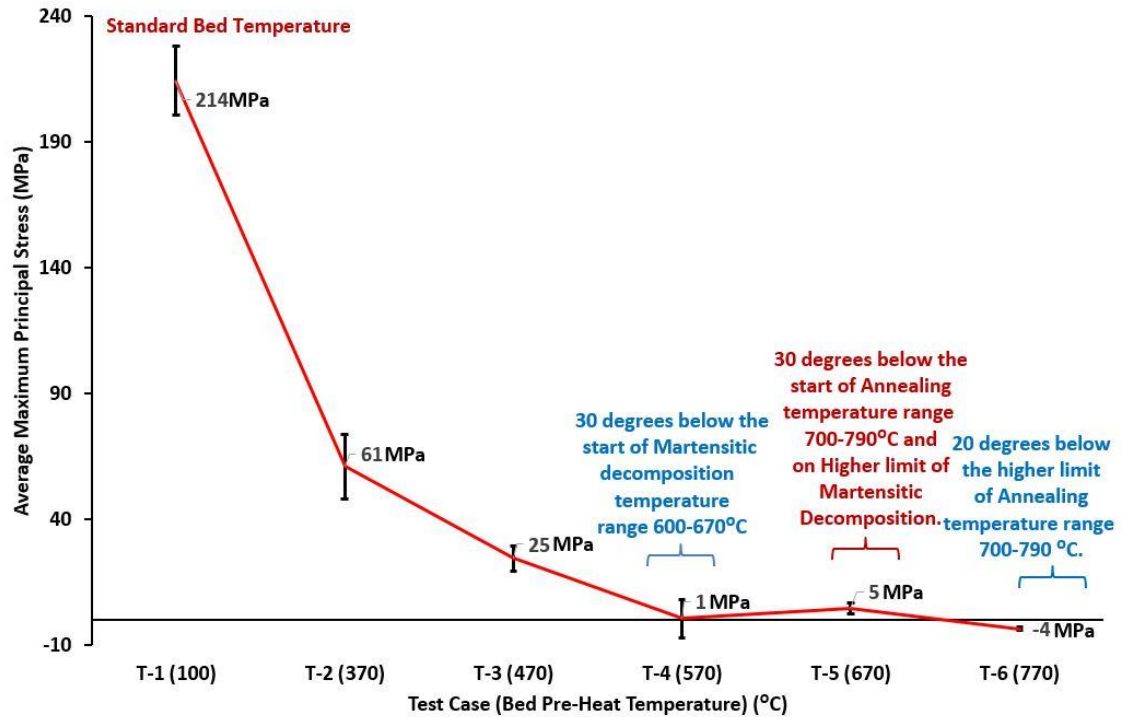


Figure 5-35 Effect of bed pre-heat temperature on residual stress

5.7.3 Effect of Bed Pre-Heat Temperature on Mechanical Properties

Mechanical properties were measured using dog bone specimens manufactured at different bed pre-heat temperatures, using the optimum combination of parameters from density optimisation trials by means of tensile testing. Figure-5.36 shows consistent UTS values up to a bed temperature of 570°C, test case T-4. Increasing the bed temperature to 670°C, test case T-5 recorded a slight decrease of 2.6% in

UTS, compared with samples built at lower bed temperatures. Samples built at 770°C, test case T-6 recorded a sharp drop of 39.3% in UTS, compared with the standard samples, test case T-1, built at 100°C bed pre-heat temperature.

Figure-5.36 shows that the yield strength values remained consistent up to a bed temperature of 670°C, test case T-5 with only a slight increase of 3% compared with standard samples built at 100°C, test case T-1. Increasing the bed temperature to 770°C for test case T-6 resulted in no yield strength values due to pre-mature failure of the test samples.

Figure-5.36 shows a clear increase in %elongation with bed pre-heat temperature. For test case T-1, samples built at 100°C bed temperature, resulted in 6.01% elongation. Increasing the bed temperature to 370°C for test case T-2, increased the elongation by 57.7% compared with T-1. Test case T-3, built at 470°C, noted a further increase of 2.6% compared with test case T-2 and compared with the standard samples of test case T-1 the elongation was higher by 61.9%. A bed pre-heat temperature of 570°C for test case T-4 resulted in the highest %elongation of 9.99, which was 66.2% higher than the elongation of the standard samples built at 100°C. Increasing the bed temperature to 670°C for test case T-5 resulted in a sharp decline in elongation by 74.7% compared with test cas-T-4 (samples with the highest recorded elongation) and the elongation was 57.9% lower than standard samples of test case T-1. With a bed temperature of 770°C, test case T-6 did not record any elongation due to the premature failure of the test samples.

The results in Figure-5.36, therefore show that a bed temperature of 570°C yielded the highest mechanical properties. Considering the mechanical properties along with residual stress results (see-section 5.7.2), a bed pre-heat temperature of 570°C was used for investigating the geometrical dependence of residual stress.

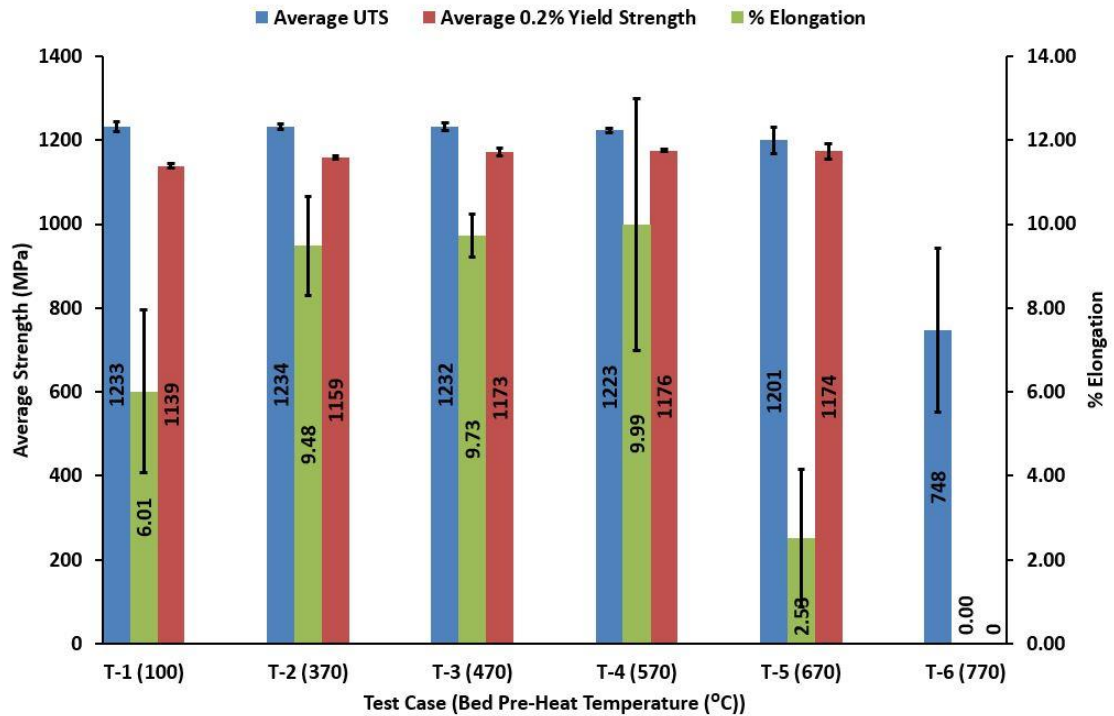


Figure 5-36 Effect of bed pre-heat temperature on UTS, Yield Strength and % Elongation

Cross sectioned residual stress blocks were used for micro hardness analysis, after residual stress measurement. Results of micro Vickers hardness test for samples created at different bed pre-heat temperatures using the optimum combination of parameters from density optimisation trials are presented in Figure-5.37.

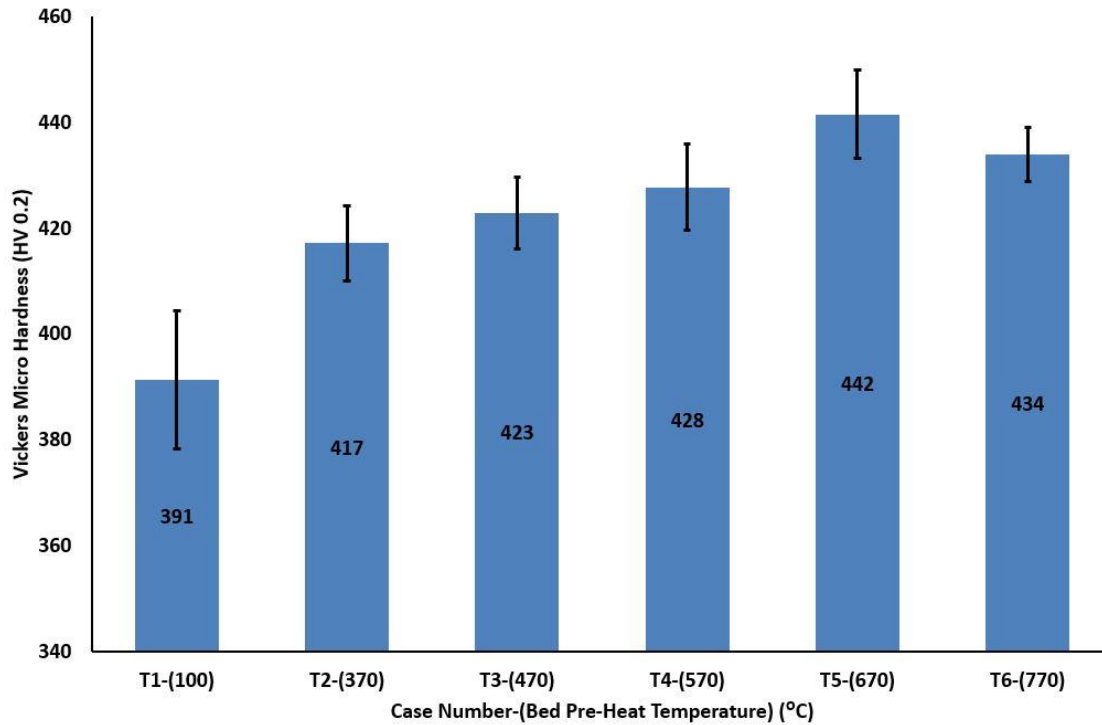


Figure 5-37 Effect of bed pre-heat temperature on Vickers Micro Hardness

Figure-5.37 shows a clear increasing trend in Vickers micro hardness with increasing bed pre-heat temperature. The standard samples test case T-1, built at 100°C bed pre-heat temperature resulted in 391 HV0.2, Vickers micro hardness. Increasing the bed temperature to 370°C for test case T-2 resulted in 6.7% increase in Vickers micro hardness compared with T-1. Test case T-3, built at 470°C resulted in a further increase of 1.4% compared with T-2 and the micro hardness was 8.2% higher compared with the standard samples built at 100°C bed pre-heat temperature. A further increase of 1.2% in micro hardness was recorded for test case T-4, samples built at 570°C compared with T-3. Bed temperature of 670°C resulted in the highest Vickers micro hardness of 442 HV0.2, 13% higher than

standard test samples T-1, built at 100°C bed temperature. Test case T-6, built at 770°C resulted in a slight decrease of 1.8% in the micro hardness compared with test case T-5 (Samples with highest Vickers micro hardness), but the values were still 11% higher than the standard samples, test case T-1. Based on the Vickers micro hardness results shown in Figure-5.37, 570°C bed pre-heat temperature is still a good choice to be used in the investigation of geometrical dependence of residual stress.

6 Discussion (Effect of Individual SLM Parameters)

6.1 SLM parameter optimisation for Ti6Al4V

SLM parameter optimisation trials for achieving nearly fully dense Ti6Al4V parts showed that a combination of 200W power and 100µs exposure, resulted in the highest density. Table-6.1 shows the part density for the range of power and exposure combinations from density optimisation trial.

Table 6-1 Part density for different power and exposure time combination

P(W)	E(µs)	60	80	100	120	140	160	180
120		90.49	95.03	98.88	99.61	99.17	99.81	99.95
140		96.57	98.5	99.52	99.37	99.05	99.17	99.06
160		98.62	99.80	99.18	99.46	99.18	98.13	96.91
180		99.25	99.84	99.89	99.56	98.95	97.59	95.69
200		99.54	99.83	99.99	99.37	98.97	97.85	94.41

Laser Energy Density input into the powder bed determines the amount of melting that can be achieved in SLM parts. Table-6.2 shows Energy Density for the range of power and exposure combinations from the density optimisation trials. From Table-6.1 and 6.2, the range of Energy Densities for achieving good melting ($\geq 99\%$ part density), for Ti6Al4V is quite wide. Energy Density between $41.54 \frac{J}{mm^3}$ to $92.31 \frac{J}{mm^3}$

resulted in nearly fully dense parts. The optimum Energy Density which resulted in 99.99% dense parts was noted to be $76.92 \frac{J}{mm^3}$ for 200W power and 100 μ s exposure. Parts built with Energy Density below $76.92 \frac{J}{mm^3}$ showed some lack of fusion porosity and parts built with higher than optimum Energy Density resulted in spherical gas porosity, a characteristic of overmelting.

Table 6-2. Energy density for different power and exposure time combination

P(W)	E(μs)	60	80	100	120	140	160	180
120		27.69	36.92	46.15	55.38	64.62	73.85	83.08
140		32.31	43.08	53.85	64.62	75.38	86.15	96.92
160		36.92	49.23	61.54	73.85	86.15	98.46	110.77
180		41.54	55.38	69.23	83.08	96.92	110.77	124.62
200		46.15	61.54	76.92	92.31	107.69	123.08	138.46

Another important aspect worth noting from Table-6.1 and 2 is the pronounced effect of power on part density. Varying the level of power affects the minimum Energy Density required for achieving greater than 99% dense Ti6Al4V SLM parts. Table-6.1 and 2 show an inverse correlation between power and the minimum Energy Density required for good melting of Ti6Al4V powder in the SLM process. It can be seen that for a power of 120W the minimum Energy Density required is $55.38 \frac{J}{mm^3}$, while increasing the power by 20W to 140W reduces the minimum

Energy Density required for good melting to $53.85 \frac{J}{mm^3}$. For a power of 180W the minimum Energy Density required for achieving nearly fully dense ($\geq 99\%$ density) parts is reduced to $41.54 \frac{J}{mm^3}$ only. Therefore it can be concluded from this analysis that power has a more pronounced effect on Ti6Al4V melting in the SLM process and the processing window for Ti6Al4V spreads over a wide range. Martensitic microstructure of SLM Ti6Al4V is a result of high cooling rates associated with the process. Columnar prior β grains is a characteristic of the layer wise melting in SLM.

6.2 Effect of Scanning Strategy

Understanding the effect of scanning strategy on SLM parts is a complex problem in itself due to the number of parameters associated with scanning strategy. Varying the size of the scan vector length, the orientation of the scan vectors, the order of scanning and the rotation of each subsequent layer can result in endless combination of scanning strategies.

In order to understand the effect of scan vector length on the temperature of the powder bed an FEA simulation with varying scan vector length was carried out to simulate six scan vectors. The temperature history of a point in the center of the surface of the first meltpool was extracted from the FEA simulation. Figure-6.1 shows the temperature variation of a single point on the top center of the first meltpool. It can be seen from Figure-6.1 that residual heat in the already scanned region decreases with increasing scan vector length. When the laser comes back to scan a region adjacent with the already sintered material it reheats the previously

solidified material. As the laser moves further from the sintered region of interest the effect of the laser on the temperature decreases.

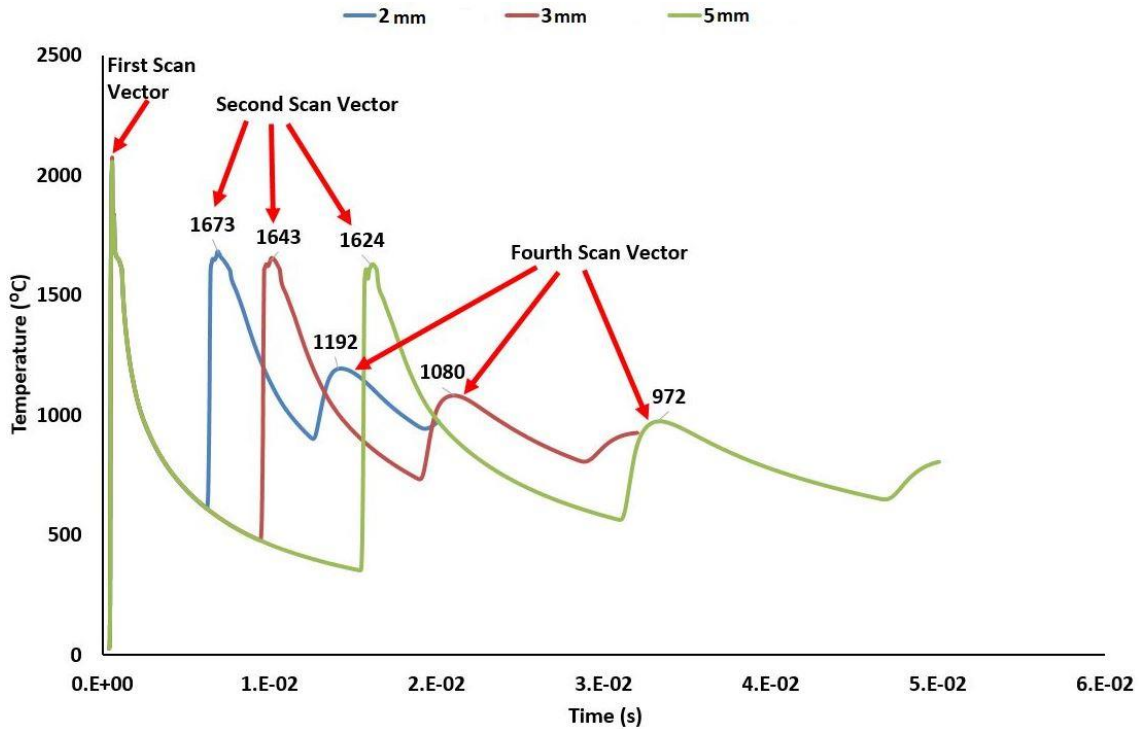


Figure 6-1 Effect of scan vector length on temperature

In order to better understand the effect of scan vector lengths on SLM parts cooling rates were calculated for the same spot based on the reheating effect from the next scan vectors. Figure-6.2 shows the effect of scan vector length on the cooling rate of the top center of the first meltpool. It can be seen from Figure-6.2 that the initial cooling rate of the meltpool is independent of the scan vector length. When the laser comes back adjacent to the point of interest in the second scan vector it reheats the already sintered material as indicated by the temperature history shown in Figure-

6.1. It can be seen that increasing the scan vector length increases the cooling rate of the reheated sintered material. The laser comes back adjacent to the point of interest in the fourth scan vector and reheats the point of interest as can be seen in Figure-6.1. It can be seen from Figure-6.1 that the cooling curve becomes less steep for the reheated sintered material with increasing scan vector length. Figure-6.2 also shows that the sintered material reheated due to the effect of the fourth scan vector adjacent to it cools more slowly with increasing scan vector length. Figure-6.1 and 6.2 show a complicated cooling behavior with varying scan vector length.

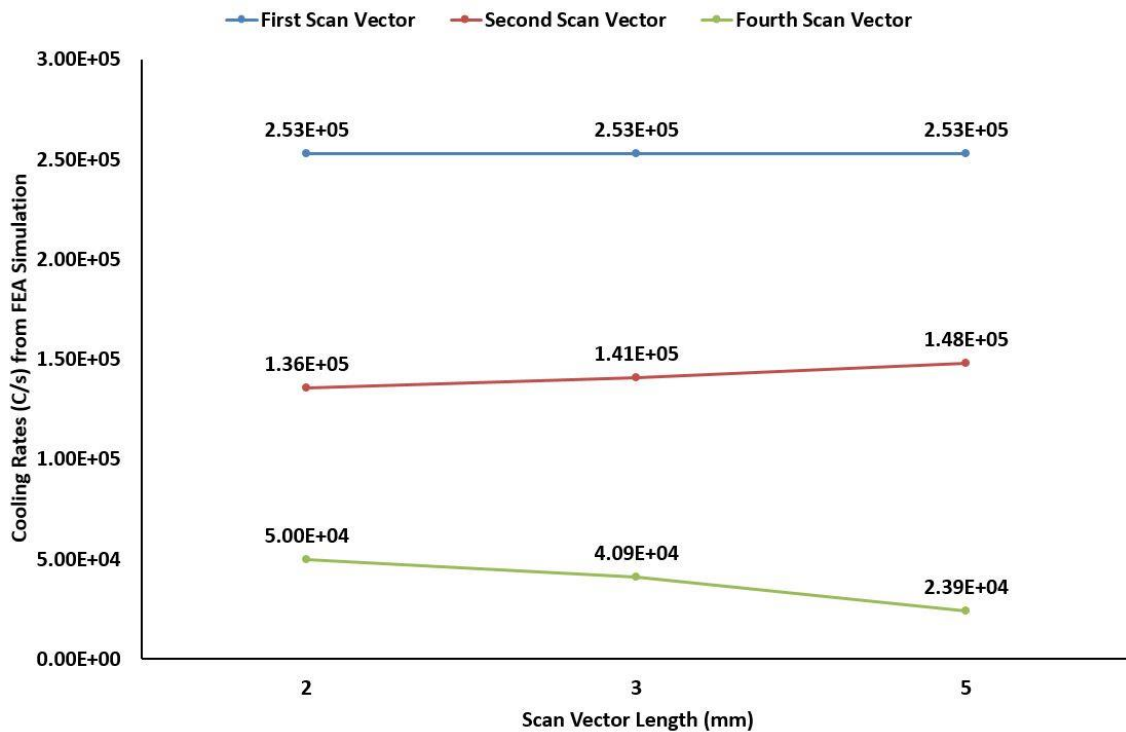


Figure 6-2 Effect of scan vector length on cooling rate

6.2.1 Effect of Scanning Strategy on Porosity and Microstructure

The porosity level in test case S-1 built with a 90° alternating strategy agrees with initial parameter optimisation trials presented in section-6.1. The decreasing trend in the % porosity with increasing scan vector length for samples built with chessboard scanning strategy, can be attributed to the fact that increasing scan vector length will result in a decrease in residual heat effect from the previous scan vector as shown in Figure-6.1 and thus a decrease in the maximum temperature. A decrease in residual heat effect due to increasing scan vector length has also been reported in ref-[44]. Test case S-2 built with a scan vector length of 2mm resulted in the highest residual heat effect due to shorter scan vectors and thus highest porosity. Increasing the scan vector length to 5mm for test case S-4 resulted in reduced residual heat effect from the previous scan vector and thus the porosity level has decreased to 0.2%. The reason for a decrease in %porosity to 0.1 when the scan vectors are rotated by 90°, in adjacent chessboard squares for test case S-5, for 5mm scan vectors is unclear as no change in residual heat effect compared to test case S-4 would be expected.

Even though the cooling rates are lowered with decreasing scan vector length they are still much higher than the cooling rate required for fully martensitic microstructure in Ti6Al4V. According to ref-[124], cooling rates higher than $410 \frac{^{\circ}\text{C}}{\text{s}}$ leads to fully martensitic microstructure for Ti6Al4V. Therefore irrespective of scanning strategy, samples from all test cases S-1 to S-5 resulted in fully martensitic microstructure with martensitic α' laths growing inside columnar prior β grains.

6.2.2 Effect of Scanning Strategy on Residual Stress

The effect of scanning strategy on residual stress is very complicated and as shown in section-2.6 the results shown in published literature show varying effects of scan vector length and rotation on residual stress. The cooling rates estimated from FEA simulation shown in Figure-6.2 also confirm the complexity of the relationship between scanning strategy and material behavior. An island scanning strategy has been proposed as a means of residual stress reduction in SLM components by many researchers [4, 43, 49]. This work used different chessboard squares sizes to see the effect of chessboard scanning strategy on residual stress but 90° Alternating strategy proved to be the best for achieving minimum residual stress.

Since the results contradicted the popular conception of chessboard scanning strategy being better for residual stress reduction in SLM parts, a different machine (Renishaw SLM125 at the University of Sheffield) was used to analyse the effect of scanning strategy on residual stress. Only 90° alternating and 5x5 chessboard scanning strategies were tested on the SLM125 samples. In order to make sure that enough parameters have been changed, the sample size was chosen to be 25x25x10mm instead of the 30x30x10mm used for samples built on the Renishaw AM250 machine at TWI, South Yorkshire. Instead of using the optimum combination of parameters of 200W power and 100µs exposure for these samples a power of 120W and exposure of 180µs was used. It can be seen from section 6.1 that these set of parameters lie at the other end of the parameter optimisation array but still resulted in 99.95% dense parts. To further clarify the effect of scanning strategy on

residual stress 25x25x10mm samples were also built at a bed pre-heat temperature of 470°C on a custom designed heated bed used in the Renishaw SLM125 machine using 90° alternating and 5x5 chessboard scanning strategies. Figure-6.3 shows that samples built at 100°C bed pre-heat temperature on the standard Renishaw SLM125 machine resulted in 179MPa residual stress using 5x5 chessboard scanning strategy while 90° alternating scanning strategy resulted in 43.6% lower residual stress in the 25x25x10mm samples built with 120W power and 180µs exposure.

Raising the bed temperature to 470°C resulted in a decrease in residual stress for both scanning strategies as shown in Figure-6.3. It can be seen that 5x5 chessboard scanning strategy resulted in 100MPa residual stress in the samples built at 470°C bed pre-heat temperature while 90° alternating scanning strategy resulted in only 63MPa residual stress in the higher temperature samples.

Even though the relationship between scanning strategy and its effect on residual stress could not be established it will require a more detailed investigation to properly understand the effect of scanning strategy on residual stress, it was established from this work that 90° alternating scanning strategy results in lower residual stress in SLM parts built on Renishaw SLM machines. Therefore for the rest of this work 90° alternating scanning strategy was used for all samples.

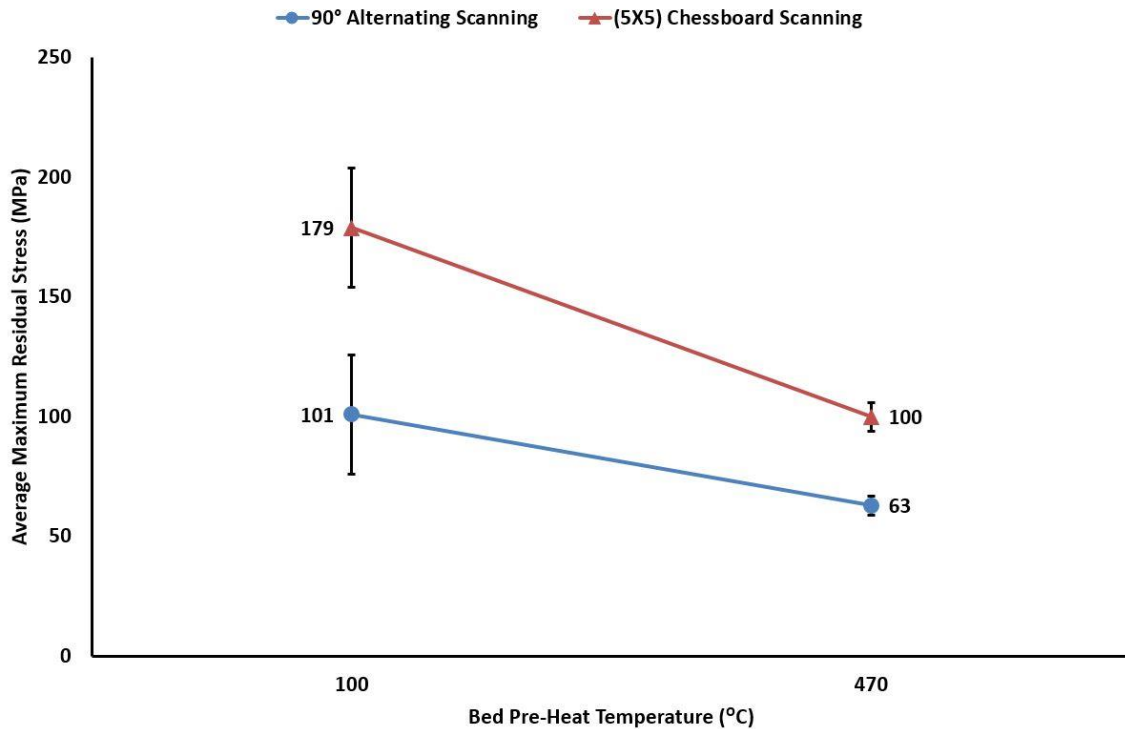


Figure 6-3 Effect of scanning strategy on residual stress in 25x25x10mm samples built at different bed pre-heat temperatures using Renishaw SLM125 machine.

Note: All the residual stress measurements reported in this work were taken on the top surface of the SLM manufactured Ti6Al4V blocks using hole drilling method. Hole drilling measures bi-axial residual stress. The measurements in this work were taken in the XY plane on sample blocks removed from the substrate. The residual stress values in this work should not be directly compared to values in published literature without taking into consideration that samples removal from substrate results in partial relaxation and redistribution of the residual stress state in SLM samples. The extent of residual stress relaxation on removal from substrate can be assessed by taking residual stress measurements on samples manufactured with same parameters set both in the attached and detached state.

6.2.3 Effect of Scanning Strategy on Mechanical Properties

It can be seen from Figure-6.4 that the scanning vector length or rotation does not affect the yield strength of SLM Ti6Al4V samples considerably and the small variation can be attributed to the stochastic nature of the process. The chessboard scanning strategy did not show any clear trend in % elongation values with increasing chessboard squares size. Figure-6.4 also shows that there is no clear correlation between % elongation and % porosity. Even though test case S-3 has lower porosity than S-2, it also has low elongation. The porosity decreases only slightly for test case S-4 and S-5 but there is a considerable improvement in elongation. Therefore it is not possible to establish any clear relationship between porosity and elongation.

Similarly the cooling rates for reheated sintered material from subsequent scan vectors presented in Figure-6.2 also does not show any clear relationship with the elongation of the SLM Ti6Al4V samples. Therefore it requires a more detailed work focussed on scanning strategy to understand its effect on mechanical properties of SLM components.

Scanning strategy did not have any considerable effect on the Vickers hardness of the samples as all the samples had similar martensitic microstructures.

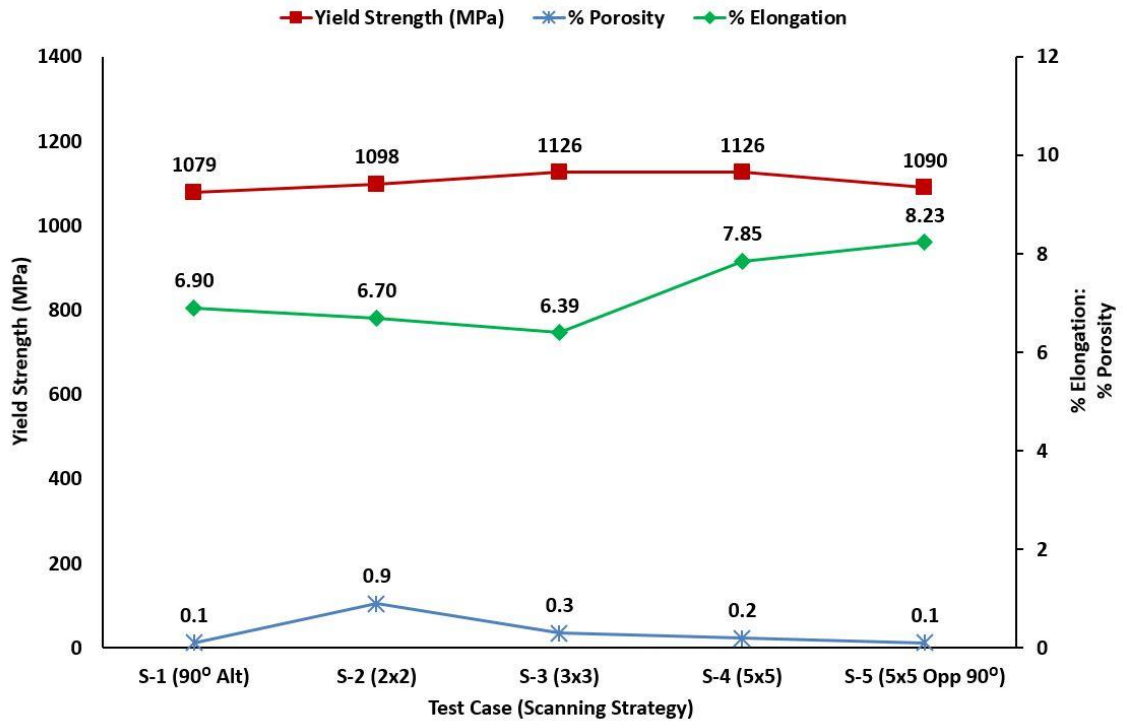


Figure 6-4. Relationship between scanning strategy % Porosity, % Elongation and Yield Strength.

6.3 Effect of Layer Thickness

In order to understand the effect of layer thickness on residual stress and mechanical properties, FEA simulation with different layer thicknesses was used to estimate the effect of layer thickness on cooling rates.

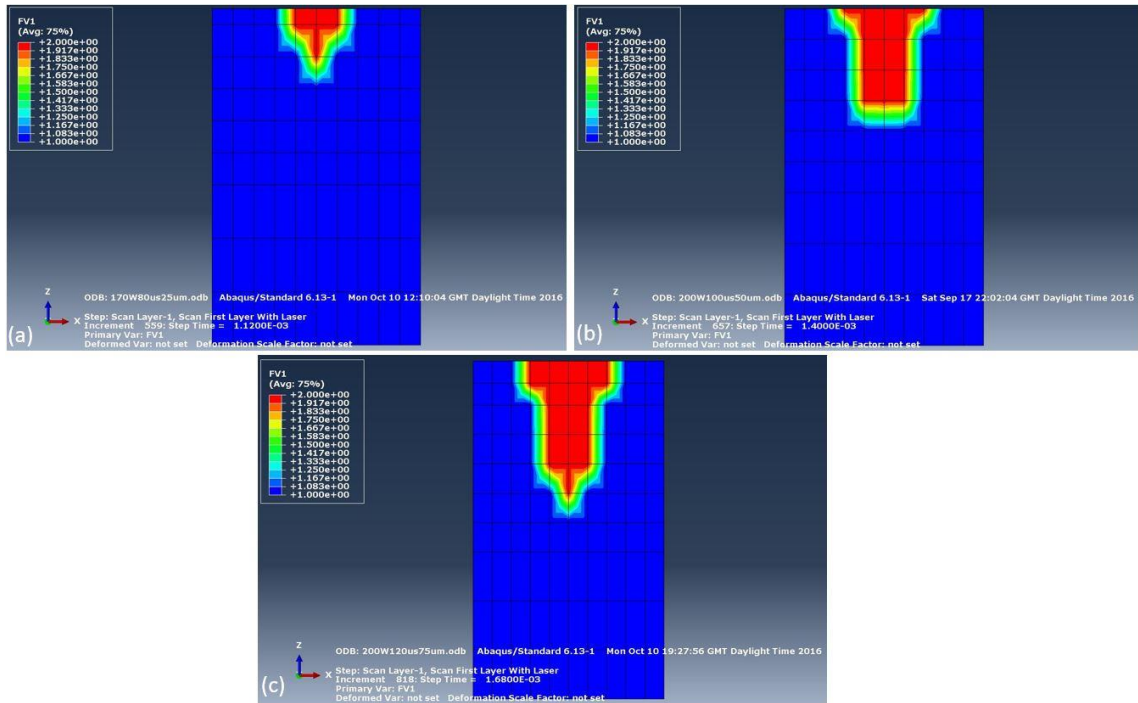


Figure 6-5. Effect of layer thickness on melt pool dimensions (a) Test Case LT-1 (25µm Layer Thickness). (b) Test Case LT-2 (50µm Layer Thickness) and (c) Test Case LT-3 (75µm Layer Thickness)

Figure-6.5 shows a direct relation between layer thickness and melt pool size. Increasing layer thickness results in a larger melt pool. A larger melt pool means more material to cool and thus a reduced cooling rate. Figure-6.6 shows that there is an inverse relationship between layer thickness and cooling rates. Increasing layer thickness results in lowering the cooling rates.

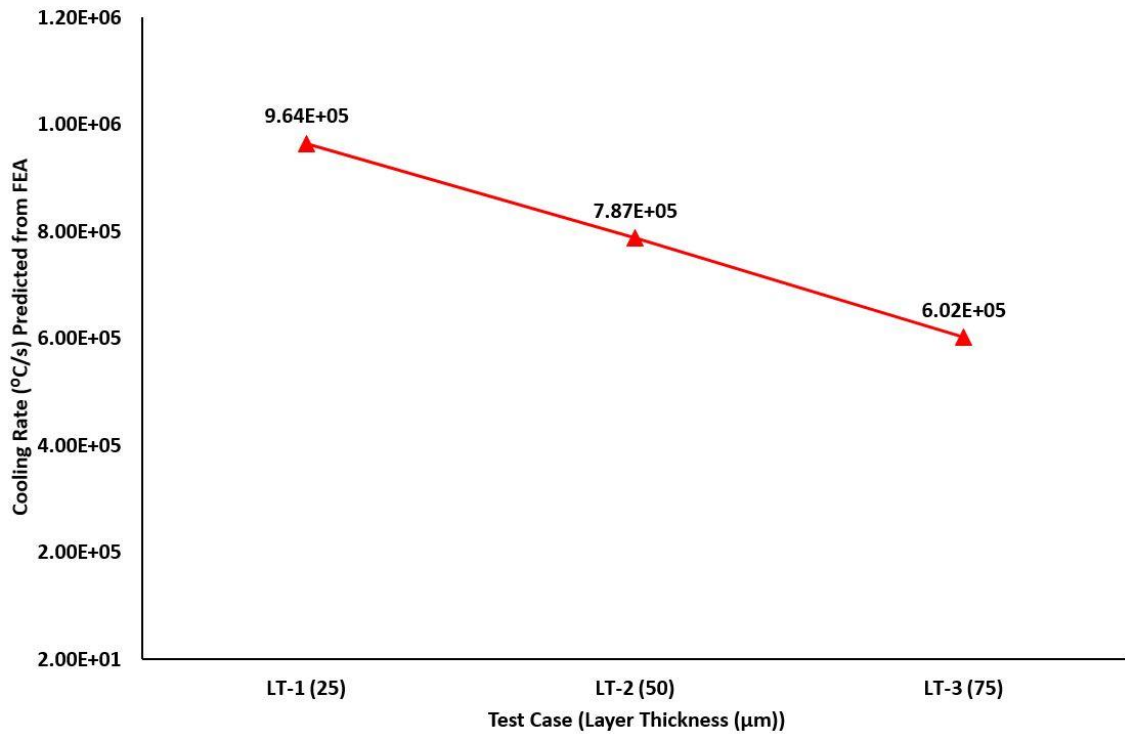


Figure 6-6 Effect of layer thickness on cooling rates

6.3.1 Effect of Layer Thickness on Porosity and Microstructure

Increasing layer thickness resulted in an increase in porosity even though the parameters were optimised separately for each layer thickness. Figure-6.7 shows optical images for inter layer defects and it can be seen that with increasing the layer thickness the amount of inter layer defects increases. This increase in inter layer defects has led to an increase in %porosity with increasing layer thickness.



Figure 6-7 Inter layer defects (a) LT-1 (b) LT-2 (c) LT-3

Figure-6.6 shows that increasing layer thickness leads to reduced cooling rates. Even though the cooling rates are lowered with increasing layer thickness, they are still much higher than the cooling rate required for a fully martensitic microstructure in Ti6Al4V. According to ref-[124], cooling rates higher than $410 \frac{^{\circ}\text{C}}{\text{s}}$ leads to a fully martensitic microstructure for Ti6Al4V. Therefore irrespective of the layer thickness samples from all test cases LT-1, LT-2 and LT-3 resulted in fully martensitic microstructure with martensitic α' laths growing inside columnar prior β grains.

6.3.2 Effect of Layer Thickness on Residual Stress

Figure-6.8 shows that increasing layer thickness results in increasing the peak temperature in the melt pool. Test case LT-1 was built with 170W power and 80 μs exposure, resulting in an Energy Density of $104.62 \frac{\text{J}}{\text{mm}^3}$. Test case LT-2 was built with 200W power and 100 μs exposure, resulting in an Energy Density of $76.92 \frac{\text{J}}{\text{mm}^3}$. Test case LT-3 was built with 200W power and 120 μs exposure, resulting in an Energy Density of $61.54 \frac{\text{J}}{\text{mm}^3}$. This shows that the required Energy Density for fully dense parts decreased with increasing layer thickness. The only probable explanation for

this behavior is that increasing powder layer thickness hinders the conduction of heat away to the substrate and thus more energy is retained in the powder. This leads to higher peak temperatures as shown in Figure-6.8 and larger melt pool size as shown in Figure-6.5. Another important feature from Figure-6.8 is the decrease in temperature gradient with increasing layer thickness, between the top and 50 μ m depth across a melt pool, as illustrated by the slope of the line equations. Thus according to the temperature gradient mechanism[28] and cool down phase model[28, 29], increasing layer thickness, should lead to a decrease in residual stress.

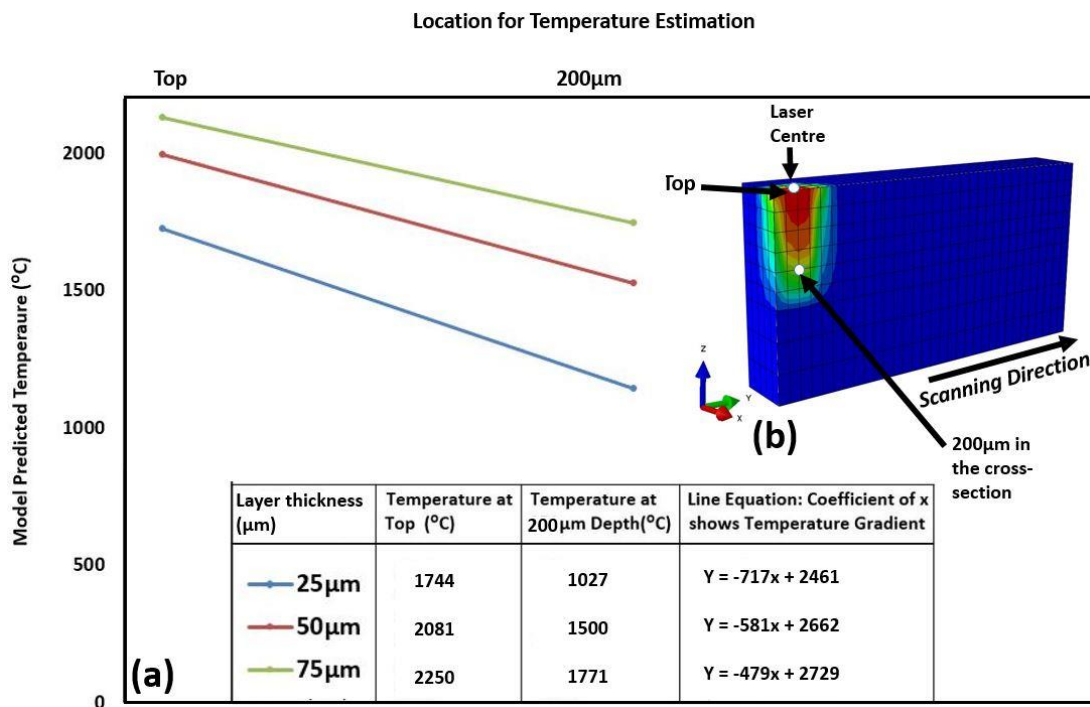


Figure 6-8 Effect of layer thickness on temperature gradient

Residual stress shows an inverse relationship with layer thickness. A decrease in residual stress with increasing layer thickness is consistent with the findings of ref-

[43], reporting a reduction in deformation of cantilever specimens with increasing layer thickness. The findings also agree with a decreasing trend in the deformation of bridge shaped specimens with increasing layer thickness reported in ref-[4]. In ref-[42], Van Belle et al also reported a reduction in the deformation of thin plates onto which powder layers were deposited with increasing layer thickness. Figure-6.9 shows that increasing layer thickness leads to a reduction in cooling rates and this decrease in cooling rates is responsible for the reduction in residual stress for samples manufactured with higher layer thickness.

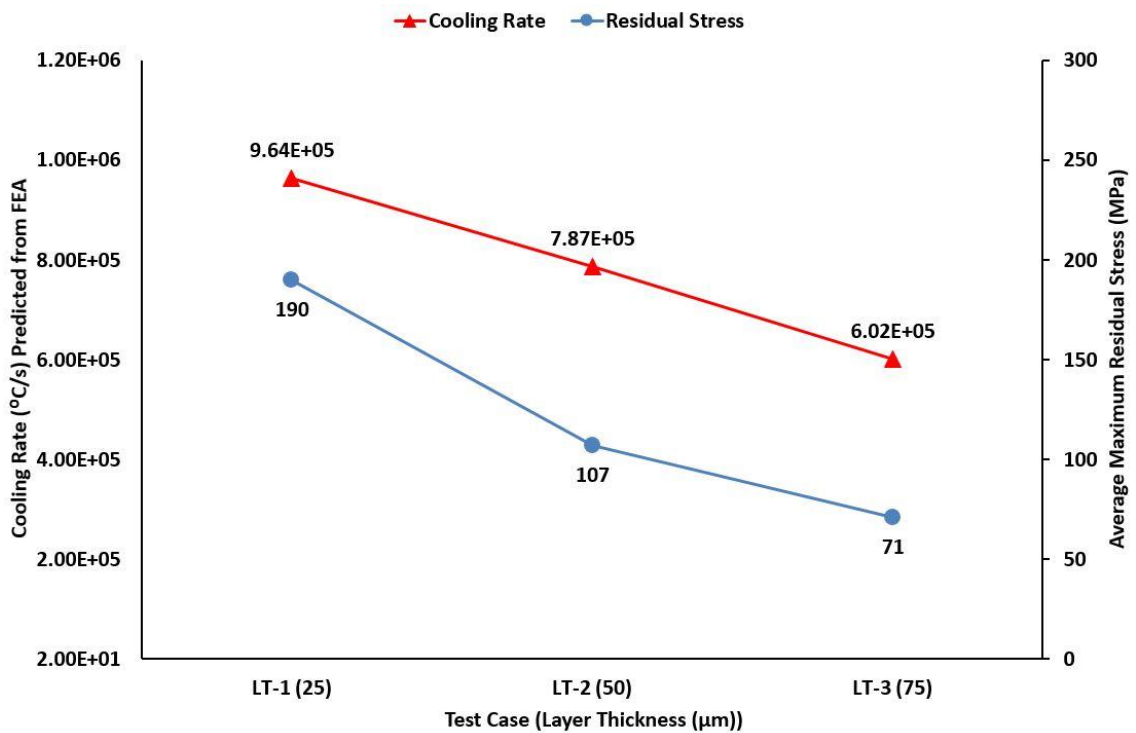


Figure 6-9 Effect of layer thickness on cooling rate and residual stress

6.3.3 Effect of Layer Thickness on Mechanical Properties

Mechanical properties show an inverse relationship with layer thickness. Increasing layer thickness leads to a reduction in the yield strength as well as % elongation of SLM samples. Figure-6.10 shows a decreasing trend in % elongation and yield strength with increasing layer thickness, while % porosity increases (see section 6.3.1)

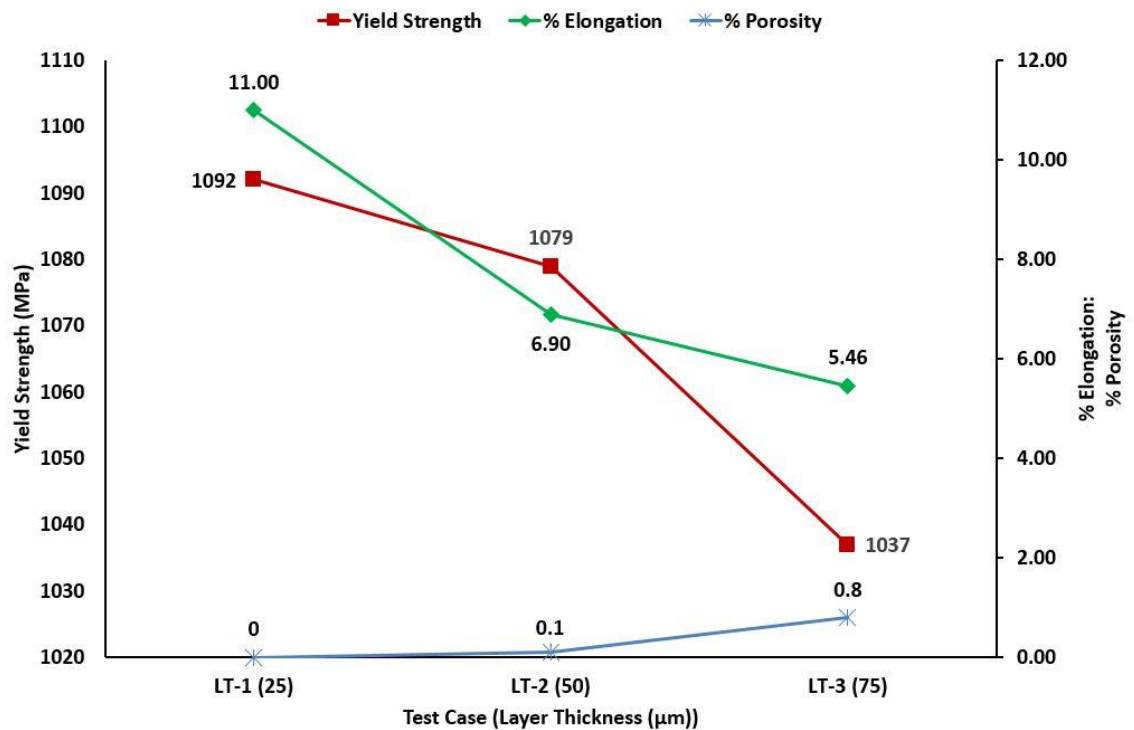


Figure 6-10 Relationship between layer thickness, % Porosity, % Elongation and Yield Strength

Figure-6.6 showed that increasing layer thickness also leads to a reduction in cooling rates. For lamellar microstructure the mechanical properties are greatly affected by

the α colony size [65, 81]. Colony size determines the effective slip length and is inversely proportional to the cooling rate from the β phase field. According to Figure-2.19(a) yield strength is inversely proportional to slip length and Figure-2.19(b) shows that yield strength grows exponentially with cooling rate, over $1000 \frac{^{\circ}\text{C}}{\text{min}}$ (air cooling). According to Manikandakumar et al [83], the mechanical properties of SLM Ti6Al4V parts depend on the α colony and α lath size. The α lath and α colony size is equal to single martensitic α' laths for a martensitic microstructure. The movement of dislocations is restricted due to the smaller α colony sizes in martensitic microstructures for SLM Ti6Al4V, which leads to limited plastic deformation in SLM Ti6Al4V components. Limited plastic deformation of SLM parts lead to higher yield strength and UTS. According to the effective slip length and dislocation movement theories [65, 81], increasing layer thickness should lead to a decrease in yield strength as increased layer thickness means slower cooling rate and thus lower yield strength. According to ref- [72], specimens can fail prematurely due to process induced porosity acting as stress concentrators. Figure-6.10 shows that increasing layer thickness leads to an increase in porosity. Therefore the increase in inter layer porosity with increasing layer thickness is another factor contributing to the reduction in yield strength with increasing layer thickness.

The relationship between cooling rates and ductility is more complex [65, 81]. According to Figure-2.19(a) decrease in slip length leads to an increase in ductility. According to Figure-2.19(b) ductility increases with increasing cooling rate up to a certain point, and beyond this point of maximum ductility, it decreases sharply with further increase in the cooling rate. The intermediate cooling rate resulting in

maximum ductility from Figure-2.19(b) is much lower than the SLM cooling rates. The cooling rate decreases with increasing layer thickness which should lead to an increase in ductility as the cooling rate is moving towards the intermediate optimum cooling rate for maximised ductility (Figure-2.19(b)). Since the ductility is decreasing despite the cooling rates moving towards the optimum, the only explanation for this decrease can be attributed to the increase in inter layer porosity with increasing layer thickness. Therefore it is valid to say that porosity defects act as stress concentrators which leads to premature failure of tensile specimens and thus results in deterioration of mechanical properties.

Figure-6.6 showed that increasing layer thickness led to a decrease in cooling rate but the cooling rates are still much higher than $410\frac{^{\circ}\text{C}}{\text{s}}$, cooling rate leading to a totally martensitic microstructure for Ti6Al4V[124]. Since all the test cases LT-1, LT-2 and LT-3 had a totally martensitic microstructure, there is no major variation in Vickers hardness values for samples manufactured with different layer thicknesses.

6.4 Effect of Re-Scanning Varying Exposure

In order to understand the effect of Re-Scanning with varying exposure times on residual stress and mechanical properties, FEA simulation with different re-scanning exposure was used to estimate the effect of re-scanning with varying exposure on cooling rates. Energy Density for re-scanning each layer was varied by keeping power constant at 200W and varying the exposure time in proportion to the optimum exposure time of $100\mu\text{s}$ (from density optimisation trials section 6.1).

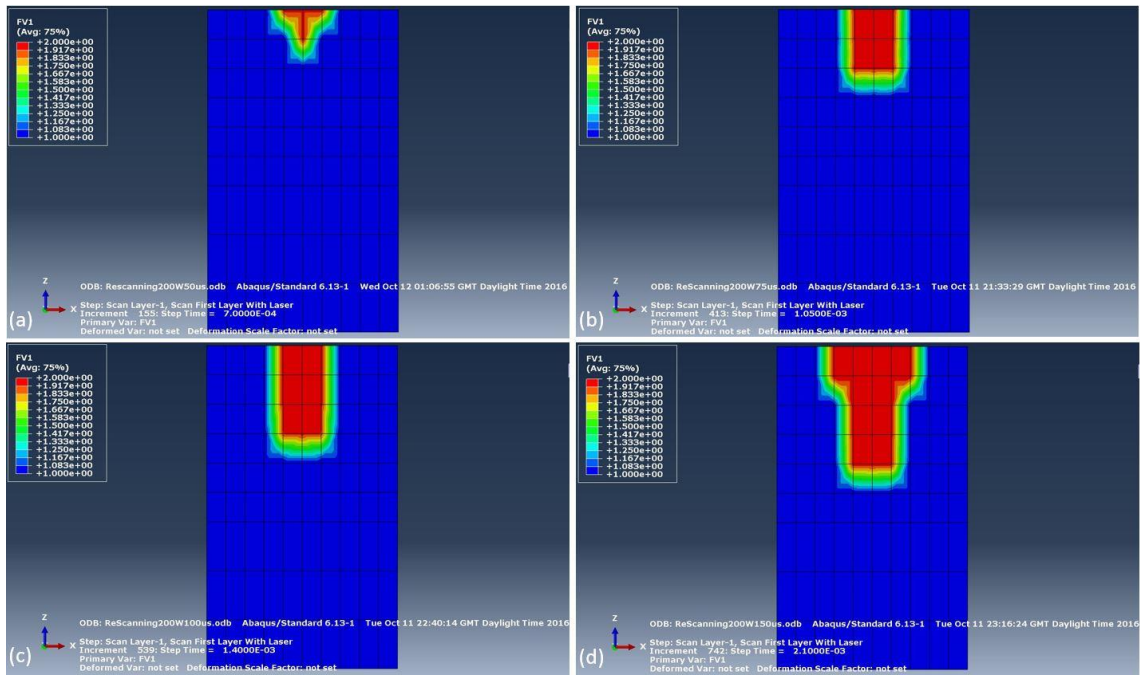


Figure 6-11 Effect of re-scanning with varying exposure on melt pool dimensions (a) Test Case RSE-1 (50 μ s Exposure), (b) Test Case RSE-2 (75 μ s Exposure), (c) Test Case RSE-3 (100 μ s Exposure) and (d) Test Case RSE-4 (150 μ s Exposure).

Figure-6.11 shows a direct relation between re-scanning exposure and melt pool size of the re-melted material. Increasing the rescanning exposure resulted in a larger re-melted melt pool. A larger melt pool means more material to cool and thus a reduced cooling rate. An important feature to note from the FEA results in Figure-6.11 is that for test case RSE-1, using 50 μ s exposure for re-scanning shown in Figure-6.11(a), the size of the re-melted melt pool is quite small. With 50 μ s exposure time, the FEA predicted isolated re-melted spots. Figure-6.12 shows that there is an inverse relationship between re-scanning exposure and cooling rates for re-melted material. Increasing re-scanning exposure results in lowering the cooling rates. Another

important feature worth noting from Figure-6.12 is that the only re-scanning case resulting in a cooling rate lower than test case S-1, samples built without rescanning is test case RSE-4, with a re-scanning, exposure time of 150 μ s (Re-Scanning Energy Density is 150% of the Energy Density used for melting each layer). The trends in cooling rate agree with the amount of re-melted material.

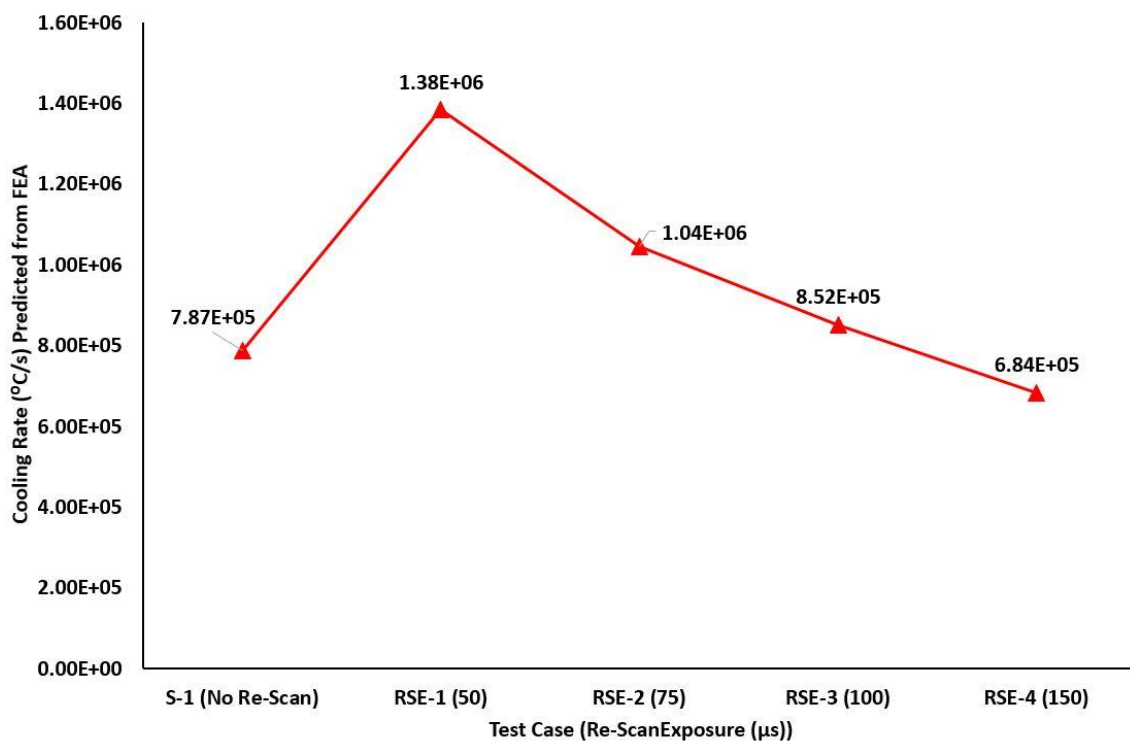


Figure 6-12. Effect of re-scanning with varying exposure on cooling rates

6.4.1 Effect of Re-Scanning with Varying Exposure on Porosity and Microstructure

All the re-scanning test cases with varying exposure resulted in nearly fully dense SLM Ti6Al4V parts. Figure-6.11 showed that increasing the re-scanning exposure

resulted in an increase in the re-melted meltpool dimensions, but porosity analysis on the experimental samples did not show any variation in the density of the samples. Getting nearly fully dense SLM parts with re-scanning is consistent with the findings of ref-[33], reporting a reduction in porosity of SLM parts from 0.77% to 0.032% with re-melting. Figure-6.12 shows that for rescanning with varying exposure, increasing the rescanning exposure leads to reduced cooling rates. Even though the cooling rates are lowered with increasing exposure but they are still much higher than the cooling rate required for fully martensitic microstructure in Ti6Al4V. According to ref-[124], cooling rates higher than $410 \frac{^{\circ}\text{C}}{\text{s}}$ leads to fully martensitic microstructure for Ti6Al4V. Therefore irrespective of the rescanning exposure samples from all test cases RSE-1, RSE-2, RSE-3 and RSE-4 resulted in fully martensitic microstructure with martensitic α' laths growing inside columnar prior β grains.

Porosity analysis showed nearly fully dense samples for all the test cases of rescanning with varying exposure but a careful examination of the microstructural images revealed that there was a considerable amount of micro porosity in the samples not picked up in porosity analysis. The reason for not seeing this micro porosity in polished samples is because of the smearing effect as reported by ref-[73].

Figure-6.13 shows that the amount of micro porosity in test case RSE-1, samples built with rescanning exposure of $50\mu\text{s}$ is higher than test case S-1, samples built without rescanning. Increasing the rescanning exposure to $75\mu\text{s}$ for test case RSE-2

the micro porosity disappeared. Test case RSE-3, built with 100 μ s rescanning exposure shown in Figure-6.13(d), shows the highest amount of micro porosity. Test case RSE-4 shows some micro porosity as well. Therefore in order to better understand the amount of porosity in samples, either porosity analysis needs to be performed on etched samples as in ref-[73] or more detailed analysis techniques such as micro CT should be used.

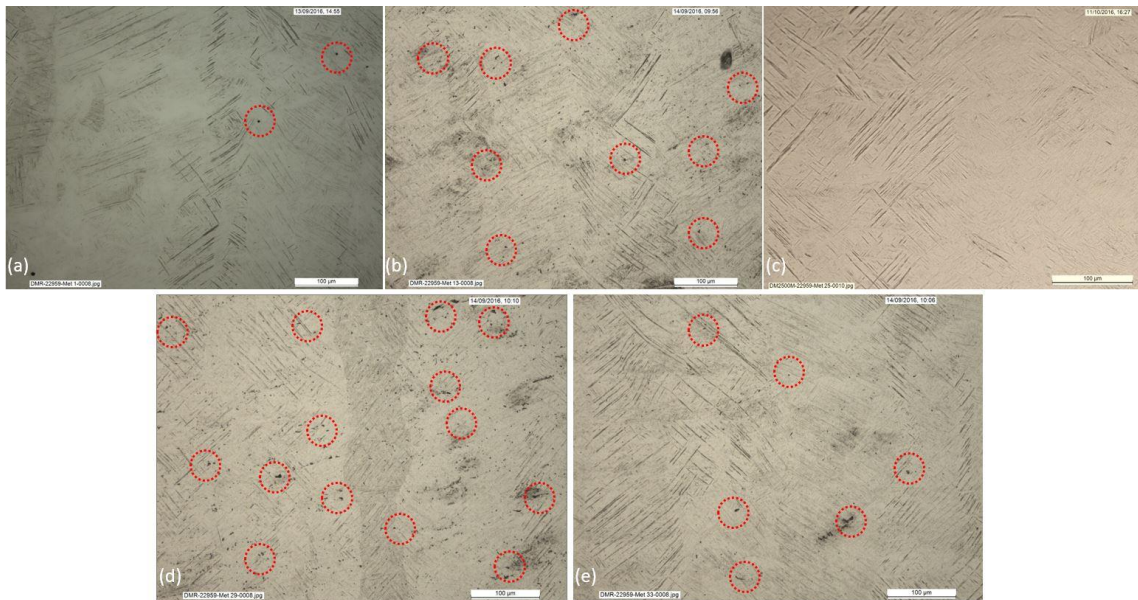


Figure 6-13. Effect of re-scanning with varying exposure on micro porosity (a) Test Case S-1 (No ReScanning) (b) Test Case RSE-1 (50 μ s Exposure), (c) Test Case RSE-2 (75 μ s Exposure), (d) Test Case RSE-3 (100 μ s Exposure) and (e) Test Case RSE-4 (150 μ s Exposure).

Figure-6.13 shows that the amount of micro porosity in test case RSE-1, samples built with rescanning exposure of 50 μ s is higher than test case S-1, samples built without rescanning. Increasing the rescanning exposure to 75 μ s for test case RSE-2

the micro porosity disappeared. Test case RSE-3, built with 100 μ s rescanning exposure shown in Figure-6.13(d), shows the highest amount of micro porosity. Test case RSE-4 shows some micro porosity as well. Therefore in order to better understand the amount of porosity in samples, either porosity analysis needs to be performed on etched samples as in ref-[73] or more detailed analysis techniques such as micro CT should be used.

6.4.2 Effect of Re-Scanning with Varying Exposure on Residual Stress

Figure-6.14 shows that increasing rescanning exposure results in increasing the peak temperature in the meltpool. For test case RSE-1 every layer was rescanned with 200W power and 50 μ s exposure, resulting in rescanning Energy Density of $38.46 \frac{J}{mm^3}$. Test case RSE-2 was rescanned with 200W power and 75 μ s exposure, resulting in rescanning Energy Density of $57.69 \frac{J}{mm^3}$. Test case RSE-3 was rescanned with 200W power and 100 μ s exposure, resulting in an Energy Density of $76.92 \frac{J}{mm^3}$. For test case RSE-4 each layer was rescanned with 200W power and 150 μ s exposure, resulting in rescanning Energy Density of $115.38 \frac{J}{mm^3}$. This leads to higher peak temperatures as shown in Figure-6.14 and larger re-melted meltpool size as shown in Figure-6.11. It can be seen from Figure-6.14 that irrespective of the rescanning Energy Density a temperature gradient exists, between the top and 50 μ m depth across the re-melted meltpool. Thus according to the temperature gradient

mechanism[28] and cool down phase model[28, 29], irrespective of the rescanning Energy Density, residual stress will be generated in the SLM samples.

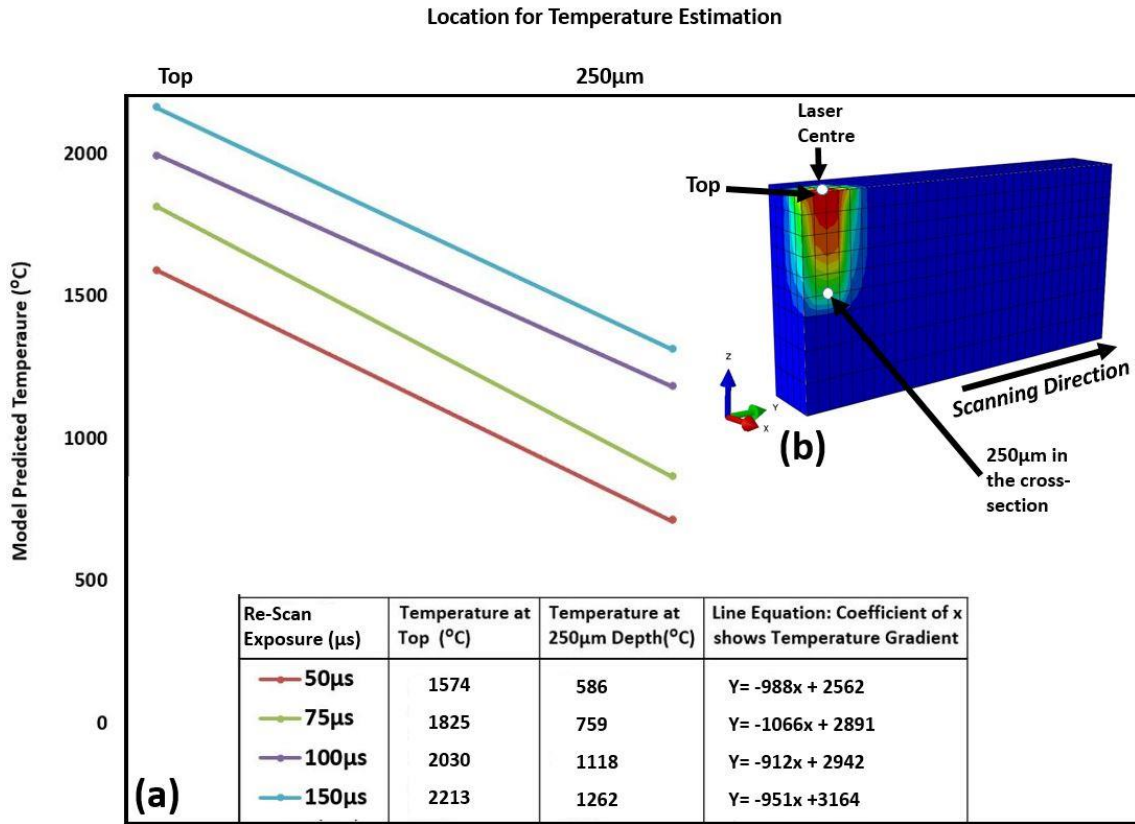


Figure 6-14 Effect of re-scanning with varying exposure on temperature gradient

Residual stress shows an increasing trend with rescanning exposure up to a point of 75 μs rescanning exposure and starts decreasing with further increase in rescanning exposure. According to ref-[49] rescanning with 50% Energy Density resulted in 30% reduction in residual stress. Figure-6.15 shows that rescanning with 50% Energy Density leads to an increase in cooling rates and this increase in cooling rates is responsible for the increase in residual stress of samples manufactured with rescanning each layer with 50% Energy. The cooling rates trend seems to be

agreeing well with all the cases of rescanning with varying exposure except rescanning with 50 μ s exposure. This probably is a consequence of not considering the effect of the first scan on the temperature of the solidified powdered layer. Thus the FEA simulation needs further refinement for properly predicting the cooling rates for re-melting in SLM samples

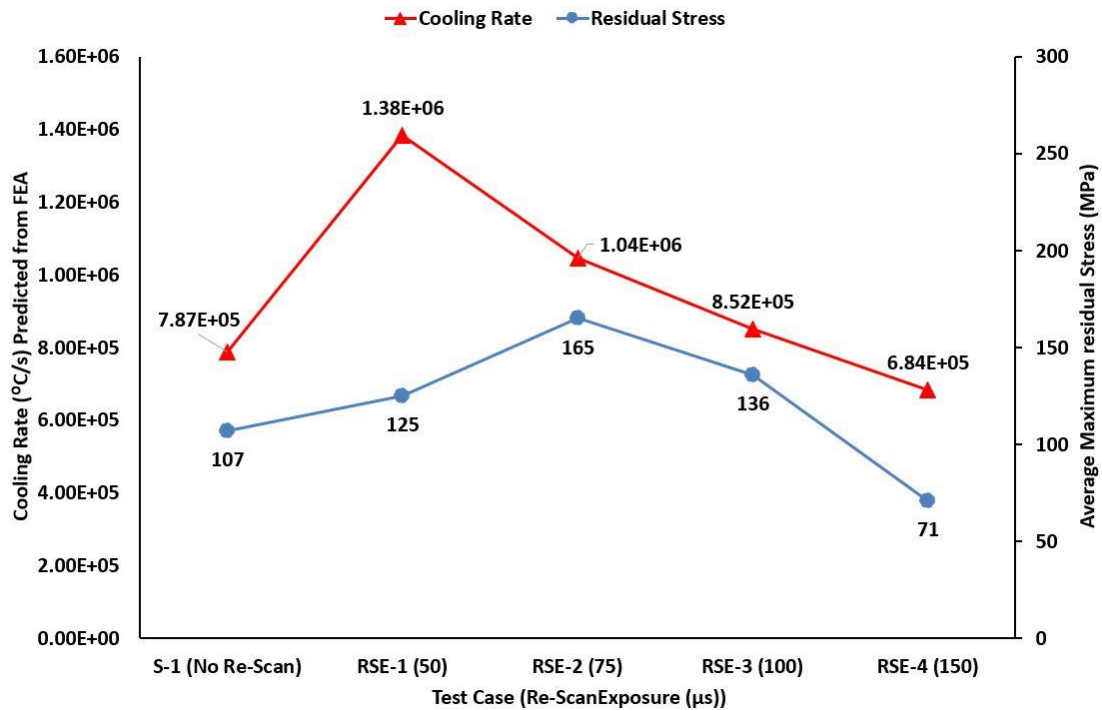


Figure 6-15. Effect of re-scanning with varying exposure on cooling rate and residual stress

Figure-6.15 shows that the only rescanned samples resulting in residual stress lower than samples without rescanning were the ones rescanned with 150 μ s rescanning exposure. Rescanning with 150% Energy Density for test case RSE-4 resulted in 33.6% reduction in residual stress compared with test case S-1, samples made without rescanning. This finding agrees with findings of ref-[29] reporting a 55%

reduction in residual stress when rescanned with 150% Energy Density. The cooling rate curve in Figure-6.15 also shows a decrease in cooling rate for test case RSE-4 compared with S-1 and thus the decrease in residual stress when rescanning with 150% Energy.

6.4.3 Effect of Re-Scanning with Varying Exposure on Mechanical Properties

Figure-6.16 does not show any clear trend in yield strength for test cases RSE-1 to RSE-3 compared with the standard test case S-1 without any rescan. Test case RSE-4, rescanning with 150 μ s exposure showed 0.03MPa yield strength, suggesting premature failure of the tensile samples. According to ref-[125], skin re-melting of SLM Ti6Al4V parts resulted in an oxide layer manufactured on Renishaw AM250 SLM machine with oxygen content in the chamber set at 50 ppm. Ref-[125] also reports the oxide layer being thicker on samples with skin re-melting compared to samples without re-melting. This increase in thickness of oxide layer is being attributed to the fact that melting the surface twice increased the possibility of build atmosphere oxygen penetration further into the surface. Based on the possibility of increase in the oxygen penetration further into the surface, it is hereby proposed that increase in re-melted meltpool size has a direct relation with the oxide layer thickness. Thus the meltpool size comparison from Figure-6.11, suggests that rescanning with 150 μ s exposure would result in thicker oxide layer formation between the layers of the samples. Therefore it is valid to assume that it is these thick oxide layers resulting in

the premature failure of tensile samples for test case RSE-4 and thus no measured yield strength values.

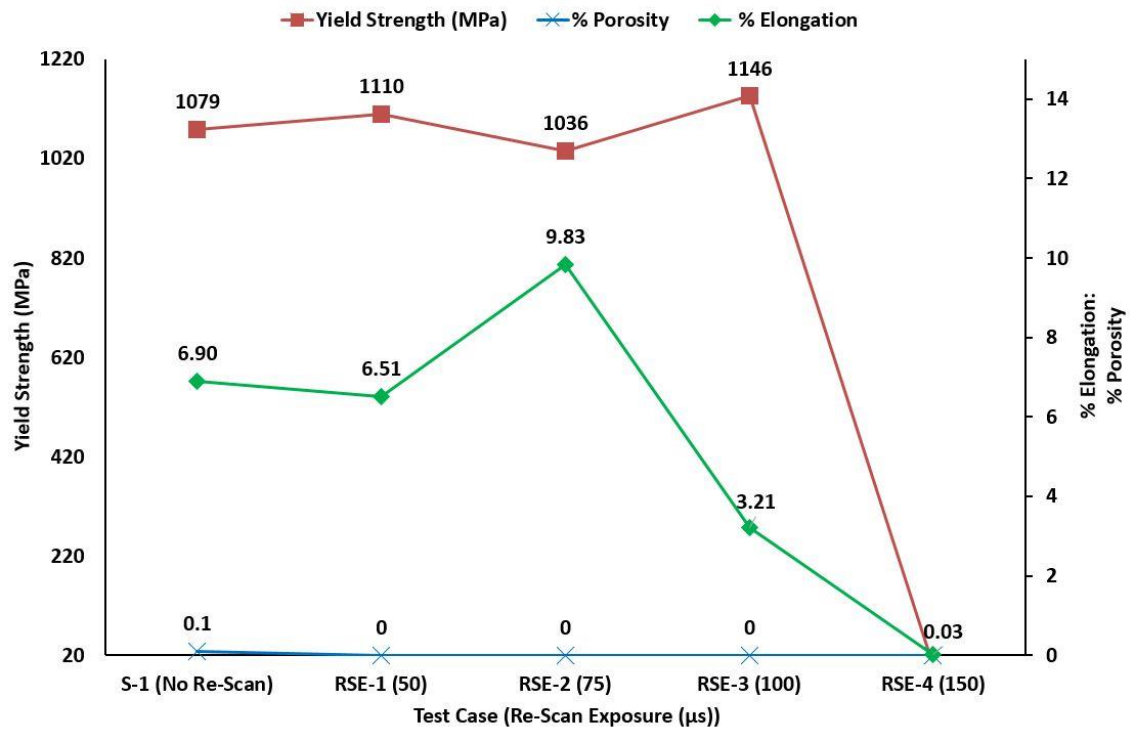


Figure 6-16. Effect of re-scanning energy varying exposure on % Porosity, % Elongation and Yield Strength

% elongation results in Figure-6.16 show a complex behavior with varying rescanning exposure times. Test case RSE-1, resulted in 5.7% decrease in % elongation compared to the standard samples, test case S-1 built without rescanning. This slight decrease in elongation can be attributed to the fact that rescanning with 50μs exposure resulted in an increase in the micro porosity of the samples (as shown in Figure-6.13(b), section-6.4.1) as ref-[72] reports a deterioration of mechanical

properties with porosity. Test case RSE-2, showed 42.5% improvement in elongation, compared to test case S-1. According to ref-[126] rescanning each layer resulted in the transformation of α' martensite into an $\alpha+\beta$ microstructure. Therefore it is valid to propose that this 42.% increase in elongation of test case RSE-2 samples is probably a consequence of martensite transformation into $\alpha+\beta$. Another factor responsible for this increase in elongation is probably the disappearance of micro porosity in test case RSE-2 samples (as shown in Figure-6.13(c)). Increasing the rescan exposure to 100 μ s, test case RSE-3 resulted in a sharp drop 53.5% in elongation compared to S-1. Figure-6.13(d) shows some micro porosity in test case RSE-3 samples but this alone does not account for such a sharp decline in elongation. Another probable reason for this decrease in elongation of test case RSE-3 samples could be the increase in the oxide layer thickness between Ti6Al4V layers due to re-melting of each layer as ref-[125] reported the formation of an oxide layer with re-melting. Increasing the exposure to 150 μ s, test case RSE-4, resulted in 0% elongation, which suggesting pre-mature failure of the tensile samples. Based on the possibility of an increase in the oxygen penetration further into the surface with re-melting[125], it is proposed that an increase in the re-melted meltpool size has a direct correlation with the oxide layer thickness. Thus the meltpool size comparison from Figure-6.11, suggests that rescanning with 150 μ s exposure would result in thicker oxide layer formation between the layers of the samples. Therefore it is valid to assume that it is these thick oxide layers which result in the premature failure of tensile samples for test case RSE-4 and no measured elongation. Figure-6.12 showed that increasing rescanning exposure led to a decrease in cooling rate but the cooling

rates are still much higher than $410 \frac{^{\circ}\text{C}}{\text{s}}$, the cooling rate leading to a totally martensitic microstructure for Ti6Al4V[124]. Since all the test cases RSE-1, RSE-2, RSE-3 and RSE-4 had a totally martensitic microstructure, there is no major variation in Vickers hardness values for samples manufactured with different layer thicknesses. The slight decrease in the Vickers hardness of test case RSE-2 could probably be a result of possible α' transformation into $\alpha+\beta$ due to re-melting as reported by ref-[126].

6.5 Effect of Re-Scanning with Varying Power

In order to understand the effect of Re-Scanning with varying power on residual stress and mechanical properties, FEA simulation with different re-scanning powers was used to estimate the effect of re-scanning with varying power on cooling rates. Energy Density for re-scanning each layer was varied by keeping exposure constant at $100\mu\text{s}$ and varying power in proportion to the optimum power of 200W (from density optimisation trials section 6.1).

Figure-6.17 shows a direct relation between re-scanning power and meltpool size of the re-melted material. Increasing the rescanning power resulted in a larger re-melted meltpool. A larger meltpool means more material to cool and thus a reduced cooling rate. An important feature to note from the FEA results in Figure-6.17 is that for test case RSP-1, using 100W power for re-scanning shown in Figure-6.17(a), the FEA simulation predicted no re-melting. This could be attributed to the fact that the FEA simulation did not take into consideration the temperature effects from the first scan used to melt the material. Thus the FEA simulation needs to be refined further

to consider the effect of the first scan on the temperature of the solidified powder layer.

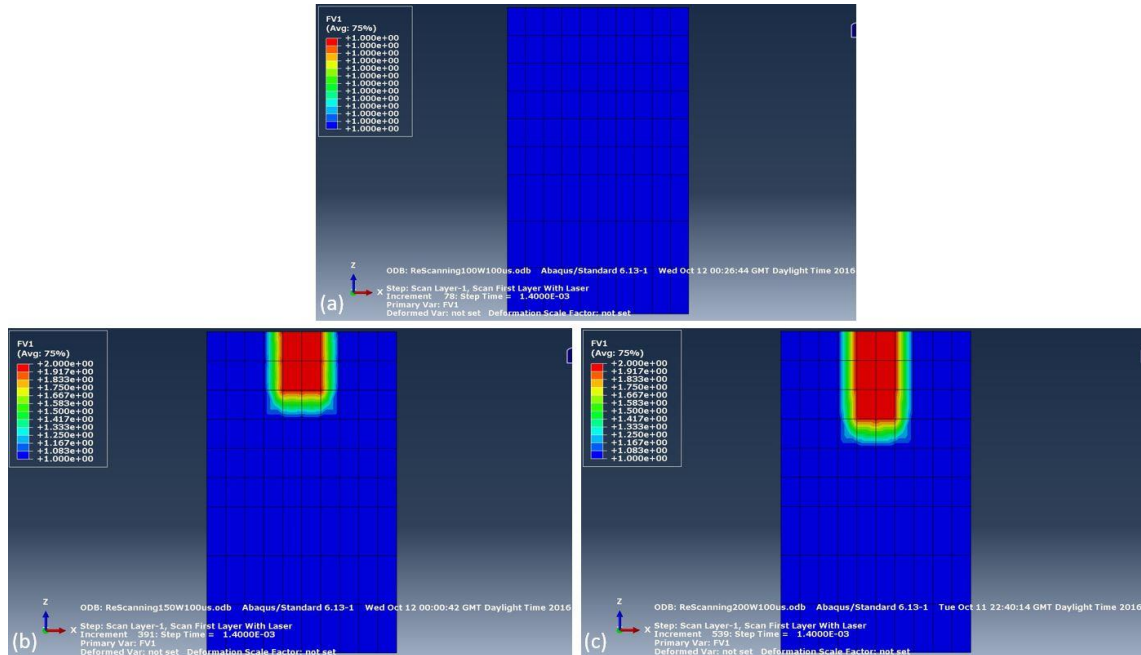


Figure 6-17 Effect of re-scanning with varying power on meltpool dimensions (a) Test Case RSP-1 (100W Power), (b) Test Case RSP-2 (150W Power), and (c) Test Case RSP-3 (200W Power)

Figure-6.18 shows that the relationship between re-scanning power and cooling rate for re-melted material is not very clear. Increasing re-scanning power results in lowering the cooling rate but with 200W power for test case RSP-3 there is a slight increase in cooling rate. Another important feature worth noting from Figure-6.18 is that none of the re-scanning cases results in a cooling rate lower than test case S-1, samples built without rescanning.

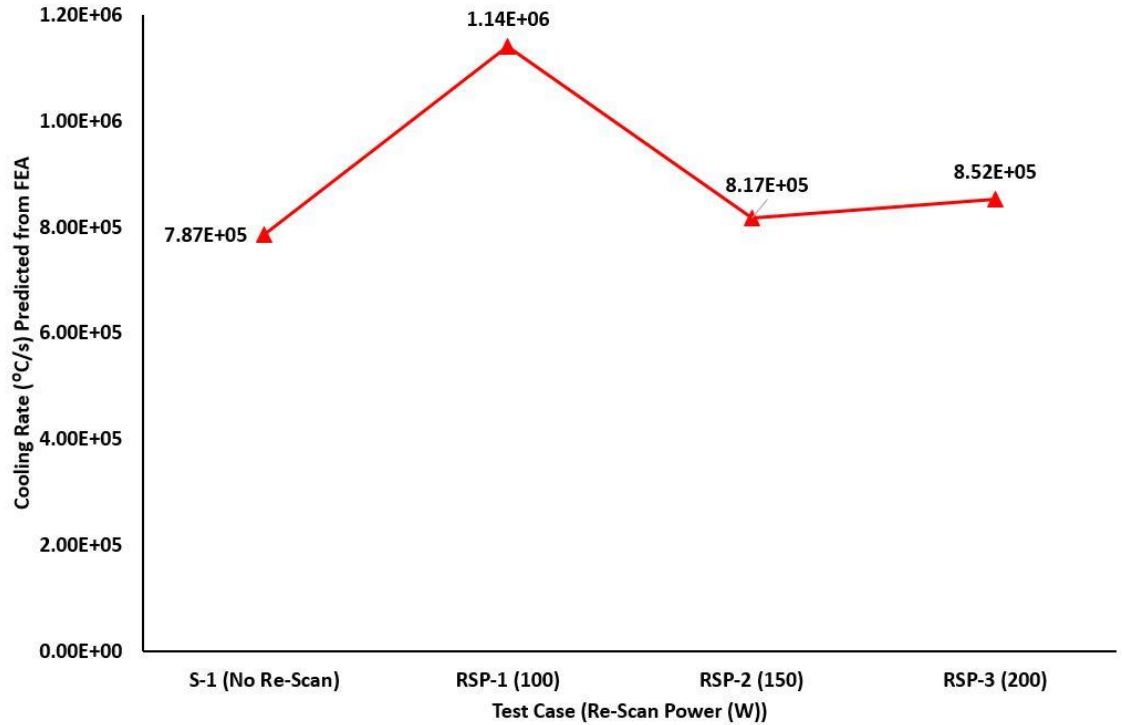


Figure 6-18 Effect of re-scanning with varying power on cooling rates

6.5.1 Effect of Re-Scanning with Varying Power on Porosity and Microstructure

Rescanning each layer of the SLM Ti6Al4V parts with varying power did not result in nearly fully dense parts, even though ref-[33] reported rescanning as a means for improving part density. This unexpected increase in porosity could possibly be an effect of rescanning with lower powers. According to Figure-6.19 the amount of minimum energy required for achieving nearly fully dense SLM Ti6Al4V parts from powder is inversely proportional to power. Re-melting the solidified layers should thus require even higher energy input. Test case RSP-1 uses 100W power, while the exposure is fixed at 100 μ s (optimum exposure from Density Optimisation Trials

section-6.1) for re-melting each layer and thus according to the results of Figure-6.19 the energy input is well below the requirement for nearly fully dense parts. This probably results in test case RSP-1 having 2.4% porosity. Test case RSP-2 uses 150W power for rescanning each layer with 100 μ s exposure and thus according to the trend in Figure-6.19 the energy input is probably well below that required for achieving a stable re-melted meltpool and thus results in 1.8% porosity in samples.

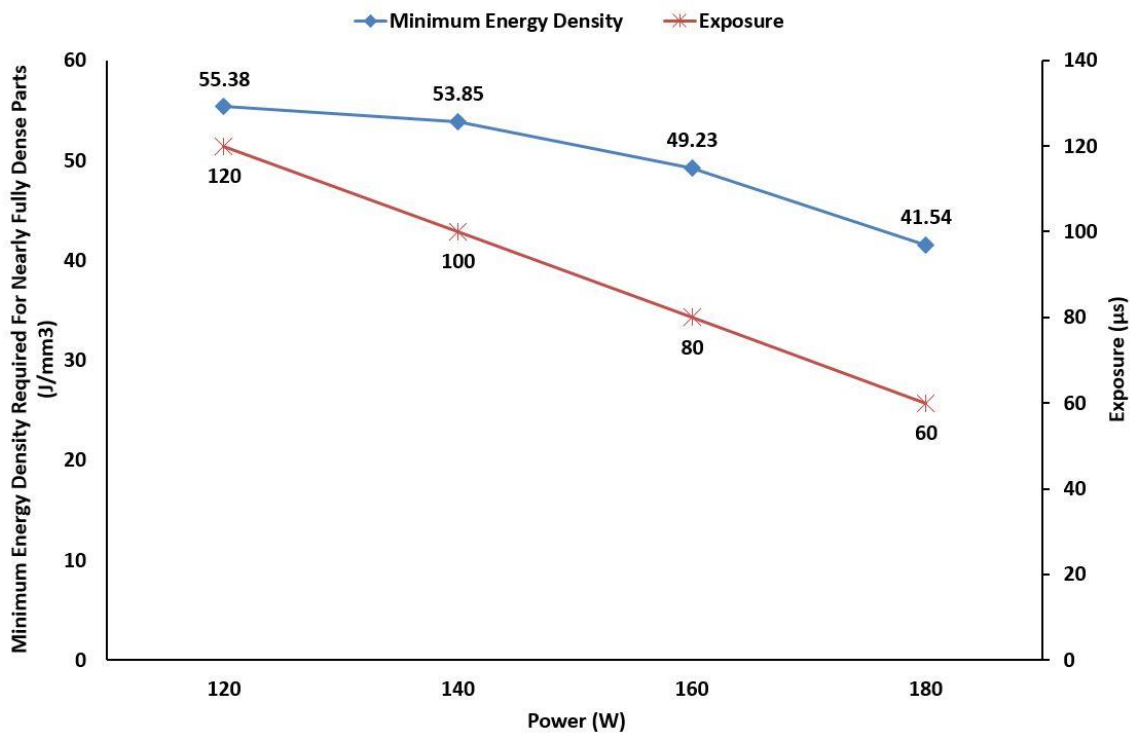


Figure 6-19 Effect of power on minimum energy density required for nearly full dense Ti6Al4V SLM parts.

Figure-6.18 shows that for rescanning with varying power, increasing the rescanning power leads to reduced cooling rates with a slight increase in cooling rate

for test case RSP-3. Even though the cooling rates are lowered with increasing power, they are still much higher than the cooling rate required for fully martensitic microstructure in Ti6Al4V. According to ref-[124], cooling rates higher than $410\frac{^{\circ}\text{C}}{\text{s}}$ leads to fully martensitic microstructure for Ti6Al4V. Therefore irrespective of the rescanning power samples from all test cases RSP-1, RSP-2 and RSP-3 resulted in fully martensitic microstructure with martensitic α' laths growing inside columnar prior β grains.

6.5.2 Effect of Re-Scanning with Varying Exposure on Residual Stress

Figure-6.20 shows that increasing rescanning results in increasing the peak temperature in the meltpool. For test case RSP-1 every layer was rescanned with 100W power and 100 μs exposure, resulting in rescanning Energy Density of $38.46\frac{\text{J}}{\text{mm}^3}$. Test case RSP-2 was rescanned with 150W power and 100 μs exposure, resulting in rescanning Energy Density of $57.69\frac{\text{J}}{\text{mm}^3}$. Test case RSP-3 was rescanned with 200W power and 100 μs exposure, resulting in an Energy Density of $76.92\frac{\text{J}}{\text{mm}^3}$. This increase in rescanning Energy Density leads to higher peak temperatures as shown in Figure-6.20 and larger re-melted meltpool size as shown in Figure-6.17. It can be seen from Figure-6.20 that irrespective of the rescanning Energy Density a temperature gradient exists, between the top and 150 μm depth across the re-melted meltpool. Thus according to the temperature gradient mechanism[28] and cool down phase model[28, 29], irrespective of the rescanning Energy Density with varying power, residual stress will be generated in the SLM samples. It can be seen

from Figure-6.20 that the trend in temperature gradient across the top and 150µm depth across the re-melted meltpool agrees well with the trend in residual stress shown in Figure-6.21.

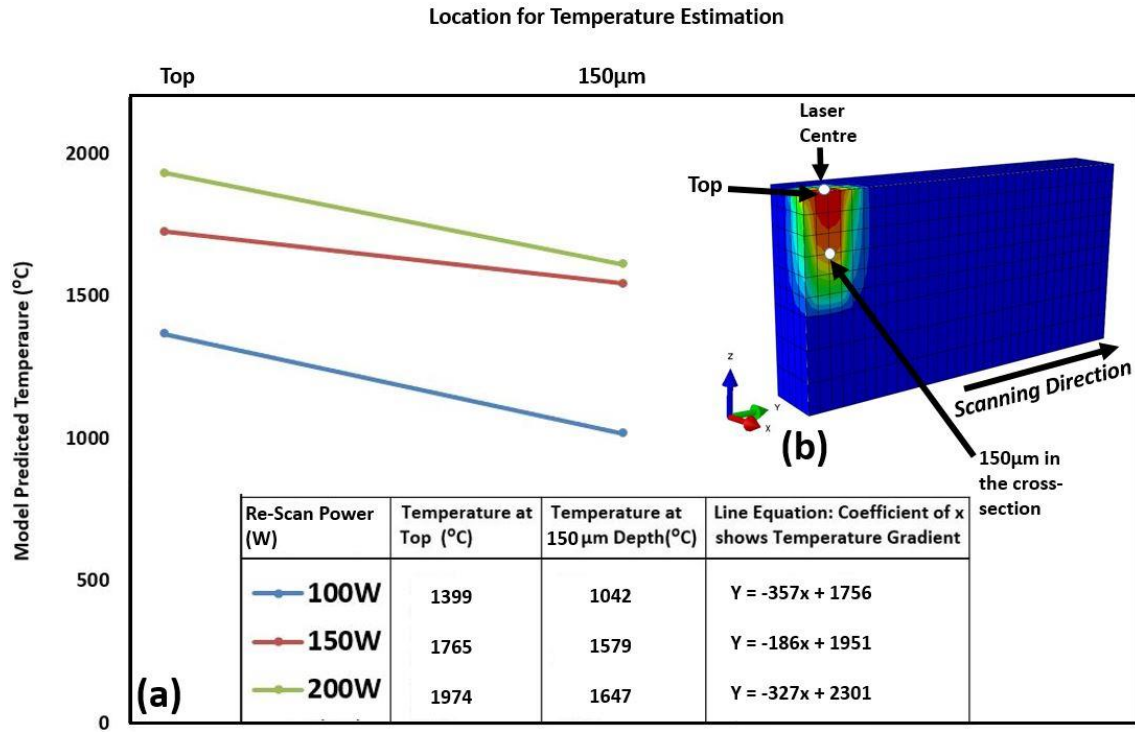


Figure 6-20 Effect of rescanning with varying power on temperature gradient

Residual stress does not show a clear trend with rescanning power. According to ref-[49] rescanning with 50% Energy Density resulted in 30% reduction in residual stress. Figure-6.21 shows that rescanning with 50% Energy Density using 100W power and 100µs exposure leads to an increase in cooling rates and this increase in cooling rates is responsible for the increase in residual stress. The cooling rates trend seems to be agreeing well with all the cases of rescanning with varying power.

Figure-6.21 shows that none of the rescanned samples with varying power resulted in residual stress lower than samples without rescanning.

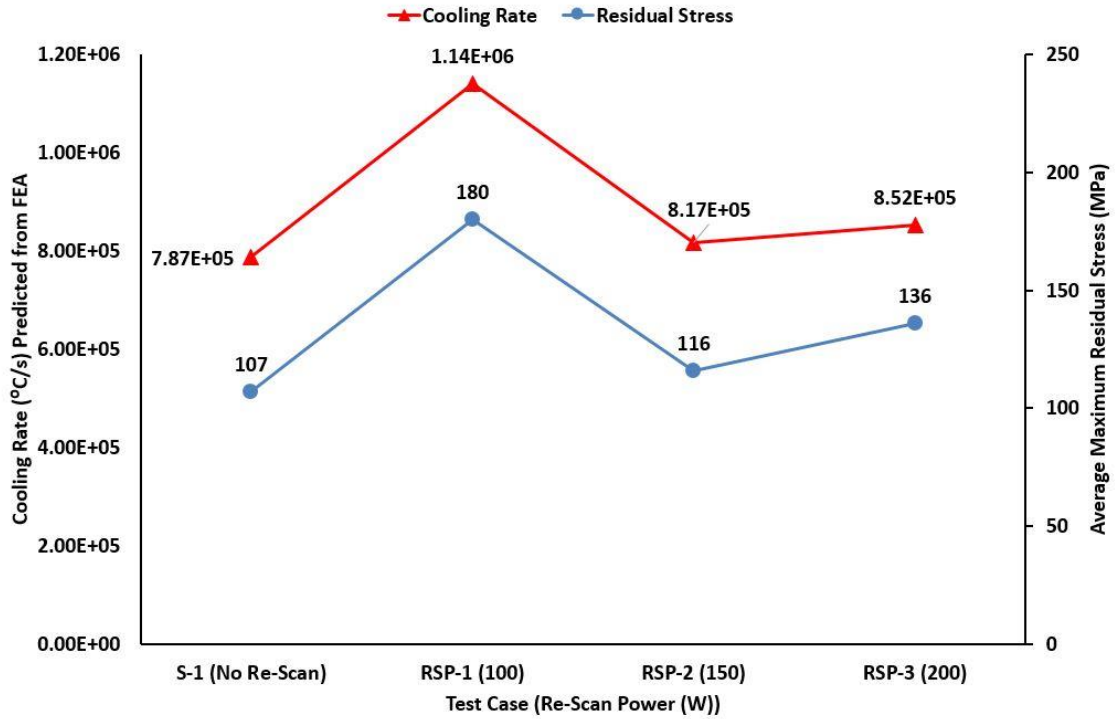


Figure 6-21. Effect of re-scanning with varying power on cooling rate and residual stress

6.5.3 Effect of Re-Scanning with Varying Power on Mechanical Properties

Figure-6.22 does not show any clear trend in yield strength for test cases RSP-1 to RSP-3 compared with the standard test case S-1 without any rescan. Test case RSP-1, rescanning with 150W showed 13.9% reduction in yield strength compared to test case S-1. According to ref-[125], skin re-melting of SLM Ti6Al4V parts resulted in an oxide layer manufactured on Renishaw AM250 SLM machine with oxygen content in

the chamber set at 50 ppm. Ref-[125] also reports the oxide layer being thicker on samples with skin re-melting compared to samples without re-melting

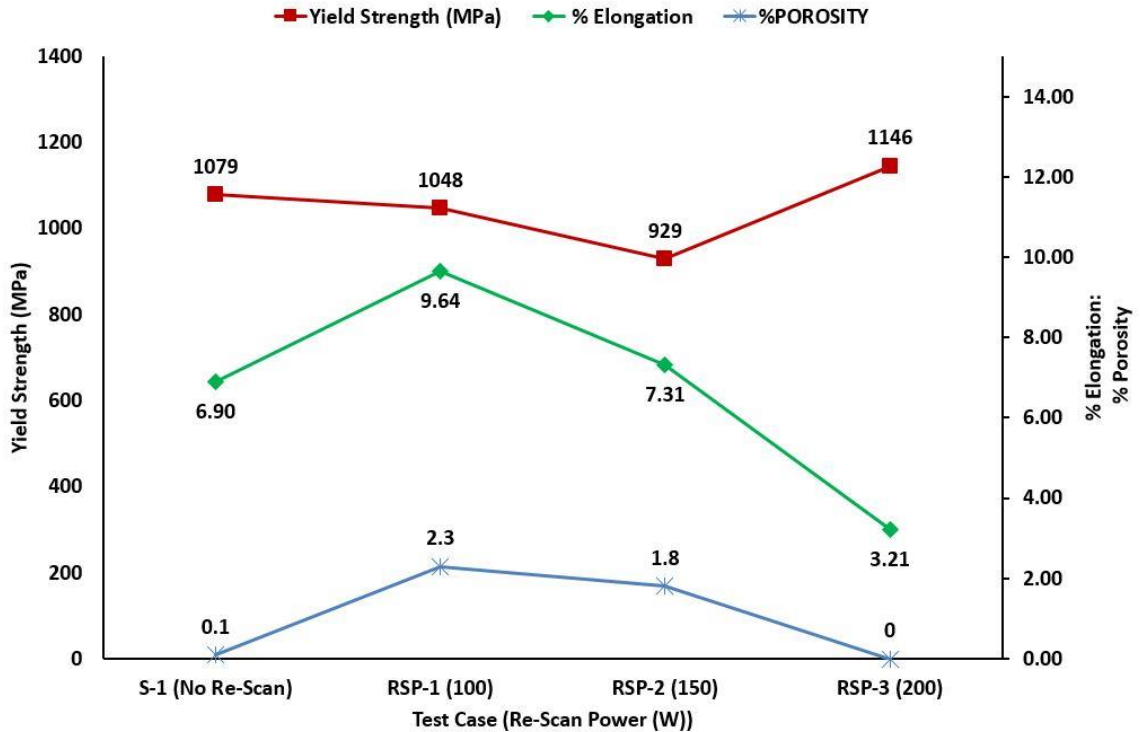


Figure 6-22 Effect of re-scanning energy varying exposure on % Porosity, % Elongation and Yield Strength

. This increase in the thickness of the oxide layer is being attributed to the fact that melting the surface twice increased the possibility of build atmosphere oxygen penetration further into the surface. Based on the possibility of an increase in the oxygen penetration further into the surface, it is hereby proposed that an increase in re-melted melt pool size has a direct relation with the oxide layer thickness. Thus the melt pool size comparison from Figure-6.17, suggests that rescanning with 150 μ s exposure would result in a thicker oxide layer formation between the layers of the

samples. Therefore it is valid to assume that it is these thick oxide layers combined with 1.8% porosity which result in the premature failure of tensile samples for test case RSP-1 resulting in 13.9% decrease in the yield strength values.

% Elongation results in Figure-6.22 show a complex behavior with varying rescanning power. Test case RSP-1, resulted in 39.7% increase in % elongation compared to the standard samples, test case S-1 built without rescanning. According to ref-[126] rescanning each layer resulted in the transformation of α' martensite into $\alpha+\beta$ microstructure. Therefore it is valid to propose here that this 39.7% increase in elongation for test case RSP-1 samples is probably a consequence of martensite transformation into $\alpha+\beta$. In test case RSP-2, rescanning each layer with 150W resulted in 24.17% decrease in elongation compared with test case RSP-1. The amount of porosity decreased as well so therefore the only probable reason for this decrease in elongation for test case RSP-2 samples could be the increase in the oxide layer thickness between Ti6Al4V layers due to re-melting of each layer as ref-[125] reported formation of oxide layer with re-melting. The elongation of test case RSP-2 is 5.9% higher than the standard samples of test case S-1, without any rescanning. This could be attributed to the probable transformation of α' martensite into $\alpha+\beta$. Increasing the rescan power to 200W, test case RSP-3 resulted in a sharp drop of 53.5% in elongation compared to S-1. Figure-6.13(d) shows some micro porosity in test case RSP-3 samples but this alone does not account for such a sharp decline in elongation. Another probable reason for this decrease in elongation for test case RSP-3 samples could be the increase in the oxide layer thickness between Ti6Al4V layers due to re-melting of each layer as ref-[125] reported formation of oxide layer

with re-melting. Increasing the rescanning power to 200W, test case RSP-3, probably increased the possibility of increase in the oxygen penetration further into the surface as ref-[125] reported increase in oxygen penetration with re-melting. It is therefore proposed that increase in re-melted meltpool size has a direct correlation with the oxide layer thickness. Thus the meltpool size comparison from Figure-6.17, suggests that rescanning with 200W exposure would result in thicker oxide layer formation between the layers of the samples. Therefore it is valid to assume that it is these thick oxide layers that result in the decreased elongation for test case RSP-3.

Figure-6.18 showed that increasing rescanning power led to a decrease in cooling rate but the cooling rates are still much higher than $410\frac{^{\circ}\text{C}}{\text{s}}$, cooling rate leading to totally martensitic microstructure for Ti6Al4V[124]. Since all the test cases RSP-1, RSP-2, and RSP-4 had a totally martensitic microstructure, there is no major variation in Vickers hardness values for samples manufactured with different rescanning powers.

6.6 Effect of Power and Exposure keeping Energy Density Constant

In order to understand the effect of varying power and exposure time combinations keeping Energy Density constant on residual stress and mechanical properties, FEA simulation with different combinations of power and exposure was used to estimate the cooling rates.

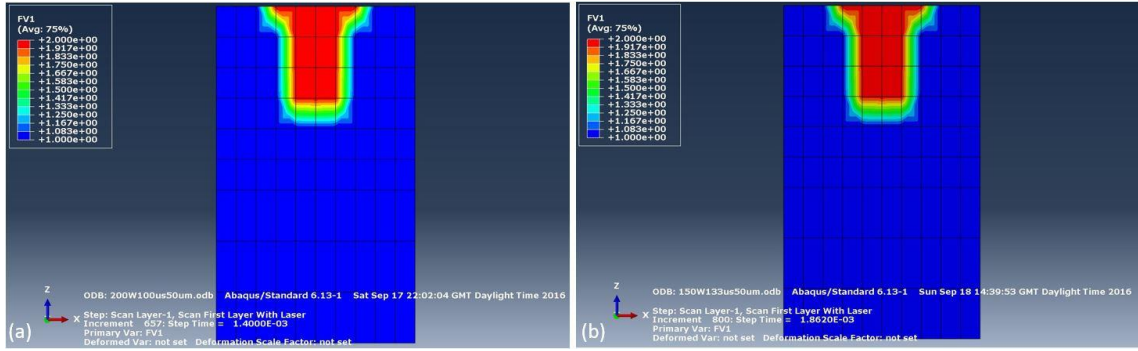


Figure 6-23 Effect of varying power and exposure time combination for a constant energy density on meltpool dimensions (a) Test Case S-1 (200W Power & 100 μ s Exposure). (b) Test Case CED-4 (150W Power & 133 μ s Exposure)

Figure-6.23(a) shows the meltpool dimensions for 200W power and 100 μ s exposure, while Figure-6.23(b) shows test case CED-4 manufactured with lowest power of 150W and the highest exposure of 133 μ s tested in this work. It can be seen from Figure-6.23 that for a constant Energy Density any combination of power and exposure will result in the same meltpool size.

Figure-6.24 shows the effect of varying power and exposure combinations with constant Energy Density on the cooling rate. It can be seen from Figure-6.24 that for a constant Energy Density, decreasing power and increasing exposure leads to a decrease in cooling rate.

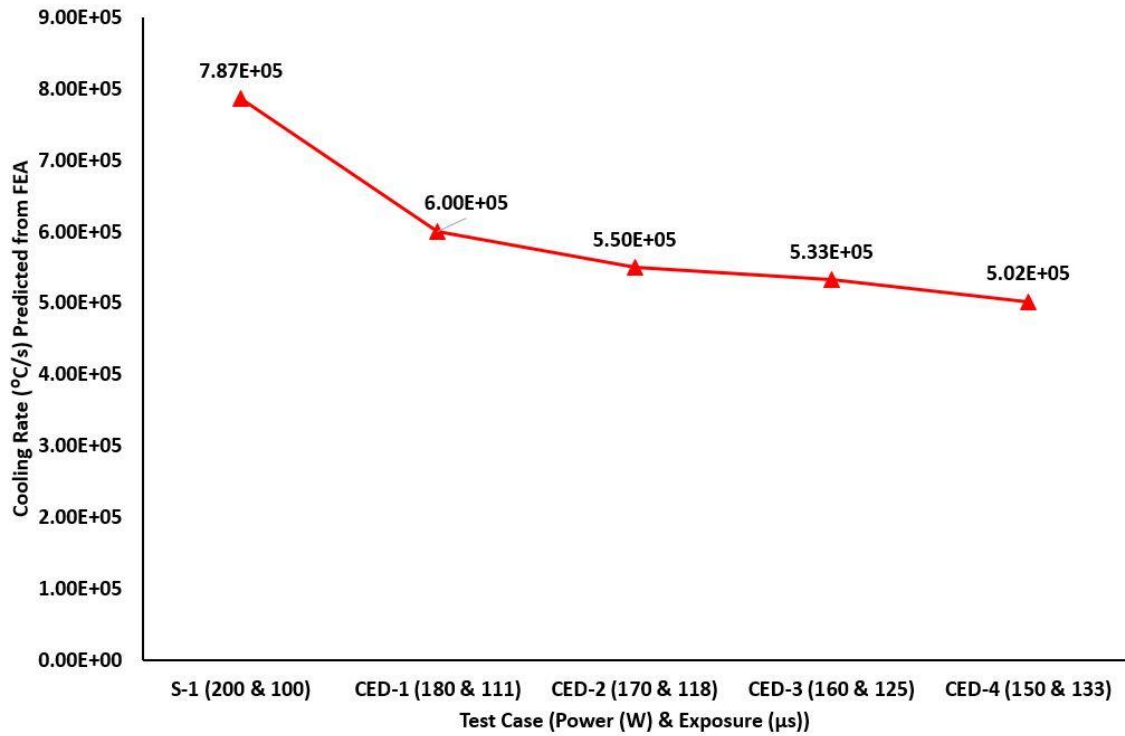


Figure 6-24 Effect of varying power and exposure time combination for a constant energy density on cooling rates

6.6.1 Effect of Power and Exposure keeping Energy Density Constant on Porosity and Microstructure

For a constant Energy Density nearly fully dense SLM Ti6Al4V parts were achieved with any combination of power and exposure. Figure-6.23 showed that keeping Energy Density constant, varying the power and exposure combination did not have any effect on the melt pool dimensions which explains why there is no variation in the % porosity of the samples. Figure-6.24 shows that for constant Energy Density, decreasing power and increasing exposure leads to reduced cooling rates. Even though the cooling rates are lowered with decreasing power and increasing

exposure, they are still much higher than the cooling rate required for fully martensitic microstructure in Ti6Al4V. According to ref-[124], cooling rates higher than $410\frac{^{\circ}\text{C}}{\text{s}}$ leads to fully martensitic microstructure for Ti6Al4V. Therefore irrespective of the power and exposure combinations for the samples, all test cases S-1, CED-1, CED-2, CED-3 and CED-4 resulted in fully martensitic microstructure with martensitic α' laths growing inside columnar prior β grains.

6.6.2 Effect of Power and Exposure keeping Energy Density Constant on Residual Stress

For constant Energy Density, Figure-6.24 shows that decreasing power and increasing exposure results in lowering the highest temperature in the meltpool. This reduction in the peak temperature with decreasing power is consistent with the findings of refs-[35, 36]. According to Ref-[35] meltpool size decreased and cooling rate increased, while studying the effect of decreasing power individually. To the author's knowledge there has been no work on varying the power and exposure together keeping Energy Density constant. Since this study varied both power and exposure proportionally for keeping Energy Density constant, there was no effect of reducing power on the meltpool size. Figure-6.22 showed no variation in meltpool size and from Figure-6.23 the cooling rate showed a decreasing trend, with decreasing power. An important feature from Figure-6.25 is the decrease in temperature gradient between the top and 50 μm depth across a meltpool, as illustrated by the slope of the line equations. The reduction in thermal gradient with increasing exposure is consistent with the findings of ref-[38], reporting slower

scanning leading to reduced thermal gradients. Thus according to the temperature gradient mechanism[28] and cool down phase model[28, 29], decreasing power and increasing exposure keeping Energy Density constant, should lead to a decrease in residual stress.

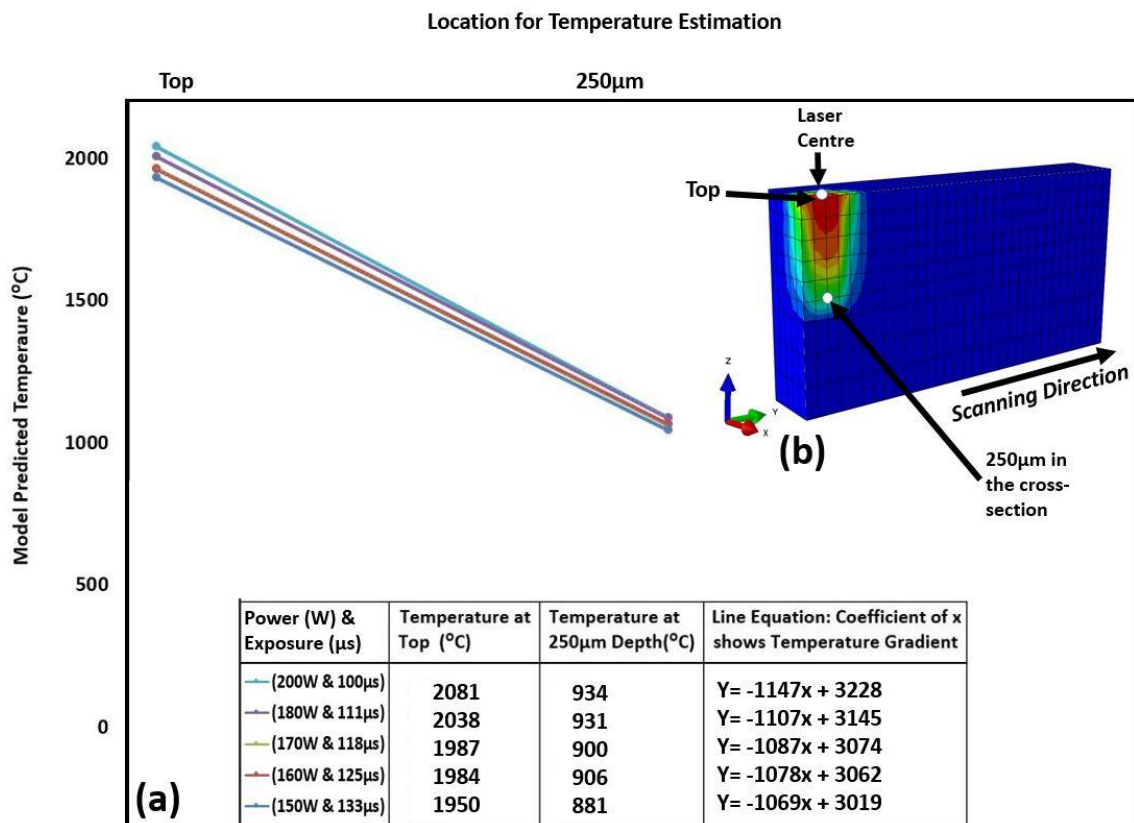


Figure 6-25 Effect of varying power and exposure time combination for a constant energy density on temperature gradient

Figure-6.26 shows a decreasing trend in cooling rate with decreasing power and increasing exposure for a constant Energy Density. This decreasing trend in cooling rate is consistent with ref-[35], reporting a decrease in cooling rate for slower scanning. This decrease in cooling rate leads to a decrease in residual stress in samples made with lower power and higher exposure. According to Ref-[39], slower

scan speed led to reducing the residual stress in a single track. Therefore it is valid to say that keeping Energy Density constant, the trend in cooling rate and residual stress follows the trend of the effect of exposure time studied individually. The correlation of cooling rate and residual stress with power is the opposite of when power is varied individually.

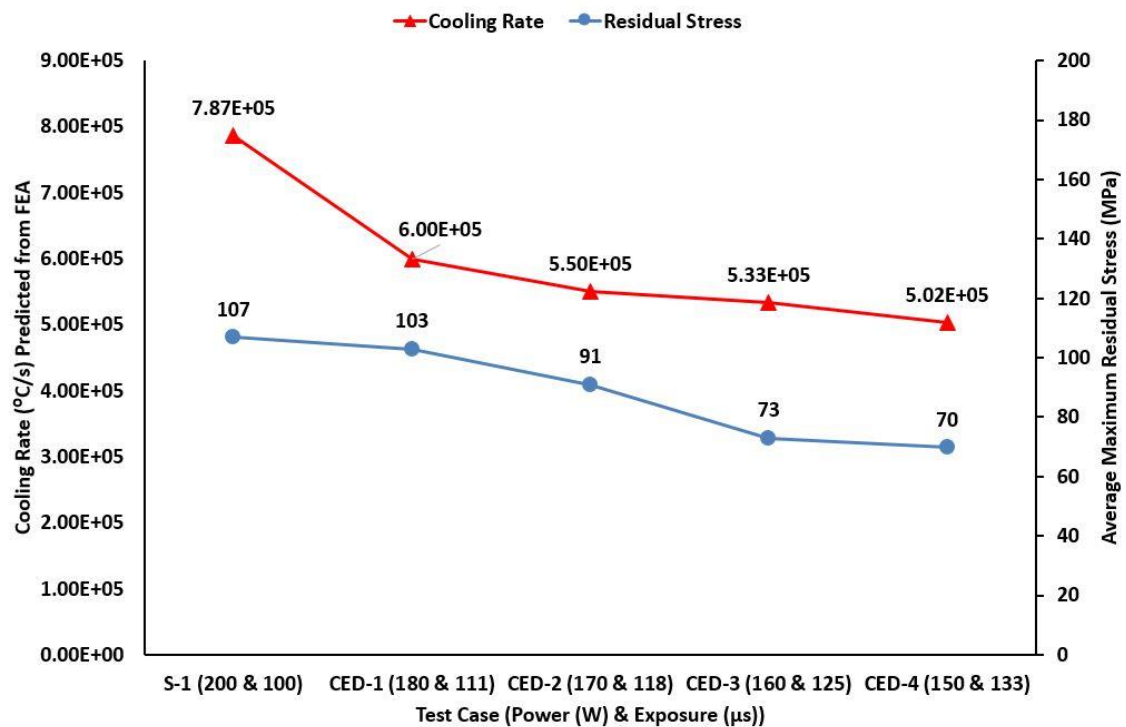


Figure 6-26 Effect of varying power and exposure time combination for a constant energy density on cooling rate and residual stress

The results in Figure-6.26 show that scanning and melting Ti6Al4V powder with slower scan speed and lower power, maintaining the optimum Energy Density, results in an improvement in residual stress within the parts. Therefore based on

these results 150W power and 133 μ s exposure resulting in minimum residual stress were used further in this work for intuitive strategic stress reduction in a complex SLM manufactured geometry.

6.6.3 Effect of Power and Exposure keeping Energy Density Constant on Mechanical properties

Mechanical properties show a direct relationship with reducing power and increasing exposure keeping Energy Density constant. Figure-6.27 shows that decreasing power and increasing exposure keeping Energy Density constant, leads to a slight increase in the yield strength, while there is a considerable improvement in % elongation of SLM samples. Figure-6.27 shows % porosity remains consistent (see section 6.6.1).

Figure-6.24 showed that for constant Energy Density, decreasing power and increasing exposure leads to a reduction in cooling rates. According to the effective slip length and dislocation movement theories [65, 81], (see section-6.3.3), decreasing power and increasing exposure should lead to a decrease in yield strength, as it decreases the cooling rate and thus should result in lower yield strength. According ref- [72] process induced porosity acts as a stress concentrator and leads to a reduction in mechanical properties. Figure-6.27 shows that for test cases CED-1 to CED-3 there is no porosity which might be the reason for 1.6% increase in yield strength of sample CED-3 compared with test case S-1. Test case CED-4 shows 0.1% porosity, similar to test case S-1 and much lower cooling rate but yet resulted in 3.9% increase in yield strength compared to S-1. Thus it is valid to

say that varying combinations of power and exposure keeping Energy Density constant has no effect on the yield strength of the samples and this small variation of 1-3% can be due to the stochastic nature of the SLM process or may even be due to the tensile testing uncertainty.

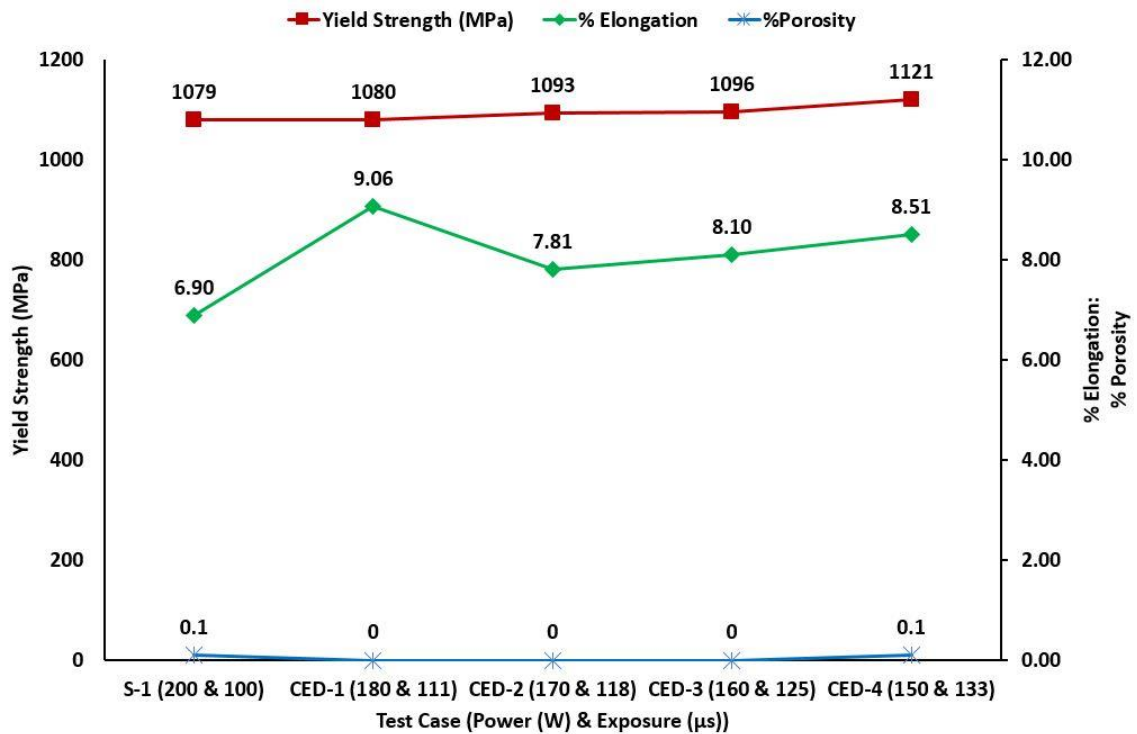


Figure 6-27 Effect of varying power and exposure time combination for a constant energy density on %Porosity, % Elongation and Yield Strength

Figure-6.27 shows an increasing trend in ductility with decreasing power and increasing exposure keeping Energy Density constant. The sudden increase in the elongation of test case CED-1 is not clear as it has cooling rates higher than test cases CED-2 to CED-4. Overall it can be seen from Figure-6.27 that lower power and higher

exposure combinations keeping energy density constant, leads to an increase in elongation. According to the effective slip length and dislocation movement theories [65, 81], ductility increases with increasing cooling rate up to a certain point, and beyond this point of maximum ductility, it decreases sharply with a further increase in the cooling rate. This intermediate optimum cooling rate for maximum ductility from Figure-2.19(b) is much lower than the SLM cooling rates. The SLM cooling rate decreases with decreasing power and increasing exposure which leads to an increase in ductility as the cooling rate is moving towards the intermediate optimum cooling rate for maximised ductility (Figure-2.19(b)).

Figure-6.24 showed that for constant Energy Density, decreasing power and increasing exposure leads to a reduction in cooling rate but the cooling rates are still much higher than $410 \frac{^{\circ}C}{s}$, the cooling rate leading totally martensitic microstructure for Ti6Al4V[124]. Since all the test cases had a totally martensitic microstructure, there is no major variation in Vickers hardness values for samples manufactured with different combinations of power and exposure.

6.7 Effect of Bed Pre-Heat Temperature

In order to understand the effect of Bed Pre-Heat Temperature on residual stress and mechanical properties, FEA simulation using the parameters optimised for 50 μ m layer thickness, with different bed temperatures was used to estimate the effect of bed temperature on cooling rates.

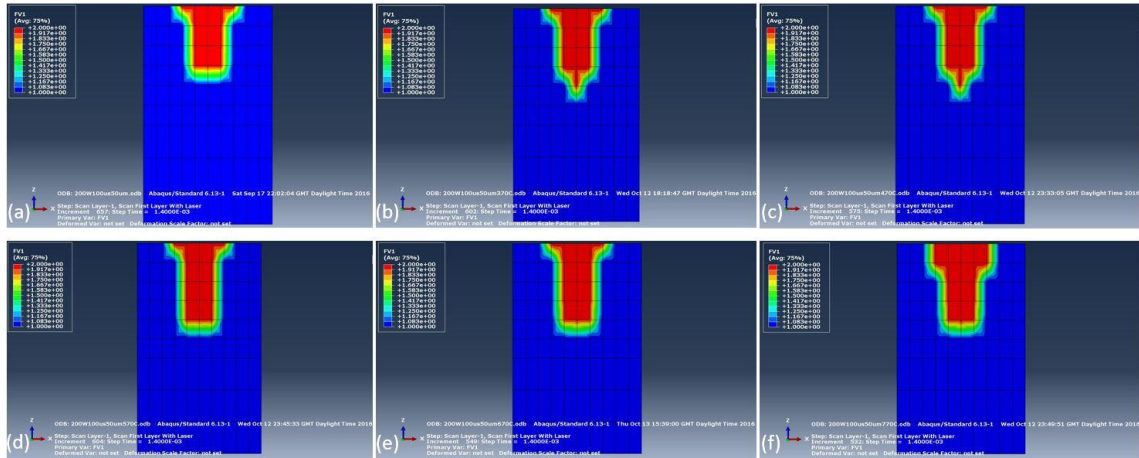


Figure 6-28 Effect of bed pre-heat temperature on melt pool dimensions (a) Test Case T-1 (100°C), (b) Test Case T-2 (370°C), (c) Test Case T-3 (470°C), (d) Test Case T-4 (570°C), (e) Test Case T-5 (670°C) and (f) Test Case T-6 (770°C)

Figure-6.28 shows a direct relation between bed pre-heat temperature and melt pool size. Increasing bed temperature resulted in larger melt pools, therefore more material to cool and thus a reduced cooling rate.

According to ref-[127], substrate pre-heating affects the rapid localised cooling rate of the melt pool and the moderate cooling rate of the part and chamber to room temperature. Figure-6.29 shows that there is an inverse relationship between bed pre-heat temperature and localised cooling rates of the melt pool. Increasing bed temperature resulted in lowering the cooling rates. Using a stop watch and reading the temperature drop from the controller after the heater has been switched off, it was found that the chamber cooled off at only 35°C per minute.

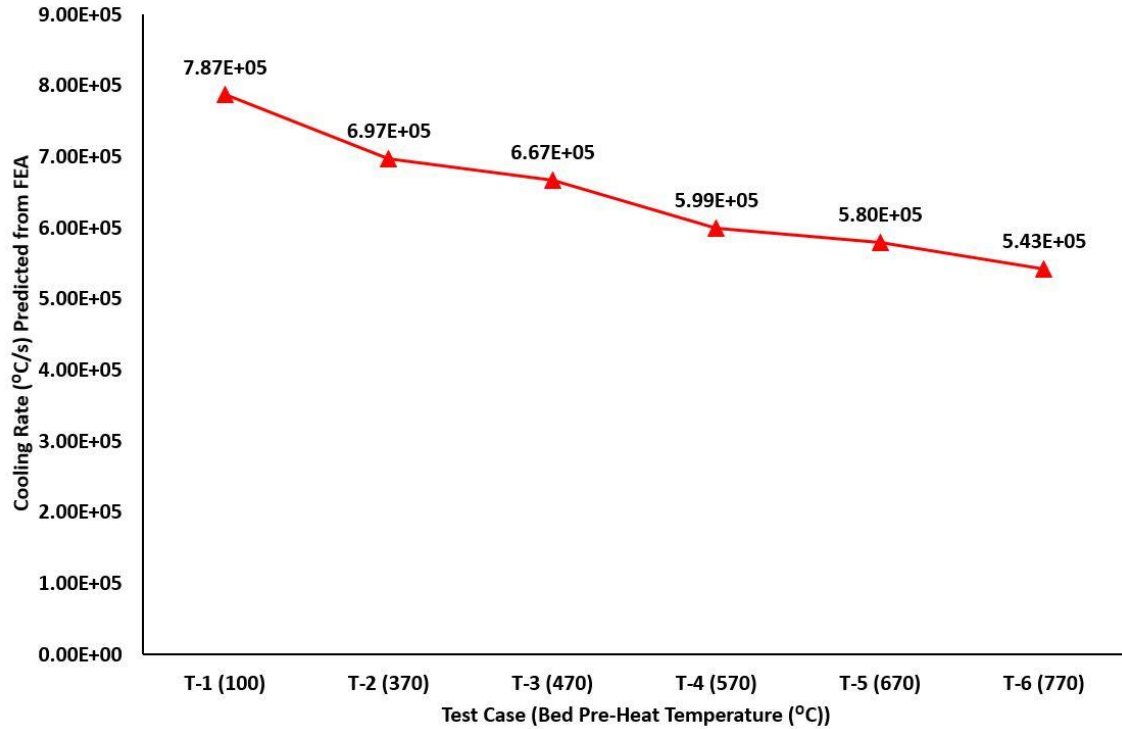


Figure 6-29 Effect of bed pre-heat temperature on cooling rates

6.7.1 Effect of Bed Pre-Heat Temperature on Porosity and Microstructure

Using the parameters optimised for density of 50µm layer thickness nearly fully dense SLM Ti6Al4V parts were achieved with varying bed pre-heat temperatures. Figure-6.28 showed that increasing bed temperature, resulted in an increase in melt-pool dimensions which is caused by the extra energy input from the bed pre-heating. Even though higher bed temperature meant more energy input into the samples, there was no variation in the % porosity of the samples. Figure-6.29 shows that increasing bed pre-heat temperature led to reduced cooling rates. Even though the cooling rates are lowered with increasing bed temperature, they are still much higher than the cooling rate required for fully martensitic microstructure in Ti6Al4V.

According to ref-[124], cooling rates higher than $410 \frac{^{\circ}\text{C}}{\text{s}}$ leads to fully martensitic microstructure for Ti6Al4V. Therefore irrespective of the bed pre-heat temperature all samples should have resulted in fully martensitic microstructure with martensitic α' laths growing inside columnar prior β grains.

The prior β grains are present in all the samples as all the test case were built at sub β transus temperatures and according to ref-[62] only heat treating above the β transus temperature resulted in the disappearance of the SLM footprint prior β columnar grains. Even though the prior β columnar grains characteristic of the layer wise building in SLM were present in all samples, the microstructure showed a clear variation with bed pre-heat temperatures. α' laths started growing in size for test case T-2 built at 370°C bed temperature, and β particles started appearing between the laths. There might have been some α' to α transformation as well but could not be identified very clearly. The increase in lath size is a consequence of the reduction in cooling rate. The bed temperature in the SLM process can be compared to the homogenisation temperature in the conventional processing route (see section-2.9.1) and therefore raising bed temperature results in a variation in the microstructure. Raising the bed temperature to 470°C for test case T-3, resulted in a further increase in α'/α lath sizes and a growth in the β particles as higher homogenisation temperature and lowered cooling rate favours grain growth. The growth in lath sizes with increasing bed temperature is consistent with the findings of ref-[128], which predicted coarser grain morphology for higher holding temperatures. Test case T-4 resulted in a basket-weave microstructure with no

martensite. Lath size increased and grain boundary β between α colonies and α laths increased. Complete transformation from a martensitic microstructure to basket-weave was due to the bed temperature being just below the martensitic decomposition temperature range of 600-650°C for Ti6AL4V. The raise in the homogenisation temperature led to grain growth and increase in β formation. Test case T-5 and T-6 led to further growth in α lath sizes with some grain boundary α globulorisation. The amount of β increased as well and all this was a consequence of further reduction in cooling rate as well as the homogenisation temperature getting closer to the β transus for Ti6Al4V. Higher growth in grain size is consistent with the findings of ref-[129], reporting that residence time just below β transus temperature greatly affects α laths growth in a basket-weave microstructure.

6.7.2 Effect of Bed Pre-Heat Temperature on Residual Stress

The results in Figure-6.30 do not show a considerable variation in the peak temperature within the meltpool and this result is consistent with the findings of ref-[127], which reported a negligible effect of bed pre-heating on the temperature of the laser irradiated zone. Figure-6.30 shows that increasing the bed pre-heat temperature reduces the temperature gradient between the top and 250 μ m depth of the meltpool. According to the Temperature Gradient Mechanism (TGM) and the cool-down phase models, the inhibition of material shrinkage during re-solidification by the underlying material leads to tensile residual stress (σ_{tens}) buildup in the top layer [28, 29]. The temperature gradient is lowered with

increasing bed pre-heat temperature as shown in Figure-6.30 and this results in a reduction in residual stress.

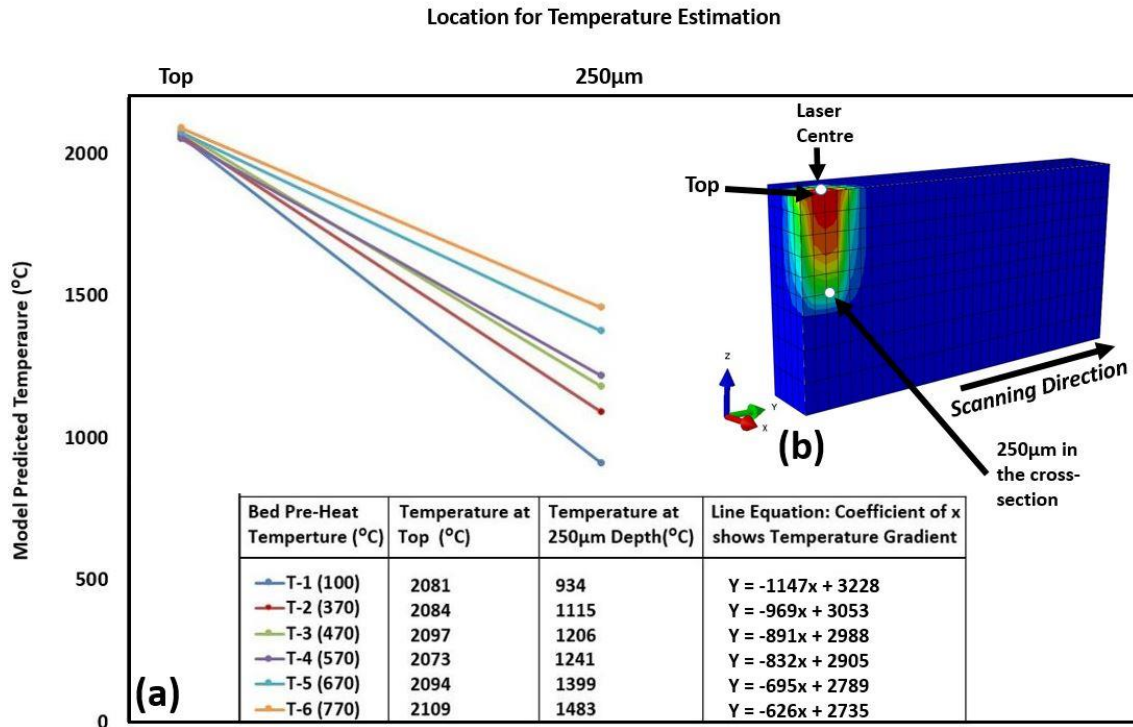


Figure 6-30 Effect of bed pre-heat temperature on temperature gradient

According to Vasinonta et al.[38], an important factor in the limited residual stress buildup at higher bed temperatures is the reduction in yield strength of materials at higher temperatures. Figure-6.31 is data adapted from ref-[130], and shows that there is an inverse relationship between yield strength of wrought annealed, Ti6Al4V and temperature, corroborating the theory of Vasinonta et al. Figure-6.31 also shows an inverse relationship between Young's Modulus and temperature. According to Figure-6.31 at 570°C both yield strength and Young's Modulus reduced to 40-45% of room temperature value, while at 100°C yield strength and Young's

Modulus were at about 90% of room temperature values [130]. This explains the reduction in residual stress with increasing bed temperatures.

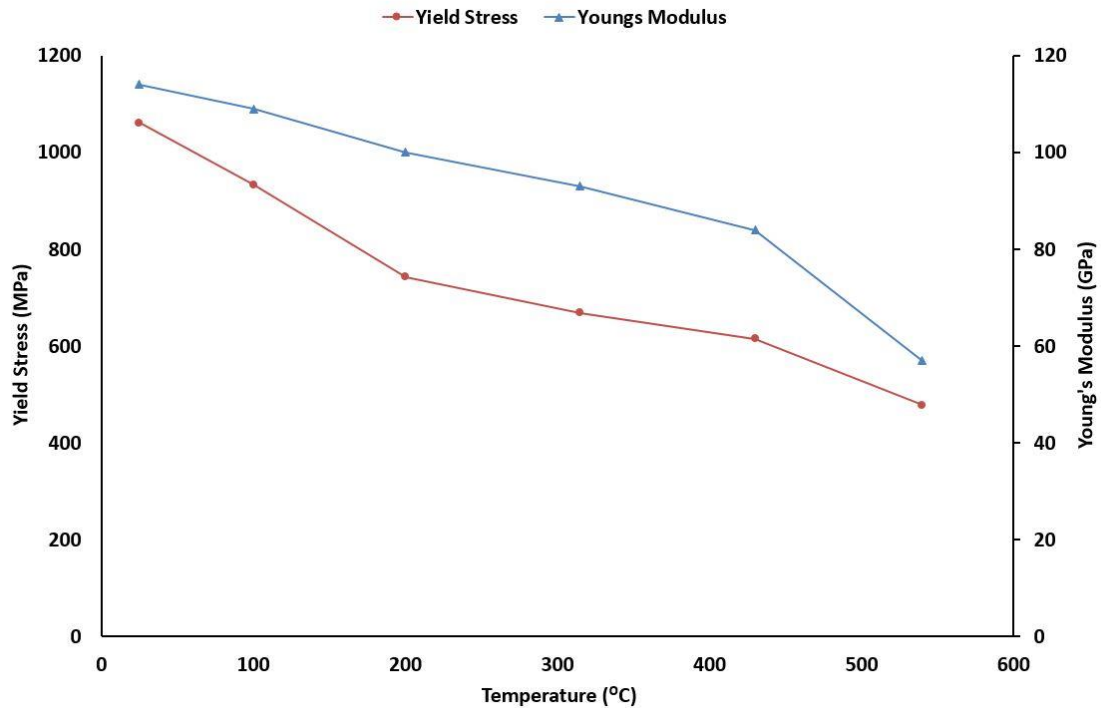


Figure-6-31 Yield stress and Young's modulus of wrought annealed Ti6Al4V as a function of temperature. Data adapted from [130].

Figure-6.32 shows an inverse relationship between cooling rate and bed pre-heat temperature. The decrease in cooling rate with increasing bed temperature is responsible for a reduction in the residual stress. The reduction in cooling rate due to increased pre-heating temperature may only be partly responsible for reducing residual stress.

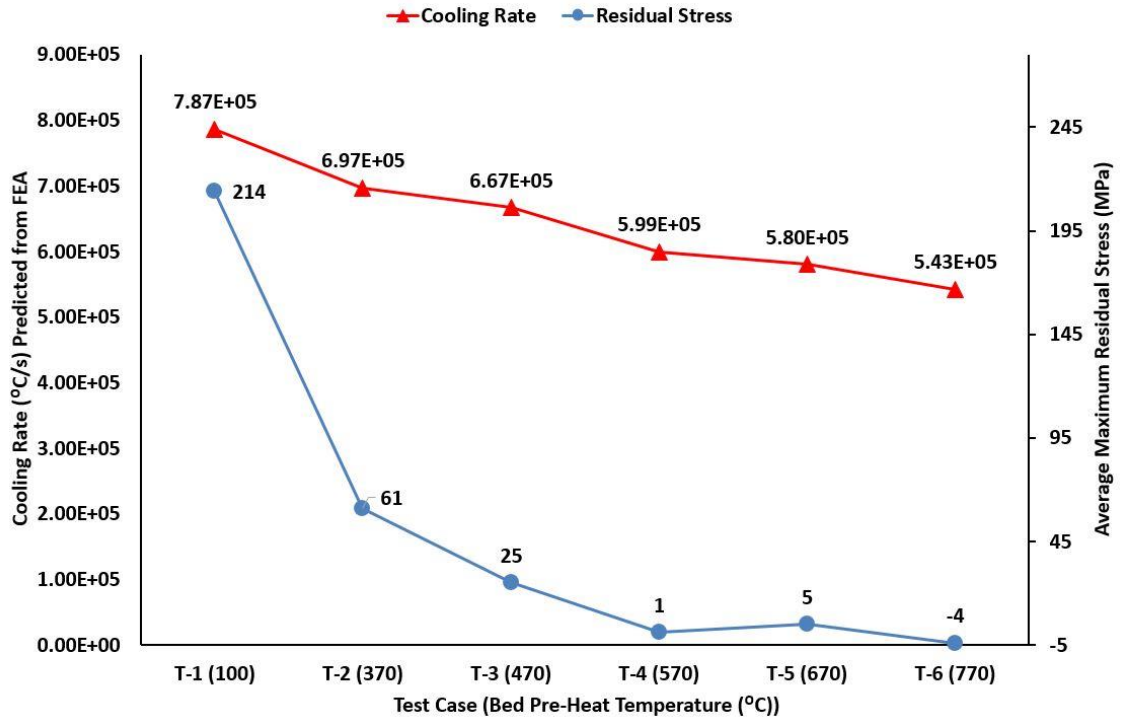


Figure 6-32 Effect of bed pre-heat temperature on cooling rate and residual stress

6.7.3 Effect of Bed Pre-Heat Temperature on Mechanical Properties

There was a slight increase of 3.2% in the yield strength of the samples with an increase in bed temperature from 100°C to 470°C. Yield strength values stayed relatively consistent up to a bed temperature of 670°C and samples built at 770°C failed prematurely resulting in no measured value for yield strength. The only probable explanation for this premature failure could be the use of sub-optimal processing parameters which were inappropriate at high bed temperatures. Using processing parameters optimised for test case T-1 at 100°C bed temperature, for high temperature builds may have caused excessive heat input into the material. Extra energy input could lead to a high level of porosity in samples due to the

initiation of key-hole melting caused by material vaporisation. Figure-6.33 shows that the amount of porosity for test case T-6 built at 770°C did not considerably increase compared with test case-T-5 samples built at 670°C, so the reason for the premature failure must be something other than porosity. Increased grain sizes generated in samples built at higher bed pre-heat temperatures (as shown in Figure-5.34), could be another factor that may have led to premature failure. According to Lütjering et al, [65, 81] the mechanical properties for lamellar microstructure are greatly dependent on the α colony. The effective slip length depends on the colony size, and has an inverse relation with the cooling rate from the β phase field. SLM Ti6Al4V samples have a totally martensitic microstructure due to the inherent high cooling rates associated with the process. The slip lengths and colony sizes of martensitic microstructure are equal to the width of the individual martensitic α' plates. Figure-2.19(a) shows that yield stress is inversely related to the slip length. Figure-2.19(b) shows that the rate of increase in yield stress with cooling rate grows exponentially, for cooling rates higher than $1000 \frac{^{\circ}\text{C}}{\text{min}}$ (cooling rate for air cooling). According to Manikandakumar et al [83], the mechanical properties of SLM Ti6Al4V parts depend on the α colony and lath sizes. α colony and lath sizes which are equal to the size of single martensitic α' lath in the martensitic microstructure, result in dislocation pile ups. Dislocations movement is restricted by the smaller α colony sizes of the martensitic microstructure which results in limited plastic deformation in SLM Ti6Al4V components. Restricted dislocations movement and limited plastic deformation result in higher yield strength and UTS of SLM parts. According to effective slip length and dislocation movement theories [65, 81], higher bed

temperature should result in lower yield strength, as increasing bed temperature results in a lower cooling rate and larger α colonies. Even though the cooling rate is decreasing with increasing bed temperature, the cooling rate at the highest bed temperature is still much higher than $10000 \frac{^{\circ}\text{C}}{\text{min}}$ (cooling rate of water quenched samples(highest yield strength)) as shown in Figure-2.19(b). Therefore no decrease in yield strength is noticed for samples built at high bed temperatures. Another factor that may be responsible for the high yield strength of high bed temperature SLM Ti6Al4V samples could be the formation of nano β particles in α laths (see SEM images in Figure-5.31 to Figure-5.34).

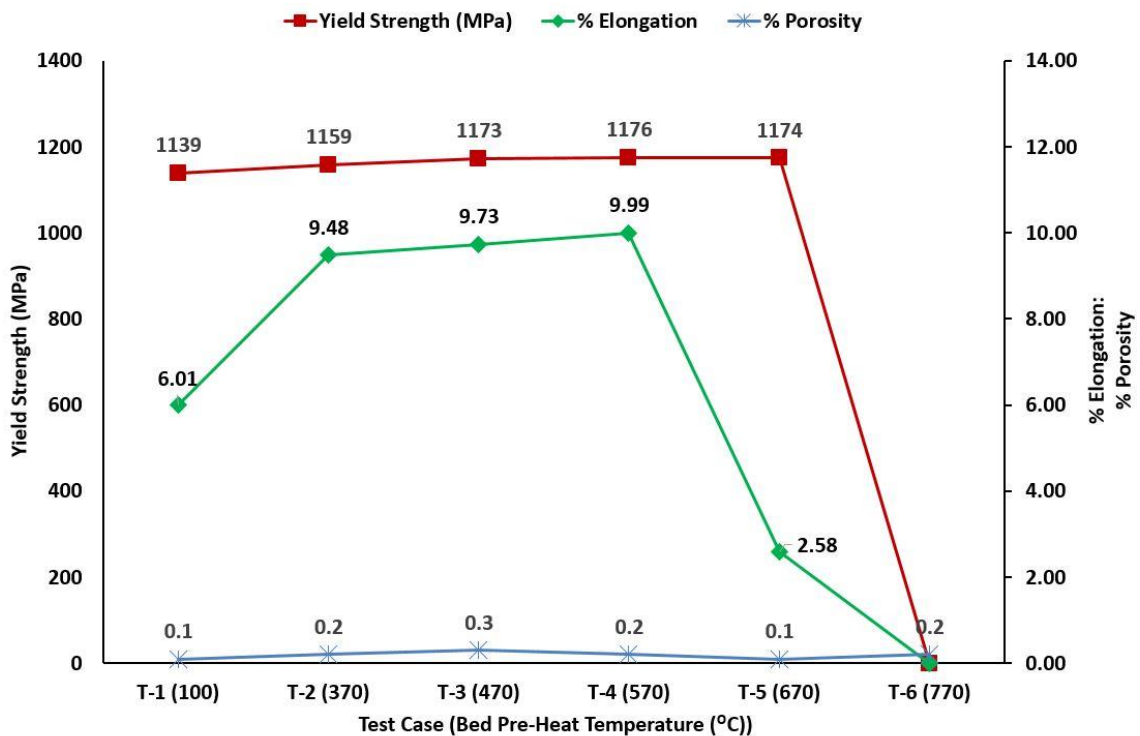


Figure 6-33 Effect of bed pre-heat temperature on %Porosity, % Elongation and Yield Strength

Figure-6.31 shows a direct relation between sample elongation and bed pre-heat temperature. %Elongation shows a considerable improvement up to 570°C bed pre-heat temperature for test case T-4, with 66.2% improvement in elongation at 570°C compared with standard samples built at 100°C. At 670°C bed temperature for test case T-5 there is a sharp decline of 74.7% compared to test case T-4 built at 570°C. Increasing the bed temperature to 770°C for test case T-6, resulted in no measured value of elongation due to premature failure. Lütjering et al. [65, 81] presented a more complex relationship between ductility and cooling rate. Figure-2.19(a) showed that decreasing slip length results in an increase in ductility. Figure-2.19(b) showed that increasing cooling rate increased ductility up to an optimum cooling rate for maximum ductility. Beyond this point of maximised ductility there is a sharp decline in ductility with any increase in the cooling rate. According to Sujoy Kumar [82] higher cooling rate results in a reduction in slip length, which causes a reduction in the pile-up length. Reduced pile-up length leads to lower stress concentrations which delays crack nucleation and thus results in improved ductility. Secondly refinement of the lamellar structure leading to the increased strength of the matrix is responsible for the decrease in ductility with increasing cooling rate beyond the point of maximised ductility. The difference in matrix strength and coarser grain boundary α along β -grain boundaries is responsible for preferential premature crack nucleation in the softer grain boundary α [82]. Increasing bed temperature results in lowering the cooling rate but is still higher than the optimum intermediate cooling rate resulting in maximised ductility. Therefore the improvement in ductility up to a bed temperature of 570°C can be attributed to the fact that increasing the

bed temperature is shifting the cooling rate closer to the cooling rate for maximum ductility. According to the cooling rate theory, test case T-5 built at 670°C and test case T-6 built at 770°C bed pre-heat temperatures should have resulted in further improvement in the ductility of the samples. However the results in Figure-6.33 show a sharp decline of 74.7% in % elongation of samples produced at a bed temperature of 670°C, test case T-5 compared to test case T-4 built at 570°C and samples built at 770°C for test case T-6, showed no measured value of % elongation due to premature failure. The second mechanism of difference in matrix strength and coarser grain boundary α resulting in premature crack nucleation in the softer grain boundary α does not explain this behavior. An increase in cooling rate would be required for premature crack nucleation in softer grain boundary α whereas in this scenario the higher bed temperature is in-fact decreasing the cooling rate.

According to Qian et al.[129], for temperatures in the range of 600-980°C, just below the β transus temperature of Ti6Al4V, the cooling rate and residence times are very critical in terms of α laths growth in a basket-weave microstructure. In Direct Laser Fabrication of Ti6Al4V components, α laths growth is enhanced when getting closer to the β transus temperature [129]. In principle SLM is very similar to DLF except the difference in delivery of powder feed (In DLF powder is blown into the path of a focused laser, much like laser cladding). Therefore it is a valid approximation that the thermal cycles experienced during the high temperature SLM process are quite similar to the DLF process. Thus extending the reasoning reported in ref-[129], to the built at 670°C and 770°C bed pre-heat temperature is quite reasonable. Figure-5.34(a) and (b), show that at 670°C and 770°C there has been a considerable grain

growth with some globular α grains highlighted by the red ellipses. A range of sizes of α laths exist in the microstructure of these high temperature samples. Similarly there is a considerable growth in grain boundary β as depicted in Figure-5.34(c). Larger α laths and colonies along with the existence of some globular α mean larger slip lengths and therefore lower yield strength and as well as lower ductility as Figure-2.19(a) shows an inverse relationship between slip lengths and mechanical properties [65, 81]. The existence of a wide range of grain sizes across the microstructure along with coarser grain boundary β would result in the creation of weaker locations for crack nucleation and growth. Premature failure of the tensile specimens outside the gauge length was most probably a consequence of the existence of these weaker sites for crack nucleation. Due to the existence of such grain boundary weak locations the effect of porosity as an internal defect becomes crucial in enhancing the possibility of premature failure. The parameters used for high temperature builds were optimised for 100°C Bed Pre-Heat Temperature. Therefore a lot more energy was inputted into the samples built at higher bed pre-heat temperatures, which led to a slight increase in porosity and combined with the non-equilibrium grain sizes it might have caused the premature failure. For further work optimising the process parameters for each bed temperature will be helpful in determining the true mode of failure and as well as improving the mechanical properties of SLM Ti6Al4V parts.

Vickers micro hardness values of the samples increased with increasing bed pre-heat temperatures up to 670°C for test case T-5, resulting in 13% increase at 670°C compared to test case T-1 built at 100°C bed temperature. Increasing the bed

temperature further to 770°C for test case T-6, resulted in 1.8% decrease compared with samples built at 670°C, test case T-5. For samples built at a bed temperature of up to 470°C the increase in micro-hardness can be attributed to the growth in the amount of β between α'/α laths. For samples built at 570°C and above the increase in micro hardness is probably a consequence of the increase in the amount of β between α colony boundaries and as well as the growth of nano β the α laths. Even though Figure-5.34c shows an increase in the amount of β between α colonies boundaries and as well as the amount of nano β particles inside α laths for samples built at 770°C bed temperature the micro-hardness decreased by 1.8%. The only probable reason for this decrease in micro-hardness despite an increase in β within the samples is the increase in the grain size (see SEM images Figure-5.31 to Figure-5.34). Figure-5.34(c) provides a clear illustration of the β growing between α colonies grain boundaries and as well as the nano β growing inside α laths. The micro-hardness results shown in Figure-5.37 illustrate an important point, that the micro-hardness values across the height of the samples built at higher bed temperatures are consistent as shown by the values for standard deviation. Less variation in the micro-hardness across the height of the samples indicates that the samples have a consistent micro structure throughout the height. However the standard deviation of samples built at 100°C bed temperature show a wide spread in the micro-hardness over the 12 indentations taken along the height of the sample in the build direction. This variation in the micro-hardness indicates that the microstructure across the sample built at 100°C bed pre-heat temperature may not be uniform. The possibility of non-uniform microstructure across the sample is

corroborated by the existence of internal microstructural defects as can be seen in the SEM image of test case T-1, built at 100°C shown in Figure-5.31.

7 Strategic Stress Reduction Strategy

7.1 Geometrical Dependence of Residual Stress

This section presents the results of contour method used for residual stress measurement in an I-Beam geometry. Figure-7.1(a) shows the dimensions of the I-Beam geometry used for strategic application of stress reduction strategies. Figure-7.1(b) shows the dimensions of the regions where stress reduction strategies were applied for the different test case.

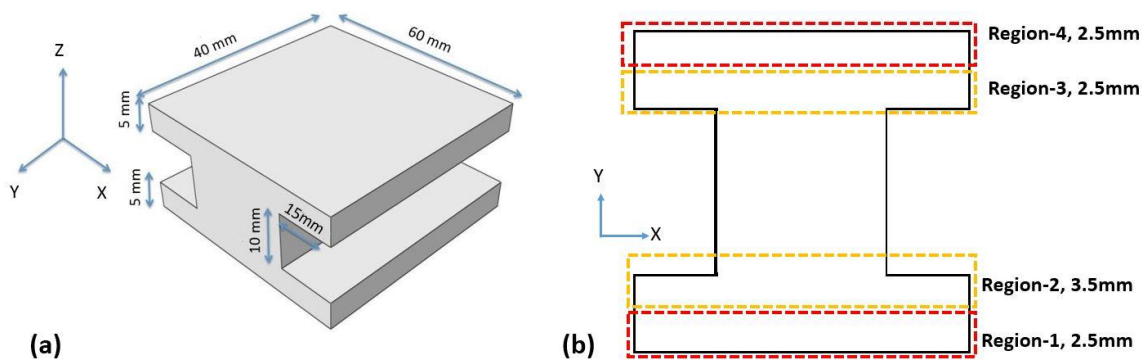


Figure 7-1 (a) Dimensioned I-Beam geometry (b) I-Beam regions for strategic application of stress reduction strategies.

7.1.1 Identifying High Stress Regions in a Complex Geometry

An I-Beam cross section was manufactured using the optimum combination of parameters for 50 μ m layer thickness, found from density optimisation trials (see section-5.1). The first sample was built at a bed temperature of 100 $^{\circ}$ C, with a

purpose of identifying the high residual stress regions in the cross section and understanding the geometrical dependence of residual stress. Contour method was used for mapping the residual stress across the cross section.

Figure-7.2 the residual stress map of the I-Beam manufactured with optimised parameters from density trials, test case IB-1. The legend shows that the highest value of residual stress measured in the test case IB-1 sample was 320MPa. Black dashed rectangles highlight the regions with high residual stress. Figure-7.2 shows that for the I-Beam geometry, test case IB-1, the high residual stress regions was identified as the corners between the lower flange and the web bottom section. The corners in Region-2 shows residual stress between 80-320MPa. Another high stress region, was identified as region-4, the top of the I-Beam geometry. Region-4, shows that the highest stress of 320MPa occurs near the top surface.

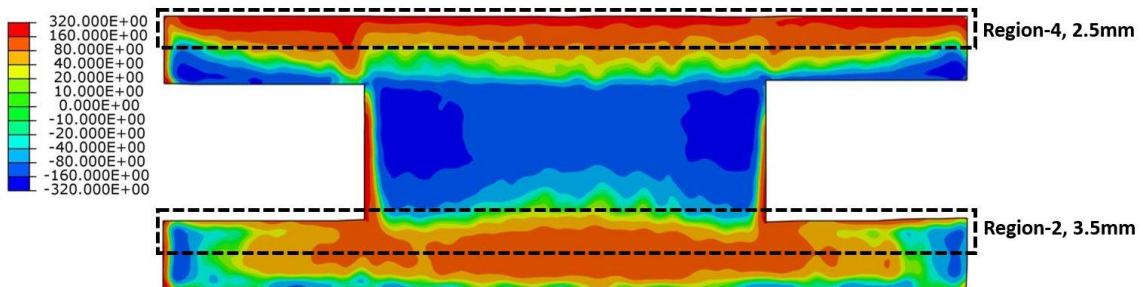


Figure 7-2. Residual Stress Map Standard I-Beam (Test Case IB-1) Manufactured with Optimum Parameters from Density Optimisation Trials (High Stress Regions Indicated by Dashed Black Rectangles, region-2 and region-4)

7.1.2 Strategic application of residual stress reduction strategies

Section-5.3.2, Figure-5.11 showed that increasing the layer thickness to 75 μ m, reduced the residual stress by 27.1%, compared to the standard samples

manufactured with 50 μ m layer thickness. Regions-2 and 4 of test case IB-1 (identified as the high stress as shown in Figure-7.2). Regions-2 and 4 were strategically built with the application of a 75 μ m layer thickness and associated optimum parameters. The strategic stress reduction in test case IB-2 cross section was managed by building the I-Beam with a combination of 50 μ m and 75 μ m layer thickness. 75 μ m layer thickness was applied in 3.5mm build height in region-2 and 2.5mm build height in region-4. The rest of test case IB-2 was built with 50 μ m layer thickness.

Section-5.6.2, Figure-5.26 showed that decreasing the power and increasing exposure time, keeping the Energy Density constant at the optimum resulted in reduction in residual stress. Using power 150W and exposure 133 μ s combination, resulted in 16.8% residual stress reduction compared with samples made with 200W power and 100 μ s exposure (Optimum power and exposure combination from density optimisation trials for 50 μ m layer thickness(see section-5.1)). Both combinations of power and exposure result in an Energy Density of $76.92 \frac{J}{mm^3}$. Test case IB-3, was manufactured using 50 μ m layer thickness. Region-2 and Region-4 of the I-Beam (identified as the high stress regions section-7.1.1), for test case IB-3 were strategically built with the application of 150W power and 133 μ s exposure. The strategic stress reduction in the I-Beam cross section was managed by building the I-Beam with the application of different power and exposure combinations to the different regions of test case IB-3. 150W power and 133 μ s exposure was applied

in 3.5mm build height in region-2 and 2.5mm build height in region-4. The rest of test case IB-3 was built with 200W power and 100µs exposure.

Section-5.7.2, Figure-5.35 showed that increasing the bed pre-heat temperature to 570°C, completely got rid of the residual stress compared with the standard samples manufactured at 100°C bed temperature resulting in 214MPa residual stress. The stress reduction in the I-Beam cross section was managed by building test case IB-4 at a bed pre-heat temperature of 570°C, using 50µm layer thickness with optimum combination of parameters from density optimisation trials (see section 5.1).

Test case IB-5 was built by applying 75µm layer thickness in the regions below the identified high stress regions for test case IB-1. The strategic stress reduction in test case IB-5 cross section was managed by building the I-Beam with a combination of 50µm and 75µm layer thickness. 75µm layer thickness was applied in 2.5mm build height in region-1 and 3. The rest of test case IB-5 was built with 50µm layer thickness.

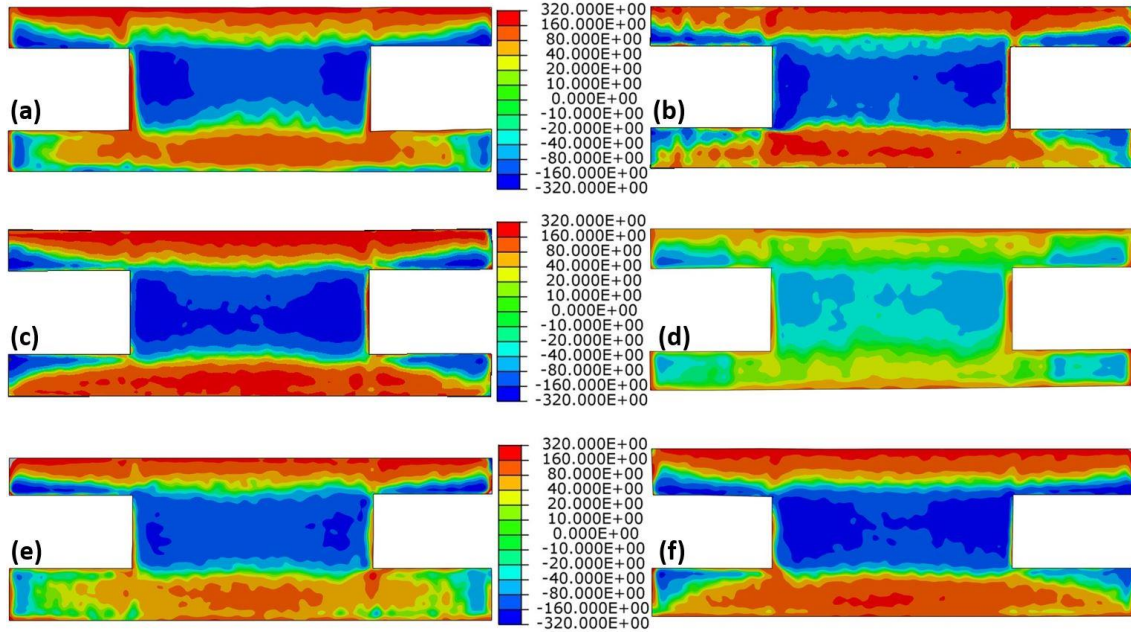


Figure 7-3. Comparison of residual stress contour maps for various test cases (a) IB-1 (Standard I-Beam with optimised parameters), (b) IB-2 (75 μ m Layer Thickness for Region-2 & Region-4), (c) IB-3 (150W power and 133 μ s exposure for Region-2 & Region-4), (d) IB-4 (570 $^{\circ}$ C Bed pre-heating on Renishaw SLM-125 machine), (e) IB-5 (75 μ m Layer Thickness for Region-1 & Region-3) and (f) IB-6 (150W power and 133 μ s exposure for Region-1 & Region-3).

Test case IB-6 was built by applying 150W power and 133 μ s exposure in the regions below the identified high stress regions for test case IB-1. The strategic stress reduction in the I-Beam cross section was managed by building the I-Beam with the application of different power and exposure combinations to the different regions of test case IB-6. 150W power and 133 μ s exposure was applied in 2.5mm build height in region-1 and 3. The rest of test case IB-3 was built with 200W power and 100 μ s exposure. Figure-7.3 shows a comparison of the residual stress contour maps for the various test cases. The contour maps of Figure-7.3 show a variation in residual stress across different samples but the trends are very hard to discern.

The effect of stress reduction strategies on the residual stress distribution in the four regions of the I-Beam samples is presented in a decreasing order of the highest stress in regions of test case IB-1. The regions of test case IB-1 can be arranged in a descending order of highest residual stress distribution as region-4, region-2, region-1 and region-3.

7.1.3 Effect of strategic stress reduction strategies on residual stress in Region-4

Matlab image analysis script was used to extract the area associated with each stress level in region-4 of the various test cases shown in Figure-7.3. Figure-7.4 shows the corresponding areas of different stress levels in region-4 (top of the I-Beam geometry), for various test cases studied.

Figure-7.5 shows the variation in residual stress for various test cases with strategic application of stress reduction strategies. The results in Figure-7.5 show that with the application of 75 μ m layer thickness to region-4 (Identified as the high stress regions see section 7.1.1), for test case IB-2 reduced the %area of maximum residual stress (320MPa) in region-4 for the cross section of test case IB-2 to 23.5%. Test case IB-2 showed a reduction of 7.5% in 320MPa residual stress region compared to the standard I-Beam, test case IB-1. Figure-7.5 shows that, test case IB-2, 160MPa residual stress region area increased by 29.2% and the 80MPa residual stress region area decreased by 67.5% compared with test case IB-1.

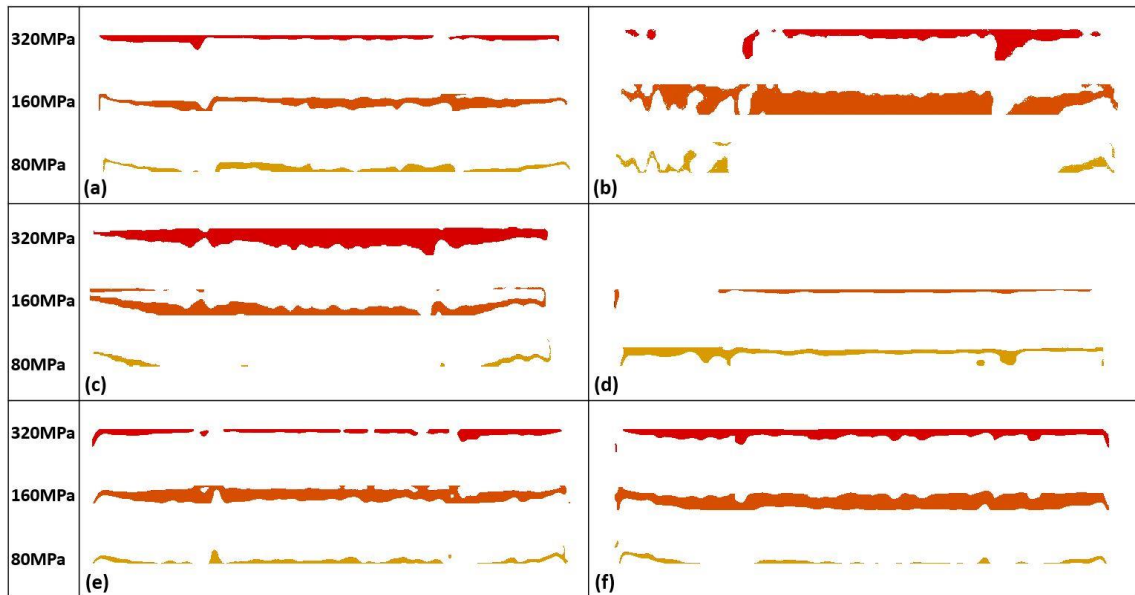


Figure 7-4. Region-4 areas corresponding to different stress levels for various test cases (a) IB-1 (Standard I-Beam with optimised parameters), (b) IB-2 (75 μ m Layer Thickness for Region-2 & Region-4), (c) IB-3 (150W power and 133 μ s exposure for Region-2 & Region-4), (d) IB-4 (570 $^{\circ}$ C Bed pre-heating on Renishaw SLM-125 machine), (e) IB-5 (75 μ m Layer Thickness for Region-1 & Region-3) and (f) IB-6 (150W power and 133 μ s exposure for Region-1 & Region-3).

Overall it can be seen that region-4 of test case IB-2 presents a more uniform stress distribution compared with test case-IB-1. From a component point of view this can be considered as an improvement as hot spots can be detrimental for preferential failure of parts.

The results in Figure-7.4 show that with the application of 150W power and 133 μ s exposure to region-4 (Identified as the high stress regions see section 7.1.1), for test case IB-3 increased the %area of maximum residual stress (320MPa) in region-4 for the cross section of test case IB-3 to 51.1%. Test case IB-3 showed an increase of 101% in 320MPa residual stress region compared to the standard I-Beam, test case

IB-1. Figure-7.5 shows that for test case IB-3, 160MPa residual stress region area reduced by 26.7% and the 80MPa residual stress region area decreased by 79.7% compared with test case IB-1. Overall it can be seen that region-4 of test case IB-3 presents a more uniform stress distribution compared with test case-IB-1. From a component point of view this can be considered as an improvement as hot spots can be detrimental for preferential failure of parts.

The results in Figure-7.5 show that building the I-Beam geometry at a bed pre-heat temperature of 570°C, for test case IB-4 resulted in the overall residual stress in region-4 for the cross section of test case IB-4. Test case IB-4 showed no 320MPa residual stress region. Figure-7.5 shows that for test case IB-4, 160MPa residual stress region area reduced by 70.5%, while the 80MPa residual stress region area increased by 34.9% compared with test case IB-1. Overall it can be seen that region-4 of test case IB-4 presents a much lower stress distribution compared with test case-IB-1. The beneficial effect of pre-heating the bed to higher temperature on residual stress reduction has also been reported in refs-[52, 63, 64, 120]. Pre-heating the bed results in the reduction of thermal gradients and cooling rates, which in turn leads to the reduction of residual stress build up[52, 120]. It was reported in the work by Ali *et al*[120], bed pre-heat temperature of 570°C totally eliminated the residual stress from block samples

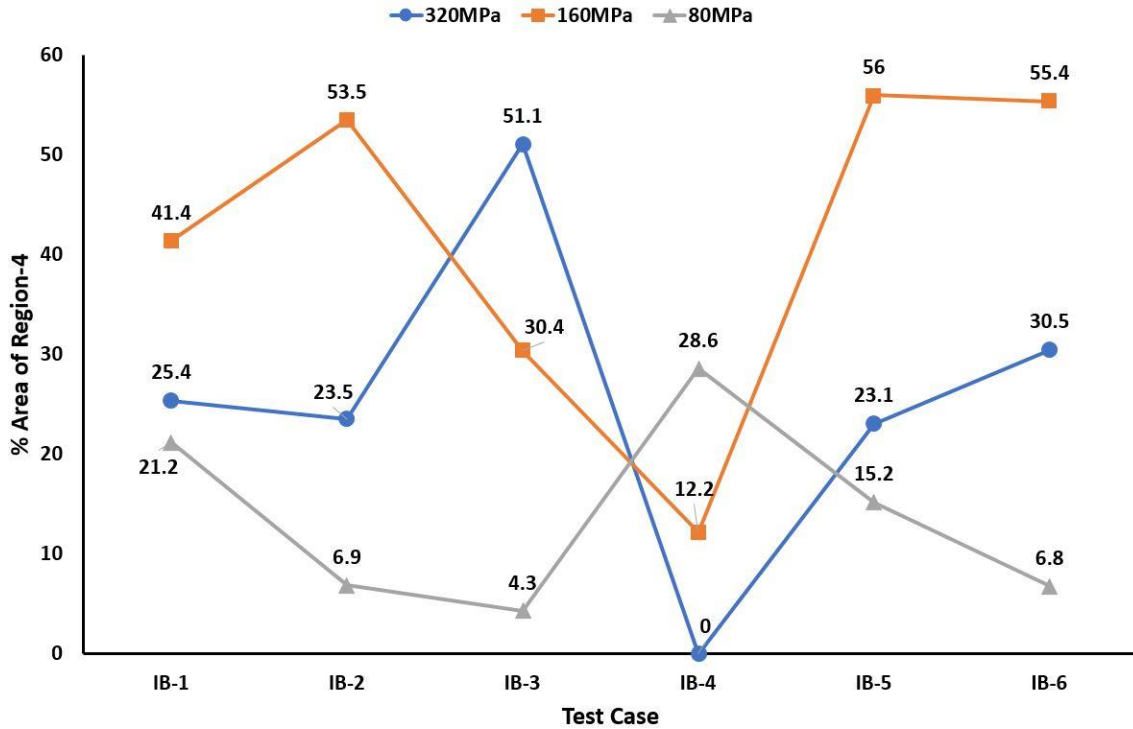


Figure 7-5. Region-4 residual stress variation in various test cases (a) IB-1 (Standard I-Beam with optimised parameters), (b) IB-2 (75 μ m Layer Thickness for Region-2 & Region-4), (c) IB-3 (150W power and 133 μ s exposure for Region-2 & Region-4), (d) IB-4 (570 $^{\circ}$ C Bed pre-heating on Renishaw SLM-125 machine), (e) IB-5 (75 μ m Layer Thickness for Region-1 & Region-3) and (f) IB-6 (150W power and 133 μ s exposure for Region-1 & Region-3).

The small high stress area in region-4 of test case IB-4 can be attributed to the differential heat flow in the web and the supports of the upper flange. Part of the top flange on the web will have higher heat flow to the substrate compared with the overhanging part. This would possibly lead to the central part of the top flange having a higher cooling rate compared with the overhanging region and thus as can be seen from Figure-7.3(d) a higher stress distribution. The results from Figure-7.5 show that pre-heating the bed is the best solution for the residual stress problem associated with SLM components.

The results in Figure-7.5 show that with the application of 75 μ m layer thickness to region-3 (just below the identified high stress region), for test case IB-5 reduced the %area of maximum residual stress (320MPa) in region-4 for the cross section of test case IB-5 to 23.1%. Test case IB-5 showed a reduction of 9.1% in 320MPa residual stress region compared to the standard I-Beam, test case IB-1. Figure-7.5 shows that, for test case IB-5, 160MPa residual stress region area increased by 35.3% and the 80MPa residual stress region area decreased by 28.3% compared with test case IB-1. Overall it can be seen that region-4 of test case IB-5 presents a more uniform stress distribution compared with test case-IB-1. From a component point of view this can be considered as an improvement as hot spots can be detrimental for preferential failure of parts.

The results in Figure-7.5 show that with the application of 150W power and 133 μ s exposure to region-3 (just below the identified high stress region-4), for test case IB-6 increased the %area of maximum residual stress (320MPa) in region-4 for the cross section of test case IB-3 to 30.5%. Test case IB-6 showed an increase of 20.1% in 320MPa residual stress region compared to the standard I-Beam, test case IB-1. Figure-7.5 shows that for test case IB-6, 160MPa residual stress region area increased by 33.8% and the 80MPa residual stress region area decreased by 67.9% compared with test case IB-1. Overall it can be seen that region-4 of test case IB-6 presents a more uniform stress distribution compared with test case-IB-1. From a component point of view this can be considered as an improvement as hot spots can be detrimental for preferential failure of parts.

The results of Figure-7.5 show that strategically applying stress reduction strategies to cross sections of complex parts can lead to a reduction in residual stress. The application of stress reduction strategies to region-3 just below the high stress region-4, for test cases IB-5 and IB-6 showed promising results compared to test cases IB-2 and IB-3 where the stress reduction strategies were directly applied to region-4(identified as high stress region in IB-1). This work shows that by experimenting with the location and build height for strategic application of stress reduction strategies a plausible solution for stress reduction in critical regions of complex parts can be possible.

7.1.4 Effect of strategic stress reduction strategies on residual stress in Region-2

Matlab image analysis script was used to extract the area associated with each stress level in region-2 of the various test cases shown in Figure-7.3. Figure-7.6 shows the corresponding areas of different stress levels in region-2 (top of the bottom flange of the I-Beam geometry), for various test cases studied.

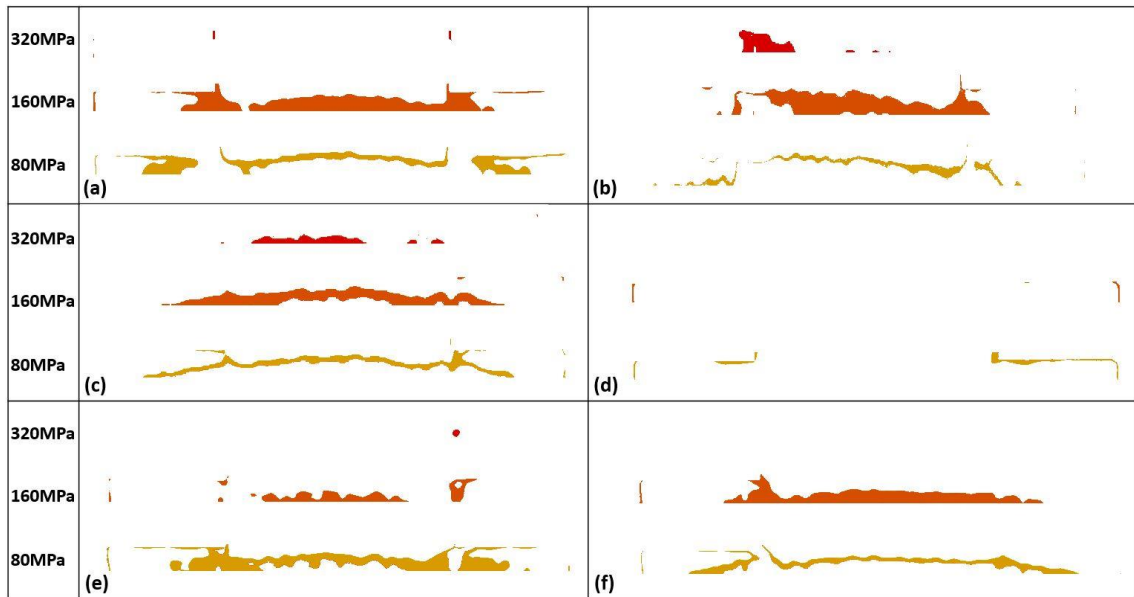


Figure 7-6. Region-2 areas corresponding to different stress levels for various test cases (a) IB-1 (Standard I-Beam with optimised parameters), (b) IB-2 (75µm Layer Thickness for Region-2 & Region-4), (c) IB-3 (150W power and 133µs exposure for Region-2 & Region-4), (d) IB-4 (570°C Bed pre-heating on Renishaw SLM-125 machine), (e) IB-5 (75µm Layer Thickness for Region-1 & Region-3) and (f) IB-6 (150W power and 133µs exposure for Region-1 & Region-3).

Figure-7.6 shows the variation of residual stress in region-2 for various test cases with strategic application of stress reduction strategies. The results in Figure-7.7 show that with the application of 75µm layer thickness to region-2 (Identified as the high stress regions see section 7.1.1), for test case IB-2 increased the %area of maximum residual stress (320MPa) in region-2 for the cross section of test case IB-2 to 4.8%. Test case IB-2 showed an increase of 1100% in 320MPa residual stress region compared to the standard I-Beam, test case IB-1. Figure-7.7 shows that, for test case IB-2, 160MPa residual stress region area decreased by 23.8% and the 80MPa residual stress region area decreased by 50.4% compared with test case IB-

1. Overall it can be seen that region-2 of test case IB-2 presents a lower stress distribution compared with test case-IB-1, except for a hot spot of 320MPa generated just below the web.

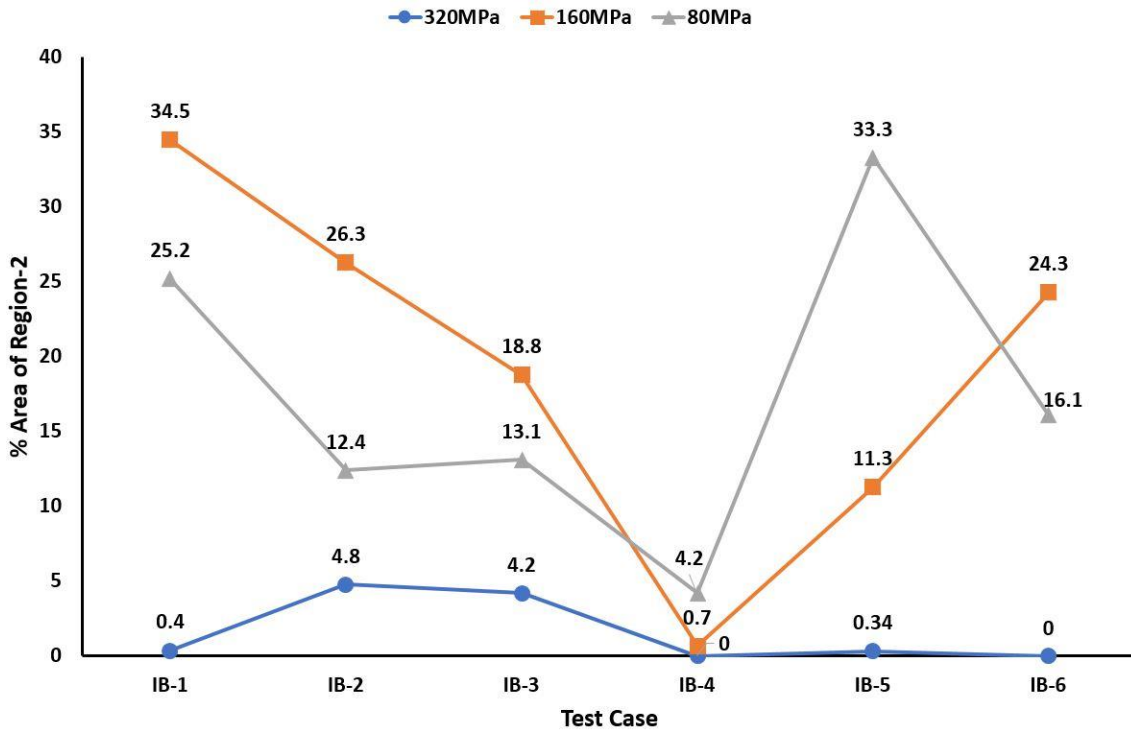


Figure 7-7. Region-2 residual stress variation in various test cases (a) IB-1 (Standard I-Beam with optimised parameters), (b) IB-2 (75 μ m Layer Thickness for Region-2 & Region-4), (c) IB-3 (150W power and 133 μ s exposure for Region-2 & Region-4), (d) IB-4 (570 $^{\circ}$ C Bed pre-heating on Renishaw SLM-125 machine), (e) IB-5 (75 μ m Layer Thickness for Region-1 & Region-3) and (f) IB-6 (150W power and 133 μ s exposure for Region-1 & Region-3).

The results in Figure-7.7 show that with the application of 150W power and 133 μ s exposure to region-2 (identified as the high stress regions see section 7.1.1), for test case IB-3 increased the %area of maximum residual stress (320MPa) in region-2 for the cross section of test case IB-3 to 4.2%. Test case IB-3 showed an increase of

950% in 320MPa residual stress region compared to the standard I-Beam, test case IB-1. Figure-7.7 shows that for test case IB-3, 160MPa residual stress region area reduced by 45.5% and the 80MPa residual stress region area decreased by 48% compared with test case IB-1. Overall it can be seen that region-2 of test case IB-3 presents a lower stress distribution compared with test case-IB-1, except for a hot spot of 320MPa, just below the web.

The results in Figure-7.7 show that building the I-Beam geometry at a bed pre-heat temperature of 570°C, for test case IB-4 resulted in a reduction in the overall residual stress in region-2 for the cross section of test case IB-4. Test case IB-4 showed no 320MPa residual stress region. Figure-7.7 shows that for test case IB-4, 160MPa residual stress region area reduced by 98%, while the 80MPa residual stress region area increased by 83.3% compared with test case IB-1. Overall it can be seen that region-2 of test case IB-4 presents a much lower stress distribution compared with test case-IB-1.

The results in Figure-7.7 show that with the application of 75µm layer thickness to region-1 (just below the identified high stress region), for test case IB-5 reduced the %area of maximum residual stress (320MPa) in region-2 for the cross section of test case IB-5 to 0.34%. Test case IB-5 showed a reduction of 15% in 320MPa residual stress region compared to the standard I-Beam, test case IB-1. Figure-7.7 shows that, for test case IB-5, 160MPa residual stress region area decreased by 67.2% and the 80MPa residual stress region area increased by 32.1% compared with test case IB-1. Overall it can be seen that region-2 of test case IB-5 presents a lower stress distribution compared with test case-IB-1. Applying the stress reduction strategy to

region-1, just below the high stress region-2 resulted in a lower overall stress state for test case IB-5 compared with test case IB-2 when the same strategy was applied directly to the high stress region-2.

The results in Figure-7.7 show that with the application of 150W power and 133 μ s exposure to region-3 (just below the identified high stress region-2), for test case IB-6 eliminated the 320MPa stress in region-2 for the cross section of test case IB-6. Figure-7.7 shows that for test case IB-6, 160MPa residual stress region area decreased by 29.6% and the 80MPa residual stress region area decreased by 36.1% compared with test case IB-1. Overall it can be seen that region-2 of test case IB-6 presents a lower stress distribution compared with test case-IB-1.

The results of Figure-7.7 show that strategically applying stress reduction strategies to cross sections of complex parts can lead to a reduction in residual stress. The application of stress reduction strategies to region-1 just below the high stress region-2, for test cases IB-5 and IB-6 showed promising results compared to test cases IB-2 and IB-3 where the stress reduction strategies were directly applied to region-2(identified as high stress region in IB-1). This work shows that by experimenting with the location and build height for strategic application of stress reduction strategies a plausible solution for stress reduction in critical regions of complex parts can be possible.

7.1.5 Effect of strategic stress reduction strategies on residual stress in Region-1

Matlab image analysis script was used to extract the area associated with each stress level in region-1 of the various test cases shown in Figure-7.3. Figure-7.8 shows the corresponding areas of different stress levels in region-1 (Bottom of the I-Beam geometry), for various test cases studied.

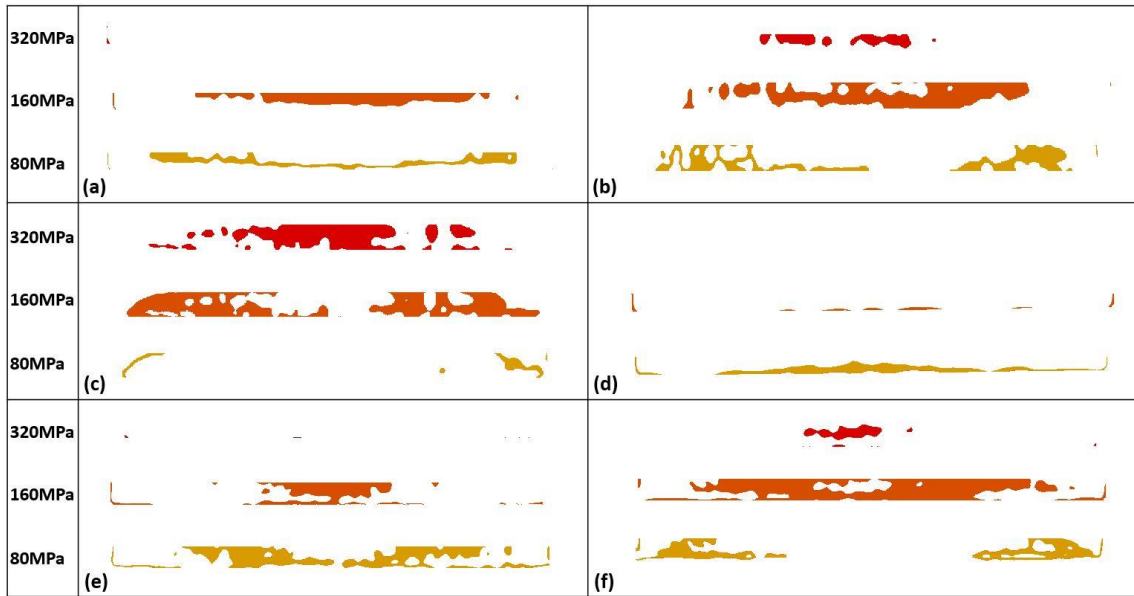


Figure 7-8. Region-1 areas corresponding to different stress levels for various test cases (a) IB-1 (Standard I-Beam with optimised parameters), (b) IB-2 (75 μ m Layer Thickness for Region-2 & Region-4), (c) IB-3 (150W power and 133 μ s exposure for Region-2 & Region-4), (d) IB-4 (570 $^{\circ}$ C Bed pre-heating on Renishaw SLM-125 machine), (e) IB-5 (75 μ m Layer Thickness for Region-1 & Region-3) and (f) IB-6 (150W power and 133 μ s exposure for Region-1 & Region-3).

Figure-7.9 shows the variation of residual stress in region-1 for various test cases with strategic application of stress reduction strategies. The results in Figure-7.9

show that with the application of 75 μ m layer thickness to region-2 (Identified as the high stress regions see section 7.1.1), for test case IB-2 increased the %area of maximum residual stress (320MPa) in region-1 for the cross section of test case IB-2 to 8.8%. Test case IB-2 showed an increase of 4300% in 320MPa residual stress region compared to the standard I-Beam, test case IB-1. Figure-7.9 shows that, for test case IB-2, 160MPa residual stress region area increased by 29.5% and the 80MPa residual stress region area increased by 2.9% compared with test case IB-1. Overall it can be seen that region-1 of test case IB-2 presents a higher stress distribution compared with test case-IB-1.

The results in Figure-7.9 show that with the application of 150W power and 133 μ s exposure to region-2 (identified as the high stress regions see section 7.1.1), for test case IB-3 increased the %area of maximum residual stress (320MPa) in region-2 for the cross section of test case IB-3 to 34.2%. Test case IB-3 showed an increase of 17000% in 320MPa residual stress region compared to the standard I-Beam, test case IB-1. Figure-7.9 shows that for test case IB-3, 160MPa residual stress region area increased by 44.4% and the 80MPa residual stress region area decreased by 80.5% compared with test case IB-1. Overall it can be seen that region-1 of test case IB-3 presents a higher stress distribution compared with test case-IB-1.

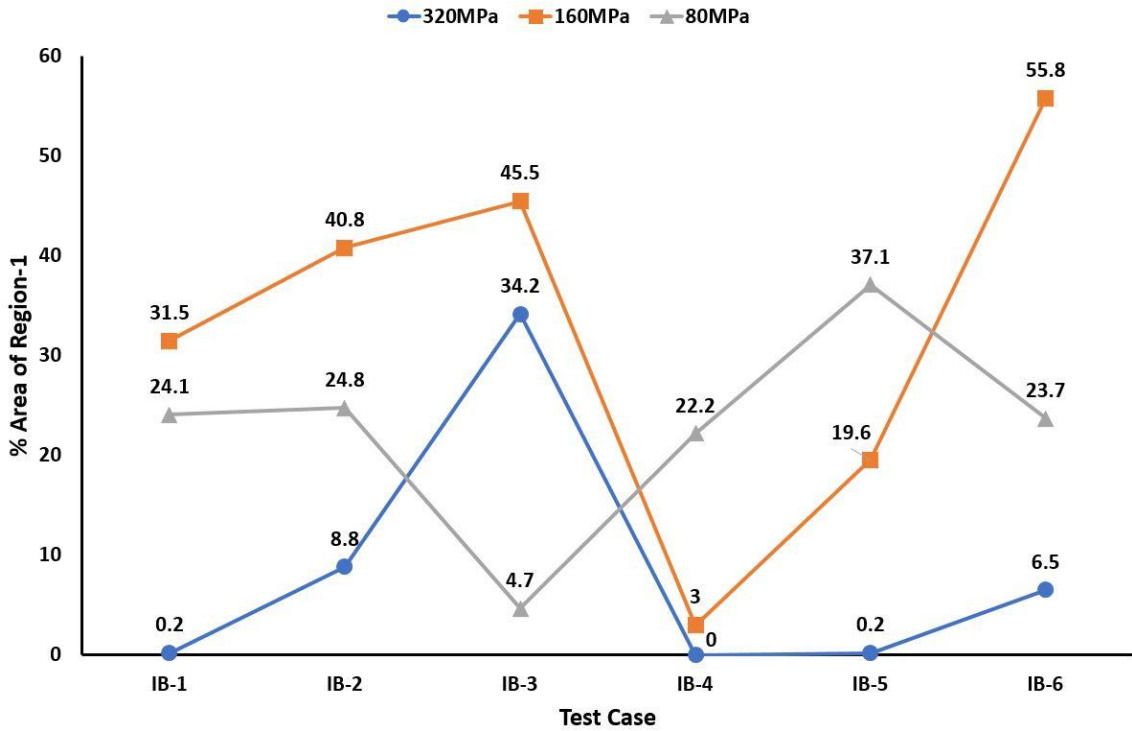


Figure 7-9. Region-1 residual stress variation in various test cases (a) IB-1 (Standard I-Beam with optimised parameters), (b) IB-2 (75 μ m Layer Thickness for Region-2 & Region-4), (c) IB-3 (150W power and 133 μ s exposure for Region-2 & Region-4), (d) IB-4 (570 $^{\circ}$ C Bed pre-heating on Renishaw SLM-125 machine), (e) IB-5 (75 μ m Layer Thickness for Region-1 & Region-3) and (f) IB-6 (150W power and 133 μ s exposure for Region-1 & Region-3).

The results in Figure-7.9 show that building the I-Beam geometry at a bed pre-heat temperature of 570 $^{\circ}$ C, for test case IB-4 resulted in a reduction in the overall residual stress in region-1 for the cross section of test case IB-4. Test case IB-4 showed no 320MPa residual stress region. Figure-7.9 shows that for test case IB-4, 160MPa residual stress region area reduced by 90.5%, while the 80MPa residual stress region area decreased by 7.9% compared with test case IB-1. Overall it can be seen that region-1 of test case IB-4 presents a much lower stress distribution compared with test case-IB-1.

The results in Figure-7.9 show that with the application of 75 μ m layer thickness to region-1 (just below the identified high stress region), for test case IB-5 did not affect the %area of maximum residual stress (320MPa) in region-1 for the cross section of test case IB-5. Figure-7.9 shows that, for test case IB-5, 160MPa residual stress region area decreased by 37.8% and the 80MPa residual stress region area increased by 53.9% compared with test case IB-1. Overall it can be seen that region-1 of test case IB-5 presents a lower stress distribution compared with test case-IB-1. Applying the stress reduction strategy to region-1, just below the high stress region-2 resulted in a lower overall stress state for test case IB-5 compared with test case IB-2 when the same strategy was applied directly to the high stress region-2.

The results in Figure-7.9 show that with the application of 150W power and 133 μ s exposure to region-3 (just below the identified high stress region-2), for test case IB-6 increased the 320MPa stress area in region-1 for the cross section of test case IB-6 by 3150% compared with test case IB-1. Figure-7.9 shows that for test case IB-6, 160MPa residual stress region area increased by 77.1% and the 80MPa residual stress region area decreased by 1.7% compared with test case IB-1. Overall it can be seen that region-1 of test case IB-6 presents a higher stress distribution compared with test case-IB-1.

The results of Figure-7.9 show that strategically applying stress reduction strategies to cross sections of complex parts can lead to a reduction in residual stress. The application of stress reduction strategies to region-1 just below the high stress region-2, for test cases IB-6 showed promising results compared to test cases IB-2 and IB-3 where the stress reduction strategies were directly applied to region-

2(identified as high stress region in IB-1). Test case IB-5 on the other hand showed an increase in the residual stress distribution in region-1.

7.1.6 Effect of strategic stress reduction strategies on residual stress in Region-3

Matlab image analysis script was used to extract the area associated with each stress level in region-3 of the various test cases shown in Figure-7.3. Figure-7.10 shows the corresponding areas of different stress levels in region-3 (Bottom of the top flange of the I-Beam geometry), for various test cases studied.

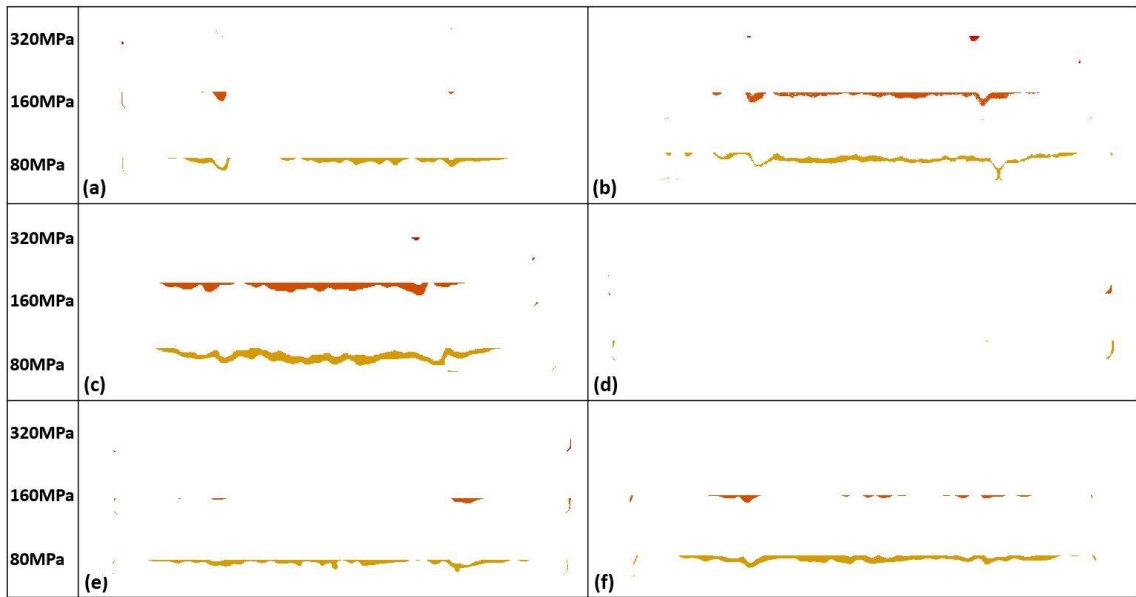


Figure 7-10. Region-3 areas corresponding to different stress levels for various test cases (a) IB-1 (Standard I-Beam with optimised parameters), (b) IB-2 (75 μ m Layer Thickness for Region-2 & Region-4), (c) IB-3 (150W power and 133 μ s exposure for Region-2 & Region-4), (d) IB-4 (570 $^{\circ}$ C Bed pre-heating on Renishaw SLM-125 machine), (e) IB-5 (75 μ m Layer Thickness for Region-1 & Region-3) and (f) IB-6 (150W power and 133 μ s exposure for Region-1 & Region-3).

Figure-7.11 shows the variation of residual stress in region-3 for various test cases with strategic application of stress reduction strategies. The results in Figure-7.11 show that with the application of 75 μ m layer thickness to region-4 (Identified as the high stress regions see section 7.1.1), for test case IB-2 increased the %area of maximum residual stress (320MPa) in region-3 for the cross section of test case IB-2 to 0.4%. Test case IB-2 showed an increase of 100% in 320MPa residual stress region compared to the standard I-Beam, test case IB-1. Figure-7.11 shows that, for test case IB-2, 160MPa residual stress region area increased by 547% and the 80MPa residual stress region area decreased by 14.6% compared with test case IB-1. Overall it can be seen that region-3 of test case IB-2 presents a higher stress distribution compared with test case-IB-1.

The results in Figure-7.11 show that with the application of 150W power and 133 μ s exposure to region-2 (identified as the high stress regions see section 7.1.1), for test case IB-3 did not affect %area of maximum residual stress (320MPa) in region-3 for the cross section of test case IB-3. Figure-7.11 shows that for test case IB-3, 160MPa residual stress region area increased by 658% and the 80MPa residual stress region area increased by 17.2% compared with test case IB-1. Overall it can be seen that region-3 of test case IB-3 presents a higher stress distribution compared with test case-IB-1.

The results in Figure-7.11 show that building the I-Beam geometry at a bed pre-heat temperature of 570 $^{\circ}$ C, for test case IB-4 resulted in a reduction in the overall residual stress in region-3 for the cross section of test case IB-4. Test case IB-4 showed no 320MPa residual stress region. Figure-7.11 shows that for test case IB-4,

160MPa and 80MPa residual stress region areas were negligible as well. Overall it can be seen that region-3 of test case IB-4 presents a much lower stress distribution compared with test case-IB-1.

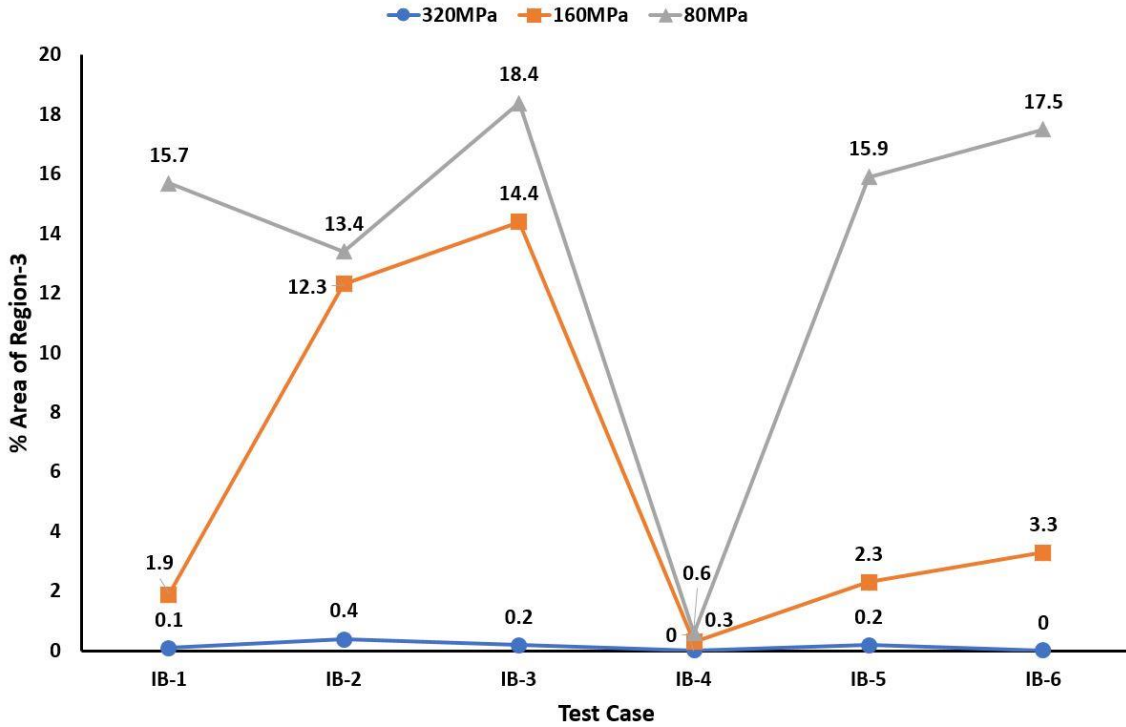


Figure 7-11. Region-3 residual stress variation in various test cases (a) IB-1 (Standard I-Beam with optimised parameters), (b) IB-2 (75 μ m Layer Thickness for Region-2 & Region-4), (c) IB-3 (150W power and 133 μ s exposure for Region-2 & Region-4), (d) IB-4 (570 $^{\circ}$ C Bed pre-heating on Renishaw SLM-125 machine), (e) IB-5 (75 μ m Layer Thickness for Region-1 & Region-3) and (f) IB-6 (150W power and 133 μ s exposure for Region-1 & Region-3).

The results in Figure-7.11 show that with the application of 75 μ m layer thickness to region-3 (just below the identified high stress region), for test case IB-5 doubled the %area of maximum residual stress (320MPa) in region-3 for the cross section of test case IB-5. Figure-7.11 shows that, for test case IB-5, 160MPa residual stress region

area increased by 21.1% and the 80MPa residual stress region area did not show much variation compared with test case IB-1. Overall it can be seen that region-3 of test case IB-5 presents a higher stress distribution compared with test case-IB-1. Applying the stress reduction strategy to region-3, just below the high stress region-2 resulted in an increased overall stress state for test case IB-5 compared with test case IB-2 when the same strategy was applied directly to the high stress region-2.

The results in Figure-7.11 show that with the application of 150W power and 133 μ s exposure to region-3 (just below the identified high stress region-4), for test case IB-6 eliminated the 320MPa stress area in region-3 for the cross section of test case IB-6. Figure-7.11 shows that for test case IB-6, 160MPa residual stress region area increased by 73.7% and the 80MPa residual stress region area increased by 11.5% compared with test case IB-1. Overall it can be seen that region-3 of test case IB-6 presents a higher stress distribution compared with test case-IB-1, even though the 320MPa hot spots are eliminated.

The results of Figure-7.11 show that strategically applying stress reduction strategies to cross sections of complex parts can lead to a reduction in residual stress. The application of stress reduction strategies to region-3 just below the high stress region-4, for test cases IB-5 and IB-6 showed promising results compared to test cases IB-2 and IB-3 where the stress reduction strategies were directly applied to region-4(identified as high stress region in IB-1).

7.1.7 Overall effect of strategic stress reduction strategies on residual stress

Figure-7.12 shows the overall variation of residual stress for various test cases with strategic application of stress reduction strategies. The results in Figure-7.12 show that overall pre-heating the bed is the most viable solution for residual stress reduction in SLM Ti6Al4V components. It can be seen from the results in Figure-7.12 that the application of 75 μ m layer thickness to region-1 and Region-3 (just below the identified high stress regions see section 7.1.1), for test case IB-5 resulted in an overall reduction in the residual stress in the I-Beam geometry.

Results from the strategic application of stress reduction strategies across different regions of the cross section of an I-Beam geometry showed a redistribution of residual stress profile. A reduction in residual stress over certain regions was also observed. It can be seen from the analysis in sections ----- that strategic application of stress reduction strategies can be a viable solution for reducing stress in critical regions of a component. This study has investigated the effect of one strategy being applied across different regions per sample. Combining the stress reduction strategies and as well as investigating the regions of application further could possibly lead to a viable solution for critical components manufacturing via SLM.

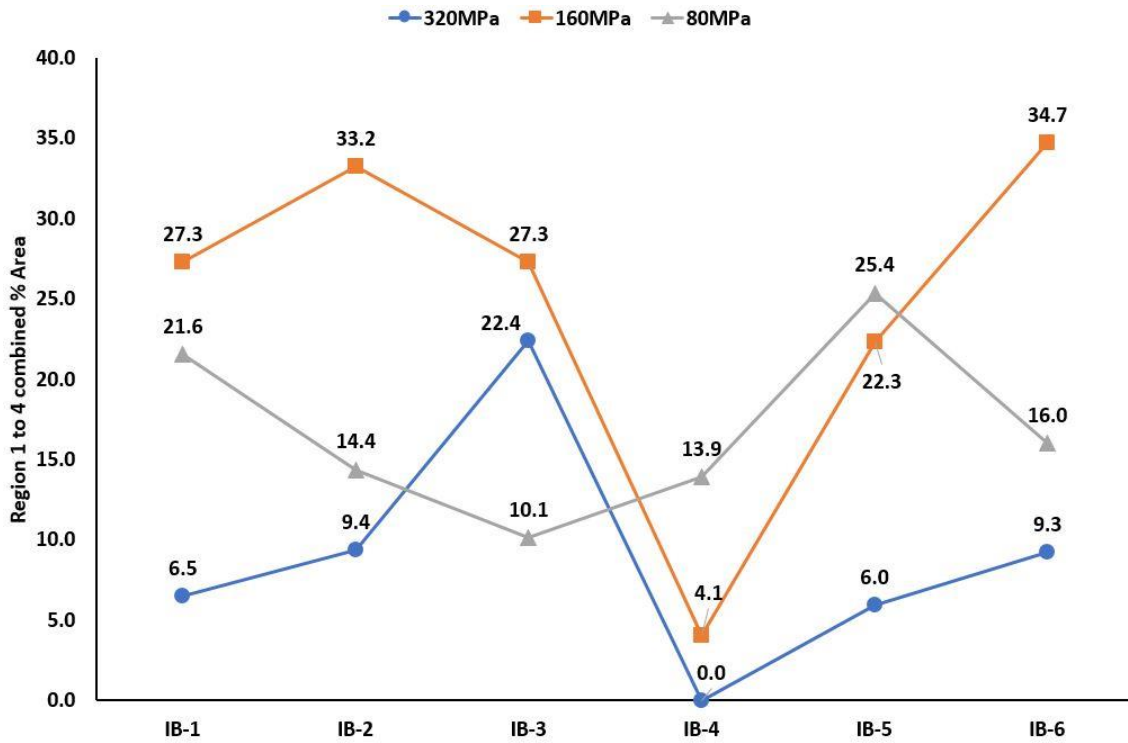


Figure 7-12 Overall residual stress variation in various test cases (a) IB-1 (Standard I-Beam with optimised parameters), (b) IB-2 (75 μ m Layer Thickness for Region-2 & Region-4), (c) IB-3 (150W power and 133 μ s exposure for Region-2 & Region-4), (d) IB-4 (570 $^{\circ}$ C Bed pre-heating on Renishaw SLM-125 machine), (e) IB-5 (75 μ m Layer Thickness for Region-1 & Region-3) and (f) IB-6 (150W power and 133 μ s exposure for Region-1 & Region-3).

8 Conclusions and Future Work

Selective Laser Melting uses a high power laser to build components by selectively melting and fusing powder material. Differential solidification in the melt pool and high solidification rates lead to directional thermal gradients. The high cooling rates and large thermal gradients associated with the SLM process lead to residual stress build up.

This work investigated residual stress build up in SLM Ti6Al4V components. The effect of SLM parameters on residual stress and mechanical properties was studied using a commercial Renishaw AM250 SLM machine and a modified Renishaw SLM125 machine. In order to understand the mechanism of residual stress build up a finite element model was create using ABAQUS with user subroutines written in FORTRAN.

8.1 Modelling

- The developed isotropic enhanced thermal conductivity model for SLM Ti6Al4V, treated the laser as an enhanced penetrating volumetric heat source was capable of predicting the melt-pool width (with 11% error) and melt-pool depth (with 1.6% error).
- The model accurately predicted the temperature evolution along the laser scan path with good correlation to the experimentally determined temperature [34] along the scan path. Accurate prediction of melt-pool

dimensions and the trend in temperature evolution along the laser scan path with high correlation to experimental data validates the modelling approach.

Therefore considering enhanced laser penetration to account for heat flow in the melt-pool due to Marangoni convection is a valid approach for modelling the SLM Ti6Al4V melting behavior.

- Enhanced penetration depth led to using isotropic enhanced thermal conductivity approach instead of anisotropic thermal enhanced conductivity approach and thus made the FEA model computationally efficient.
- The model was capable of predicting the start of the solidification region along the laser scan path that was similar to the experimentally determined[34] solidification region. The model accurately predicted the solidification behavior of the melt pool, it was then used as a tool for studying the effect of SLM process parameters variation on residual stress.

The trends in model predicted cooling rates and thermal gradients correlated with the trend in experimentally determined residual stress values.

- The model accurately predicted the effect of SLM process parameter variation on cooling rates and thermal gradients validated by comparison with the effect of SLM process parameters variation on experimentally determined residual stress.

Correlation of results between the developed model and experiments validate the effectiveness of the two proposed modelling reduction approaches.

- Using temperature dependent conductivity of powder Ti6Al4V as a convective heat transfer coefficient to account for heat loss to excess surrounding powder. This reduces the model size as there is no need for modelling excess powder.
- Similarly modelling a small substrate and adding a convection boundary condition, using temperature dependent conductivity of solid Ti6Al4V as convection coefficient accounts for heat loss to the large substrate without the need for modelling a larger substrate.

These modelling reduction approaches assisted in reducing the model size and thus improving the computational efficiency of the model.

8.2 Effect of SLM Parameters

A detailed investigation on the effect of standard SLM parameters on residual stress and mechanical properties was carried out using the Renishaw AM250 SLM machine.

8.2.1 SLM Parameter Optimisation

Parameter optimisation trials for determining the optimum combination of power and exposure time for achieving nearly fully dense parts were carried out.

- 200W power and 100 μ s exposure time resulted in 99.99% dense SLM Ti6Al4V blocks.
- The minimum energy density required for achieving nearly fully dense parts showed an inverse relationship with power.

8.2.2 Effect of Scanning Strategy

The effect of scanning strategy on residual stress, microstructure and mechanical properties was investigated by comparing 90° alternating scanning strategy with chessboard scanning strategy (chessboard squares sizes of 2x2mm, 3x3mm and 5x5mm).

- All the samples resulted in fully martensitic microstructure with prior beta grains irrespective of the scanning strategy.
- 90° alternating scanning strategy resulted in the lowest residual stress using Renishaw AM250 SLM machine.
- 90° alternating scanning strategy resulted in the lowest residual stress using Renishaw SLM125 machine.
- 90° alternating scanning strategy resulted in the lowest residual stress using Renishaw SLM125 machine with heated bed.
- Mechanical properties did not show any clear dependence on scanning strategy.

8.2.3 Effect of Layer Thickness

Three different layer thicknesses (25, 50, 75µm) were investigated to understand the effect on residual stress, microstructure and mechanical properties of SLM Ti6Al4V components.

- All the samples resulted in fully martensitic microstructure with prior beta grains irrespective of the layer thickness.
- FEA model predicted an inverse relationship between layer thickness and cooling rates.

- FEA model predicted an inverse relationship between layer thickness and temperature gradients.
- Layer thickness showed an inverse relationship with experimentally measured residual stress. 75 μm layer thickness resulted in the lowest residual stress.
- UTS, yield strength and elongation showed an inverse relationship with layer thickness. 25 μm layer thickness resulted in the highest UTS, yield strength and elongation values for SLM Ti6Al4V components.

8.2.4 Effect of Re-Scanning with Varying Exposure

The effect of re-scanning energy density on residual stress and mechanical properties was investigated by using optimum power of 200W in combination with four different exposure times (50, 75, 100 and 150 μs).

- All the samples resulted in fully martensitic microstructure with prior beta grains irrespective of the re-scanning exposure.
- FEA model accurately predicted the trends in cooling rates and temperature gradients for varying re-scanning exposure.
- Re-scanning each layer with 50, 75, and 100 μs exposure resulted in an increase in the residual stress in SLM Ti6Al4V SLM components.
- Re-scanning each layer with 150 μs exposure resulted in a reduction in residual stress.
- Re-scanning with 75 μs exposure time resulted in an increase in elongation of SLM Ti6Al4V components.
- Re-scanning with 100 and 150 μs exposure resulted in a sharp decline in elongation possibly due to an increase in oxide layer thickness.

8.2.5 Effect of Re-Scanning with Varying Power

The effect of re-scanning energy density on residual stress and mechanical properties was investigated by using optimum exposure of 100 μ s in combination with three different powers (100, 150 and 200W).

- All the samples resulted in fully martensitic microstructure with prior beta grains irrespective of the re-scanning power.
- FEA model accurately predicted the trends in cooling rates and temperature gradients for varying re-scanning power.
- Re-scanning each layer with 100, 150, and 200W power resulted in an increase in the residual stress in SLM Ti6Al4V SLM components.
- Re-scanning with 100W power resulted in an increase in elongation of SLM Ti6Al4V components.

8.2.6 Effect of Power and Exposure keeping Energy Density Constant

Keeping the energy density constant (optimum energy density determined from parameter optimisation), the effect of varying power and exposure combination on residual stress and mechanical properties was investigated.

- All the samples resulted in fully martensitic microstructure with prior beta grains irrespective of the power and exposure combination.
- For a constant energy density the FEA model predicted a direct relationship between power and cooling rates.
- For a constant energy density the FEA model predicted a direct relationship between power and temperature gradients.
- For a constant energy density the FEA model predicted an inverse relationship between exposure and cooling rates.
- For a constant energy density the FEA model predicted an inverse relationship between exposure and temperature gradients.

- For a constant energy density lower power and higher exposure combination resulted in lower residual stress in SLM Ti6Al4V components. 150W power and 133 μ s exposure combination resulted in the lowest residual stress.
- For a constant energy density the yield strength did not show any dependence on power and exposure.
- For a constant energy density the elongation of SLM Ti6Al4V showed an increasing trend with decreasing power and increasing exposure.

8.2.7 Effect of Bed Pre-Heat Temperature

Renishaw SLM125 machine was fitted with a custom designed conductive heated bed capable of achieving 800+ degrees temperature, to study the effect of bed pre-heat temperature on residual stress and mechanical properties.

- SLM Ti6Al4V martensitic microstructure was completely transformed into a basketweave $\alpha+\beta$ microstructure at 570 $^{\circ}$ C powder bed pre-heating (30 $^{\circ}$ C below the start of the martensitic decomposition range of 600-650 $^{\circ}$ C).
- α globulorisation was observed in samples built at 670 and 770 $^{\circ}$ C bed temperatures.
- Nano β started forming between and inside α laths at higher bed pre-heat temperatures.
- FEA model predicted an inverse relationship between bed pre-heat temperature and cooling rates.
- FEA model predicted an inverse relationship between bed pre-heat temperature and temperature gradients.

- Samples built at bed pre-heat temperatures of 570°C showed no measured residual stress within the SLM Ti6Al4V components.
- Some samples built at high bed temperatures (i.e 570°C and 770°C) exhibited compressive residual stress, which can be beneficial for the fatigue life of components.
- Elevated bed temperatures lead to producing parts with higher yield strength.
- At 770°C there was a sharp decline in yield strength due to pre-mature failure of tensile samples probably due to the globular α and increased grain boundary β forming weak microstructural locations.
- The ductility of the samples improved with increasing bed temperature, and at 570°C there was an improvement of 66.2% in the elongation of the samples compared to those built at a standard 100°C.
- At 670°C there was a sharp decline of 74.7% compared to 570°C in sample elongation, this again may be related to use of sub-optimal parameters, increased grain growth resulting in the growth of globular α , existence of α laths in various sizes and the growth of grain boundary β . All these factors leading to non-equilibrium micro-structure and maximising the possibility of weaker locations for crack nucleation and growth.
- Vickers micro-hardness increased with increasing bed temperature reaching a maximum of 442 [HV 0.2], at 670°C, with a 13% increase compared to samples built at 100°C. This increase in hardness was due to the increase in

β content between α/α' laths and at higher temperature nano β growing within α laths.

- At 770°C there is a 1.8% decrease due to the increase in α laths size even though the amount of β increased.

8.3 Strategic Stress Reduction

High stress regions in an I-Beam geometry were identified using contour method analysis. Stress reduction strategies identified from residual stress blocks using hole drilling measurement method were strategically applied across different regions of the I-Beam cross section in an effort to reduce residual stress. Samples were built by strategically applying 75 μ m layer thickness and a power and exposure combination of 150W and 133 μ s keeping energy density constant across different regions of the I-Beam geometry. Similarly an I-Beam geometry was also built at a bed pre-heat temperature of 570°C.

- Irrespective of the region of application all the applied stress reduction strategies resulted in redistribution of the residual stress in the cross section.
- Applying 75 μ m layer thickness just below the identified high stress regions resulted in an overall reduction in residual stress in the I-Beam geometry.
- High bed temperature of 570°C resulted in an overall reduction in residual stress in the I-Beam sample.

8.4 Suggestions for Future Work

Extensive research is going on SLM but the technique is still in the developmental stages and therefore offers numerous opportunities for further research. The

process parameters studied in this work are limited to laser scanning strategy, re-scanning each layer varying the re-scanning energy density by changing exposure or power, layer thickness, combination of power and exposure for constant energy density and the bed pre-heat temperature.

Correlations were established between the studied parameters, residual stress and mechanical properties by building three samples per parameter. The variability in the results suggest that there is still room for further work on the parameters considered in this study. For instance further variations of the scanning strategies can be studied by exploring different orientation of scan vectors or different lengths of scan vectors. The concept of power and exposure combination for constant energy density can be applied to lower thickness. Further variations of layer thickness can be studied to find the layer thickness resulting in lower residual stress and higher elongation combination. Re-scanning can be applied to specific layers across the cross section instead of re-scanning every layer.

Pre-heating the bed has shown promising results in reducing the residual stress, modifying the microstructure and enhancement of mechanical properties. This opens a new window for further investigation. Optimising the parameters for each bed temperature and studying the effect on residual stress, microstructure and mechanical properties can be one dimension. Building components with different layer thickness at higher bed pre-heat temperatures can be an interesting research. Combining the concept of power and exposure combination keeping energy density constant at optimum with bed pre-heating can be another dimension to be investigated.

Besides the parameters investigated in this study there are other SLM parameters whose effect on residual stress and mechanical properties can be investigated further. For instance the effect of support structures and part orientation. Similarly the effect of laser offset used by Xu *et al.*[9], for martensite decomposition in Ti6Al4V, on residual stress and mechanical properties needs investigation.

FEA model developed in this work can be extended further by building single lines at different parameter combinations and developing a parametric relationship with model parameters. The model can be extended further to multiple layers.

Further investigation can be carried out on the geometrical dependence of residual stress in SLM components. The location, build height and order of region selection for strategic application of stress reduction strategies can be investigated further. The effect of combining multiple stress reduction strategies in a single sample can be an interesting research as well.

References

1. ASTM, *ISO/ASTM 52921:2013-Standard Terminology for Additive Manufacturing—Coordinate Systems and Test Methodologies*, 2013, ASTM International: West Conshohocken, PA.
2. C. Casavola, S.L.C., C. Pappalettere. *Experimental analysis of residual stresses in the Selective Laser Melting process*. in *Proceedings of the XIth International Congress and Exposition*. 2008. Orlando, Florida USA.
3. L. Papadakis & A. Loizou, J.R.S.B., *A thermo-mechanical modeling reduction approach for calculating shape distortion in SLM manufacturing for aero engine components in VRAP Advanced Research in Virtual and Rapid Prototyping*: Portugal.
4. Kruth, J.-P., et al., *Assessing and comparing influencing factors of residual stresses in selective laser melting using a novel analysis method*. *Proceedings of the Institution of Mechanical Engineers, Part B: Journal of Engineering Manufacture*, 2012. **226**(6): p. 980-991.
5. Rossini, N.S., et al., *Methods of measuring residual stresses in components*. *Materials & Design*, 2012. **35**(0): p. 572-588.
6. Matsumoto, M., et al., *Finite element analysis of single layer forming on metallic powder bed in rapid prototyping by selective laser processing*. *International Journal of Machine Tools and Manufacture*, 2002. **42**(1): p. 61-67.
7. S. Das, M.W., J.J. Beaman, D.L. Bourell, *Producing metal parts with selective laser sintering/hot isostatic pressing*. *Journal JOM* 50 1998. **12**: p. 17-20.
8. Facchini, L., et al., *Ductility of a Ti-6Al-4V alloy produced by selective laser melting of prealloyed powders*. *Rapid Prototyping Journal*, 2010. **16**(6): p. 450-459.
9. Xu, W., et al., *Ti-6Al-4V Additively Manufactured by Selective Laser Melting with Superior Mechanical Properties*. *JOM*, 2015. **67**(3): p. 668-673.
10. J.-P. Kruth, M.B., E.Yasa, J. Deckers, L. Thijs, J. Van Humbeeck. *Part and material properties in selective laser melting of metals*. in *16th International Symposium on Electromachining (ISEM XVI)*. 2010. shanghai-china.
11. Gao, W., et al., *The status, challenges, and future of additive manufacturing in engineering*. *Computer-Aided Design*, 2015. **69**: p. 65-89.
12. *ASTM F2792-12a, Standard Terminology for Additive Manufacturing Technologies, (Withdrawn 2015)*, ASTM International, West Conshohocken, PA, 2012, www.astm.org.
13. Gibson, I., D.W. Rosen, and B. Stucker, *Additive Manufacturing Technologies: Rapid Prototyping to Direct Digital Manufacturing*. 2009: Springer. pp.1-14.
14. Joseph J. Beaman; Carl R. Deckard, *Selective Laser Sintering with assisted powder handling.*, U.S. Patent, Editor 1990, Board of Regents, The University of Texas System, Austin, Tex.: United States.
15. Van Der Schueren, B., *Basic Contributions to the development of the Selective Metal powder Sintering Process*, 1996, University of Leuven.

16. Kruth, J.P., Laoui, T., *Selective Laser Sintering: State of the art*. International Journal of Electrical Machining, 2001. **6**: p. pp.7-17.
17. Chatterjee, A.N., Kumar, S., Saha, Mishra, P.K. A., Choudhury, R. , *An experiment design approach to selective laser sintering of low carbon steel*, *Journal of Material Processing Technologies*. 2003. **136**: p. pp 151-157.
18. Mumtaz, K. and N. Hopkinson, *Selective laser melting of Inconel 625 using pulse shaping*. Rapid Prototyping Journal, 2010. **16**(4): p. 248-257.
19. Gu, D., et al., *Densification behavior, microstructure evolution, and wear performance of selective laser melting processed commercially pure titanium*. Acta Materialia, 2012. **60**(9): p. 3849-3860.
20. Mumtaz, K.A., P. Erasenthiran, and N. Hopkinson, *High density selective laser melting of Waspaloy®*. Journal of Materials Processing Technology, 2008. **195**(1-3): p. 77-87.
21. Kruth, J.P., et al., *Consolidation phenomena in laser and powder-bed based layered manufacturing*. CIRP Annals - Manufacturing Technology, 2007. **56**(2): p. 730-759.
22. Morgan, R., C. Sutcliffe, and W. O'Neill, *Density analysis of direct metal laser re-melted 316L stainless steel cubic primitives*. Journal of Materials Science, 2004. **39**(4): p. 1195-1205.
23. Kruth, J.P., et al., *Selective laser melting of iron-based powder*. Journal of Materials Processing Technology, 2004. **149**(1-3): p. 616-622.
24. Zhong, M., et al., *Boundary liquation and interface cracking characterization in laser deposition of Inconel 738 on directionally solidified Ni-based superalloy*. Scripta Materialia, 2005. **53**(2): p. 159-164.
25. Withers, P.J.B., H.K.D.H., *Residual stress. Part 1 – Measurement techniques*. Materials Science and Technology, 2001. **17**(4): p. 355-365.
26. Dieter, G.E. and D. Bacon, *Mechanical Metallurgy*. 1988: McGraw-Hill.
27. Withers, P.J.B., H.K.D.H., *Residual Stress Part 2- Nature and origins*. Materials Science and Technology, 2001. **17**(4): p. 366-375.
28. Mercelis, P., *Control of selective laser sintering and selective laser melting processes*, 2007, KU Leuven, Leuven, Belgium.
29. Shiomi, M., et al., *Residual Stress within Metallic Model Made by Selective Laser Melting Process*. CIRP Annals - Manufacturing Technology, 2004. **53**(1): p. 195-198.
30. Joe Elambasseril, S.F., Matthias Bringezu and Milan Brandt, *Influence of process parameters on selective laser melting of Ti 6Al-4V components*, 2012, RMIT University School of Aerospace, Mechanical and Manufacturing Engineering (SAMME).
31. Gong, H., et al. *Defect Morphology in Ti-6Al-4V Parts Fabricated by Selective Laser Melting and Electron Beam Melting*. in *Solid Freeform Fabrication Symposium Proceeding*. 2013.
32. King, W.E., et al., *Observation of keyhole-mode laser melting in laser powder-bed fusion additive manufacturing*. Journal of Materials Processing Technology, 2014. **214**(12): p. 2915-2925.

33. Yasa, E. and J.P. Kruth, *Microstructural investigation of Selective Laser Melting 316L stainless steel parts exposed to laser re-melting*. Procedia Engineering, 2011. **19**: p. 389-395.
34. Yadroitsev, I., P. Krakhmalev, and I. Yadroitsava, *Selective laser melting of Ti6Al4V alloy for biomedical applications: Temperature monitoring and microstructural evolution*. Journal of Alloys and Compounds, 2014. **583**: p. 404-409.
35. Manvatkar, V., A. De, and T. DebRoy, *Spatial variation of melt pool geometry, peak temperature and solidification parameters during laser assisted additive manufacturing process*. Materials Science and Technology, 2015. **31**(8): p. 924-930.
36. Alimardani, M., et al., *On the delamination and crack formation in a thin wall fabricated using laser solid freeform fabrication process: An experimental–numerical investigation*. Optics and Lasers in Engineering, 2009. **47**(11): p. 1160-1168.
37. Wu, A.S., et al., *An Experimental Investigation into Additive Manufacturing-Induced Residual Stresses in 316L Stainless Steel*. Metallurgical and Materials Transactions A, 2014. **45**(13): p. 6260-6270.
38. Vasinonta, A., J.L. Beuth, and M. Griffith, *Process Maps for Predicting Residual Stress and Melt Pool Size in the Laser-Based Fabrication of Thin-Walled Structures*. Journal of Manufacturing Science and Engineering, 2006. **129**(1): p. 101-109.
39. Brückner, F., D. Lepski, and E. Beyer, *Modeling the Influence of Process Parameters and Additional Heat Sources on Residual Stresses in Laser Cladding*. Journal of Thermal Spray Technology, 2007. **16**(3): p. 355-373.
40. Taha, M.A., et al., *On selective laser melting of ultra high carbon steel: Effect of scan speed and post heat treatment*
Selektives Laserschmelzen von hoch kohlenstoffhaltigen Stählen: Einfluss der Abtastgeschwindigkeit und der Wärmenachbehandlung. Materialwissenschaft und Werkstofftechnik, 2012. **43**(11): p. 913-923.
41. Pohl, H., et al. *Thermal stresses in direct metal laser sintering*. in *Proceedings of the 12th Solid Freeform Fabrication Symposium, Austin, TX*. 2001.
42. Van Belle, L.V., Guillaume Boyer, Jean Claude, *Investigation of Residual Stresses Induced during the Selective Laser Melting Process*. Key Engineering Materials, 2013. **554-557**: p. 1828-1834.
43. Zaeh, M.F.B., G., *Investigations on residual stresses and deformations in selective laser melting*. Production engineering : research and development in Germany, 2010. **4**(1).
44. Cheng, B., S. Shrestha, and K. Chou, *Stress and deformation evaluations of scanning strategy effect in selective laser melting*. Additive Manufacturing, 2016. **12, Part B**: p. 240-251.
45. Dunbar, A.J., et al., *Development of experimental method for in situ distortion and temperature measurements during the laser powder bed fusion additive manufacturing process*. Additive Manufacturing, 2016. **12, Part A**: p. 25-30.
46. Gusarov, A.V., M. Pavlov, and I. Smurov, *Residual Stresses at Laser Surface Remelting and Additive Manufacturing*. Physics Procedia, 2011. **12**: p. 248-254.

47. Parry, L., I.A. Ashcroft, and R.D. Wildman, *Understanding the effect of laser scan strategy on residual stress in selective laser melting through thermo-mechanical simulation*. Additive Manufacturing, 2016. **12, Part A**: p. 1-15.
48. Nickel, A.H., D.M. Barnett, and F.B. Prinz, *Thermal stresses and deposition patterns in layered manufacturing*. Materials Science and Engineering: A, 2001. **317**(1-2): p. 59-64.
49. Mercelis, P. and J.-P. Kruth, *Residual stresses in selective laser sintering and selective laser melting*. Rapid Prototyping Journal, 2006. **12**(5): p. 254-265.
50. R, K.J.-P.D.J.Y.E.W., *Assessing and comparing influencing factors of residual stresses in selective laser melting using a novel analysis method*. Proceedings of the Institution of Mechanical Engineers. Part B, Journal of engineering manufacture., 2012. **226**: p. 980-981.
51. Lu, Y., et al., *Study on the microstructure, mechanical property and residual stress of SLM Inconel-718 alloy manufactured by differing island scanning strategy*. Optics & Laser Technology, 2015. **75**: p. 197-206.
52. Vrancken, B., et al. *Influence of preheating and oxygen content on Selective Laser Melting of Ti6Al4V*. in *Proceedings of the 16th RAPDASA Conference. RAPDASA, Annual International Conference on Rapid Product Development Association of South Africa* 4-6 November 2015. Pretoria, South Africa.
53. *Practical Residual Stress Measurement Methods*, ed. G.S. Schajer. 2013: Wiley.
54. Thöne, M., et al. *Influence of heat-treatment on selective laser melting products—eg Ti6Al4V*. in *Solid freeform fabrication symposium SFF, Austin Texas*. 2012.
55. C.R. Knowles, T.H.B.R.B.T., *The effect of heat treatment on the residual stress levels within direct metal laser sintered Ti-6Al-4V as measured using the hole-drilling strain gauge method*, in *Rapid Product Development Association of South Africa* 2012. p. 1-10.
56. Juechter, V., et al., *Processing window and evaporation phenomena for Ti-6Al-4V produced by selective electron beam melting*. Acta Materialia, 2014. **76**: p. 252-258.
57. Kirchner, A., et al., *Process Window for Electron Beam Melting of Ti-6Al-4V*, in *Euro PM2014 – AM: Technologies* 2014.
58. Sallica-Leva, E., et al., *Ductility improvement due to martensite α' decomposition in porous Ti-6Al-4V parts produced by selective laser melting for orthopedic implants*. Journal of the Mechanical Behavior of Biomedical Materials, 2016. **54**: p. 149-158.
59. Tan, X., et al., *Revealing martensitic transformation and α/β interface evolution in electron beam melting three-dimensional-printed Ti-6Al-4V*. Scientific Reports, 2016. **6**: p. 26039.
60. Welsch, G., R. Boyer, and E.W. Collings, *Materials Properties Handbook: Titanium Alloys*. 1993: ASM International.
61. Donachie, M.J., *Titanium: A Technical Guide, 2nd Edition*. 2000: ASM International.
62. Vrancken, B., et al., *Heat treatment of Ti6Al4V produced by Selective Laser Melting: Microstructure and mechanical properties*. Journal of Alloys and Compounds, 2012. **541**: p. 177-185.

63. Roberts, I.A., *Investigation of residual stresses in the laser melting of metal powders in additive layer manufacturing*, 2012, University of Wolverhampton. p. 246.
64. Vora, P., et al., *AlSi12 in-situ alloy formation and residual stress reduction using anchorless selective laser melting*. Additive Manufacturing, 2015. **7**: p. 12-19.
65. Lütjering, G. and J.C. Williams, *Titanium*. 2003: Springer.
66. Ahmed, T. and H.J. Rack, *Phase transformations during cooling in $\alpha+\beta$ titanium alloys*. Materials Science and Engineering: A, 1998. **243**(1): p. 206-211.
67. *Titanium and Titanium Alloys. Fundamentals and Applications*. 2003: Wiley-VCH GmbH & Co. KGaA.
68. M., J.R.I.a.B.H., *Titanium Science and Technology*. Vol. 1. 1973: Springer.
69. Lütjering G., W.J.C., *Titanium*. 2003, Berlin: Springer.
70. Xu, W., et al., *Additive manufacturing of strong and ductile Ti-6Al-4V by selective laser melting via in situ martensite decomposition*. Acta Materialia, 2015. **85**: p. 74-84.
71. Thijs, L., et al., *A study of the microstructural evolution during selective laser melting of Ti-6Al-4V*. Acta Materialia, 2010. **58**(9): p. 3303-3312.
72. Leuders, S., et al., *On the mechanical behavior of titanium alloy TiAl6V4 manufactured by selective laser melting: Fatigue resistance and crack growth performance*. International Journal of Fatigue, 2013. **48**: p. 300-307.
73. Kasperovich, G. and J. Hausmann, *Improvement of fatigue resistance and ductility of TiAl6V4 processed by selective laser melting*. Journal of Materials Processing Technology, 2015. **220**: p. 202-214.
74. Vrancken, B., et al., *Microstructure and mechanical properties of a novel β titanium metallic composite by selective laser melting*. Acta Materialia, 2014. **68**: p. 150-158.
75. Vilaro, T., C. Colin, and J.D. Bartout, *As-Fabricated and Heat-Treated Microstructures of the Ti-6Al-4V Alloy Processed by Selective Laser Melting*. Metallurgical and Materials Transactions A, 2011. **42**(10): p. 3190-3199.
76. Edwards, P. and M. Ramulu, *Fatigue performance evaluation of selective laser melted Ti-6Al-4V*. Materials Science and Engineering: A, 2014. **598**: p. 327-337.
77. K.D., R., *Ductility improvement due to martensite ' α ' decomposition in porous Ti-6Al-4V parts produced by selective laser melting for orthopaedic implants*. 2015: Department of the Air force, Wright-Patterson Air force Base, Ohio, USA.
78. Rafi, H.K., T.L. Starr, and B.E. Stucker, *A comparison of the tensile, fatigue, and fracture behavior of Ti-6Al-4V and 15-5 PH stainless steel parts made by selective laser melting*. The International Journal of Advanced Manufacturing Technology, 2013. **69**(5): p. 1299-1309.
79. Qiu, C., N.J. Adkins, and M.M. Attallah, *Microstructure and tensile properties of selectively laser-melted and of HIPed laser-melted Ti-6Al-4V*. Materials Science and Engineering: A, 2013. **578**: p. 230-239.
80. Gong, H., et al., *Influence of defects on mechanical properties of Ti-6Al-4V components produced by selective laser melting and electron beam melting*. Materials & Design, 2015. **86**: p. 545-554.

81. Lütjering, G., *Influence of processing on microstructure and mechanical properties of (α + β) titanium alloys*. Materials Science and Engineering: A, 1998. **243**(1-2): p. 32-45.
82. Kar, S.K., *Modeling of mechanical properties in alpha/beta-titanium alloys*, 2005, The Ohio State University.
83. Shunmugavel, M., A. Polishetty, and G. Littlefair, *Microstructure and Mechanical Properties of Wrought and Additive Manufactured Ti-6Al-4V Cylindrical Bars*. Procedia Technology, 2015. **20**: p. 231-236.
84. Li, P., et al., *Critical assessment of the fatigue performance of additively manufactured Ti-6Al-4V and perspective for future research*. International Journal of Fatigue, 2016. **85**: p. 130-143.
85. Simchi, A., *Direct laser sintering of metal powders: Mechanism, kinetics and microstructural features*. Materials Science and Engineering: A, 2006. **428**(1): p. 148-158.
86. C.R. Knowles, T.H.B.R.B.T., *Residual stress measurements and structural integrity implications for Selective Laser Melted Ti6Al4V*. South African Journal of Industrial Engineering, 2012. **23**(3): p. 119-129.
87. P V Grant, J.D.L.a.P.S.W., *Good Practice Guide No. 53-Issue 2: The Measurement of Residual Stress by Incremental Hole Drilling Technique*, 2006, The National Physical Laboratory: UK.
88. Kandil, F., D. Lord, and A. Fry, *A review of residual stress measurement methods A guide to technique selection*. 2001.
89. Prime, M.B., *Cross-Sectional Mapping of Residual Stresses by Measuring the Surface Contour After a Cut*. Journal of Engineering Materials and Technology, 2000. **123**(2): p. 162-168.
90. Roberts, I.A., et al., *A three-dimensional finite element analysis of the temperature field during laser melting of metal powders in additive layer manufacturing*. International Journal of Machine Tools and Manufacture, 2009. **49**(12-13): p. 916-923.
91. Gusarov, A.V. and I. Smurov, *Modeling the interaction of laser radiation with powder bed at selective laser melting*. Physics Procedia, 2010. **5**: p. 381-394.
92. Dai, K. and L. Shaw, *Thermal and mechanical finite element modeling of laser forming from metal and ceramic powders*. Acta Materialia, 2004. **52**(1): p. 69-80.
93. Shiomi, M., et al., *Finite element analysis of melting and solidifying processes in laser rapid prototyping of metallic powders*. International Journal of Machine Tools and Manufacture, 1999. **39**(2): p. 237-252.
94. Guo-feng, Y. and C. Guang-nan, *Numerical simulation of transient thermal field in laser melting process*. Applied Mathematics and Mechanics, 2004. **25**(8): p. 945-950.
95. Gusarov, A.V., et al., *Heat transfer modelling and stability analysis of selective laser melting*. Applied Surface Science, 2007. **254**(4): p. 975-979.
96. Gusarov, A.V. and I. Smurov, *Two-dimensional numerical modelling of radiation transfer in powder beds at selective laser melting*. Applied Surface Science, 2009. **255**(10): p. 5595-5599.

97. Körner, C., E. Attar, and P. Heintl, *Mesosopic simulation of selective beam melting processes*. Journal of Materials Processing Technology, 2011. **211**(6): p. 978-987.
98. Song, B., et al., *Process parameter selection for selective laser melting of Ti6Al4V based on temperature distribution simulation and experimental sintering*. The International Journal of Advanced Manufacturing Technology, 2012. **61**(9): p. 967-974.
99. Safdar, S., et al., *An anisotropic enhanced thermal conductivity approach for modelling laser melt pools for Ni-base super alloys*. Applied Mathematical Modelling, 2013. **37**(3): p. 1187-1195.
100. Loh, L.-E., et al., *Numerical investigation and an effective modelling on the Selective Laser Melting (SLM) process with aluminium alloy 6061*. International Journal of Heat and Mass Transfer, 2015. **80**(0): p. 288-300.
101. Foroozmehr, A., et al., *Finite Element Simulation of Selective Laser Melting process considering Optical Penetration Depth of laser in powder bed*. Materials & Design, 2016. **89**: p. 255-263.
102. Zehner, P. and E.U. Schlunder, *Thermal conductivity of granular materials at moderate temperatures (in German)*. Chemie Ingr. Tech., 1970(42): p. 933-941.
103. Fischer, P., et al., *A model for the interaction of near-infrared laser pulses with metal powders in selective laser sintering*. Applied Physics A, 2002. **74**(4): p. 467-474.
104. Mills, K.C., et al., *Marangoni effects in welding*. Philosophical Transactions of the Royal Society of London A: Mathematical, Physical and Engineering Sciences, 1998. **356**(1739): p. 911-925.
105. Khairallah, S.A. and A. Anderson, *Mesosopic simulation model of selective laser melting of stainless steel powder*. Journal of Materials Processing Technology, 2014. **214**(11): p. 2627-2636.
106. Pengpeng, Y. and G. Dongdong, *Molten pool behavior and its physical mechanism during selective laser melting of TiC/AlSi10Mg nanocomposites: simulation and experiments*. Journal of Physics D: Applied Physics, 2015. **48**(3): p. 035303.
107. Fu, C. and Y. Guo. *3-Dimensional Finite Element Modeling of Selective Laser Melting Ti-6Al-4V Alloy*. in *Solid Freeform Fabrication Symposium 2014 Proceedings*. 2014.
108. Lopez-Botello, O., et al., *Two-dimensional simulation of grain structure growth within selective laser melted AA-2024*. Materials & Design, 2017. **113**: p. 369-376.
109. Van Zyl, I., I. Yadroitsev, and I. Yadroitsava, *Residual stresses in direct metal laser sintered parts*. 2015.
110. Mugwagwa, L., et al., *A methodology to evaluate the influence of part geometry on residual stresses in selective laser melting*. 2016.
111. ASTM, *E2109-01(2007), Standard Test Methods for Determining Area Percentage Porosity in Thermal Sprayed Coatings*, 2007, ASTM International: West Conshohocken, PA.
112. BSI, *BS 7590:1992, Method for statistically estimating the volume fraction of phases and constituents by systematic manual point counting with a grid*, 1992, BSI.

113. Liu, Y., Y. Yang, and D. Wang, *A study on the residual stress during selective laser melting (SLM) of metallic powder*. The International Journal of Advanced Manufacturing Technology, 2016. **87**(1): p. 647-656.
114. Beaney, E.M., *Accurate measurement of residual stress on any steel using the centre hole method*. Strain, 1976. **12**(3): p. 99-106.
115. ASTM, *E8 / E8M-13a, Standard Test Methods for Tension Testing of Metallic Materials*, 2013, ASTM International: West Conshohocken, PA.
116. BSEN, *ISO 6892-1, Metallic materials. Tensile testing. Method of test at ambient temperature*, 31 August, 2009.
117. BSEN, *ISO 6507-1:2005, Metallic materials. Vickers hardness test. Test method*, 2006.
118. Hosseinzadeh, F., J. Kowal, and P.J. Bouchard *Towards good practice guidelines for the contour method of residual stress measurement*. The Journal of Engineering, 2014.
119. Tolochko, N.K., et al., *Absorptance of powder materials suitable for laser sintering*. Rapid Prototyping Journal, 2000. **6**(3): p. 155-161.
120. Ali, H., et al., *In-situ residual stress reduction, martensitic decomposition and mechanical properties enhancement through high temperature powder bed pre-heating of Selective Laser Melted Ti6Al4V*. Materials Science and Engineering: A, 2017. **695**: p. 211-220.
121. Cheng, B. and K. Chou. *Melt pool evolution study in selective laser melting*. in *26th Annual International Solid Freeform Fabrication Symposium-An Additive Manufacturing Conference, Austin, TX, USA*. 2015.
122. Polivnikova, T., *Study and Modelling of the Melt Pool Dynamics during Selective Laser Sintering and Melting*, 2015, EPFL.
123. Shi, Y., et al., *Temperature gradient mechanism in laser forming of thin plates*. Optics & Laser Technology, 2007. **39**(4): p. 858-863.
124. Ahmed, T. and H.J. Rack, *Phase transformations during cooling in $\alpha+\beta$ titanium alloys*. Materials Science and Engineering: A, 1998. **243**(1-2): p. 206-211.
125. Vaithilingam, J., et al., *The effect of laser remelting on the surface chemistry of Ti6Al4V components fabricated by selective laser melting*. Journal of Materials Processing Technology, 2016. **232**: p. 1-8.
126. Simonelli, M., Y.Y. Tse, and C. Tuck, *The formation of $\alpha+\beta$ microstructure in as-fabricated selective laser melting of Ti-6Al-4V*. Journal of Materials Research, 2014. **29**(17): p. 2028-2035.
127. Dai, K., X.X. Li, and L.L. Shaw, *Comparisons between thermal modeling and experiments: effects of substrate preheating*. Rapid Prototyping Journal, 2004. **10**(1): p. 24-34.
128. Katarov, I., S. Malinov, and W. Sha, *Finite element modeling of the morphology of β to α phase transformation in Ti-6Al-4V alloy*. Metallurgical and Materials Transactions A, 2002. **33**(4): p. 1027-1040.
129. Qian, L., J. Mei, and X.H. Wu. *An experimental and modelling study of laser fabricated samples*. in *Materials science forum*. 2007. Trans Tech Publ.

130. USDD, *Military Handbook-MIL-HDBK-5J: Metallic Materials and Elements for Aerospace Vehicle Structures*. 2003: U.S. Department of Defence.
131. Fitzpatrick, M., et al., *NPL Good Practice Guide no. 52: determination of residual stresses by x-ray diffraction*. 2002: March.

Appendix-A. Residual Stress Measurement Techniques

Technique	Brief Description
Deformation Assessment	This involves the manufacture of test samples which are designed to deform on removal from the SLM base plate as a result of residual stresses. The amount of distortion is a measure of the residual stress levels developed within the sample during manufacture. It is a fast and cost effective qualitative method for through thickness residual stress estimation. Deformation assessment works best for quick comparative analysis of specimens but does not provide any quantitative results and choosing the optimum geometry for deformation assessment is very important[10, 25, 27, 30].
Splitting	A cut is made into the specimen and the opening or closing of the material adjacent to the cut shows the sign and magnitude of Residual Stress. Strain relaxation gives an indication of the residual stress. Splitting gives a quick qualitative measure of residual stress through the specimen thickness.

It is a quick and cost effective analysis method which is useful for routine comparative quality control as it can give an indication of the direction to reduce residual stress.

Splitting does not work well with non-uniform and untypical stresses and since there is no quantification of stresses so is only valid for comparative analysis[5, 53].

Sectioning Specimen is sectioned into strips and strain gages (Mechanical or Electrical) or diffraction methods can be used to measure strain relaxation to get the size and location of residual stress. Strain relaxation gives a measure of the residual stress through the specimen thickness.

Sectioning is a quick and cost effective method with 10-30% precision. It is useful for specimens with more regular shaped geometry where uni-axial stresses are important while calculations for multiple sectioning can be challenging. Useful for measuring uniaxial stresses in regular geometries[5, 53].

Layer Removal Layers of material are removed while strain gages attached to the opposite surface are used to measure the stress relaxation in the remaining material. Strain relaxation gives a measure of the residual stress through the specimen thickness.

Layer removal is a relatively simple method applicable to a wide range of materials with 10-30% precision in measurements. It can be combined with other techniques such as X-ray diffraction and magnetic techniques to give a stress profile or it can be modified into non-destructive technique to suite the process (e.g. Additive manufacturing).

It is a laboratory based method suitable for measurements in flat Plates and cylinders of uniform thickness. Layer removal can be a time consuming procedure and is subject to measurement drift used for specific geometries where stresses are uniform parallel to surface [5, 42, 53, 88].

Hole Drilling
(uniform
stress)

A hole is drilled through the specimen and strain gages on the surface or full field optical techniques measure the change in strain. Strain relaxation in the surroundings of the hole gives a measure of the residual stress. Residual stress can be measured up to 2mm and measurement precision typically ranges between 5–20%. Hole drilling is a semi-destructive method with portable equipment capable of measuring bi-axial stress σ_{xx} , σ_{yy} , and τ_{xy} . It is a quick, easy and cost effective method capable of measurements for both metals and non-metals as hole drilling is indifferent to grain structure. Hole drilling is only capable of near surface measurements of in-plane stress profiles. Stresses are non-uniform

and max stress can range up to 70% of yield stress. Since it is a semi destructive so can be used to take measurements and different locations and different points in life of specimen. Hole needs to be filled after testing and since the hole is very small so the part can still be used. σ_{zz} cannot be measured and for residual stresses greater than 80% σ_{yield} the uncertainty in measurements increases. This method is not suitable for complex geometries as surface preparation is needed and measurements are sensitive to non-concentricity of the hole and strain gage.

Strain gage noise can result in inaccuracies. Stresses are being relieved at depth and strains measured at surface is a source of inaccuracy [2, 5, 25, 27, 53, 85-88].

Hole Drilling (stress profile) A hole is drilled through the specimen and strain gages on the surface or full field optical techniques measure the change in strain. Strain relaxation in the surroundings of the hole gives a measure of the residual stress. Residual stress can be measured up to 2mm and measurement precision typically ranges between 5–20%. Hole drilling is a semi-destructive method with portable equipment capable of measuring bi-axial stress σ_{xx} , σ_{yy} , and τ_{xy} .

It is a quick, easy and cost effective method capable of measurements for both metals and non-metals as hole drilling is indifferent to grain structure. Hole drilling is only capable of near

surface measurements of in-plane stress profiles. Stresses are non-uniform and max stress can range up to 70% of yield stress. Since it is a semi destructive method so can be used to take measurements and different locations and different points in life of specimen. Hole needs to be filled after testing and since the hole is very small so the part can still be used. σ_{zz} cannot be measured and for residual stresses greater than 80% σ_{yield} the uncertainty in measurements increases. This method is not suitable for complex geometries as surface preparation is needed and measurements are sensitive to non-concentricity of the hole and strain gage.

Strain gage noise can result in inaccuracies. Stresses are being relieved at depth and strains measured at surface is a source of inaccuracy [2, 5, 25, 27, 53, 85-88].

Deep Hole

A hole is drilled into the specimen and then the surrounding material is over cored to see how the diameter of the hole changes which gives a measure of the residual stress. Strain relaxation gives a measure of the residual stress through the specimen thickness. Measurement precision typically ranges between 5–15%.

It is a semi-destructive so can be used to take measurements at different locations and different points in life of specimen. Portable equipment capable of bi-axial measurements (σ_{xx} , σ_{yy} or τ_{xy})

including stress gradients. Measuring σ_{zz} is possible but tedious and not precise. Applicable to even complex geometries. It can be used for both metals and non-metals as measurements are indifferent to grain structure and surface finish. Relatively fast process based on the amount of stress data produced.

Can be done only by specialists and the measurements are compromised by plasticity. Semi-destructive so hole may need filling up. Cannot be applied to specimens less than 6mm thickness [5, 53, 88].

Slitting (Crack Compliance or Slotting) A long slit is made into the specimen and strain gages attached on the same or opposite surface measure the deformation in the surrounding material to give a measure of Residual Stress. Strain relaxation gives a measure of the residual stress.

Measurements can be made through specimen thickness with an accuracy of 5–20%. It is a quick and easy to apply technique which can provide a good residual stress gradient data. The technique is applicable to both metals and non-metals as measurement is indifferent to grain structure. A good EDM cut can provide a surface for further analysis such as contour measurement. Strain gages on both surfaces can be used for cross referencing.

Cutting machine determines the limitation on depth of cut. Only 1-D perpendicular stress in prismatic shaped specimens can be measured. It is a laboratory based destructive measurement technique only due to the nature of the equipment. Uni-Axial Residual Stress measurements with increased uncertainty and cannot be used for complex geometries or evaluation of complex stress fields. Uncertainty increases for higher magnitude of residual stresses. Surface preparation needed as strain gages are susceptible to noise [23, 29].

Contouring

In contour method a specimen is sectioned along cross-section using a wire EDM. The surface height profiles of both the cut surfaces are measured using a coordinate measuring machine or a laser profilometer to account for cutting asymmetry. The deformation of the cut surfaces are a result of the Residual Stresses (pull inwards for tensile stresses, bulge outward for compressive stresses). Residual Stresses normal to the cut are given by finite element calculations and are equal to the stresses required to return the deformed surface shape acquired from the average of the two cut surfaces to a flat plane. Strain Relaxation combined with Bueckner's superposition principle gives a measure of the Residual Stress.

Contour method gives a stress full 2D stress map along specimen cross section and the measurements are accurate with 5–20%. Wire EDM and Coordinate Measurement Machine's axis ranges can limit the depth of measurement. Accuracy is independent of the depth of cut and indifferent to grain structure. A good EDM cut can provide surface for further processing such as etching.

It is a destructive technique which requires very accurate cutting and is not good for near-surface measurements. Data needs to be filtered and smoothed which compromises accuracy. Getting residual stress data from the contour measurement requires awareness of Finite Element Software. The costs of measurement are really high and the availability of the testing mechanism is limited which makes it very difficult to get a large number of samples to be tested [5, 53, 89].

X-ray
Diffraction

One of the most widely used non-destructive techniques for residual stress measurement. X-rays are directed to the test specimen surface and diffracted X-rays are capture by a detector. X-rays interact with electrons of the atoms and therefore their penetration depth will vary according to changing atomic number of a material. Stress is evaluated from strain values using Young's

modulus, Poisson ratio and taking into consideration the Elastic Anisotropy of the material.

Residual stress in the material causes the inter-planar spacing of the material to change from their stress free spacing d_0 . Changes in the inter-planar spacing “d” can be used with the Bragg’s equation to detect elastic strain “ ε ” through a change in the Bragg scattering angle $\Delta\theta$.

Depth of penetration is less than 0.03mm and stress can be measured within 20 MPa. With X-ray diffraction both macro and micro stresses can be measured. It is a widely available and relatively quick, easily applicable and cost effective non-destructive technique capable of accurate measurement of high magnitude residual stress. Portable equipment makes bi-Axial (σ_{xx} and σ_{yy}) on site measurements possible. This technique is very good for surface stress gradient measurements. As long as the measuring head can be rotated freely stresses any complex geometry can be measured. The technique is good for near surface measurements on crystalline materials.

Measurement depth is limited and a stress free reference required. Diffraction is selective and hence biased towards a particular sets of grains. Variations in grain structure and surface texture affects accuracy. The technique is only applicable to polycrystalline

materials and requires a high surface finish[5, 25, 27, 43, 53, 88, 131].

Synchrotron
Diffraction

Similar to X-ray Diffraction but the X-rays are of much higher power. Residual stress in the material causes the inter-planar spacing of the material to change from their stress free spacing d_0 . Changes in the interplanar spacing “d” can be used with the Bragg’s equation to detect elastic strain “ ε ” through a change in the Bragg scattering angle $\Delta\theta$. Sometimes the Bragg angle θ is held constant and the energy change of the diffracted rays is measured.

It is a fast and non-destructive technique capable of measurement depths greater than 5mm within 50 MPa. The technique has a good penetration depths (varies according to the material) and is capable of measuring tri-axial stresses (σ_{xx} , σ_{yy} and σ_{zz}). Stress gradients can be measured effectively because of the small gauge volume (typically $< 1mm^3$) and is well suited for good measurement of high residual stresses. Can be used for complex geometries as only a beam access window is needed. No surface finish is required as the technique is indifferent to surface finish and capable of measuring both macro and micro stresses.

Requires synchrotron radiation source and zero stress reference. Laboratory based measurement restricts size and weight of specimens. Material need to be polycrystalline accuracy is

dependent on grain size and texture. This a very expensive technique with limited availability [5, 53, 88].

Neutron
Diffraction

Neutrons are directed to the surface of the test specimen and diffracted neutrons are captured by a detector similar to the X-ray diffraction method. Since the neutrons interact with the nucleus of an atom therefore they penetrate equally in materials of varying atomic numbers. Residual stress in the material causes the interplanar spacing of the material to change from their stress free spacing d_0 . Changes in the interplanar spacing “d” can be used with the Bragg’s equation to detect elastic strain “ ε ” through a change in the Bragg scattering angle $\Delta\theta$. Penetration depth ranges 25mm for steel and 100mm for Aluminum giving measurements within 50 MPa.

It is a non-destructive technique with good penetration depths (varies according to the material) capable of measuring tri-axial stresses (σ_{xx} , σ_{yy} and σ_{zz}). Neutron diffraction can be used for measuring stress gradients and is good for measurement of high residual stresses. It can be used for complex geometries as only a beam access window is needed and no surface finish is required since it is indifferent to surface finish. Both macro and micro stresses measured and is deeper non-destructive measurement technique than synchrotron.

Requires neutron radiation source and zero stress reference. It is a laboratory based measurement technique which restricts size and weight of specimens. Material need to be polycrystalline and accuracy is dependent on grain size and texture. The method is not suitable for surface measurements. It is an expensive method with limited availability [5, 25, 27, 43, 53, 88].

Magnetic BNA Magnetization of ferromagnetic material is reversed and the re-orientations of the magnetic domains are observed as pulses which are called noise due to their random amplitude, duration and temporal separation. Based on measurement of Magnetic Barkhausen Noise capable of measurements up to 1mm depth within >25 MPa.

This is a very fast method and there are a variety of magnetic techniques available. Equipment is portable so can be used in field.

This technique can be used for stress measurement in ferromagnetic materials only and the equipment requires material-specific calibration. Application is restricted due to ferromagnetic material requirement and the microstructure signals need to be separated from those due to stress which can result in inaccuracy [5, 53, 88].

Ultrasonic An ultrasonic (acoustic) wave is induced in the material and the reflected, transmitted, or scattered wave's velocity is measured. The velocity of some mode of reflected transmitted or scattered ultrasonic wave gives a measure of the residual stress.

Ultrasonic residual stress measurement is capable of measurement in the depth range of 1–20mm within >25 MPa.

It is readily available, very fast and low cost technique with portable equipment so can be used in field. A good method for low-cost comparative measurements.

Equipment requires material-specific calibration and the velocity of ultrasonic waves can also be affected by the grain size, texture, second phases and other micro-structural characteristics which affects accuracy of measurements. Limited resolution and only good for bulk measurements over the whole volume [5, 53, 88].

Residual stress measurement is derived from the dependency of changes in thermal energy of an elastic material with changes in the mechanical elastic strain. Dynamically loaded specimen's rate of change in temperature can be compared to the rate of change of the principal stresses sum under adiabatic conditions to infer a relationship between thermal emission and stress. Changes in infrared emission due to minute changes in the temperature of

Thermoelastic

dynamically stressed material is measured to infer a measure of Stresses.

It is a low cost qualitative comparative technique and low sensitivity of the temperature changes to residual stresses limits its applicability[53].

Photoelastic (Birefringent) Polarized light is transmitted through a stressed specimen which produces a colored fringe pattern indicating the shear stresses within the material. Commonly used for transparent materials but can be modified but a variation of the method (coating opaque materials with photoelastic polymer) can be used in combination with some strain relieving methods to see birefringence patterns through a reflection polariscope. The directional change in the refractive index of a material gives a measure of the Residual Stress. This method is capable of measuring residual stress through the specimen thickness with 10–30% accuracy. Full-field measurements in transparent materials.

It is a qualitative method applicable to transparent materials only whereas quantitative measure can be achieved with calibration[53].

Indentation Surface hardness is measured by indentation. The presence of tensile residual stresses slightly decrease the hardness while compressive residual stresses slightly increase the hardness. Change in the hardness of a material due to the presence of stresses is used as a measure of residual stress.

It is a qualitative measurement method which can be used for comparative measurement to a depth under 1mm[53].

Appendix-B. FORTRAN Subroutines

B.1 DFLUX

```
c      DFLUX SUBROUTINE
      subroutine dflux(flux,sol,kstep,kinc,time,noel,npt
2      ,coords,jltyp,temp,press)
c
      include 'ABA_PARAM.INC'
c
c      Initialising variables
      dimension flux(2),time(2),coords(3)
      parameter (PI=3.1415926535)
      integer NI, SpotNumber, LineNumber, SpotsPerLine
      real*8 x0, y0, z0, x, y, z, L0, SpotDistance, Exposure
      real*8 xinc, W, H, yinc, TimeToSwitchLines
      real*8 vw,r,rp,rs,d,lt
      real*8 q,tho,Hs,Iz
      real*8 omega
      real*8 temp
      real*8 N
c      Defining Laser scan speed in mm/sec.
      PARAMETER(vw=650)
c      Defining the laser's spot size in mm.
      PARAMETER(rlas=0.05)
      PARAMETER(d=0.1)
c      Laser's Efficiency
      PARAMETER(eff=1)
c      Power of Laser in milli Watts
      PARAMETER(pow=200000)
c
c      Define the hatch distance (Distance between two scan
lines).
      xinc=0.08
      yinc=0.08
c      Width of the powder layer.
      W=0.33
c      Length of the powder layer.
      H=1.04
c      Layer Thickness
      lt=0.05
c -----
-----
c -----
-----
```

```

c -----
-----
c
    ts=time(1)
c    Define Spot Distance
    SpotDistance=0.065
c
c    Define Exposure
    Exposure=0.00065
c
c    Define Line Number
    LineNumber=(ts*vw)/H
    LineNumber=INT(LineNumber)
c
c    Define Number of Spots per Line
    SpotsPerLine=H/SpotDistance
    SpotsPerLine=INT(SpotsPerLine)
c
c    Define Spot Number
    SpotNumber=INT(SpotNumber)
    SpotNumber=((ts-(LineNumber*Exposure))/Exposure)
c
c    Iniatilize tool centre.
    x0=0
    y0=0
c
c    Define Overall length of scan vector to control rotation
of laser direction.
    L0=((y0)+(vw*ts))
    N=L0/H
    NI=INT(N)
    N=REAL(NI)
c
c    Define condition for laser movement direction for Layer
number 1,5,9,....
    If (MOD((KSTEP-3),8).eq.0) THEN
c    Increment X by Hatch distance.
    x0=x0+(LineNumber*xinc)
c    Condition for scanning Odd vectors from bottom-end at 0 to
top-end 0.025.
        IF ((MOD (NI,2).eq.0)) THEN
c    Keep the Laser moving in Positive-Y direction till the
top-end of Odd vectors (1,3,5...) is reached.
        y0=y0+(SpotDistance)*(SpotNumber-
(LineNumber*SpotsPerLine))
        Else

```

```

c      Keep the Laser moving in Negative-Y direction till the
bottom-end of Even Vectors (0,2,4,6...) is reached.
      y0=H-(SpotDistance)*((SpotNumber)-
(LineNumber*SpotsPerLine))
      END IF

c
c      Define condition for laser movement direction for Layer
number 2,6,10,.....
      ELSE IF (MOD((KSTEP-5),8).eq.0) THEN
c      Increment Y by Hatch distance.
      y0=y0+(LineNumber*yinc)

c
c      Define condition for laser movement direction.
      IF ((MOD (NI,2).eq.0)) THEN
c      Keep the Laser moving in Negative-X direction till the
Left-end of Even Vectors (0,2,4,6...) is reached.
      x0=W-(SpotDistance)*((SpotNumber)-
(LineNumber*SpotsPerLine))
      Else
c      Keep the Laser moving in Positive-X direction till the
Right-end of Odd vectors (1,3,5...) is reached.
      x0=x0+(SpotDistance)*((SpotNumber)-
(LineNumber*SpotsPerLine))
      END IF

c
c      Define condition for laser movement direction for Layer
number 3,7,11,.....
      ELSE IF (MOD((KSTEP-7),8).eq.0) THEN
c      Decrement X by Hatch distance.
      x0=W-(LineNumber*xinc)
c      Condition for scanning Odd vectors from bottom-end to top-
end.
      IF ((MOD (NI,2).eq.0)) THEN
c      Keep the Laser moving in Negative-Y direction till the
bottom-end of Even Vectors (2,4,6...) is reached.
      y0=H-(SpotDistance)*((SpotNumber)-
(LineNumber*SpotsPerLine))
      Else
c      Keep the Laser moving in Positive-Y direction till the
top-end of Odd vectors (1,3,5...) is reached.
      y0=y0+(SpotDistance)*((SpotNumber)-
(LineNumber*SpotsPerLine))
      END IF

c
c      Define condition for laser movement direction for Layer
number 4,8,12,.....

```

```

ELSE IF (MOD((KSTEP-9),8).eq.0) THEN
c
c   Decrement Y by Hatch distance.
   y0=H-(LineNumber*yinc)
c
       IF ((MOD (NI,2).eq.0)) THEN
c       Keep the Laser moving in Positive-X direction till the
Right-end of Odd vectors (1,3,5...) is reached.
           x0=x0+(SpotDistance)*((SpotNumber)-
(LineNumber*SpotsPerLine))
           Else
c       Keep the Laser moving in Negative-X direction till the
Left-end of Even Vectors (0,2,4,6...) is reached.
           x0=W-(SpotDistance)*((SpotNumber)-
(LineNumber*SpotsPerLine))
           END IF
c
       END IF
c
c
c   Calculation of polar coordinates
       x=coords(1)
       y=coords(2)
       z=coords(3)
       r=sqrt((x-x0)**2+(y-y0)**2)
c
c       Define Laser intensity in radial direction.
       Hs=(2.55*pow/(pi*(rlas**2)))
c
c       Define Laser intensity variation in depth direction (z-
axis)
       Iz=(-15*(z)**2+4*(z)+2)
c
c       Defining that temperature is evaluated from solution.
       temp=sol
c
c       Test of node position and flux assignment
       if (r.le.rlas) then
           flux(1)=(0.6*0.864*(Hs*Iz))
       Else
           flux(1)=0
       end if
c
       return
end

```

B.2 USDFLD

```
C    USDFLD SUBROUTINE
      SUBROUTINE USDFLD(FIELD,STATEV,PNEWDT,DIRECT,T,CELENT,
1    TIME,DTIME,CMNAME,ORNAME,NFIELD,NSTATV,NOEL,NPT,LAYER,
2    KSPT,KSTEP,KINC,NDI,NSHR,COORD,JMAC,JMATYP,MATLAYO,
3    LACCFLA)
C
      INCLUDE 'ABA_PARAM.INC'
C
      CHARACTER*80 CMNAME,ORNAME
      CHARACTER*3  FLGRAY(15)
      DIMENSION FIELD(NFIELD),STATEV(NSTATV),DIRECT(3,3),
1    T(3,3),TIME(2)
      DIMENSION ARRAY(15),JARRAY(15),JMAC(*),JMATYP(*),
1    COORD(*)
C
C Get temperatures from previous increment
      call getvrm('TEMP',array,jarray,flgray,jrcd,
1    jmac, jmatyp, matlayo, laccfla)
      TEMP = array(1)
C*****
C define the melting temperature and create logic to change
field variable
      TMELT=1660
      If (TEMP.GT.TMELT) then
        FIELD(1)=2.0
        STATEV(1) = 2.0
      ENDIF
      FIELD(1)=STATEV(1)
C write statement to verify the change in values
C This will print the value in the command window
c    write(*,*) time(1), field(1),STATEV(1)
      RETURN
      END
```